

University of London  
**Imperial College of Science, Technology, and Medicine**  
Mechanical Engineering Department  
Exhibition Road  
London SW7 2BX

# **Leaky Guided Ultrasonic Waves in NDT**

by

**Brian Nicholas Pavlakovic**

A thesis submitted to the Univeristy of London for the degree of

**Doctor of Philosphy**

**October 1998**

# Abstract

This thesis concentrates on the development of a general purpose model of ultrasonic wave propagation in leaky cylindrical structures and the integration of this model with finite element modeling so that effective ultrasonic non-destructive testing (NDT) techniques can be developed. The analytical model that has been developed provides information on the guided modes that can exist in a wide range of infinitely-long, multi-layered, isotropic and transversely isotropic, Cartesian and cylindrical systems. The discussions in this thesis concentrate on the complicated case of cylindrical layers whose energy leaks into surrounding semi-infinite spaces. Using techniques developed in this thesis, the analytical wave modeling results are integrated with time domain finite element modeling to extract additional information about the behaviour of the guided ultrasonic waves, such as how they will interact with defects. This information allows non-destructive testing strategies to be developed for many challenging applications. One such application that motivated much of the work on this wave propagation model is the inspection of post-tensioned bridges. The recent unexpected collapse of this type of bridge in Wales emphasised that there are currently no inspection techniques that are reliable, practical, and inexpensive enough to routinely evaluate the integrity of this type of bridge. The model that is developed in this work has been applied to this inspection problem to evaluate the possibility of propagating guided waves down embedded steel tendons to evaluate the condition of post-tensioned bridges by looking for reflections from fractures or loss of section due to corrosion. Several modes that would allow reasonable amounts of the tendons to be tested from their ends have been identified and confirmed experimentally on realistic test specimens. These modes can provide valuable information on the integrity of the anchorages, a sensitive region that cannot currently be inspected.

# Acknowledgements

I would like to thank my supervisors, Mike Lowe and Peter Cawley, for their invaluable guidance. They have injected me with knowledge and new ideas, as well as providing support.

I would also like to thank the other members of the non-destructive testing laboratory who have helped me understand guided waves, computer systems, and friendship. Together, we make a powerful team.

The Marshall Aid Commemoration Commission must be thanked for their financial assistance, which helped support this work and my stay in the United Kingdom.

Finally, I must acknowledge the support of my family and friends, whom I feel are always at my side although we may be separated by many miles.

# Contents

<b>1</b>	<b>Introduction</b>	<b>19</b>
<b>2</b>	<b>Derivation of Cylindrical Wave Propagation Model</b>	<b>24</b>
2.1	Introduction to Global Matrix Solution Method . . . . .	25
2.2	Historical Background of Cylindrical Wave Propagation . . . . .	26
2.3	Assumptions and Limitations . . . . .	27
2.4	Boundary Conditions . . . . .	28
2.5	Wave Propagation in Infinite Media . . . . .	29
2.6	Development of Cylindrical Isotropic Model . . . . .	30
2.6.1	Expansion in Cylindrical Coordinates . . . . .	33
2.6.2	Displacement Field . . . . .	40
2.6.3	Stress Field . . . . .	41
2.6.4	Material Layer Matrix . . . . .	42
2.6.5	Liquids . . . . .	45
2.7	Transversely Isotropic Cylindrical Layers . . . . .	46
2.7.1	Equations of Motion . . . . .	47
2.7.2	Determination of Potential Functions . . . . .	48
2.7.3	Solution of the Potential Functions . . . . .	51
2.7.4	Creation of the Layer Matrix . . . . .	53
2.8	Software Implementation of Model . . . . .	56
2.8.1	Global Matrix method . . . . .	56
2.8.2	Finding a Root . . . . .	57
2.8.3	Tracing a Dispersion Curve . . . . .	60
2.8.4	Mode Shapes . . . . .	61
<b>3</b>	<b>Cylindrical Wave Propagation Examples</b>	<b>62</b>
3.1	Cylinders in Vacuum . . . . .	63
3.1.1	Projections . . . . .	63
3.1.2	Naming . . . . .	66
3.1.3	Nature of the Modes in Solid Cylinders . . . . .	67
3.1.4	Nature of the Modes in Hollow Cylinders . . . . .	69
3.1.5	Effect of Changing the Radius . . . . .	74
3.2	Cylinders Immersed in a Fluid . . . . .	76
3.2.1	Modelling the Fluid inside the Cylinder . . . . .	76
3.2.2	Leakage into the Surrounding Medium . . . . .	80
3.3	Cylinders Embedded in a Solid . . . . .	81
3.3.1	Different Types of Leakage . . . . .	83
3.3.2	Multi-layered Cylinders Embedded in a Solid . . . . .	84
3.4	Summary of Cylindrical Examples . . . . .	92
<b>4</b>	<b>Validation of Cylindrical Wave Propagation Model</b>	<b>94</b>
4.1	Validation against Asymptotic Limits . . . . .	95

4.2	Validation against Published Literature on Cylindrical Wave Propagation . . . . .	99
4.2.1	Gazis . . . . .	99
4.2.2	Nagy and Nayfeh . . . . .	101
4.2.3	Berliner and Solecki . . . . .	104
4.3	Internal Consistency of Solutions . . . . .	105
4.3.1	Multiple Layers . . . . .	106
4.3.2	Mode Shape Consistency . . . . .	107
4.4	Agreement with Finite Element Results . . . . .	115
4.4.1	Phase Velocity Extraction . . . . .	117
4.4.2	Attenuation Extraction . . . . .	121
4.5	Experimental Verification of Leakage Rate Along a Bar . . . . .	123
4.6	Summary of Validation . . . . .	131
<b>5</b>	<b>Finite Element Techniques Used in Combination with the Wave Propagation Model</b>	<b>132</b>
5.1	Why Finite Element Modelling . . . . .	133
5.2	Review of Finite Element Techniques used for Guided Wave Propagation . . . . .	135
5.3	Extension of the Finite Element Techniques to Model Leakage . . . . .	136
5.4	Separation of Propagating Modes - Review of the 2-D FFT . . . . .	138
5.5	Through Thickness Mode Extraction . . . . .	139
5.5.1	Overview of Mode Extraction . . . . .	139
5.5.2	Benefits of Using Mode Extraction . . . . .	140
5.5.3	Solution Algorithm . . . . .	141
5.5.4	Results . . . . .	145
5.5.5	Mode Extraction Conclusions . . . . .	148
5.6	Pure Mode Excitation . . . . .	149
5.6.1	Centre Mode Shapes . . . . .	151
5.6.2	Exact Mode Shapes . . . . .	153
5.6.3	Cylindrical Example of Exact Mode Shapes . . . . .	155
5.6.4	Leaky Example of Exact Mode Shapes . . . . .	158
5.6.5	Summary of Pure Mode Excitation . . . . .	160
<b>6</b>	<b>Finite Element Determination of Reflection Coefficients</b>	<b>161</b>
6.1	Review of Techniques for Low Frequency Free Systems . . . . .	161
6.2	Extension to Leaky Systems . . . . .	165
6.3	Reflection Coefficients for L(0,1) in an Embedded Steel Bar . . . . .	168
6.3.1	Comparison Between Free and Embedded Systems . . . . .	169
6.3.2	Grout Filled Square Notches . . . . .	171
6.3.3	Orientation of the Notch . . . . .	173
6.3.4	Defects in the Surrounding Grout . . . . .	176
6.3.5	Transition between Leaky and Free Systems . . . . .	178
6.4	Higher Order Reflection Coefficients . . . . .	183
6.5	Summary of Embedded Reflection Coefficients . . . . .	185
<b>7</b>	<b>Application to Post Tensioned Bridges</b>	<b>186</b>
7.1	Background of Post Tensioned Bridge Inspection . . . . .	186
7.1.1	Construction . . . . .	187
7.1.2	Current Inspection Techniques . . . . .	187
7.1.3	Guided Wave Access . . . . .	189
7.2	Model Parameters . . . . .	190
7.2.1	How the System is Modelled . . . . .	190
7.2.2	Mode Selection Criteria . . . . .	191
7.3	Search for a Non-Leaky Mode . . . . .	193
7.4	Search for a High Frequency Alternative . . . . .	199
7.5	Experimental Results . . . . .	202

---

7.5.1	Experiments on Grouted Bars . . . . .	203
7.5.2	Experiments on Grouted Seven Wire Strands . . . . .	208
7.6	Summary of Grouted Tendon Inspection . . . . .	210
<b>8</b>	<b>Conclusions</b>	<b>213</b>

# Nomenclature

<b>A</b>	vector of partial wave amplitudes
$A, A_i, A'_i$	unknown amplitudes
$a$	constant
$a, a_{ref}$	values of the amplitude of the normalised frequency response
$\alpha^2$	$\omega^2/c_1^2 - \xi^2$
$\alpha_l$	longitudinal material damping coefficient
$\alpha_s$	shear material damping coefficient
$B$	unknown amplitude
$B_{n,r}$	Bessel function differential operator
$b$	constant
$\beta$	$\omega^2/c_2^2 - \xi^2$
$c_{ijkl}$	stiffness tensor (of rank 4)
$\hat{C}_{ij}$	stiffness constants (abbreviated subscripts)
$C_i$	unknown amplitude
$c_1$	bulk longitudinal velocity (for isotropic materials)
$c_2$	bulk shear velocity (for isotropic materials)
$c_{ph}$	phase velocity
$c_r$	Rayleigh velocity
<b>D</b>	material layer matrix
$d$	thickness of a plate (as in $fd$ for frequency-thickness)
$d$	length of protruding end of an embedded bar
$\partial$	partial differential operator
$\nabla$	vector differential operator
$\nabla^2$	Laplace operator
$\Delta$	dilatation
$E$	Young's modulus
$\epsilon_{ij}$	a strain component
$e$	2.71828... ( $\ln(e) = 1$ )

$F$	external force
$f(r)$	radial behaviour of scalar potential function
$f$	frequency (non-circular – not used in derivation)
$f_{min}$	minimum frequency
$[\mathbf{G}]$	global matrix
$g_i(r)$	radial behaviour of equivoluminal potential function
$\gamma_1, \gamma_2$	parameter to account for difference in recurrence relations
$\mathbf{H}$	equivoluminal vector potential
$H_i$	equivoluminal vector potential component
$\mathbf{H}_n^{(1)}$	Hankel function of the first kind
$\mathbf{H}_n^{(2)}$	Hankel function of the second kind
$h$	thickness of the plate
$\mathbf{I}$	identity matrix
$i$	$\sqrt{-1}$
$i, j, k, l$	indices
$\mathbf{I}_n$	modified Bessel function of the first kind
$\infty$	infinity
$\mathbf{J}_n$	Bessel function of the first kind
$\mathbf{K}_n$	modified Bessel function of the second kind
$\mathbf{KE}$	kinetic energy
$\mathbf{k}$	wavenumber vector
$\mathbf{k}_{real}, \mathbf{k}_r$	real part of the wavenumber vector
$\mathbf{k}_{imag}, \mathbf{k}_i$	imaginary part of the wavenumber vector
$k_i$	a wavenumber component
$\kappa, \kappa_0, \kappa_i$	value of the attenuation (in nepers per wavelength or nepers per metre)
$L$	compressional partial wave amplitude
$\lambda$	a Lamé constant (isotropic case)
$\lambda$	a constant (transversely isotropic case)
$\lambda$	wavelength (discussion of results)
$m, n$	mode indices
$\mu$	a Lamé constant
$n$	circumferential order
$\eta$	constant = $-i\lambda$ (transversely isotropic case)



---

$\langle O \rangle$	result of applying mode orthogonality relationship
$\omega$	the frequency (circular)
$P$	power flow
$\langle \mathbf{P} \rangle$	average total power flow
$p^2, p_1^2, p_2^2$	wavenumber component roots (see equations 2.58 and 2.61)
$\phi$	compressional scalar potential (isotropic case)
$\varphi, \psi$	potential functions (transversely isotropic case)
$\pi$	3.141592...
$\langle Q \rangle$	result of applying half of the orthogonality relationship
$q_2$	wavenumber component root (see equation 2.65)
$R$	$(c_2/c_1)^2$ (in Rayleigh velocity calculation)
$\rho$	the density
$r$	radius
$r_{inner}$	the inner radius of a pipe
$\hat{r}$	the radial direction
$\mathbf{r}$	positional vector
$rc$	reflection coefficient ratio
$S$	cross sectional area
<b>SE</b>	strain energy
<b>SED</b>	strain energy density
$SH$	shear horizontal partial wave amplitude
$SV$	shear vertical partial wave amplitude
$\sigma_{ij}$	a stress component
$\vec{\sigma}$	stress diadic
$T$	$(c_r/c_2)^2$ (in Rayleigh velocity calculation)
$t$	time
$\theta$	circumferential angle
$\Theta(\theta)$	circumferential dependence of wave potential
$\theta_{leak}$	leakage angle
$\mathbf{u}$	particle displacement vector
$u_r$	radial displacement component
$u_\theta$	circumferential displacement component
$u_z$	axial displacement component

---

$\mathbf{v}$	partical velocity vector
$v_{inc}$	velocity of an incident bulk wave
$v_{gr}$	group velocity
$v_{long}, v_l$	bulk longitudinal velocity
$v_{ph}$	phase velocity
$v_s$	bulk shear velocity
$\nu$	Poisson's ratio
$W_n$	placeholder for a Bessel function of the second kind
$\mathbf{x}$	positional vector
$x$	distance measurement
$\chi$	an arbitrary function
$\Xi$	an arbitrary function
$\xi$	the axial wavenumber (real or complex)
$\xi_r$	real part of the axial wavenumber
$\xi_i$	imaginary part of the axial wavenumber
$\zeta_1 = \sqrt{\pm p_1^2}$	a radial wavenumber component
$\zeta_2 = \sqrt{\pm p_2^2}$	a radial wavenumber component
$\zeta_3 = \sqrt{\pm q^2}$	a radial wavenumber component
$\mathbf{Y}_n$	Bessel function of the second kind
$Z_n$	placeholder for a Bessel function of the first kind
$z, z_0, z_1$	axial position
$\hat{z}$	unit vector in axial direction

# List of Tables

2.1	Substitutions that should be made and criteria that should be used for the selection of the type of Bessel functions to be used for the cylindrical layer matrix. . . . .	38
2.2	Criteria for the the choice of phase for the arguments of the Bessel functions depending on the type of Bessel function and the type of wave (homogeneous or inhomogeneous). . . . .	40
2.3	Substitutions that should be made and criteria that should be used for the selection of the type of Bessel functions to be used for the transversely isotropic cylindrical layer matrix. . . . .	55
3.1	Material constants used for isotropic materials in the wave propagation modelling. . . . .	93
3.2	Material constants used for transversely isotropic materials in the wave propagation modelling. . . . .	93
6.1	Summary of the reflection coefficients for four different types of notches in a steel bar. . . . .	177
7.1	Material constants used in the wave propagation modelling of grouted tendons. . . . .	191

# List of Figures

1.1	An illustration of how guided ultrasonic waves could be used in a pulse-echo configuration to examine the ends of embedded tendons in post-tensioned bridges. . . . .	21
2.1	Sample geometry of a five layer cylindrical system showing the partial waves in each layer (L <sup>+</sup> , SV <sup>+</sup> , and SH <sup>+</sup> ) that combine to produce a guided wave. . . . .	26
2.2	The structure of the global matrix for a (a) solid, (b) liquid, and (c) vacuum half-space, where blank spaces are zeros, $D_{ij}$ is the layer matrix, and L <sup>+</sup> , SV <sup>+</sup> , and SH <sup>+</sup> are the partial waves amplitudes in the various layers. . . . .	58
2.3	The process of finding a root involves a coarse sweep (thick line) to find an initial minimum and a fine search (dashed lines) to narrow down on a root (solid circle). The example above shows the absolute value of the determinant of the global matrix for a 1 mm steel plate immersed in water at a wave number of 4 rad/mm. . . . .	59
2.4	Using an extrapolating routine to trace modes dramatically improves the program's speed and reliability. . . . .	60
3.1	Various views of the dispersion curves for a 2 mm diameter steel bar in vacuum (zero and first circumferential order), including (a) real wave number, (b) phase velocity, (c) group velocity, and (d) angle of incident wave (in a perspex wedge) for optimal generation of modes. . . . .	64
3.2	Phase velocity dispersion curves for a 2 mm diameter steel steel bar with mode shapes super-imposed on the (a) fundamental modes and (b) higher order modes. . . . .	68
3.3	(a) The phase velocity dispersion curves for the six lowest-order axi-symmetric modes in a free SCS fibre (equivalent to figure 3 of Nayfeh and Nagy(1996)). (b) The phase velocity dispersion curves for the first circumferential order flexural modes in a free SCS fibre. The dashed lines correspond to the case when the materials are considered to be isotropic and the solid lines correspond to the solutions when the material anisotropy is included. . . . .	70
3.4	Phase velocity and group velocity dispersion curves for an empty 1 mm thick steel pipe with an inner radius of 2 mm. Modes of the lowest twenty circumferential orders have been shown. . . . .	72
3.5	Phase velocity and group velocity dispersion curves for the zero and first circumferential order modes of an empty 1 mm thick steel pipe with an inner radius of 2 mm. . . . .	73
3.6	The effect of increasing the inner radius of a 1 mm thick steel pipe. As the inner radius increases, the dispersion curves begin to very closely match the dispersion curves for a plate (shown in section f), except for very low frequencies. . . . .	75
3.7	A comparison of phase velocity and attenuation dispersion curves for three cases: a water filled steel pipe immersed in water, a water filled steel pipe immersed in water with a sink in the centre, and a steel plate in water. . . . .	77
3.8	A comparison of the axial displacement for a fluid filled pipe for a mode that is (a) predominantly in the fluid and (b) predominantly in the pipe wall. The top of the graph represents the fluid filled core, the middle section the steel wall of the pipe, and the bottom section the first 10 mm of the surrounding fluid . . . . .	78

3.9	Phase velocity dispersion curves for a 2 mm diameter steel bar immersed in water with mode shapes super-imposed on the fundamental modes. . . . .	80
3.10	As a guided wave travels down a bar, it couples energy into the surrounding fluid, creating a leaky bulk wave at a characteristic angle. . . . .	82
3.11	Phase velocity and attenuation dispersion curves for an empty 1 mm thick steel pipe with a 10 mm inner radius that is surrounded by soft stone (mudstone). . . . .	83
3.12	Phase velocity and attenuation dispersion curves for the zero and first circumferential order modes of a 1 mm radius steel bar embedded in a stiff material. The arrows and labels correspond to the positions for which the mode shapes are given in the next figure. The straight dotted lines correspond to the bulk velocities in the surrounding solid and divide the dispersion curves into different leaky regimes. . . . .	85
3.13	Mode shapes for a steel bar embedded in a stiff material in (a) a non-leaky region, (b) a region where only shear waves leak, and (c) a region where both shear and longitudinal bulk waves leak into the surrounding solid. . . . .	85
3.14	Phase velocity and attenuation dispersion curves (zero circumferential order modes) for a 1 mm thick steel pipe with a 10 mm inner radius that is lined with lossy grout and is surrounded by lossy soft stone (mudstone). . . . .	86
3.15	Phase velocity dispersion curves for the axi-symmetric modes of a 70 micron SCS fibre embedded in a titanium matrix. The width of the lines indicates the relative attenuation of the points on the mode (thicker lines correspond to lower attenuation values). . . . .	87
3.16	Phase velocity dispersion curves for 70 micron SCS fibre embedded in a titanium matrix (solid lines) overlaid on the dispersion curves for the free system (dashed lines). . . . .	87
3.17	Attenuation dispersion curves for the axi-symmetric modes of a 70 micron SCS fibre embedded in a titanium matrix. . . . .	88
3.18	Phase velocity dispersion curves for the first circumferential order modes of a 70 micron SCS fibre embedded in a titanium matrix. The line thickness indicates the amount of attenuation present (thin lines indicate high attenuation). The mode shapes for the points marked (a), (b), and (c) are shown in the following figure. . . . .	89
3.19	A comparison of the grid and line mode shapes for the three points marked on the dispersion curves for an embedded SCS fibre that are shown in the previous figure. . . . .	90
3.20	Phase velocity dispersion curves for the first circumferential order modes of a 70 micron SCS fibre embedded in a titanium matrix. The dashed lines represent the phase velocity curves for the free fibre and the solid lines correspond to the embedded case (with the thickness dictated by the attenuation of the embedded mode). . . . .	91
3.21	Phase velocity dispersion curves for the axi-symmetric modes of an embedded SCS fibre when an imperfect bond exists between the fibre and the surrounding titanium matrix. For comparison, the free case is shown as dashed lines. . . . .	92
4.1	A comparison between the wave number dispersion curves for a large radius steel pipe immersed in water and a steel plate that is water loaded on one side. (Solid lines = plate, tightly dashed lines = axi-symmetric modes, loosely dashed line = first order flexural modes) . . . . .	97
4.2	The low frequency, low wavenumber region of the wave number dispersion curves for a large radius steel pipe immersed in water and a steel plate that is water loaded on one side. (Solid lines = plate, tightly dashed lines = axi-symmetric modes, loosely dashed line = first order flexural modes) . . . . .	98
4.3	A comparison between the attenuation dispersion curves for a large radius steel pipe immersed in water and a steel plate that is loaded with water on one side. (Solid lines = plate, tightly dashed lines = axi-symmetric modes, loosely dashed line = first order flexural modes) . . . . .	99
4.4	The normalised frequency ( $fd/(2v_2)$ ) versus the normalised wavenumber ( $kd$ ) for the first circumferential order modes of a hollow cylinder consisting of a single isotropic layer which has a Poisson's ratio of 0.30 and a thickness ( $d$ ) to mean radius ratio of 1.0. (equivalent to (Gazis 1959) fig. 4) . . . . .	100

4.5	The normalised frequency ( $fd/(2v_2)$ ) versus the normalised wavenumber ( $kd$ ) for the first circumferential order modes of a hollow cylinder consisting of a single isotropic layer which has a Poisson's ratio of 0.30 and a thickness ( $d$ ) to mean radius ratio of 1/4. (equivalent to (Gazis 1959) fig. 5)	101
4.6	Detail of the three lowest first circumferential order (dashed) and second circumferential order (solid) modes near the zero frequency - wavenumber origin for a hollow cylinder consisting of a single isotropic layer which has a Poisson's ratio of 0.30 and a thickness ( $d$ ) to mean radius ratio of 1/30. (equivalent to (Gazis 1959) fig. 7)	102
4.7	Phase velocity dispersion curves for a 1 mm radius steel bar in water. Three sets of solutions have been overlaid; solid lines = isotropic solution, tight dashed lines = anisotropic solution, loosely dashed lines = Nagy's analytical solution. The dashed lines cannot be seen because all three curves overlay each other very well.	103
4.8	Phase velocity dispersion curves for a 1 mm radius graphite reinforced epoxy rod immersed in water. Two sets of solutions, which lie directly on top of each other, have been plotted; solid lines for the anisotropic solution and loosely dashed lines for Nagy's analytical solution.	103
4.9	Comparison of dispersion curves for a hollow (dashed lines) and fluid filled (solid lines) transversely isotropic cylinders (equivalent to Berliner and Solecki figure 4).	105
4.10	Comparison of dispersion curves for fluid filled (dashed lines) and fluid filled immersed (solid) transversely isotropic cylinders (equivalent to Berliner and Solecki figure 5).	106
4.11	Comparison of dispersion curves for an immersed SCS fibre when each constituent layer is modelled as a single layer (thin solid lines) and when each consistent layer is divided into sub layers (thicker dashed lines). As expected, the agreement between the two solutions is excellent.	108
4.12	Comparison of dispersion curves for an immersed SCS fibre when all of the layers use the isotropic model (thicker dashed lines) and when half of the sub-layers use the transversely isotropic model.	109
4.13	Dispersion curves for an immersed SCS fibre showing the locations used for the mode shape calculations in the following figures.	111
4.14	Comparison of the mode shapes for an immersed SCS fibre when the system is defined as 3 isotropic layers (solid lines) and when the system is defined with the same materials but as a combination of isotropic and anisotropic layers (dashed lines) for two points on the dispersion curves, (a) the L(0,3) mode at 8.4 MHz-mm and (b) the F(1,2) mode at 4.2 MHz-mm.	111
4.15	The ratio of the strain energy to the kinetic energy for a (a) 3 layer system with 120 integration points (zero and first order modes) and a (b) 7 layer system with 280 points (zero order modes only).	113
4.16	A comparison between the group velocity (dashed lines) and energy velocity (solid lines) dispersion curves for a free isotropic SCS fibre. The average difference between the two cases is less than 0.1 percent.	114
4.17	A comparison between the group velocity (dashed lines) and energy velocity (solid lines) dispersion curves for an immersed isotropic SCS fibre. As expected, the differences become apparent when the attenuation becomes very large. In many cases the group velocity curves had to be truncated at points where the attenuation of the mode starts to become excessive.	116
4.18	A comparison between the group velocity (dashed lines) and energy velocity (solid lines) dispersion curves for an isotropic SCS fibre embedded in a titanium matrix. Because of the high attenuation associated with most of the modes in this system, there is very little agreement between the two sets of curves.	116
4.19	A comparison between the phase velocity as calculated for by finite element modelling (dashed lines) and the wave propagation model (solid lines) for the fundamental axisymmetric mode of a 1 mm thick steel pipe with an inner radius of 0.5 mm.	119

4.20	Comparison of predicted time traces for the (a) 30 mm and (b) 50 mm propagation distance of the fundamental longitudinal mode of a 1 mm thick steel pipe with an inner radius of 0.5 mm, as calculated by the wave propagation model solution (solid lines) and finite element solution (dashed lines). The input signal consisted of a 10 cycle Gaussian windowed tone burst with a centre frequency of 0.885 MHz. . . . .	120
4.21	A comparison between the phase velocity as calculated by finite element modelling (dashed lines) and the wave propagation model (solid lines) for the third, first circumferential order, flexural mode of a 1 mm thick steel pipe with an inner radius of 0.5 mm. . . . .	120
4.22	A comparison between the phase velocity as calculated by finite element modelling (dashed lines) and the wave propagation model (solid lines) for the fundamental longitudinal mode of a 1 mm thick steel pipe with an inner radius of 0.5 mm that is surrounded by grout. . . . .	121
4.23	A plot of the decay of the maximum amplitude of the frequency spectrum of the fundamental longitudinal mode as it propagates in a 1 mm thick steel pipe with an inner radius of 0.5 mm that is surrounded by grout. . . . .	122
4.24	A comparison of the attenuation of the fundamental longitudinal mode of a 1 mm thick steel pipe with an inner radius of 0.5 mm that is surrounded by grout as calculated by finite element modelling (short dashes), the wave propagation model (solid lines), and the wave propagation model with the stiffness of the steel increased by five percent (long dashes). . . . .	124
4.25	The (a) wave number and (b) attenuation dispersion curves for zero, first, and second circumferential order modes, of a half inch (12.7 mm) diameter steel bar. The circles represent the experimental data that was obtained and the labels indicate the equivalent points on the dispersion curves. The dispersion curves were cropped to only show locations with moderate attenuations. . . . .	126
4.26	The (a) experimental configuration and (b,c) time traces that were used to experimentally determine the leakage rate of the fundamental longitudinal mode, L(0,1), in a half inch steel bar. . . . .	127
4.27	The (a) experimental configuration and (b,c) time traces that were used to experimentally determine the leakage rate of the fundamental flexural mode, F(1,1), in a half inch steel bar. . . . .	128
4.28	The experimental configuration used to collect the signals that were used for the two dimensional Fourier transform. . . . .	129
4.29	The (a) two dimensional transform obtained from a half inch diameter steel bar immersed in water along with (b) an example of a slice through the largest peak, whose irregularity indicates that the peak is composed of multiple modes. . . . .	130
4.30	Plots of the rate of decay of the (a) F(1,2) and (b) L(0,3) modes in a half inch diameter steel bar immersed in water. The dashed lines represent exponential decays that were fitted to the decays obtained from the 2-D FFT. . . . .	130
5.1	A schematic diagram showing how the two-dimensional transform technique[3] determines the amplitude of propagating Lamb wave modes by first transforming time into the frequency domain and then space into the wavenumber domain. . . . .	139
5.2	An example time trace from the finite element model of the A0 mode reflecting from the end of a 1 mm steel plate. . . . .	146
5.3	Group velocity dispersion curves for the anti-symmetric modes of a 1 mm steel plate. The frequency profile of a 15 cycle Gaussian windowed toneburst is shown as the greyed shape in the background. . . . .	146
5.4	The amplitude reflection coefficients (in terms of out-of-plane surface displacement) for the A0 mode incident on the edge of a 1 mm steel plate. The lines represent results obtained from the mode extraction technique and the circles represent results obtained using the 2-D FFT technique. . . . .	147

5.5	The group velocity dispersion curves for an aluminum plate. The three points marked (a), (b), and (c) correspond to the locations where modes are generated in the examples. . . . .	150
5.6	A schematic view of how the centre mode shape technique scales the input signal by the displacement profile at the desired centre frequency. . . . .	151
5.7	The (a) 2-D FFT and (b) sample time history for the generation of the A0 mode at 1.0 MHz using the centre mode shape technique and a 12 cycle Gaussian windowed tone-burst. . . . .	152
5.8	The (a) 2-D FFT and (b) sample time history for the generation of the A0 mode at 5.0 MHz-mm using centre mode shapes and a 2 cycle Gaussian windowed tone-burst. . . . .	152
5.9	The (a) 2-D FFT and (b) sample time history for the generation of the S2 mode at its maximum group velocity using centre mode shapes and a 10 cycle Gaussian windowed tone-burst. . . . .	153
5.10	A contour view and profile of the displacements in the direction of propagation of the S2 mode as a function of frequency-thickness and position through the thickness of the plate using (a) exact mode shapes and (b) centre mode shapes. The amplitudes shown in the contour view account for generation by a 10 cycle Gaussian windowed tone-burst at 6.8 MHz-mm. . . . .	154
5.11	The (a)2-D FFT and (b)sample time history for the generation of the A0 mode at 5.0 MHz-mm using exact mode shapes and a 2 cycle Gaussian windowed tone-burst. . . . .	155
5.12	The (a)2-D FFT and (b)sample time history for the generation of the S2 mode at its maximum group velocity using exact mode shapes and a 10 cycle Gaussian windowed tone-burst. . . . .	155
5.13	The 2-D FFTs and sample time histories for the generation of the L(0,2) mode in a steel bar at its maximum group velocity (around 2.5 MHz-mm frequency-radius) using (a) centre mode shape and (b) exact mode shapes, both with a 15 cycle Gaussian windowed tone burst. . . . .	157
5.14	Snap shots (in time) of the displacement field as a 10 cycle Gaussian windowed tone burst of the L(0,2) mode of an embedded steel bar propagates, when (a) only the nodes in the steel bar are forced and (b) when both the nodes of the steel bar and the surrounding grout are forced. . . . .	159
6.1	Series of snap-shots of the S0 mode in a steel plate reflecting from a 50 percent loss of section. The circles represent nodes whose displacements were monitored. . . . .	163
6.2	A sample time trace from the top monitoring location shown in the previous figure. . . . .	164
6.3	Amplitude reflection coefficients for the S0 mode in a 1 mm steel plate impinging on a notch that extends half way through the thickness. . . . .	164
6.4	Energy reflection coefficients for the S0 mode in a 1 mm steel plate impinging on a notch that extends half way through the thickness. . . . .	166
6.5	Time trace of the axial displacement at the centre of an embedded steel bar with a notch that extends half way through the thickness of the bar. The trace shows the incident wave passing, the reflected wave returning and unwanted reflections from the outer boundary of the embedding grout. . . . .	168
6.6	A schematic of the geometry used in for the modelling of the L(0,1) mode in an embedded steel bar. . . . .	169
6.7	Comparison of the reflection and transmission coefficients for a free and embedded 1 mm radius steel bar. . . . .	170
6.8	Comparison of the profile of the power flow of the L(0,1) mode at 0.70 MHz through the radius of a 1 mm steel bar when it is free and when it is embedded in grout. . . . .	171
6.9	Comparison of the reflection and transmission coefficients at different frequencies for an embedded bar. . . . .	172
6.10	Comparison of the reflection and transmission coefficients for a vacuum filled versus a grout filled defect for an embedded bar. . . . .	173
6.11	A schematic diagram showing how energy would be redirected by (a) a diagonal notch and (b) a corrosion step if the L(0,1) mode behaved as a bulk wave. . . . .	174



6.12	A portion of the finite element mesh used to create a diagonal notch extending through two thirds of the radius of the bar. . . . .	174
6.13	Comparison of the reflection and transmission coefficients for different notch orientations in a free bar. . . . .	175
6.14	Comparison of the reflection and transmission coefficients for different notch orientations in an embedded bar. . . . .	175
6.15	A portion of the finite element mesh used to create a corrosion patch extending through two thirds of the radius of the bar. . . . .	176
6.16	Comparison of the reflection coefficients for a square notch and a corrosion patch in an embedded bar. . . . .	177
6.17	The reflection coefficients for the L(0,1) mode in a steel bar as it transitions from an embedded section to a free section and visa versa. . . . .	179
6.18	A schematic view of the geometry used to evaluate the size of the reverberations in the protruding end of an embedded bar. . . . .	180
6.19	Plots of the decay in amplitude of a signal propagating in an embedded section of bar (with an attenuation of 530 dB/m) and the decay in amplitude of the reverberations in the free end of a bar that protrudes from the embedding material 10 mm (in part (a)) and 50 mm (in part (b)). The plots assume that 3 percent of the wave is reflected from the free / embedded boundary. . . . .	181
6.20	A diagram relating the maximum length of the protruding end of an embedded bar to the maximum attenuation that the mode in the embedded section can experience for the amplitude of the embedded signal to remain larger than the reverberations. . . . .	182
6.21	The dispersion curves for an embedded steel bar. . . . .	183
6.22	A comparison of the energy velocity dispersion curves, strain energy density profile, and displacement profiles for the L(0,4) mode in a free and embedded steel bar. . . . .	184
6.23	The reflection coefficients for a free steel bar when the L(0,4) mode is incident on a square notch. . . . .	185
7.1	Comparison of the phase velocity dispersion curves for (a) a 5 mm steel plate and (b) a 5 mm diameter bar embedded in grout. . . . .	195
7.2	A three dimensional comparison of the dispersion curves for (a) a 5 mm steel plate and (b) a 5 mm diameter steel bar embedded in grout. The bottom plane shows the projection of the frequency and phase velocity and the back plane shows the projection of the frequency and attenuation. . . . .	195
7.3	The phase velocity dispersion curves for the F(1,1) mode of a 5 mm diameter steel bar embedded in different densities of grout. . . . .	196
7.4	The phase velocity dispersion curves for the A0 mode of a 5 mm thick steel plate embedded in different densities of grout. . . . .	196
7.5	The displacement and strain energy density (SED) profile at a non-leaky section of the F(1,1) mode in a steel bar embedded in very low density grout. (A non-leaky mode section has not been found for a steel bar embedded in normal density grout) . . . . .	197
7.6	A comparison of the attenuation values for the non-leaky mode section of a 5 mm diameter steel bar and a 5 mm thick steel plate embedded in grout that has a density of 500 $kg/m^3$ . . . . .	198
7.7	(a) Phase velocity, (b) attenuation, and (c) energy velocity dispersion curves for the longitudinal modes of a 5 mm diameter steel bar embedded in grout. . . . .	200
7.8	The mode shapes corresponding to the points marked (a) and (b) in the previous figure. Only the displacements in the steel bar are shown. . . . .	201
7.9	A schematic view of the proposed test procedure. Once access to the ends of the tendons has been gained by removing protective coverings, a guided ultrasonic wave can be launched down each grouted tendon. Reflections from any defects in the tendon will then return to the transducer. . . . .	203

---

7.10	Sample time traces from 8.1 mm steel bars embedded in grout after reflection from a 2 mm saw cut 450 mm into the grout, after reflection from a 4 mm saw cut 450 mm into the grout, and after transmission along two metres of undamaged embedded steel bar. . . . .	204
7.11	Sample time trace showing the reflection from the end of a 2 metre long 8.1 mm diameter steel bar embedded in grout. . . . .	205
7.12	The reflection of a five cycle Gaussian windowed tone burst from a 4 mm deep square notch in an embedded 8.1 mm steel bar, showing (a) the time trace and (b) the wavelet transform. The lines which overlay the wavelet transform correspond to the arrival times predicted by the wave propagation model. . . . .	206
7.13	The frequency spectrum of a signal transmitted through two metres of embedded steel bar as the centre frequency of the input signal was changed from 3.0 to 8.0 MHz. . . . .	207
7.14	The profile of the experimental frequency response shown in the previous figure. The dashed line represents the frequency response of the test equipment used for these experiments. . . . .	207
7.15	The response of an 8.1 mm diameter steel bar embedded in grout converted to a relative attenuation. The dotted lines indicate the attenuation predicted by the wave propagation model. . . . .	208
7.16	The enveloped reflections from complete breaks in grouted strands at (a) 500 mm, (b) 1000 mm, (c) 1500 mm, and (d) 2000 mm from the beginning of the grout. . . . .	209
7.17	A comparison of the enveloped reflections of the guided waves (a) when there is a defect very close to the end of the embedded strand and (b) when the strand is undamaged. . . . .	209
7.18	A comparison of the enveloped reflections of the guided waves (a) when 5 of the 7 wires (including the centre wire) in the embedded strand are cut and (b) when 3 of the wires are cut. . . . .	210
7.19	The frequency response of the reflection from 5 wires cut in a 15.2 mm embedded Dyform strand, converted to a relative attenuation. The dotted lines indicate the predicted attenuation in (a) a 5.5 mm diameter bar and (b) a 15.2 mm diameter bar. . . . .	211

# Chapter 1

## Introduction

In 1985, the Ynys-y-Gwas bridge, a 18.3 m post-tensioned segmental road bridge, collapsed in South Wales only 32 years after its construction[1]. This unexpected collapse led to the 1992 temporary ban on grouted tendon construction in the United Kingdom and the development of new construction standards. In addition, the collapse aggravated concern about the over 3000 other post-tensioned bridges that exist in the United Kingdom[2]. It highlighted the need for a reliable non-destructive testing technique to characterise these bridges.

Post-tensioned construction allows very efficient bridges to be built. Large spans can be constructed with a light, elegant design. The technique involves constructing the framework of the bridge out of concrete, which can either be poured in place or pre-formed in sections that are assembled on site. Hollow, continuous, metal or plastic tubes called ducts are left in the concrete at predetermined locations. Steel strands or wires (collectively referred to as tendons) are then threaded through the ducts once the concrete has hardened. The steel tendons are tensioned using large hydraulic jacks and are anchored by small collets at their ends. The tensioned steel forces the concrete into compression so that it is better able to support the loads required of it. Once the steel is tensioned, the ducts are filled with grout to provide corrosion protection and the ends of the tendons are covered in a protective layer of concrete.

Ideally, the alkaline nature of the grout protects the steel tendons indefinitely. However, when the grout is being pumped into the ducts, large air voids can form. Over time, these voids can fill with salt water as de-icing salts leach through small cracks or expansion joints in the concrete. Contact with salt water causes the tendons to corrode quickly. Eventually they may snap and the entire bridge may collapse as load is shifted onto the other tendons.

The current evaluation techniques are not adequate[3]. Section 7.1 describes the inspection methods that are currently being used to determine which bridges are most at risk. However, the benefits of these techniques are limited because most of them provide insufficient information to fully evaluate

the condition of the bridge and others cannot be applied to the majority of existing bridges. An ideal inspection method would be able to examine large portions of the bridge for corrosion on individual tendons and perform the inspection from a single location that is easy to access.

Ultrasonic testing using guided waves has the potential to satisfy these testing requirements. Guided waves is the general term for waves which propagate in a waveguide. They differ from bulk ultrasonic waves because they continually interact with the boundaries of the material in which they propagate and require these boundaries in order to exist. The boundaries confine the waves and allow them to propagate over long distances, which makes them attractive for rapid, long-range screening of many types of systems.

In order to test the regions of the tendons near their anchorages, guided ultrasonic waves could be used in a simple pulse-echo configuration. The waves could be generated at the end of the tendons and allowed to propagate along the tendon. Upon interaction with a defect, a portion of the propagating wave would be reflected back towards the transducer that transmitted the guided wave. By switching the transducer to a receiving mode, this reflection can be detected and used to identify the presence of the defect. This simple concept is illustrated in figure 1.1.

To optimise this technique and determine its sensitivity, two things must be known, the wave propagation characteristics of the guided waves that can exist in this system and the behaviour of the guided waves as they interact with different types of defects. However, studying the behaviour of guided ultrasonic waves is not as straight forward as the study of ultrasonic bulk waves. Because of the constant interaction with the boundaries, the velocity and the behaviour of guided waves depends on their frequency. In addition, there are an infinite number of guided waves that can exist in a finite structure, in contrast to the three orthogonal bulk waves (one longitudinal and two shear) that can exist in a boundless material. The guided waves are formed by combinations of bulk waves in each of the layers that combine to satisfy all of the boundary conditions. In order to understand what guided waves can exist and how they can be used to create a reliable non-destructive ultrasonic test, a wave propagation model must be developed. Developing this model is not a trivial task, especially for cylindrical geometries. The grout that surrounds the tendons further complicates the modelling of the system. As a guided wave travels down the embedded tendon, it can 'leak' energy into the surrounding grout, exciting bulk waves and attenuating the amplitude of the guided wave. To find valid guided wave propagation solutions, this leakage rate, in addition to the velocity and frequency, must be determined for each point on each guided wave mode.

This thesis develops the techniques that are needed to study leaky guided ultrasonic waves in cylindrical systems and then uses them to evaluate the inspection of post-tensioned bridges. Considerable effort has been made to allow the techniques to be as general purpose and as easy to use as possible so that other systems in addition to post-tensioned bridges could be quickly evaluated in the future.

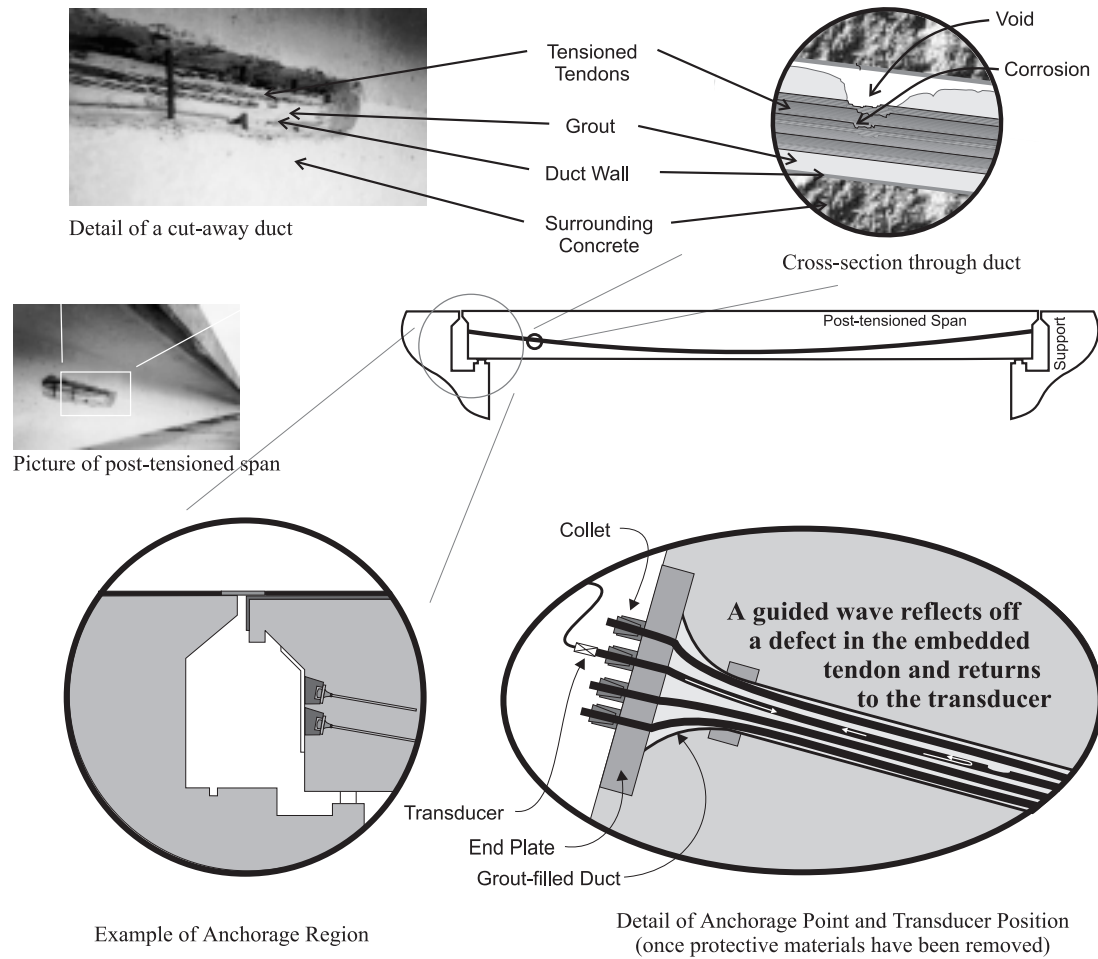


Figure 1.1: An illustration of how guided ultrasonic waves could be used in a pulse-echo configuration to examine the ends of embedded tendons in post-tensioned bridges.

Chapter 2 derives the analytical wave propagation model for multi-layered cylindrical systems comprised of elastic liquids, isotropic solids (that can incorporate material damping), and transversely isotropic elastic materials. The system can be surrounded by vacuum, immersed in a liquid, or embedded in a solid. The solution employs potential wave fields, similar to those used by Gazis[4] and Mirsky[5], and the global matrix method[6–9] to obtain its generality. Disperse, the general purpose wave propagation modelling software program begun by Mike Lowe in the Imperial College Non-destructive Testing Laboratory[10], has been expanded by the author to include the cylindrical wave propagation solutions[11] developed in chapter 2. During this expansion, Disperse was converted into an interactive windows based program that incorporates many facilities to help interpret the results.

Chapter 3 discusses the guided wave propagation in several typical cylindrical systems. These examples are used to provide a background on the type of guided waves that can exist and introduce the reader to leaky systems and the nomenclature that will be used throughout the thesis.

The validation of the wave propagation model is in chapter 4. The model is validated against known asymptotic solutions, published literature, its own internal consistency, finite element results, and experimental results.

Knowing the wave propagation characteristics of a particular system allows promising guided wave modes to be identified. However, the interaction with various types of defects cannot be predicted using the modal wave propagation solutions such as the one developed in chapter 2. To obtain this information, the wave propagation solutions must be combined with finite element predictions. Chapter 5 develops the techniques that have been used to integrate the two types of modelling.

The techniques developed in chapter 5 are used in chapter 6 to predict the reflection coefficients for defects in embedded bars.

Chapter 7 applies the wave propagation model and the reflection coefficient results to the problem of inspecting post-tensioned bridges. Effective guided wave modes are identified, a practical test arrangement is proposed, and experimental results are explained.

Some brief conclusions are contained in the final chapter.

The work presented in this thesis forms a submission for a Ph.D. in Mechanical Engineering from the University of London (Imperial College). Unless stated otherwise, the work is the author's own. It builds upon a long history of guided wave work, which is summarised within the relevant sections of later chapters. The novelty of the work contained in this thesis includes,

- The development and implementation of a general purpose model of wave propagation in cylindrical structures that includes an arbitrary number of layers, materials that can be elastic liquids, isotropic elastic solids (including material damping), or transversely isotropic elastic solids, and immersion or embedding in other media. As explained later in section 2.2, many solutions for in-

dividual cases have been developed, but a general purpose application has never been published. In addition, many specific cases that can be calculated using the model developed in this thesis have not been published; these include leakage into materials with material damping and multi-layered transversely isotropic bars immersed in a fluid.

- The pre and post processing techniques that are used to integrate the cylindrical wave propagation solutions with finite element modelling. Pure mode excitation, a method originally developed by David Alleyne[12] to create an appropriate input to the finite element model, has been extended so that it can now work with multi-layered systems, leaky systems, and cylindrical systems. A through-thickness mode extraction technique that determines the amplitude of various propagating modes from the displacement profile of a finite element model has been developed to help relate finite element results back to the modal wave propagation model.
- The examination of reflection coefficients for the L(0,1) mode for various types of simulated defects in embedded steel bars. Although the determination of reflection coefficients from finite element predictions is a well established procedure for free systems, very little work has been conducted on the reflection of guided waves in embedded systems.
- The development of a technique to inspect grouted tendons in post tensioned bridges using the analytical wave propagation solutions of guided ultrasonic waves.

## Chapter 2

# Derivation of Cylindrical Wave Propagation Model

This chapter describes the development of a general purpose model for wave propagation in cylindrical systems. The model can account for single or multi-layered structures, and free or leaky systems. Elastic isotropic and elastic transversely-isotropic materials are supported as well as isotropic materials with material damping.

Based on the geometry and material properties of the system, the model determines what resonances can exist in order to satisfy the boundary conditions and the bulk wave propagation characteristics in each of the layers. These resonances control how ultrasonic waves will be guided in the system and what properties each of these waves will have. The solutions to the guided wave problem lie on continuous lines called dispersion curves that must be found iteratively in frequency – wave number – attenuation space. Once the solutions have been found and the characteristics of the waves have been determined, they can be used to design an effective non-destructive testing system.

The modelling described in this chapter continues the work that Mike Lowe started[6,10], expanding it to cover cylindrical systems. During this expansion, the software tool for calculating dispersion curves, called Disperse, was converted from MS-DOS to X-Windows and Microsoft Windows to make the information more accessible. In addition, several options have been added to help interpret and use the data contained within the dispersion curves. The derivation for isotropic cylindrical systems is strongly based on the work that Gazis did in 1959 on hollow, single layer, elastic, circular cylinders in vacuum [4]. This work adapts it to handle multi-layered, leaky cases that incorporate material damping. Some trivial errors are also corrected. The derivation for transversely-isotropic materials is based on Mirsky's adaptation of Gazis' isotropic solution to transversely isotropic materials[5].



## 2.1 Introduction to Global Matrix Solution Method

For the wave propagation solution to model as many different systems as possible, it must be able to handle wave propagation in an arbitrary number of layers. There are two primary methods that are used to model multilayered media[6]. These are the transfer matrix method, developed by Thomson[13] and Haskell [14] and the global matrix method, developed by Knopoff [7] and Randall[8]. To be consistent with previous work on multilayered wave propagation that was performed at Imperial College [10] and to benefit from better stability at high frequency-thicknesses[6], the global matrix method, which will be explained in detail in section 2.8.1, was chosen.

The first process in solving for the wave propagation solutions via the global matrix method involves determining the nature of the bulk waves which can exist in the boundless material. Once the nature of the bulk waves is known, the stresses and displacements in a layer can be expressed in terms of the amplitudes of all of the bulk waves that can exist in that layer. The stresses and displacements at the boundaries of each layer can be combined with the boundary conditions to describe the entire system in one large global matrix that relates the bulk wave amplitudes to the physical constraints. Figure 2.1 demonstrates the construction of a five layer system. The partial (or bulk) waves labelled  $L_{+-}$ ,  $SV_{+-}$ , and  $SH_{+-}$  are assembled by matching the boundary conditions at each of the interfaces. At certain frequency, wave number, and attenuation combinations, these partial waves combine to form a guided wave which propagates down the axis of the infinitely long cylinder. These valid combinations may be found by solving the global matrix equation for its modal behaviour. For a given system, the global matrix equation is a function of frequency (time varying component), real wave number (spatially varying component), and attenuation (spatial decay rate). Solutions must be found iteratively by varying these three parameters until a valid root is converged upon. Once an initial root has been found, roots that lie on the same line of solutions, or dispersion curve, can be traced. This process can then be repeated to find other dispersion curves that exist. Once all of the dispersion curves have been traced, further information about the guided waves can be extracted and used to help determine their usefulness.

Using the global matrix method has several benefits. Since additional interfaces can be easily added, the global matrix method allows for a general solution to the multi-layered problem. Because the boundary conditions at all of the interfaces are solved simultaneously, the solution is inherently more stable than solution routines, such as the transfer matrix method, which solve the wave propagation problem layer by layer. Assembling the global matrix also simplifies the calculation of the mode shapes discussed in section 2.8.4. The derivation for cylindrical systems is continued in this chapter. A derivation for Cartesian geometries can be found in reference [6].

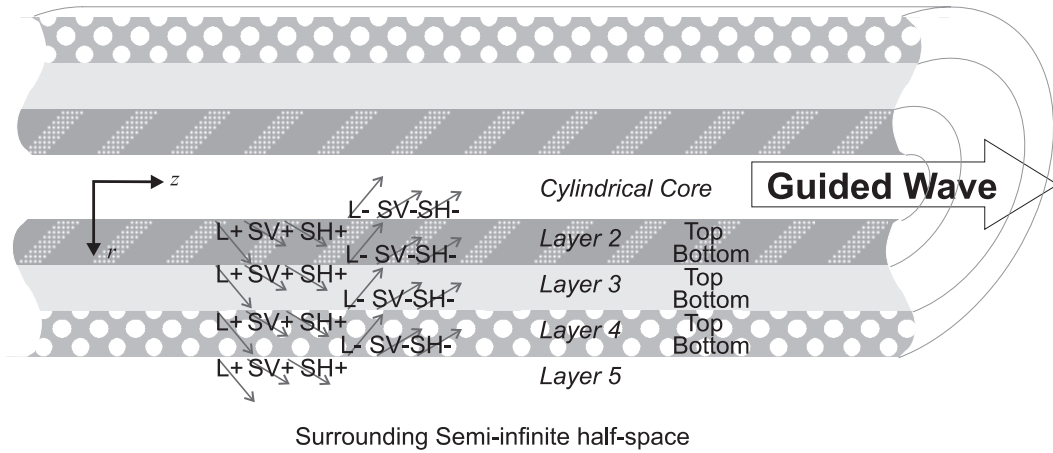


Figure 2.1: Sample geometry of a five layer cylindrical system showing the partial waves in each layer ( $L^+$ ,  $SV^+$ , and  $SH^+$ ) that combine to produce a guided wave.

## 2.2 Historical Background of Cylindrical Wave Propagation

An enormous amount of work has contributed to our current understanding of cylindrical wave propagation. This section highlights some of the previous achievements. However, it is far from comprehensive.

Cylindrical wave propagation problems were first studied numerically in the late nineteenth century. Pochhammer [15] and Chree [16] were the first researchers to mathematically investigate the propagation of guided waves in a free bar and their names are still associated with the equation that describes the modes of a solid cylinder.

However, most of the applications of cylindrical wave propagation have occurred much more recently. In the mid twentieth century, a good deal of research was performed on the modes of solid bars [17–23]. Much of this work concentrated on the use of rods as acoustic waveguides for use in delay lines that could be used in electronic devices, such as radar. In 1943, Hudson used shell approximations to study the dispersive nature of the fundamental flexural mode in a solid cylinder [18]. The longitudinal modes of a bar were first examined by Davies in 1948 [17]. Later work by researchers such as Pao and Mindlin [21,22], Onoe, McNiven, and Mindlin [20], and Meeker and Meitzler [19] fully developed all of the branches of the complete three dimensional problem of a solid circular cylinder in vacuum. The dispersion curves for a hollow isotropic cylinder were definitively treated by Gazis in 1959 [4,24]. The derivation for the general isotropic case that follows is largely based on his work. Fitch [25] matched Gazis's predictions for axially symmetric and non-symmetric wave propagation with experimental data. Later researchers, such as Kumar [26,27], have examined the effect that fluid filling has on the wave propagation in cylinders.

In 1965, Mirsky expanded Morse's work on axi-symmetric wave propagation in the transversely isotropic solid cylinders [28] and Gazis' [4] exact non-axi-symmetric isotropic wave propagation solution so that

cylindrical wave propagation in transversely isotropic materials could be studied. Subsequently, several other authors have examined the propagation in transversely isotropic rods and cylinders, for example Xu and Datta [29], Dayal [30], Nagy [31], and Berliner and Solecki[32]. The derivation for a transversely isotropic material in section 2.7 of this thesis, closely follows the technique that Mirsky used, incorporating adaptations similar to those used by Berliner and Solecki.

Leaky cylindrical systems have been much more difficult to model than their free counterparts. Much of the difficulty comes from the need to calculate complex Bessel functions, which until recently were not readily available. Therefore, early work, such as that conducted by Thurston[23], concentrated on portions of the dispersion curves that could be calculated using only real Bessel functions. However, more recent work by Safaai-Jazi et al.[33], Simmons et al. [34], and Viens et al. [35], has been able to model the entire range of dispersion curve solutions. In addition, recent work by Nagy[31] and Berliner and Solecki [32,36] has looked at wave propagation in transversely isotropic rods that are immersed in a fluid. A recent paper by Nayfeh and Nagy [37] considers leaky axi-symmetric waves in multilayered transversely isotropic fibres that are embedded in a solid.

All of these previous solutions to wave propagation in cylindrical systems solve a very limited wave propagation problem. For example, the solution presented in Berliner and Solecki's work [32] only accommodates a single layer and does not present solutions for materials that are embedded in a solid. Nayfeh and Nagy's work [37] allows an arbitrary number of layers and the possibility of embedding the structure in a solid, however it does not model non-axi-symmetric wave propagation nor immersion in a fluid. The originality of the work outlined in this thesis derives from the application of the global matrix method (described in section 2.8.1) to cylindrical wave propagation so that a general purpose solution is obtained. The system can be consist of as many layers as needed. Each layer can be an elastic isotropic material, an isotropic material with material damping, a transversely isotropic material, or a fluid. Different material types can be easily combined. The solution is valid for both axi-symmetric and non-axi-symmetric wave propagation (longitudinal, torsional, and flexural modes) and can model leakage into a solid or liquid medium. In addition, many utilities have been incorporated into the model to enhance our understanding of the wave propagation characteristics.

## 2.3 Assumptions and Limitations

In developing a cylindrical wave propagation model, certain assumptions will need to be made that limit the scope of systems that the model can handle. These assumptions are explained below.

This model assumes that the cylindrical system is axi-symmetric and infinitely long. The material properties may only vary in the radial direction and all of the variations must occur as instantaneous changes at the boundaries of discrete layers, within which the material is homogeneous. The boundaries between these layers will be assumed to be perfect. These assumptions imply that local phenomena,

such as defects, cannot be modelled. It should be noted that although the geometry of the system must be axi-symmetric, non-axi-symmetric wave propagation will be permitted.

All of the materials are assumed to be isotropic or transversely isotropic. Isotropic materials may be elastic or may incorporate material damping. The material damping will be modelled using hysteretic damping model that is explained in section 2.6. Anisotropic materials must be isotropic in the  $\hat{r} - \hat{\theta}$  plane and must be elastic. All liquids will be assumed to be inviscid. The different material types can be combined in the same model.

The waves will be assumed to be continuous, the frequency real, and the energy finite. The assumptions of a continuous wave and real frequency indicate that transient effects cannot be directly incorporated into the model. The assumption that the system contains finite energy implies that energy is not being added to the system from external sources, although energy may be lost due to material damping effects and waves leaking into an infinitely large surrounding medium. A wave is continually created at one end of the cylindrical structure and allowed to propagate. Solutions will only be sought for guided waves which propagate axially.

## 2.4 Boundary Conditions

This model assumes that the system consists of infinitely long, concentric cylinders of homogeneous materials. Therefore, the boundaries between layers are defined by a surface with a constant radius, extending infinitely in the axial ( $\hat{z}$ ) direction. Three different types of interfaces are considered, solid-solid, solid-vacuum, and solid-liquid.

It is also assumed that all boundaries between two solid layers are perfect. This assumption implies that the displacements and the stresses are continuous at the interface. All three displacements,  $\hat{r}$ ,  $\hat{\theta}$ , and  $\hat{z}$ , must be continuous or there would have to be void at the boundary. In addition, the normal stress,  $\sigma_{rr}$ , and the two tangential stresses along the interface,  $\sigma_{rz}$  and  $\sigma_{r\theta}$  will be transmitted across the boundary and must be continuous. The in-plane stresses, such as  $\sigma_{zz}$ , do not need to be continuous across the interface because they are not coupled from one medium to the next. These boundary conditions can be summarised as,

$$\begin{aligned}
 u_r \Big|_{r=a^+} &= u_r \Big|_{r=a^-} \\
 u_\theta \Big|_{r=a^+} &= u_\theta \Big|_{r=a^-} \\
 u_z \Big|_{r=a^+} &= u_z \Big|_{r=a^-} \\
 \sigma_{rr} \Big|_{r=a^+} &= \sigma_{rr} \Big|_{r=a^-} \\
 \sigma_{r\theta} \Big|_{r=a^+} &= \sigma_{r\theta} \Big|_{r=a^-} \\
 \sigma_{rz} \Big|_{r=a^+} &= \sigma_{rz} \Big|_{r=a^-}
 \end{aligned} \tag{2.1}$$

for a boundary of radius,  $r$ , equal to  $a$ , where the  $+$  superscript indicates that interface is approached from the inner material (with respect to  $r$ ) and the  $-$  indicates that it is approached from the outer material. It is also possible to define other types of solid-solid interfaces to model the behaviour of non-perfect boundaries. These are not included in this model but in some cases may be simulated by adding thin interface layers with reduced stiffnesses.

The boundary conditions change when a layer is bordered by a vacuum. In this case, the displacements are no longer constrained at the surface. In addition, since there is no medium on the other side of the interface to support a stress field, the normal and two tangential stresses that used to be continuous across the interface must now equal zero. For a boundary at radius,  $r$ , equal to  $a$ , these conditions may be written,

$$\begin{aligned} \sigma_{rr} \Big|_{r=a} &= 0 \\ \sigma_{r\theta} \Big|_{r=a} &= 0 \\ \sigma_{rz} \Big|_{r=a} &= 0. \end{aligned} \tag{2.2}$$

The third type of interface that is important for our modelling is the boundary between a liquid and solid layer. In this model, we assume perfect liquids that do not support shear. Therefore, instead of the tangential stresses being transferred across the interface as they are for solid-solid boundaries, the tangential stresses must be zero at the interface. In addition, there will no longer be constraints on the displacements which are tangential to the interface because the two materials are free to slip over each other. However, the displacement and compressional stress normal to the boundary must still be continuous across the interface to avoid the formation of voids. These conditions are summarised as,

$$\begin{aligned} u_r \Big|_{r=a_{solid}} &= u_r \Big|_{r=a_{liquid}} \\ \sigma_{rr} \Big|_{r=a_{solid}} &= \sigma_{rr} \Big|_{r=a_{liquid}} \\ \sigma_{r\theta} \Big|_{r=a_{solid}} &= 0 \\ \sigma_{rz} \Big|_{r=a_{solid}} &= 0. \end{aligned} \tag{2.3}$$

## 2.5 Wave Propagation in Infinite Media

Before deriving equations that describe the behaviour of layered media, it is important to understand the principles of wave propagation in unbounded media. In other words, we need to know the bulk behaviour of a material. This information can be readily found in most text books on the subject[38–40], but is repeated here for completeness.

Beginning with Newton's second law and the principle of conservation of mass within an arbitrary volume within an elastic solid, Euler's equation of motion can be derived. Euler's equation of motion relates the particle displacement field  $\mathbf{u}(\mathbf{x}, t)$ , which is a function of the position  $\mathbf{x}$ , and time,  $t$ , to the stress tensor,  $\sigma_{ij}$  (of rank two), in the following way,

$$\rho \frac{\partial^2 u_i}{\partial t^2} = \frac{\partial \sigma_{ij}}{\partial x_j}, \quad i, j = 1, 2, 3 \quad (2.4)$$

when the mass density of the layer,  $\rho$ , is assumed to be constant, the material is assumed to be linearly elastic, and the body forces (e.g. gravity) are neglected.

The generalised Hooke's law relates the stress tensor,  $\sigma_{ij}$ , to the strain tensor components,  $\epsilon_{kl}$ , and the adiabatic elastic stiffnesses of the material,  $c_{ijkl}$ .

$$\sigma_{ij}(\mathbf{x}, t) = c_{ijkl}(\mathbf{x}, t) \epsilon_{kl}(\mathbf{x}, t), \quad i, j, k, l = 1, 2, 3 \quad (2.5)$$

where summation over repeated indices is assumed. The stiffness tensor,  $c_{ijkl}$  is of rank 4, which implies that there are  $3^4 = 81$  coefficients. However, symmetry concerns and the requirement of a positive definite strain energy, reduce these 81 constants to 21 independent elements.

For a linear system, the strain components can be expressed in terms of the gradients of the particle displacements,

$$\epsilon_{ij}(\mathbf{x}) = \frac{1}{2} \left( \frac{\partial u_i}{\partial x_j} + \frac{\partial u_j}{\partial x_i} \right) \quad (2.6)$$

## 2.6 Development of Cylindrical Isotropic Model

The derivation of the wave propagation characteristics in a layered isotropic material in a cylindrical coordinate system was definitively treated by Denos Gazis in 1959 [4]. This section closely follows his work, adapting it for multi-layered geometries (that include material damping) and correcting some small errors.

### Specialisation to Isotropic Case

For a homogeneous, isotropic material, the theory of elasticity shows that the 21 possible components of the elastic stiffness tensor reduce to two material constants,  $\lambda = c_{1122}$  and  $\mu = c_{1212}$  which are called the Lamé constants (See, for example, reference [39]). Simplifying the generalised Hooke's law (eqn. 2.5) for the isotropic case and converting to a vector notation system leads to the equations,

$$\vec{\sigma} = \lambda \mathbf{I} \nabla \cdot \mathbf{u} + \mu (\nabla \mathbf{u} + \mathbf{u} \nabla) \quad (2.7)$$

where  $\mathbf{I}$  is the identity matrix,  $\vec{\sigma}$  is the stress diadic, a two dimensional vector field, and  $\nabla$  is the three-dimensional differential operator. Rewriting Euler's equation of motion (equation 2.4) in vector format as,

$$\rho(\partial^2 \mathbf{u} / \partial t^2) = \nabla \cdot \vec{\sigma} \quad (2.8)$$

and combining it with equation 2.7 leads to Navier's displacement equation of motion for an isotropic, elastic, medium which is, in invariant form,

$$(\lambda + \mu) \nabla \nabla \cdot \mathbf{u} + \mu \nabla^2 \mathbf{u} = \rho(\partial^2 \mathbf{u} / \partial t^2). \quad (2.9)$$

This equation may also be written as,

$$\begin{array}{cc} \text{dilatational} & \text{rotational} \\ (\lambda + 2\mu) \widehat{\nabla}(\nabla \cdot \mathbf{u}) & + \mu \nabla \times (\widehat{\nabla} \times \mathbf{u}) = \rho(\partial^2 \mathbf{u} / \partial t^2) \end{array} \quad (2.10)$$

where  $\mathbf{u}$  is the displacement vector,  $\rho$  is the density,  $\lambda$  and  $\mu$  are the Lamé constants, and  $\nabla^2$  is the three-dimensional Laplace operator. In the second form,  $(\lambda + 2\mu) \widehat{\nabla}(\nabla \cdot \mathbf{u})$  accounts for the dilatation (compressional) portion and  $\mu \nabla \times (\widehat{\nabla} \times \mathbf{u})$  accounts for the rotational (equivoluminal) portion of the solution.

### Material Damping

Material damping may be introduced into the system in a number of ways. For most of the materials that will be modelled using this derivation, a hysteretic (or structural) damper provides an adequate representation of the actual material behaviour that is easy to implement numerically and has been frequently used in ultrasonic modelling [6,9,10,41–51]. Work in structural dynamics has shown that hysteretic damping more realistically models solids than either a Maxwell or Voigt viscous damping model [52,53]. The hysteretic model implies that the energy loss per cycle (or alternatively, the attenu-

ation per wavelength) is constant. For harmonic solutions such as the one developed in this chapter, a true viscous damping model can be approximated by varying the hysteretic damping constants before calculating each frequency. Although the analysis of the hysteretic damping model is not rigorous for transient problems (it does not obey causality for a unit step function), it is admissible for describing harmonic vibration [54,53] and is therefore valid for the solutions developed in this chapter. Using a hysteretic damping model will cause the bulk velocities to depend slightly on the value of the damping, which is not strictly correct. However, in practical situations, this effect is very small and can be safely ignored[53].

The introduction of hysteretic material damping simply replaces the Lamé constants  $\lambda$  and  $\mu$  by complex values such that,

$$\lambda \text{ becomes } \lambda + i\lambda' \quad \text{and} \quad \mu \text{ becomes } \mu + i\mu' \quad (2.11)$$

where the constants  $\lambda'$  and  $\mu'$  are the hysteretic damping material constants. The damped model clearly reduces to the elastic model if the hysteretic damping constants are zero. Thus, the displacement equation of motion (equation 2.9) remains

$$(\lambda + \mu)\nabla(\nabla \cdot \mathbf{u}) + \mu\nabla^2 \mathbf{u} = \rho \frac{\partial^2 \mathbf{u}}{\partial t^2}, \quad (2.12)$$

however, the Lamé constants  $\lambda$  and  $\mu$  are now complex quantities.

### Potential Functions

Using Helmholtz decomposition (See reference [38] pages 52-53 for more information), the three dimensional displacement vector in equation 2.9,  $\mathbf{u}$ , which is finite, uniform, and continuous, and vanishes at infinity, can be expressed as a sum of a compressional scalar potential,  $\phi$ , and an equivoluminal vector potential,  $\mathbf{H}$ ,

$$\mathbf{u} = \nabla\phi + \nabla \times \mathbf{H} \quad (2.13)$$

with,

$$\nabla \cdot \mathbf{H} = F(\mathbf{r}, t)$$

where  $F$  is a function of the coordinate vector,  $\mathbf{r}$ , and the time,  $t$ . Gazis[4] points out that the function  $F$  can be chosen arbitrarily due to the gauge invariance of the field transformations (See reference [38] pages 207-211 for more information). In other words, the relation between the fields and the potentials is not unique. The scalar potential  $\phi$  can be replaced with  $\phi' + (1/c)(\partial\chi/\partial t)$  and the vector potential,  $\mathbf{H}$  by  $\mathbf{H}' - \nabla\chi$  and provided that  $\chi$  satisfies the appropriate boundary conditions, the new potentials represent the same field. In this way, functions can be combined to represent the entire field. We choose  $F(\mathbf{r}, t)$  to be identically zero, making the equivoluminal vector potential a zero-divergence vector, which implies that the field is solenoidal, i.e. there are no sources or sinks of energy within the region. Specifying the divergence provides the necessary additional condition to uniquely determine the three components of  $\mathbf{u}$



from the four components of the two potentials, which was introduced by the Helmholtz decomposition.

Substituting the expression for  $\mathbf{u}$  into Navier's equation of motion (equation 2.9), and using the identities,

$$\nabla \cdot \nabla \phi = \nabla^2 \phi \quad \nabla^2 (\nabla \phi) = \nabla (\nabla^2 \phi) \quad \nabla \cdot \nabla \times \mathbf{H} = 0,$$

the resulting equation is

$$\nabla [(\lambda + 2\mu)\nabla^2 \phi - \rho(\partial^2 \phi / \partial t^2)] + \nabla \times [\mu\nabla^2 \mathbf{H} - \rho(\partial^2 \mathbf{H} / \partial t^2)] = 0. \quad (2.14)$$

This equation is satisfied if either of the two expressions in square brackets vanishes. Setting these expressions equal to zero leads to the standard equations,

$$\begin{aligned} c_1^2 \nabla^2 \phi &= \partial^2 \phi / \partial t^2 \\ c_2^2 \nabla^2 \mathbf{H} &= \partial^2 \mathbf{H} / \partial t^2 \end{aligned} \quad (2.15)$$

where

$$c_1 = \left( \frac{\lambda + 2\mu}{\rho} \right)^{1/2} \quad c_2 = \left( \frac{\mu}{\rho} \right)^{1/2}, \quad (2.16)$$

and  $\lambda$  and  $\mu$  are the Lamé constants, which can be complex if there is material damping present.

### 2.6.1 Expansion in Cylindrical Coordinates

Equation 2.15 describes how a wave will propagate in an infinitely large medium. The vector operations that are specified in the equations are independent of the coordinate system that is used to solve the problem. This section expands on this knowledge to solve these equations for a specific coordinate system and to investigate how waves will propagate when boundaries are added. The first part of the section explores possible solutions of equation 2.15 in cylindrical coordinates. These solution types are then used to determine the displacement and stress fields that arise because of the propagation of the wave. Finally, these fields are combined with the boundary conditions to create a layer matrix that may be used to describe a complete system.

#### Proposed Solution for Cylindrical Geometry

Since the Helmholtz equation (2.13) is separable, the solution may be divided into the product of functions of each of the spatial dimensions[38]. If we assume a harmonically oscillating source, the solutions to equation 2.15 will each be of the form,

$$\phi, \mathbf{H} = \Xi_1(r)\Xi_2(\theta)\Xi_3(z)e^{i(\mathbf{k} \cdot \mathbf{r} - \omega t)} \quad (2.17)$$

where  $\mathbf{k}$  is the wavenumber, and  $\Xi_1(r)$ ,  $\Xi_2(\theta)$ , and  $\Xi_3(z)$  describe how the field varies in each spatial coordinate.

For elastic materials with material damping, the wavenumber,  $\mathbf{k}$ , is a complex number, with the real part,  $\mathbf{k}_{real}$ , describing the propagation of the wave and the imaginary part,  $\mathbf{k}_{imag}$ , the attenuation of the wave in space. The real and imaginary parts may be separated, and equation 2.17 may be rewritten as,

$$\phi, \mathbf{H} = \Xi_1(r)\Xi_2(\theta)\Xi_3(z)e^{i(\mathbf{k}_{real}\cdot\mathbf{r}-\omega t)}e^{-\mathbf{k}_{imag}\cdot\mathbf{r}} \quad (2.18)$$

where the first exponential term, which is wholly imaginary, describes the harmonic propagation of the wave in the direction of the vector  $\mathbf{k}_{real}$  and the second, real term describes the exponential decay of the wave with distance in the direction of the vector  $\mathbf{k}_{imag}$ .

If the real part and imaginary part of the wavenumber are parallel the material constants can be related to the measurable wave speed and attenuation [10],

$$c_1 \text{ or } c_2 = \frac{\omega}{|\mathbf{k}_r| + i|\mathbf{k}_i|} = \frac{c_{ph}}{1 + \frac{|\mathbf{k}_i|}{|\mathbf{k}_r|}} = \frac{c_{ph}}{1 + i\kappa/(2\pi)} \quad (2.19)$$

where  $c_{ph}$  is the phase velocity of the wave and  $\kappa$  is the attenuation in Nepers per wavelength, such that a wave of unit amplitude is reduced to an amplitude of  $e^{-\kappa}$  after travelling one wavelength.

The attenuation of cylindrically guided waves due to the leakage of energy into the surrounding media presents a similar problem to the attenuation due to material damping. An attenuation term must be added even if all of the materials are elastic to account for decay in energy of the guided wave as energy propagates away to infinity. This attenuation due to leakage can be introduced by allowing the wavenumber to be complex [6,9,10,46,47,49,55–58]. A complex wavenumber implies that as the mode propagates its amplitude decays spatially. This implication matches our perception of the behaviour of a leaky guided wave. When the frequency is real and all of the materials are elastic, then  $\mathbf{k}_{imag}$  may exist but it must be normal to  $\mathbf{k}_{real}$ . When both material damping and leakage are present, the imaginary part of the wavenumber vector, which in general is not necessarily parallel to the real part, accounts for both types of attenuation [10].

Returning to the proposed solution of equation 2.17 and assuming a complex vector wavenumber,  $\mathbf{k}$ , to account for the attenuation, we rewrite the proposed solutions as,

$$\phi, \mathbf{H} = \Xi_1(r)\Xi_2(\theta)\Xi_3(z)e^{i(\mathbf{k}\cdot\mathbf{r}-\omega t)} \quad (2.20)$$

where  $\mathbf{k}$  is the complex vector wavenumber,  $\mathbf{r}$  is the position vector, and  $\omega$  the circular frequency. Assuming that the wave does not propagate in the  $\hat{r}$  direction and assuming that the displacement field does not vary in the  $\hat{z}$  or  $\hat{\theta}$  direction except for the harmonic oscillation described by the real part of the

vector wavenumber and the attenuation described by the imaginary part , we can rewrite equation 2.20 as,

$$\phi, \mathbf{H} = \Xi_2(r) e^{i(k_\theta \theta + \xi z - \omega t)} \quad (2.21)$$

where  $k_\theta$  is the angular wavenumber component,  $\xi$  is the component of the complex vector wavenumber in the  $\hat{z}$  direction, which will henceforth be referred to simply as the wavenumber. The angular wavenumber component,  $k_\theta$  must be an integer,  $n$ . Otherwise the solution would be different at  $\theta$  and  $\theta + 2\pi$  and the solution would not be unique. Phase angles may be arbitrarily added to each of the functions, since the added phases will be compensated for by the coefficients of the functions themselves. Choosing the phase angles to match those used by Gazis yields the following expressions for the components of the Helmholtz potentials in equation 2.13, for cylindrical waves propagating in the  $\hat{z}$  direction,

$$\begin{aligned} \phi &= f(r) e^{i(n\theta + \xi z - \omega t)} \\ H_r &= -g_r(r) e^{i(n\theta + \xi z - \omega t)} \\ H_\theta &= -i g_\theta(r) e^{i(n\theta + \xi z - \omega t)} \\ H_z &= -i g_3(r) e^{i(n\theta + \xi z - \omega t)} \end{aligned} \quad (2.22)$$

Another possible solution results in sines and cosines for the  $\theta$  dependence. This formulation more closely follows Gazis' formulation and more clearly demonstrates the wave's behaviour for torsional and longitudinal modes, when  $n = 0$ . The choice of the phase angles and the sine or cosine function is constrained by the expressions for the displacements, which are developed below.

$$\begin{aligned} \phi &= f(r) \cos(n\theta) e^{i(\xi z - \omega t)} \\ H_r &= -i g_r(r) \sin(n\theta) e^{i(\xi z - \omega t)} \\ H_\theta &= -i g_\theta(r) \cos(n\theta) e^{i(\xi z - \omega t)} \\ H_z &= g_3(r) \sin(n\theta) e^{i(\xi z - \omega t)} \end{aligned} \quad (2.23)$$

Substituting the equation for  $\phi$  from equation 2.22 into equation 2.15

$$c_1^2 \nabla^2 \phi = \partial^2 \phi / \partial t^2$$

yields,

$$\frac{d^2 f}{dr^2} + \frac{1}{r} \frac{df}{dr} - \left( \frac{n^2}{r^2} - \left( \frac{\omega^2}{c_1^2} - \xi^2 \right) \right) f = 0. \quad (2.24)$$

The series solution of this differential equation is a Bessel function, whose differential operator is defined as,

$$B_{n,r} = \left( \frac{\partial^2}{\partial r^2} + \frac{1}{r} \frac{\partial}{\partial r} - \left( \frac{n^2}{r^2} - 1 \right) \right). \quad (2.25)$$

Therefore,

$$B_{n,\alpha r}[f] = 0 \quad (2.26)$$

is a valid solution for the potential function  $\phi$  when  $\alpha^2 = \omega^2/c_1^2 - \xi^2$ . In equation 2.26,  $\alpha$  corresponds to the radial component of the wave number vector, which is used to describe the radial variation of the potential function  $\phi$ .

Substitution of the vector potential,  $\mathbf{H}$  from 2.22 into equation 2.15 produces three coupled scalar equations, as revealed by the Laplacian,

$$\begin{aligned} c_2^2 \nabla^2 \mathbf{H} &= \nabla(\nabla \cdot \mathbf{H}) - \nabla \times (\nabla \times \mathbf{H}) = \partial^2 \mathbf{H} / \partial t^2 \\ &= \hat{r} \left( \nabla^2 H_r - \frac{H_r}{r^2} - \frac{2}{r^2} \frac{\partial H_\theta}{\partial \theta} \right) + \hat{\theta} \left( \nabla^2 H_\theta - \frac{H_\theta}{r^2} + \frac{2}{r^2} \frac{\partial H_r}{\partial \theta} \right) + \hat{z} (\nabla^2 H_z) \end{aligned} \quad (2.27)$$

Separating equation 2.27, results in the following equations,

$$\frac{d^2 g_3}{dr^2} + \frac{1}{r} \frac{dg_3}{dr} - \left( \frac{n^2}{r^2} - \left( \frac{\omega^2}{c_2^2} - \xi^2 \right) \right) g_3 = 0 \quad (2.28)$$

$$\frac{d^2 g_r}{dr^2} + \frac{1}{r} \frac{dg_r}{dr} + \frac{1}{r^2} (-n^2 g_r + 2n g_\theta - g_r) - \xi^2 g_r + \frac{\omega^2}{c_2^2} g_\theta = 0 \quad (2.29)$$

$$\frac{d^2 g_\theta}{dr^2} + \frac{1}{r} \frac{dg_\theta}{dr} + \frac{1}{r^2} (-n^2 g_\theta + 2n g_r - g_\theta) - \xi^2 g_\theta + \frac{\omega^2}{c_2^2} g_r = 0 \quad (2.30)$$

Equation 2.28 is uncoupled and has a solution of the form,

$$B_{n,\beta r}[g_3] = 0 \quad (2.31)$$

where  $\beta^2 = \omega^2/c_2^2 - \xi^2$

Adding and subtracting equations 2.29 and 2.30 leads to the following solutions of the wave potential functions,

$$\begin{aligned} B_{n+1,\beta r}[g_r - g_\theta] &= 0 \\ B_{n+1,\beta r}[g_r + g_\theta] &= 0 \end{aligned} \quad (2.32)$$

Gauge invariance tells us that one of the potentials can be set to zero without loss of generality. In other words the displacement field corresponding to an equivoluminal potential can be derived by a combination of the other two equivoluminal potentials. So we set  $g_2 = 0$  such that

$$g_r = -g_\theta = g_1 \quad (2.33)$$

and we are left with three independent potential functions,  $f(r)$ ,  $g_1(r)$ , and  $g_3(r)$ , which each satisfy the Bessel differential operator.

### Choice of Bessel functions

Each of the three of independent potential functions,  $f(r)$ ,  $g_1(r)$ , and  $g_3(r)$ , satisfy the Bessel differential operator. However, there are several different combinations of Bessel functions that may be used to satisfy this differential operator. In order to fully satisfy the operator, a pair of linearly independent Bessel functions is required. The 'standard' pair of functions that satisfy the Bessel differential operator are the Bessel function of the first kind ( $\mathbf{J}_n$ ) and the second kind ( $\mathbf{Y}_n$ ). These functions represent a pair of oscillating standing waves, similar to the Cartesian functions sine and cosine. The modified Bessel functions,  $\mathbf{I}_n$  and  $\mathbf{K}_n$ , may also be used, although their use requires a sign change in the Bessel differential operator. They correspond to a monotonic decay or increase and are similar to the hyperbolic sine and cosine functions in a Cartesian system. The third valid combination of functions are the Hankel functions of the first and second kind ( $\mathbf{H}_n^{(1)}$  and  $\mathbf{H}_n^{(2)}$ ). Similar to complex exponential functions, these functions represent oscillating waves that propagate toward or away from the origin. The best choice of functions depends on several factors, which are explained below.

For internal layers, all three of the functions combinations are valid. However, certain combinations are more stable than others. In practice, the Hankel functions, which are always complex, prove to be the least stable and are therefore not used for internal layers. The choice between the unmodified or modified Bessel functions depends on the argument of the Bessel functions,  $\alpha r$  or  $\beta r$ .

For a system that does not experience attenuation, the frequency,  $\omega$ , the wavenumber,  $\xi$ , and the bulk velocities,  $c_1$  and  $c_2$  are all real. Therefore,  $\alpha^2$ , defined as  $\omega^2/c_1^2 - \xi^2$ , will also be real. It will be positive when the  $\omega^2/c_1^2$  is greater than the wavenumber (or the phase velocity is greater than  $c_1$ ) and negative when  $\omega^2/c_1^2$  is less than the wavenumber (or the phase velocity is less than  $c_1$ ). Therefore,  $\alpha r$ , an argument to the Bessel functions, will be purely real when the phase velocity is greater than the longitudinal bulk velocity and purely imaginary when the phase velocity is less. The same is true for the functions that have  $\beta r$  for their argument, except the references to the longitudinal bulk velocity must be replaced by references to the shear bulk velocity. When using Bessel functions that take complex arguments, the unmodified Bessel functions  $\mathbf{J}_n$  and  $\mathbf{Y}_n$  could be used for both the real and imaginary cases. However it is more stable (and elegant) to use  $\mathbf{J}_n$  and  $\mathbf{Y}_n$  when the arguments are real and use the modified Bessel functions,  $\mathbf{I}_n$  and  $\mathbf{K}_n$ , when the arguments would be imaginary. Since both of the unmodified Bessel functions ( $\mathbf{J}_n$  and  $\mathbf{Y}_n$ ) increase exponentially along the imaginary axis, their effect cannot be clearly separated and the solution becomes unstable as the arguments become large. This problem is analogous to the "large fd" problem that is discussed for plates [6] and is especially important for large radius pipes. However the modified Bessel functions separate with  $\mathbf{I}_n(z) = (-i)^n \mathbf{J}_n(iz)$  increasing and  $\mathbf{K}_n(z) = (1/2)\pi i^{(n+1)} \mathbf{H}_n^{(1)}(iz)$  decreasing as the argument grows [59]. This leads to a more stable solution. Because of the sign change in the differential operator of the modified Bessel functions, some changes need to be made to the definition of  $\alpha$ , and  $\beta$ . In addition, two parameters,  $\gamma_1$ , and  $\gamma_2$ , have been defined to account for the differences in recurrence relationships that are employed when derivatives of the functions need to be taken. The first parameter,  $\gamma_1$ , relates to recurrence rela-

Table 2.1: Substitutions that should be made and criteria that should be used for the selection of the type of Bessel functions to be used for the cylindrical layer matrix.

when $V_{ph} > c_1$	when $c_1 > V_{ph} > c_2$	when $c_1 > c_2 > V_{ph}$
$\alpha = \sqrt{\alpha^2}$	$\alpha = \sqrt{-\alpha^2}$	$\alpha = \sqrt{-\alpha^2}$
$\beta = \sqrt{\beta^2}$	$\beta = \sqrt{\beta^2}$	$\beta = \sqrt{-\beta^2}$
$\gamma_1 = 1$	$\gamma_1 = -1$	$\gamma_1 = -1$
$\gamma_2 = 1$	$\gamma_2 = 1$	$\gamma_2 = -1$
$Z_n(\alpha r) = \mathbf{J}_n(\alpha r)$	$Z_n(\alpha r) = \mathbf{I}_n(\alpha r)$	$Z_n(\alpha r) = \mathbf{I}_n(\alpha r)$
$W_n(\alpha r) = \mathbf{Y}_n(\alpha r)$	$W_n(\alpha r) = \mathbf{K}_n(\alpha r)$	$W_n(\alpha r) = \mathbf{K}_n(\alpha r)$
$Z_n(\beta r) = \mathbf{J}_n(\beta r)$	$Z_n(\beta r) = \mathbf{J}_n(\beta r)$	$Z_n(\beta r) = \mathbf{I}_n(\beta r)$
$W_n(\beta r) = \mathbf{Y}_n(\beta r)$	$W_n(\beta r) = \mathbf{Y}_n(\beta r)$	$W_n(\beta r) = \mathbf{K}_n(\beta r)$

tionships that involve  $\alpha$  and  $\gamma_2$  relates to those that involve  $\beta$ . The substitutions that need to be made, as well as the criteria for when these substitutions should be made, are collected in table 2.1. This table introduces the functions  $Z_n$  and  $W_n$  which will be used in the rest of the derivation to represent inward ( $Z_n$ ) and outward ( $W_n$ ) oriented Bessel functions. The function  $Z_n$  can be substituted by  $\mathbf{J}_n$ ,  $\mathbf{I}_n$ , or  $\mathbf{H}_n^{(1)}$  and the function  $W_n$  takes the place of  $\mathbf{Y}_n$ ,  $\mathbf{K}_n$ , or  $\mathbf{H}_n^{(2)}$ .

When there is attenuation in the model, the wavenumber,  $\xi$ , will be complex and therefore  $\alpha^2$ ,  $\beta^2$ ,  $\alpha r$ , and  $\beta r$  will all be complex, instead of being purely real or purely imaginary. Thus, complex Bessel functions will need to be used for the calculation. However, the same substitutions can still be used for internal layers to stabilise the solutions.

### Leakage into a surrounding medium

For systems which leak energy into a surrounding medium, such as a bar embedded in an infinitely large medium, an appropriate Hankel function must be chosen for the outward propagating wave in the layer that represents the infinite surrounding medium. The unmodified Bessel function,  $\mathbf{Y}_n$ , which represents standing waves in a layer that has finite size, will not correctly describe an infinitely thick layer because it does not provide for the propagation of energy away from the origin. The modified Bessel function,  $\mathbf{K}_n$ , which represents a decaying wave, only forms a valid solution when the phase velocity is less than the bulk velocity of interest ( $c_1$  for  $\alpha$  and  $c_2$  for  $\beta$ ). This criterion corresponds to regions where the respective bulk wave does not leak from the structure. The Hankel functions,  $\mathbf{H}_n^{(1)}$  and  $\mathbf{H}_n^{(2)}$ , which represent propagating waves, are able to correctly model the leakage for all regions of the dispersion curves. Since using the modified Bessel function  $\mathbf{K}_n$  for modelling the surrounding medium does not improve the stability of the solution, the Hankel functions are used for all cases.

For the direction of the wave used in this thesis,  $e^{i(\xi z - \omega t)}$ , the Hankel function of the first kind  $\mathbf{H}_n^{(1)}$ , which decays at infinity, is used to describe the outward propagating wave in the infinitely thick surrounding medium. The Hankel function of the second kind,  $\mathbf{H}_n^{(2)}$ , which represents the incoming waves, increases as its argument approaches infinity. If this function is included in the solution, the assumption

that the energy is finite would be violated because there would be constant energy input along the entire infinite length of the system. Instead, the three incoming partial wave amplitudes ( $L_-$ ,  $SV_-$ , and  $SH_-$ ) are set to zero. The Hankel functions follow the same recurrence relationships as the unmodified Bessel functions of the first and second kind (**J** and **Y**). Therefore,  $\gamma_1$  and  $\gamma_2$  must always be 1,  $\alpha$  always equals  $\sqrt{\alpha^2}$ ,  $\beta$  always equals  $\sqrt{\beta^2}$ . The same Bessel functions are used whether the surrounding material is a solid or a liquid, however, as will be seen later, only one partial wave amplitude,  $L$ , is needed to describe the field in a liquid.

The cylindrical core of the system may also be modelled as a semi-infinite half-space. The core can only have three partial waves (one for a liquid), all of which propagate inward, as opposed to the other internal layers that can contain six partial waves each (two for a liquid), three of which propagate inward and three of which propagate outward. For the core, the outward travelling waves are represented by the inward travelling waves from the other side of the bar. These waves are normally represented by the **J** or **I** Bessel functions, which represent standing resonances through the thickness of the core. However, some cases arise when it is advantageous to eliminate the transmission of the inward propagating waves from one side of the core to the other. An example, which is discussed in section 3.2.1, is the modelling of a large radius pipe that is partially filled with a fluid. In this case, the partial waves that are excited in the liquid core can reflect off of the top surface of the liquid and be scattered. When the reflected partial waves reach the pipe wall, they will no longer be propagating at the proper incident angle for them to contribute to the energy of the mode that generated them. Therefore, the attenuation of the mode will be significantly higher than for the model, which assumes that the partial waves continue to contribute to the energy of the mode. By numerically absorbing the partial waves that are propagating in the liquid core, the attenuation caused by such an effect can be approximated.

In order to eliminate the transmission of the partial waves through the liquid core, the normal wave solution that uses the **J** or **I** Bessel function can be replaced by a solution that incorporates the Hankel function of the second kind,  $H_n^{(2)}$ . The Hankel function of the second kind has a sink at the origin which absorbs the incoming bulk waves. When using the Hankel function of the second kind, the parameters  $\gamma_1$  and  $\gamma_2$  should be set to one and the values of  $\alpha$  and  $\beta$  must be defined in the same manner as for Hankel functions of the first kind.

### Choice of the phase for $\alpha$ and $\beta$

The phase of the arguments to the Bessel functions,  $\alpha r$  and  $\beta r$ , strongly affects the behaviour of the solution and must therefore be chosen with care. Since  $\alpha$  and  $\beta$  are defined by the value of their squares, they may take on two different values that are 180 degrees out of phase. The choice of roots depends on the type of Bessel function and whether the partial wave is homogeneous or inhomogeneous. Homogeneous waves propagate with components both along the direction of propagation of the guided wave and normal to the interface between layers. On the other hand, inhomogeneous waves propagate along the direction of propagation of the guided wave, but die away exponentially in the direction

Table 2.2: Criteria for the the choice of phase for the arguments of the Bessel functions depending on the type of Bessel function and the type of wave (homogeneous or inhomogeneous).

Bessel Function	Phase ( $\phi$ ) for homogeneous wave	Phase ( $\phi$ ) for inhomogeneous wave
$J_n, Y_n, \text{ and } H_n$	$e^{-i\pi/2} < \phi < e^{i\pi/2}$	$e^{i0} < \phi < e^{i\pi}$
$I_n \text{ and } K_n$	$e^{i0} < \phi < e^{i\pi}$	$e^{-i\pi/2} < \phi < e^{i\pi/2}$

normal to the interface between layers. When there is no attenuation, it is easy to determine which waves are homogeneous and which are inhomogeneous. If the argument to the Bessel function is real then the wave is homogeneous, but if the argument to the Bessel function is imaginary, the partial wave is inhomogeneous. The circumstances when these conditions apply may be extracted from the definition of  $\alpha$ ,

$$\alpha = \sqrt{\left(\frac{\omega}{v_1}\right)^2 - \left(\frac{\omega}{v_{ph}}\right)^2} \quad (2.34)$$

where the expression  $\omega/v_{ph}$  has been substituted for the axial wavenumber,  $\xi$ . Whenever the phase velocity of the guided wave,  $v_{ph}$ , is greater than the bulk velocity,  $v_1$ ,  $\alpha^2$  is positive and  $\alpha$  is real. Conversely, when the phase velocity is below the bulk velocity,  $\alpha^2$  is negative and  $\alpha$  is imaginary. With attenuation present, the arguments of the Bessel functions will be complex. In this case, a wave can be considered to be 'homogeneous' when the real part of  $(\omega/c_{bulk})^2$  is greater than the real part of  $\xi^2$ . This condition is also usually true when the phase velocity of the wave is greater than the appropriate bulk velocity ( $c_1$  for  $\alpha$  and  $c_2$  for  $\beta$ ). Otherwise the partial wave will be inhomogeneous. Since  $\alpha$  and  $\beta$  represent the wave number in the direction normal to the interface between the layers, it is necessary to choose their phase so that the behaviour is consistent with the nature of the homogeneous or inhomogeneous waves. Both the propagation of homogeneous waves and the decay of inhomogeneous waves should be away from the interface. Tabulating this information for the different types of Bessel functions leads to the selection criteria found in table 2.2.

## 2.6.2 Displacement Field

We are now ready to apply the information that we know about the solution in order to calculate the displacements at an arbitrary location in the medium. Recalling from equation 2.13 that  $\mathbf{u} = \nabla\phi + \nabla \times \mathbf{H}$  and the vector operations in cylindrical coordinates given in Auld[60],

$$\begin{aligned} u_r &= \frac{\partial\phi}{\partial r} + \frac{1}{r} \frac{\partial H_z}{\partial\theta} - \frac{\partial H_\theta}{\partial z} \\ u_\theta &= \frac{1}{r} \frac{\partial\phi}{\partial\theta} + \frac{\partial H_r}{\partial z} - \frac{\partial H_z}{\partial r} \\ u_z &= \frac{\partial\phi}{\partial z} + \frac{1}{r} \frac{\partial}{\partial r}(rH_\theta) - \frac{1}{r} \frac{\partial H_r}{\partial\theta} \end{aligned} \quad (2.35)$$



leads to the displacement field in terms of the potential functions of equation 2.22,

$$\begin{aligned}
 u_r &= \left( f' + \xi g_1 + \frac{n}{r} g_3 \right) e^{i(n\theta + \xi z - \omega t)} \\
 u_\theta &= i \left( \frac{n}{r} f - \xi g_1 + g_3' \right) e^{i(n\theta + \xi z - \omega t)} \\
 u_z &= i \left( \xi f + \frac{(n+1)}{r} g_1 + g_1' + 0 \right) e^{i(n\theta + \xi z - \omega t)}
 \end{aligned} \tag{2.36}$$

where the prime notation indicates the derivative with respect to the radius,  $r$ . The expressions for the displacements may also be expressed in sine and cosine notation,

$$\begin{aligned}
 u_r &= \left( f' + \xi g_1 + \frac{n}{r} g_3 \right) \cos(n\theta) e^{i(\xi z - \omega t)} \\
 u_\theta &= - \left( \frac{n}{r} f - \xi g_1 + g_3' \right) \sin(n\theta) e^{i(\xi z - \omega t)} \\
 u_z &= i \left( \xi f + \frac{(n+1)}{r} g_1 + g_1' \right) \cos(n\theta) e^{i(\xi z - \omega t)}.
 \end{aligned} \tag{2.37}$$

Equation 2.37 clearly shows that longitudinal modes ( $n = 0$ ) have no  $\hat{\theta}$  displacement and have a constant displacement profile around the circumference.

### 2.6.3 Stress Field

Knowing the expressions for the displacements and the relations between the displacement and the stresses, we can now determine expressions for the stresses. Hooke's Law defines the stress as  $\tau_{ij} = \lambda \Delta \delta_{ij} + 2\mu \epsilon_{ij}$ , where in cylindrical coordinates,

$$\begin{aligned}
 \epsilon_{rr} &= \frac{\partial u_r}{\partial r} & \epsilon_{\theta\theta} &= \frac{1}{r} \frac{\partial u_\theta}{\partial \theta} + \frac{u_r}{r} & \epsilon_{zz} &= \frac{\partial u_z}{\partial z} \\
 \epsilon_{rz} &= \frac{1}{2} \left( \frac{\partial u_r}{\partial z} + \frac{\partial u_z}{\partial r} \right) \\
 \epsilon_{r\theta} &= \frac{1}{2} \left( r \frac{\partial}{\partial r} \left( \frac{u_\theta}{r} \right) + \frac{1}{r} \frac{\partial u_r}{\partial \theta} \right) \\
 \epsilon_{\theta z} &= \frac{1}{2} \left( \frac{\partial u_\theta}{\partial z} + \frac{1}{r} \frac{\partial u_z}{\partial \theta} \right)
 \end{aligned} \tag{2.38}$$

and

$$\begin{aligned}
 \sigma_{rr} &= \lambda \Delta + 2\mu \epsilon_{rr} \\
 \sigma_{rz} &= 2\mu \epsilon_{rz} \\
 \sigma_{r\theta} &= 2\mu \epsilon_{r\theta}
 \end{aligned} \tag{2.39}$$

where  $\Delta$  is the dilatation given by

$$\Delta = \nabla^2 \phi = -(\omega^2/c_1^2) f e^{i(n\theta + \xi z - \omega t)} = -(\alpha^2 + \xi^2) f e^{i(n\theta + \xi z - \omega t)}.$$

Applying these expressions to the displacements in equation 2.36, the stresses that are specified in the boundary conditions become

$$\begin{aligned} \sigma_{rr} &= \mu \left( -\frac{\lambda}{\mu} (\alpha^2 + \xi^2) f + 2f'' + 2\xi g_1' - 2\frac{n}{r^2} g_3 + \frac{2n}{r} g_3' \right) \\ \sigma_{r\theta} &= i\mu \left( -\frac{2n}{r^2} f + \frac{2n}{r} f' + \frac{(n+1)\xi}{r} g_1 - \xi g_1' + 2g_3'' + \beta^2 g_3 \right) \\ \sigma_{rz} &= i\mu \left( 2\xi f' + \left( \frac{n}{r} \frac{n+1}{r} + \xi^2 - \beta^2 \right) g_1 + \frac{n}{r} g_1' + \frac{n}{r} \xi g_3 \right) \end{aligned} \quad (2.40)$$

In calculating  $\sigma_{r\theta}$  and  $\sigma_{rz}$  the substitutions, taken from the Bessel equation,

$$\begin{aligned} -\frac{1}{r} g_3' &= g_3'' + \left( \beta^2 - \frac{n^2}{r^2} \right) g_3 \\ g_1'' &= -\frac{1}{r} g_1' + \left( \frac{(n+1)^2}{r^2} - \beta^2 \right) g_1 \end{aligned} \quad (2.41)$$

were used to match the form of the expressions given by Gazis[4]. Please note that the  $g_1$  term of  $\sigma_{rz}$  does not match Gazis; he also incorrectly multiplies  $\xi^2 - \beta^2$  by  $n/r$ . This error is not propagated through to his other results.

## 2.6.4 Material Layer Matrix

The expressions for the displacement and stress fields in equations 2.36 and 2.40 are expressed in terms of the potential functions. The solutions for these potential functions that are given in section 2.6.1 must be substituted into these equations before the actual stress field can be calculated. These substitutions provide six equations in terms of six unknown partial wave amplitudes (three for incoming waves and three for outgoing waves) that correspond to the coefficients of the Bessel functions that are used in the solution. The use of these partial waves is shown in figure 2.1, where six bulk waves are present in each interior layer. The partial waves amplitudes in figure 2.1 are labelled by their Cartesian equivalents, L, SH, and SV, which stand for Longitudinal waves (equivalent to the solutions of  $f(r)$ ), Shear Vertical waves ( $g_1$ ), and Shear Horizontal waves ( $g_3$ ).

We can assemble a 6 by 6 matrix from the six equations for the displacements (eqn. 2.36) and pertinent stresses (eqn. 2.40) in terms of the amplitudes of the 6 partial waves. The resulting matrix is called a

material layer matrix and solves the equation

$$\begin{pmatrix} u_r \\ u_\theta \\ u_z \\ \sigma_{rr} \\ \sigma_{r\theta} \\ \sigma_{rz} \end{pmatrix} = [\mathbf{D}] \begin{pmatrix} L_+ \\ L_- \\ SV_+ \\ SV_- \\ SH_+ \\ SH_- \end{pmatrix} \quad (2.42)$$

where  $[\mathbf{D}]$  is the material layer matrix. This matrix expresses all of the displacements and stresses that are required to evaluate the boundary conditions described in section 2.4 and will be used in following sections to assemble an equation that represents the entire system. The layer matrix has been organised so that the columns are ordered, outward propagating  $f$ , inward propagating  $f$ , outward propagating  $g_1$ , inward propagating  $g_1$ , outward propagating  $g_3$ , and inward propagating  $g_3$ , and the rows are ordered, in-plane displacement,  $u_z$ , normal displacement,  $u_r$ , shear displacement,  $u_\theta$ , normal stress,  $\sigma_{rr}$ , shear stress (in direction of propagation),  $\sigma_{rz}$ , and shear stress perpendicular to the direction of propagation,  $\sigma_{r\theta}$ . This order was chosen to match the pre-existing layer matrix for flat plates that is used in Disperse. It is shown below in graphical form, where the + subscripts denote outward propagating waves (downward direction for the plate case), the – subscripts denote the inward propagating waves (upward direction for the plate case) and the partial wave amplitudes are denoted  $L$ ,  $SV$ , and  $SH$ .

$$\begin{array}{cccccc} & L_+ & L_- & SV_+ & SV_- & SH_+ & SH_- \\ u_z & \mathbf{D}(1, 1) & \mathbf{D}(1, 2) & & \cdots & & \mathbf{D}(1, 6) \\ u_r & \mathbf{D}(2, 1) & & & & & \\ u_\theta & & & & & & \\ \sigma_{rr} & \vdots & & & & & \ddots \\ \sigma_{rz} & & & & & & \\ \sigma_{r\theta} & \mathbf{D}(6, 1) & & & \cdots & & \mathbf{D}(6, 6) \end{array}$$

For a cylindrical isotropic material layer, the material layer matrix is given by,

$$\begin{array}{ll}
 \begin{array}{l}
 u_z \\
 \mathbf{D}(1, 2) = \imath(\xi r^2 Z_n(\alpha r)) \\
 \mathbf{D}(1, 4) = \imath(\beta r^2 Z_n(\beta r)) \\
 \mathbf{D}(1, 6) = 0 \\
 \mathbf{D}(1, 1) = \imath(\xi r^2 W_n(\alpha r)) \\
 \mathbf{D}(1, 3) = \imath(\gamma_2 \beta r^2 W_n(\beta r)) \\
 \mathbf{D}(1, 5) = 0
 \end{array}
 &
 \begin{array}{l}
 \sigma_{rr} \\
 \mathbf{D}(4, 2) = ((\xi^2 - \beta^2)r^2 + 2n(n-1))Z_n(\alpha r) + 2\gamma_1 \alpha r Z_{n+1}(\alpha r) \\
 \mathbf{D}(4, 4) = 2\xi \beta r^2 Z_n(\beta r) - 2\xi r(n+1)Z_{n+1}(\beta r) \\
 \mathbf{D}(4, 6) = 2n(n-1)Z_n(\beta r) - 2\gamma_2 n \beta r Z_{n+1}(\beta r) \\
 \mathbf{D}(4, 1) = ((\xi^2 - \beta^2)r^2 + 2n(n-1))W_n(\alpha r) + 2\alpha r W_{n+1}(\alpha r) \\
 \mathbf{D}(4, 3) = 2\gamma_2 \xi \beta r^2 W_n(\beta r) - 2(n+1)\xi r W_{n+1}(\beta r) \\
 \mathbf{D}(4, 5) = 2n(n-1)W_n(\beta r) - 2n\beta r W_{n+1}(\beta r)
 \end{array}
 \end{array}$$
  

$$\begin{array}{ll}
 \begin{array}{l}
 u_r \\
 \mathbf{D}(2, 2) = nr Z_n(\alpha r) - \gamma_1 \alpha r^2 Z_{n+1}(\alpha r) \\
 \mathbf{D}(2, 4) = \xi r^2 Z_{n+1}(\beta r) \\
 \mathbf{D}(2, 6) = nr Z_n(\beta r) \\
 \mathbf{D}(2, 1) = nr W_n(\alpha r) - \alpha r^2 W_{n+1}(\alpha r) \\
 \mathbf{D}(2, 3) = \xi r^2 W_{n+1}(\beta r) \\
 \mathbf{D}(2, 5) = nr W_n(\beta r)
 \end{array}
 &
 \begin{array}{l}
 \sigma_{rz} \\
 \mathbf{D}(5, 2) = \imath(2n\xi r Z_n(\alpha r) - 2\gamma_1 \xi \alpha r^2 Z_{n+1}(\alpha r)) \\
 \mathbf{D}(5, 4) = \imath(n\beta r Z_n(\beta r) + (\xi^2 - \beta^2)r^2 Z_{n+1}(\beta r)) \\
 \mathbf{D}(5, 6) = \imath(n\xi r Z_n(\beta r)) \\
 \mathbf{D}(5, 1) = \imath(2n\xi r W_n(\alpha r) - 2\xi \alpha r^2 W_{n+1}(\alpha r)) \\
 \mathbf{D}(5, 3) = \imath(\gamma_2 n \beta r W_n(\beta r) + (\xi^2 - \beta^2)r^2 W_{n+1}(\beta r)) \\
 \mathbf{D}(5, 5) = \imath(n\xi r W_n(\beta r))
 \end{array}
 \end{array}$$
  

$$\begin{array}{ll}
 \begin{array}{l}
 u_\theta \\
 \mathbf{D}(3, 2) = \imath(nr Z_n(\alpha r)) \\
 \mathbf{D}(3, 4) = \imath(-\xi r^2 Z_{n+1}(\beta r)) \\
 \mathbf{D}(3, 6) = \imath(nr Z_n(\beta r) - \beta \gamma_2 r^2 Z_{n+1}(\beta r)) \\
 \mathbf{D}(3, 1) = \imath(nr W_n(\alpha r)) \\
 \mathbf{D}(3, 3) = \imath(-\xi r^2 W_{n+1}(\beta r)) \\
 \mathbf{D}(3, 5) = \imath(nr W_n(\beta r) - \beta r^2 W_{n+1}(\beta r))
 \end{array}
 &
 \begin{array}{l}
 \sigma_{r\theta} \\
 \mathbf{D}(6, 2) = \imath(2n(n-1)Z_n(\alpha r) - 2\gamma_1 n \alpha r Z_{n+1}(\alpha r)) \\
 \mathbf{D}(6, 4) = \imath(-\xi \beta r^2 Z_n(\beta r) + 2\xi r(n+1)Z_{n+1}(\beta r)) \\
 \mathbf{D}(6, 6) = \imath((2n(n-1) - \beta^2 r^2)Z_n(\beta r) + 2\gamma_2 \beta r Z_{n+1}(\beta r)) \\
 \mathbf{D}(6, 1) = \imath(2n(n-1)W_n(\alpha r) - 2n \alpha r W_{n+1}(\alpha r)) \\
 \mathbf{D}(6, 3) = \imath(-\xi \gamma_2 \beta r^2 W_n(\beta r) + 2\xi r(n+1)W_{n+1}(\beta r)) \\
 \mathbf{D}(6, 5) = \imath((2n(n-1) - \beta^2 r^2)W_n(\beta r) + 2\beta r W_{n+1}(\beta r))
 \end{array}
 \end{array}$$

(2.43)

where  $Z_n()$  and  $W_n()$  represent incoming and outgoing Bessel functions,  $n$  is the circumferential order,  $r$  is the radius,  $\xi$  is the axial wavenumber (the wavenumber in the direction of propagation),  $\mu$  is one

of Lamé's constants,  $\alpha^2$  is  $(\omega/v_1)^2 - \xi^2$ ,  $\beta^2$  is  $(\omega/v_2)^2 - \xi^2$ ,  $v_1$  and  $v_2$  are the longitudinal and shear bulk velocities, and  $\gamma_1$  and  $\gamma_2$  account for differences in the recurrence relationships of different Bessel functions as will be discussed in the following paragraph. The labels above each of the rows of the matrix specify which displacement or stress corresponds to that component. In the formation of the above matrix, the displacements have been multiplied by  $r^2$  and the stresses by  $r^2/\mu$  to simplify the resulting expressions and avoid dividing by the radius. For single layered problems the scaling factors can be omitted during the formation of the global matrix (see section 2.8.1) and the solution is not affected. However, for multilayered problems, Lamé's constant,  $\mu$ , must be included in the expressions for the stresses. The phase factors,  $\iota$ , are normally included so that the relative phases of the various components are expressly shown. With the exception of the scaling factors, the expressions for the stresses that appear in equation 2.43 closely match those that Gazis derived[4]. However, it should be noted that the  $\alpha_1$  in the first part of Gazis expression for the inward longitudinal component of  $\sigma_{rz}$  ( $c_{31}$  in his derivation) should actually be an  $a$ .

In equation 2.43,  $Z_n$  represents the inward directed waves, which can be expressed by the Bessel functions,  $\mathbf{J}_n$ ,  $\mathbf{I}_n$ , or  $\mathbf{H}_n^{(2)}$ , depending on the solution type and the phase of the argument.  $W_n$  represents the outward directed wave and can be expressed by  $\mathbf{Y}_n$ ,  $\mathbf{K}_n$ , or  $\mathbf{H}_n^{(1)}$ . Since the recurrence relations for  $\mathbf{I}_n$ , and  $\mathbf{K}_n$ , are different from the relations for  $\mathbf{J}_n$ ,  $\mathbf{Y}_n$ ,  $\mathbf{H}_n^{(1)}$ , or  $\mathbf{H}_n^{(2)}$ , the parameters  $\gamma_1$  and  $\gamma_2$  have been introduced into the equations. These parameters are  $-1$  when the Bessel functions  $\mathbf{I}_n$  and  $\mathbf{K}_n$  are used and are  $1$  when any of the other Bessel functions are used. The parameters have been divided into two parts,  $\gamma_1$  and  $\gamma_2$ , the first of which relates to the longitudinal component and the second of which relates to the shear component. Table 2.1 and section 2.6.1 detail under what conditions the different types of Bessel functions should be used.

### 2.6.5 Liquids

In the cylindrical case, liquids cannot be simulated by creating the material matrix for a solid with a very low shear speed, as can be done with the plate case [6]. A small shear velocity forces the arguments of the Bessel functions to be too large for the numerical routines to be able to calculate them. However the material matrix can easily be simplified for the case of an ideal liquid layer by eliminating the shear components. To model an ideal inviscid liquid, only the scalar potential  $\phi$  needs to be used since the stress now becomes a single dimensional, scalar field. In addition, the material property,  $\mu$ , which most strongly influences the shear action of the material, is now set to be zero. Thus the displacements and stresses become,

$$\begin{aligned} u_r &= f' e^{\iota(n\theta + \xi z - \omega t)} \\ u_\theta &= i \frac{n}{r} f e^{\iota(n\theta + \xi z - \omega t)} \\ u_z &= i \xi f e^{\iota(n\theta + \xi z - \omega t)} \\ \sigma_{rr} &= -\lambda(\alpha^2 + \xi^2) f e^{\iota(n\theta + \xi z - \omega t)} \end{aligned}$$

$$\begin{aligned}\sigma_{r\theta} &= 0 \\ \sigma_{rz} &= 0\end{aligned}\tag{2.44}$$

Since an inviscid liquid does not support shear, the boundary conditions for a solid-liquid interface are different from those for a solid-solid interface. As expressed in equation 2.3, only the normal (perpendicular to the axis of the cylinder) displacement and the normal, compressional stress need to be continuous at the boundary between a liquid and a solid.

From these conditions and equation 2.44, we can assemble a material matrix for a cylindrical liquid layer that is equivalent to the material layer matrix for a solid layer in equation 2.43. All of the elements of the liquid material matrix are zero, except for the following,

$$\begin{aligned}u_r \\ \mathbf{D}(2, 1) &= nrW_n(\alpha r) - \alpha r^2 W_{n+1}(\alpha r) \\ \mathbf{D}(2, 2) &= nrZ_n(\alpha r) - \alpha r^2 Z_{n+1}(\alpha r)\end{aligned}\tag{2.45}$$

$$\begin{aligned}\sigma_{rr} \\ \mathbf{D}(4, 1) &= -\rho\omega^2 r^2 W_n(\alpha r) \\ \mathbf{D}(4, 2) &= -\rho\omega^2 r^2 Z_n(\alpha r)\end{aligned}\tag{2.46}$$

where both the displacements and the stresses are scaled by  $1/r^2$ .

## 2.7 Transversely Isotropic Cylindrical Layers

This section derives the material layer matrix for the transversely isotropic cylindrical layers whose material axis of symmetry is aligned with the global  $\hat{z}$  axis. The derivation closely follows that of Mirsky [5] for single layered, hollow, free, transversely isotropic circular cylinders. A very similar derivation can also be found in Berliner and Solecki's 1996 work on fluid-loaded, single layered, transversely isotropic cylinders [32].

The derivation proceeds in a similar manner to the isotropic case. The coupled equations of motion are expressed in cylindrical coordinates and uncoupled by expressing the displacements in terms of two potential functions. Then, the stresses are derived as functions of the wave potentials. The assumptions and boundary conditions for this problem remain the same as for the isotropic case, however the stress-strain relationships must change to accommodate the anisotropy. All of the elastic stiffness constants are treated as real, therefore only elastic materials are considered in this transversely isotropic derivation.

### 2.7.1 Equations of Motion

The general Euler equations of motion (given in equation 2.4) can be expressed in cylindrical coordinates  $(r, \theta, z, t)$  as,

$$\begin{aligned} \frac{\partial \sigma_{rr}}{\partial r} + \frac{1}{r} \frac{\partial \sigma_{\theta\theta}}{\partial \theta} + \frac{\partial \sigma_{zz}}{\partial z} + \frac{1}{r} (\sigma_{rr} - \sigma_{\theta\theta}) &= \rho \frac{\partial^2 u_r}{\partial t^2}, \\ \frac{\partial \sigma_{\theta z}}{\partial z} + \frac{1}{r} \frac{\partial \sigma_{\theta\theta}}{\partial \theta} + \frac{2}{r} \sigma_{r\theta} + \frac{\partial \sigma_{r\theta}}{\partial r} &= \rho \frac{\partial^2 u_\theta}{\partial t^2}, \\ \frac{\partial \sigma_{zz}}{\partial z} + \frac{1}{r} \frac{\partial \sigma_{\theta z}}{\partial \theta} + \frac{1}{r} \sigma_{rz} + \frac{\partial \sigma_{rz}}{\partial r} &= \rho \frac{\partial^2 u_z}{\partial t^2}, \end{aligned} \quad (2.47)$$

where  $\sigma$  represents the stress components and  $u$  represents the displacement.

Similarly the strains,  $\epsilon$ , in equation 2.6 can be expressed in cylindrical coordinates as,

$$\begin{aligned} \epsilon_{rr} &= \frac{\partial u_r}{\partial r}, & \epsilon_{\theta\theta} &= \frac{1}{r} \frac{\partial u_\theta}{\partial \theta} + \frac{u_r}{r}, & \epsilon_{zz} &= \frac{\partial u_z}{\partial z}, \\ \epsilon_{rz} &= \frac{\partial u_r}{\partial z} + \frac{\partial u_z}{\partial r}, \\ \epsilon_{r\theta} &= r \frac{\partial}{\partial r} \left( \frac{u_\theta}{r} \right) + \frac{1}{r} \frac{\partial u_r}{\partial \theta}, \\ \epsilon_{\theta z} &= \frac{\partial u_\theta}{\partial z} + \frac{1}{r} \frac{\partial u_z}{\partial \theta}. \end{aligned} \quad (2.48)$$

For the case of a transversely isotropic material whose material axis of symmetry is aligned along the axis of the cylinder, the generalised Hooke's law (equation 2.5) can be simplified as,

$$\begin{aligned} \sigma_{rr} &= C_{11}\epsilon_{rr} + C_{12}\epsilon_{\theta\theta} + C_{13}\epsilon_{zz}, \\ \sigma_{\theta\theta} &= C_{12}\epsilon_{rr} + C_{11}\epsilon_{\theta\theta} + C_{13}\epsilon_{zz}, \\ \sigma_{zz} &= C_{13}\epsilon_{rr} + C_{13}\epsilon_{\theta\theta} + C_{33}\epsilon_{zz}, \\ \sigma_{\theta z} &= C_{44}\epsilon_{\theta z}, \\ \sigma_{zr} &= C_{44}\epsilon_{zr}, \\ \sigma_{r\theta} &= C_{66}\epsilon_{r\theta} \end{aligned} \quad (2.49)$$

where an abbreviated subscript notation has been used for the  $c_{ijkl}$  stiffness constants, such that the following indices have been substituted (as in Auld, reference [39]),

$$\begin{aligned} 1 & rr \text{ (11)} \\ 2 & \theta\theta \text{ (22)} \\ 3 & zz \text{ (33)} \\ 4 & \theta z \text{ (23)} \\ 5 & rz \text{ (31)} \\ 6 & r\theta \text{ (12)} \end{aligned} \quad (2.50)$$

This operation reduces the fourth rank stiffness tensor,  $c_{ijkl}$ , to a 6 by 6 matrix,  $C_{mn}$ , which is more convenient to use.

Since the material is transversely isotropic, the material can be described by five independent stiffness constants. The sixth stiffness constant appearing in equations 2.49, can be related to two others by the relation  $C_{12} = C_{11} - 2C_{66}$ .

Substituting equation 2.48 for the cylindrical strains into equation 2.49 of the stress-strain relationship, yields the following three-dimensional equations of motion in cylindrical coordinates,

$$\begin{aligned}
\rho \frac{\partial^2 u_r}{\partial t^2} &= C_{11} \left( \frac{\partial^2 u_r}{\partial r^2} + \frac{1}{r} \frac{\partial u_r}{\partial r} - \frac{u_r}{r^2} \right) + \frac{C_{66}}{r^2} \frac{\partial^2 u_r}{\partial \theta^2} + C_{44} \frac{\partial^2 u_r}{\partial z^2} \\
&\quad + \frac{1}{r} (C_{66} + C_{12}) \frac{\partial^2 u_\theta}{\partial r \partial \theta} - \frac{1}{r^2} (C_{66} + C_{11}) \frac{\partial u_\theta}{\partial \theta} \\
&\quad + (C_{44} + C_{13}) \frac{\partial^2 u_z}{\partial r \partial z} \\
\rho \frac{\partial^2 u_\theta}{\partial t^2} &= \frac{1}{r} (C_{66} + C_{12}) \frac{\partial^2 u_r}{\partial r \partial \theta} + \frac{1}{r^2} (C_{66} + C_{11}) \frac{\partial u_r}{\partial \theta} \\
&\quad + C_{66} \left( \frac{\partial^2 u_\theta}{\partial r^2} + \frac{1}{r} \frac{\partial u_\theta}{\partial r} - \frac{u_\theta}{r^2} \right) + \frac{C_{11}}{r^2} \frac{\partial^2 u_\theta}{\partial \theta^2} + C_{44} \frac{\partial^2 u_\theta}{\partial z^2} \\
&\quad + \frac{1}{r} (C_{44} + C_{13}) \frac{\partial^2 u_z}{\partial \theta \partial z} \\
\rho \frac{\partial^2 u_z}{\partial t^2} &= (C_{44} + C_{13}) \left( \frac{\partial^2 u_r}{\partial r \partial z} + \frac{1}{r} \frac{\partial u_r}{\partial z} + \frac{\partial^2 u_\theta}{\partial \theta \partial z} \right) \\
&\quad + C_{44} \left( \frac{\partial^2 u_z}{\partial r^2} + \frac{1}{r} \frac{\partial u_z}{\partial r} + \frac{1}{r^2} \frac{\partial^2 u_z}{\partial \theta^2} \right) + C_{33} \frac{\partial^2 u_z}{\partial z^2}
\end{aligned} \tag{2.51}$$

## 2.7.2 Determination of Potential Functions

As Berliner and Sulecki indicate in reference [32], the coupled equations 2.51 can be uncoupled by eliminating two of the three displacement components through two of the three equations. However, this results in sixth order partial equations. Therefore, like Berliner[32] and Mirsky[5], this derivation uncouples equations 2.51 by expressing the displacements in terms of derivatives of potential functions,  $\varphi$  and  $\psi$ . Mirsky gives the potentials as,

$$\begin{aligned}
u_r(r, \theta, z, t) &= \left( \frac{\partial \varphi(r, \theta)}{\partial r} + \frac{1}{r} \frac{\partial \psi(r, \theta)}{\partial \theta} \right) \cos(\omega t + \xi z), \\
u_\theta(r, \theta, z, t) &= \left( \frac{1}{r} \frac{\partial \varphi(r, \theta)}{\partial \theta} - \frac{\partial \psi(r, \theta)}{\partial r} \right) \cos(\omega t + \xi z), \\
u_z(r, \theta, z, t) &= \lambda \varphi(r, \theta) \sin(\omega t + \xi z),
\end{aligned} \tag{2.52}$$

where  $\omega$  is the angular frequency,  $\xi$  is the wavenumber (in the direction of propagation), and  $\lambda$  is an arbitrary constant that will be determined later. He assumes a sinusoidal variation with time and distance along the cylinder.



To match the isotropic derivation, and to simplify the handling of complex wavenumbers, these expressions are modified so that an exponential dependence on  $z$  and  $t$  is assumed, as done in Berliner and Soleccki [32]. This dependence yields the following displacement forms,

$$\begin{aligned} u_r(r, \theta, z, t) &= \left( \frac{\partial \varphi(r, \theta)}{\partial r} + \frac{1}{r} \frac{\partial \psi(r, \theta)}{\partial \theta} \right) e^{\iota(\xi z - \omega t)}, \\ u_\theta(r, \theta, z, t) &= \left( \frac{1}{r} \frac{\partial \varphi(r, \theta)}{\partial \theta} - \frac{\partial \psi(r, \theta)}{\partial r} \right) e^{\iota(\xi z - \omega t)}, \\ u_z(r, \theta, z, t) &= \lambda \varphi(r, \theta) e^{\iota(\xi z - \omega t)}. \end{aligned} \quad (2.53)$$

Substituting these potentials into the equations of motion (equations 2.51) and simplifying the expressions yields the following expressions for the displacement potentials,

$$\begin{aligned} 0 &= \frac{\partial}{\partial r} [C_{11} \nabla^2 \varphi + (\rho \omega^2 - \xi^2 C_{44} + \iota \lambda \xi (C_{13} + C_{44})) \varphi] \\ &\quad + \frac{1}{r} \frac{\partial}{\partial \theta} [C_{66} \nabla^2 \psi + (\rho \omega^2 - \xi^2 C_{44}) \psi], \\ 0 &= \frac{1}{r} \frac{\partial}{\partial \theta} [C_{11} \nabla^2 \varphi + (\rho \omega^2 - \xi^2 C_{44} + \iota \lambda \xi (C_{13} + C_{44})) \varphi] \\ &\quad - \frac{\partial}{\partial r} [C_{66} \nabla^2 \psi + (\rho \omega^2 - \xi^2 C_{44}) \psi], \\ 0 &= [\iota \xi (C_{13} + C_{44}) + \lambda C_{44}] \nabla^2 \varphi \\ &\quad + [\rho \omega^2 - \xi^2 C_{33}] \lambda \varphi, \end{aligned} \quad (2.54)$$

where  $\nabla^2$  is the two-dimensional Laplacian operator,

$$\nabla^2 = \frac{\partial^2}{\partial r^2} + \frac{1}{r} \frac{\partial}{\partial r} + \frac{1}{r^2} \frac{\partial^2}{\partial \theta^2}. \quad (2.55)$$

The first two equations of 2.54 are satisfied if

$$C_{11} \nabla^2 \varphi + [\rho \omega^2 - \xi^2 C_{44} + \iota \lambda \xi (C_{44} + C_{13})] \varphi = 0 \quad (2.56)$$

$$C_{66} \nabla^2 \psi + [\rho \omega^2 - \xi^2 C_{44}] \psi = 0 \quad (2.57)$$

In equations 2.56 and 2.57, the potentials  $\varphi$  and  $\psi$  are decoupled and can be solved separately. The solutions to the potential function  $\varphi$  (equation 2.56) will be sought first and then the potential function  $\psi$  (equation 2.57) will be examined.

Since the potential  $\varphi$  appears both in the third equation of motion (equation 2.54) and in equation 2.56, which satisfies the first two equations of motion, the value of  $\lambda$  must be chosen so that the equations are consistent. Matching the coefficients of the  $\varphi$  and  $\nabla^2 \varphi$  terms demands that the following ratio, labelled

as  $p^2$ , must hold true,

$$\frac{[\rho\omega^2 - \xi^2 C_{33}]\lambda}{i\xi(C_{13} + C_{44}) + \lambda C_{44}} = \frac{\rho\omega^2 - \xi^2 C_{44} + i\lambda\xi(C_{44} + C_{13})}{C_{11}} \equiv p^2 \quad (2.58)$$

Solving equation 2.58 for  $\lambda$ , yields the two following equivalent expressions,

$$\begin{aligned} \lambda &= i\eta = \frac{i\xi p^2 (C_{13} + C_{44})}{\rho\omega^2 - \xi^2 C_{33} - p^2 C_{44}} \quad \text{and} \\ \lambda &= i\eta = i \frac{\rho\omega^2 - \xi^2 C_{44} - p^2 C_{11}}{\xi(C_{13} + C_{44})}. \end{aligned} \quad (2.59)$$

The  $\eta$  parameter, a phase shifted variant of  $\lambda$ , has been introduced here to simplify later expressions. Setting the two expressions in equations 2.59 equal to each other reveals that  $p^2$  must satisfy the following equation,

$$\begin{aligned} &[C_{11}C_{44}](p^2)^2 \\ &+ [C_{11}C_{33} - C_{13}^2 - 2C_{13}C_{44}]\xi^2 - (C_{11} + C_{44})\rho\omega^2]p^2 \\ &+ (C_{44}\xi^2 - \rho\omega^2)(C_{33}\xi^2 - \rho\omega^2) = 0 \end{aligned} \quad (2.60)$$

There are two roots to this equation,  $p_1^2$  and  $p_2^2$ , which can be calculated as,

$$\begin{aligned} p_1^2 &= \frac{-B - \sqrt{B^2 - 4AC}}{2A}, \\ p_2^2 &= \frac{-B + \sqrt{B^2 - 4AC}}{2A}, \end{aligned} \quad (2.61)$$

where,

$$\begin{aligned} A &= C_{11}C_{44} \\ B &= C_{11}C_{33} - C_{13}^2 - 2C_{13}C_{44}\xi^2 - (C_{11} + C_{44})\rho\omega^2 \\ C &= (C_{44}\xi^2 - \rho\omega^2)(C_{33}\xi^2 - \rho\omega^2) \end{aligned} \quad (2.62)$$

Both of these roots satisfy equation 2.56 for the potential  $\varphi$ . These solutions can be written as,

$$\begin{aligned} \nabla^2 \varphi_1(r, \theta) + p_1^2 \varphi_1(r, \theta) &= 0 \\ \nabla^2 \varphi_2(r, \theta) + p_2^2 \varphi_2(r, \theta) &= 0 \end{aligned} \quad (2.63)$$

The roots  $p_1^2$  and  $p_2^2$  represent the square of the wavenumber component in the  $\hat{r} - \hat{\theta}$  plane. For an isotropic material, they are equivalent to  $\alpha^2$  and  $\beta^2$  in the isotropic derivation of section 2.6. These roots can be inserted into equation 2.59 to obtain values for  $\eta$ . The value,  $\eta_1$  corresponds to the value used with root  $p_1$  and  $\eta_2$  corresponds to the value used with root  $p_2$ . When the material is isotropic

these values simplify to,

$$\begin{aligned}\eta_1 &= \xi, \\ \eta_2 &= \frac{p_2^2}{\xi}.\end{aligned}\tag{2.64}$$

The roots  $p_1^2$  and  $p_2^2$  can also be found by solving for the eigenvalues of Christoffel's equation for a transversely isotropic medium in cylindrical coordinates, as Nagy does in reference [31]. When this technique is used, the displacements are equal to the eigenvectors of Christoffel's equation and the same results are obtained as when the potential method is used.

Now that we have solved for  $\varphi$  in equation 2.56, we are ready to solve for  $\psi$  in equation 2.57, which is much more straight forward.

The  $\psi$  component in the first two of the three equations of motion given in equation 2.54 can be satisfied by satisfying equation 2.57,

$$C_{66}\nabla^2\psi + [\rho\omega^2 - \xi^2 C_{44}]\psi = 0.$$

A third root for the wavenumber component in the  $\hat{r} - \hat{\theta}$  plane,  $q^2$ , can be defined as

$$q^2 = \frac{\rho\omega^2 - \xi^2 C_{44}}{C_{66}},\tag{2.65}$$

such that it satisfies the equation,

$$\nabla^2\psi(r, \theta) + q^2\psi(r, \theta) = 0\tag{2.66}$$

### 2.7.3 Solution of the Potential Functions

As for isotropic materials in section 2.6.1, a separation of variables can be performed to determine the solution to the potential functions,  $\varphi_1$ ,  $\varphi_2$ , and  $\psi$ . By substituting a separated equation for the potential  $\varphi_1$ ,

$$\varphi_1 = g_1(r)\Theta_1(\theta)\tag{2.67}$$

into equation 2.63 yields

$$\begin{aligned}\nabla^2 [g_1(r)\Theta_1(\theta)] + p_1^2 [g_1(r)\Theta_1(\theta)] &= 0, \\ \left(\frac{\partial^2}{\partial r^2} + \frac{1}{r}\frac{\partial}{\partial r} + \frac{1}{r^2}\frac{\partial^2}{\partial \theta^2}\right) [g_1(r)\Theta_1(\theta)] + p_1^2 [g_1(r)\Theta_1(\theta)] &= 0.\end{aligned}\tag{2.68}$$

Provided that  $\frac{\partial \Theta_1}{\partial^2 \theta} = -n^2 \Theta_1$ , the Bessel function differential operator,

$$B_{n,r} = \left( \frac{\partial^2}{\partial r^2} + \frac{1}{r} \frac{\partial}{\partial r} - \left( \frac{n^2}{r^2} - 1 \right) \right), \quad (2.69)$$

will adequately describe the radial dependence of the potential function,  $g_1$ . Therefore a valid solution for the radial component is,

$$g_1(r) = A_1 \mathbf{J}_n(p_1 r) + B_1 \mathbf{Y}_n(p_1 r), \quad (2.70)$$

where  $\mathbf{J}_n$  and  $\mathbf{Y}_n$  represent Bessel functions of the first and second kind, and  $p_1 = \sqrt{p_1^2}$  is the wavenumber in the radial direction, and  $A_1$  and  $B_1$  are unknown amplitudes. As discussed in section 2.6.1 for isotropic materials, the solution can be made more stable if the modified Bessel functions are used whenever the partial waves are inhomogeneous. Therefore, whenever  $\rho\omega^2 > \xi^2 C_{33}$ ,  $\mathbf{I}_n$  and  $\mathbf{K}_n$  should replace the Bessel functions  $\mathbf{J}_n$  and  $\mathbf{Y}_n$ . In this case the argument of the Bessel functions will change from  $\sqrt{p_1^2}$  to  $\sqrt{-p_1^2}$ , since the modified Bessel function differential operator is slightly different. This general solution can be written as

$$g_1(r) = Z_1 Z_n(\zeta_1 r) + W_1 Z_n(\zeta_1 r), \quad (2.71)$$

where  $Z_n$  represents  $\mathbf{J}_n$  or  $\mathbf{I}_n$ ,  $W_n$  represents  $\mathbf{Y}_n$  or  $\mathbf{K}_n$ , and  $\zeta_1$  represents  $\sqrt{p_1^2}$  or  $\sqrt{-p_1^2}$ , depending on nature of the partial wave.

Valid solutions for the  $\theta$  dependence,  $\frac{\partial \Theta_1}{\partial^2 \theta} = -n^2 \Theta_1$ , may take two forms,

$$\Theta_1(\theta) = C_1 e^{i n \theta} + C_2 e^{-i n \theta}, \quad \text{or} \quad (2.72)$$

$$\Theta_1(\theta) = C_1 \sin(n\theta) + C_2 \cos(n\theta), \quad (2.73)$$

where  $C_1$  and  $C_2$  are complex constants and  $n$  is the number of wavelengths around the circumference of the cylinder, which must be an integer to ensure that the solution is the same at  $\theta$  and  $\theta + 2\pi$ . The exponential dependence for  $\theta$  is chosen for the rest of the derivation to match the previously derived isotropic case. However, both solutions produce the same dispersion curves since sine and cosine can be expressed as a linear combination of  $e^{i n \theta}$  and  $e^{-i n \theta}$  and vice versa. Although the dispersion curves are identical, the expressions for the elements of the material layer matrix will vary considerably.

The same separation of variables that was performed on  $\varphi_1$  can be performed for the other two potential functions,  $\varphi_2$  and  $\psi$ , and the phase angles,  $C_i$  can be adjusted so that the phases of the components in equation 2.53 are consistent. Performing these operations yields the following equations for the potential functions,

$$\begin{aligned} \varphi_1(r, \theta) &= g_1(r) e^{i n \theta} = (A_1 Z_n(\zeta_1 r) + B_1 W_n(\zeta_1 r)) e^{i n \theta}, \\ \varphi_2(r, \theta) &= g_2(r) e^{i n \theta} = (A_2 Z_n(\zeta_2 r) + B_2 W_n(\zeta_2 r)) e^{i n \theta}, \\ \psi(r, \theta) &= -i g_3(r) e^{i n \theta} = -i (A_3 Z_n(\zeta_3 r) + B_3 W_n(\zeta_3 r)) e^{i n \theta}. \end{aligned} \quad (2.74)$$

### 2.7.4 Creation of the Layer Matrix

Substituting the expressions for the potentials in equations 2.74 into the expressions for the displacements in equations 2.53 yields,

$$\begin{aligned}
 u_r(r, \theta, z, t) &= \left( \frac{\partial g_1(r)}{\partial r} + \frac{\partial g_1(r)}{\partial r} + \frac{n}{r} g_3 \right) e^{i(n\theta + \xi z - \omega t)}, \\
 u_\theta(r, \theta, z, t) &= i \left( n \frac{g_1(r) + g_2(r)}{r} + \frac{\partial g_3(r)}{\partial r} \right) e^{i(n\theta + \xi z - \omega t)}, \\
 u_z(r, \theta, z, t) &= i(\eta_1 g_1(r) + \eta_2 g_2(r)) e^{i(n\theta + \xi z - \omega t)},
 \end{aligned} \tag{2.75}$$

where  $g_1$ ,  $g_2$ , and  $g_3$ , are potential functions defined in equation 2.74,  $\eta_1$  and  $\eta_2$  are the constants defined in equation 2.59 evaluated for each of the two roots,  $p_1$  and  $p_2$ ,  $n$  is the circumferential order,  $\omega$  the angular frequency, and  $\xi$  the axial wavenumber.

Since the displacements are known in terms of the potentials, the strain and stress fields can be easily derived using equations 2.48 and 2.49. Once the stress fields are known, the material layer matrix,  $[\mathbf{D}]$ , can be assembled in the same fashion as for the isotropic case, such that it satisfies the following equation,

$$\begin{Bmatrix} u_r \\ u_\theta \\ u_z \\ \sigma_{rr} \\ \sigma_{r\theta} \\ \sigma_{rz} \end{Bmatrix} = [\mathbf{D}] \begin{Bmatrix} \varphi_{1+} \\ \varphi_{1-} \\ \varphi_{2+} \\ \varphi_{2-} \\ \psi_+ \\ \psi_- \end{Bmatrix} \tag{2.76}$$

For a transversely isotropic layer, the components of the material layer matrix,  $[\mathbf{D}]$  are given by,

$$\begin{aligned}
 u_z \\
 \mathbf{D}(1, 2) &= i \eta_1 r^2 \mathbf{Z}_n(r \zeta_1) \\
 \mathbf{D}(1, 4) &= i \eta_2 r^2 \mathbf{Z}_n(r \zeta_2) \\
 \mathbf{D}(1, 6) &= 0 \\
 \mathbf{D}(1, 1) &= i \eta_1 r^2 \mathbf{W}_n(r \zeta_1) \\
 \mathbf{D}(1, 3) &= i \eta_2 r^2 \mathbf{W}_n(r \zeta_2) \\
 \mathbf{D}(1, 5) &= 0
 \end{aligned}$$

$u_r$ 

$$\mathbf{D}(2, 2) = n r \mathbf{Z}_n(r \zeta_1) - \gamma_1 r^2 \zeta_1 \mathbf{Z}_{n+1}(r \zeta_1)$$

$$\mathbf{D}(2, 4) = n r \mathbf{Z}_n(r \zeta_2) - \gamma_2 r^2 \zeta_2 \mathbf{Z}_{n+1}(r \zeta_2)$$

$$\mathbf{D}(2, 6) = n r \mathbf{Z}_n(r \zeta_3)$$

$$\mathbf{D}(2, 1) = n r \mathbf{W}_n(r \zeta_1) - r^2 \zeta_1 \mathbf{W}_{n+1}(r \zeta_1)$$

$$\mathbf{D}(2, 3) = n r \mathbf{W}_n(r \zeta_2) - r^2 \zeta_2 \mathbf{W}_{n+1}(r \zeta_2)$$

$$\mathbf{D}(2, 5) = n r \mathbf{W}_n(r \zeta_3)$$

 $u_\theta$ 

$$\mathbf{D}(3, 2) = m r \mathbf{Z}_n(r \zeta_1)$$

$$\mathbf{D}(3, 4) = m r \mathbf{Z}_n(r \zeta_2)$$

$$\mathbf{D}(3, 6) = i (n r \mathbf{Z}_n(r \zeta_3) - \gamma_2 r^2 \zeta_3 \mathbf{Z}_{n+1}(r \zeta_3))$$

$$\mathbf{D}(3, 1) = m r \mathbf{W}_n(r \zeta_1)$$

$$\mathbf{D}(3, 3) = m r \mathbf{W}_n(r \zeta_2)$$

$$\mathbf{D}(3, 4) = i (n r \mathbf{W}_n(r \zeta_3) - r^2 \zeta_3 \mathbf{W}_{n+1}(r \zeta_3))$$

 $\sigma_{rr}$ 

$$\mathbf{D}(4, 2) = 2C_{66} ((-n + n^2 - [C_{13} \xi \eta_1 r^2 + C_{11} r^2 \zeta_1^2])/2C_{66}) \mathbf{Z}_n(r \zeta_1) + \gamma_1 r \zeta_1 \mathbf{Z}_{n+1}(r \zeta_1)$$

$$\mathbf{D}(4, 4) = 2C_{66} ((-n + n^2 - [C_{13} \xi \eta_2 r^2 + C_{11} r^2 \zeta_2^2])/2C_{66}) \mathbf{Z}_n(r \zeta_2) + \gamma_2 r \zeta_2 \mathbf{Z}_{n+1}(r \zeta_2)$$

$$\mathbf{D}(4, 6) = 2C_{66} ((-n + n^2) \mathbf{Z}_n(r \zeta_3) - \gamma_2 n r \zeta_3 \mathbf{Z}_{n+1}(r \zeta_3))$$

$$\mathbf{D}(4, 1) = 2C_{66} ((-n + n^2 - [C_{13} \xi \eta_1 r^2 + C_{11} r^2 \zeta_1^2])/2C_{66}) \mathbf{W}_n(r \zeta_1) + r \zeta_1 \mathbf{W}_{n+1}(r \zeta_1)$$

$$\mathbf{D}(4, 3) = 2C_{66} ((-n + n^2 - [C_{13} \xi \eta_2 r^2 + C_{11} r^2 \zeta_2^2])/2C_{66}) \mathbf{W}_n(r \zeta_2) + r \zeta_2 \mathbf{W}_{n+1}(r \zeta_2)$$

$$\mathbf{D}(4, 5) = 2C_{66} ((-n + n^2) \mathbf{W}_n(r \zeta_3) - n r \zeta_3 \mathbf{W}_{n+1}(r \zeta_3))$$

 $\sigma_{rz}$ 

$$\mathbf{D}(5, 2) = iC_{44} ((\xi n r + \eta_1 n r) \mathbf{Z}_n(r \zeta_1) + \gamma_1 (-\xi r^2 - \eta_1 r^2) \zeta_1 \mathbf{Z}_{n+1}(r \zeta_1))$$

$$\mathbf{D}(5, 4) = iC_{44} ((\xi n r + \eta_2 n r) \mathbf{Z}_n(r \zeta_2) + \gamma_2 (-\xi r^2 - \eta_2 r^2) \zeta_2 \mathbf{Z}_{n+1}(r \zeta_2))$$

$$\mathbf{D}(5, 6) = iC_{44} \xi n r \mathbf{Z}_n(r \zeta_3)$$

$$\mathbf{D}(5, 1) = iC_{44} ((\xi n r + \eta_1 n r) \mathbf{W}_n(r \zeta_1) + (-\xi r^2 - \eta_1 r^2) \zeta_1 \mathbf{W}_{n+1}(r \zeta_1))$$

$$\mathbf{D}(5, 3) = iC_{44} ((\xi n r + \eta_2 n r) \mathbf{W}_n(r \zeta_2) + (-\xi r^2 - \eta_2 r^2) \zeta_2 \mathbf{W}_{n+1}(r \zeta_2))$$

$$\mathbf{D}(5, 5) = iC_{44} \xi n r \mathbf{W}_n(r \zeta_3)$$

Table 2.3: Substitutions that should be made and criteria that should be used for the selection of the type of Bessel functions to be used for the transversely isotropic cylindrical layer matrix.

when $\rho\omega^2 > \xi^2 C_{33}$	when $\xi^2 C_{44} < \rho\omega^2 < \xi^2 C_{33}$	when $\rho\omega^2 < \xi^2 C_{44}$
$\zeta_1 = \sqrt{p_1^2}$	$\zeta_1 = \sqrt{-p_1^2}$	$\zeta_1 = \sqrt{-p_1^2}$
$\zeta_2 = \sqrt{p_2^2}$	$\zeta_2 = \sqrt{p_2^2}$	$\zeta_2 = \sqrt{-p_2^2}$
$\zeta_3 = \sqrt{q^2}$	$\zeta_3 = \sqrt{q^2}$	$\zeta_3 = \sqrt{-q^2}$
$\zeta_1^2 = p_1^2$	$\zeta_1^2 = p_1^2$	$\zeta_1^2 = p_1^2$
$\zeta_2^2 = p_2^2$	$\zeta_2^2 = p_2^2$	$\zeta_2^2 = p_2^2$
$\zeta_3^2 = q^2$	$\zeta_3^2 = q^2$	$\zeta_3^2 = q^2$
$\gamma_1 = 1$	$\gamma_1 = -1$	$\gamma_1 = -1$
$\gamma_2 = 1$	$\gamma_2 = 1$	$\gamma_2 = -1$
$\mathbf{Z}_n(\zeta_1 r) = \mathbf{J}_n(\zeta_1 r)$	$\mathbf{Z}_n(\zeta_1 r) = \mathbf{I}_n(\zeta_1 r)$	$\mathbf{Z}_n(\zeta_1 r) = \mathbf{I}_n(\zeta_1 r)$
$\mathbf{Z}_n(\zeta_2 r) = \mathbf{J}_n(\zeta_2 r)$	$\mathbf{Z}_n(\zeta_2 r) = \mathbf{J}_n(\zeta_2 r)$	$\mathbf{Z}_n(\zeta_2 r) = \mathbf{I}_n(\zeta_2 r)$
$\mathbf{Z}_n(\zeta_3 r) = \mathbf{J}_n(\zeta_3 r)$	$\mathbf{Z}_n(\zeta_3 r) = \mathbf{J}_n(\zeta_3 r)$	$\mathbf{Z}_n(\zeta_3 r) = \mathbf{I}_n(\zeta_3 r)$
$\mathbf{W}_n(\zeta_1 r) = \mathbf{Y}_n(\zeta_1 r)$	$\mathbf{W}_n(\zeta_1 r) = \mathbf{K}_n(\zeta_1 r)$	$\mathbf{W}_n(\zeta_1 r) = \mathbf{K}_n(\zeta_1 r)$
$\mathbf{W}_n(\zeta_2 r) = \mathbf{Y}_n(\zeta_2 r)$	$\mathbf{W}_n(\zeta_2 r) = \mathbf{Y}_n(\zeta_2 r)$	$\mathbf{W}_n(\zeta_2 r) = \mathbf{K}_n(\zeta_2 r)$
$\mathbf{W}_n(\zeta_3 r) = \mathbf{Y}_n(\zeta_3 r)$	$\mathbf{W}_n(\zeta_3 r) = \mathbf{Y}_n(\zeta_3 r)$	$\mathbf{W}_n(\zeta_3 r) = \mathbf{K}_n(\zeta_3 r)$

$$\sigma_{r\theta}$$

$$\begin{aligned}
\mathbf{D}(6, 2) &= 2C_{66} ((-n + n^2) \mathbf{Z}_n(r \zeta_1) - \gamma_1 n r \zeta_1 \mathbf{Z}_{n+1}(r \zeta_1)) \\
\mathbf{D}(6, 4) &= 2C_{66} ((-n + n^2) \mathbf{Z}_n(r \zeta_2) - \gamma_2 n r \zeta_2 \mathbf{Z}_{n+1}(r \zeta_2)) \\
\mathbf{D}(6, 6) &= 2C_{66} ((-n + n^2 - (1/2)r^2 \zeta_3^2) \mathbf{Z}_n(r \zeta_3) + \gamma_2 r \zeta_3 \mathbf{Z}_{n+1}(r \zeta_3)) \\
\mathbf{D}(6, 1) &= 2C_{66} ((-n + n^2) \mathbf{W}_n(r \zeta_1) - n r \zeta_1 \mathbf{W}_{n+1}(r \zeta_1)) \\
\mathbf{D}(6, 3) &= 2C_{66} ((-n + n^2) \mathbf{W}_n(r \zeta_2) - n r \zeta_2 \mathbf{W}_{n+1}(r \zeta_2)) \\
\mathbf{D}(6, 5) &= 2C_{66} ((-n + n^2 - (1/2)r^2 \zeta_3^2) \mathbf{W}_n(r \zeta_3) + r \zeta_3 \mathbf{W}_{n+1}(r \zeta_3)) \quad (2.77)
\end{aligned}$$

where the following variables are defined as

$r$	the radius	$i$	$\sqrt{-1}$
$\theta$	the circumferential angle	$n$	circumferential order
$z$	the axial direction	$\eta_{1,2}$	matching constants (eqn. 2.59)
$t$	the time	$p_1^2, p_2^2, q^2$	radial wavenumber roots (eqns. 2.58, 2.65)

The values for the variables,  $\zeta_1, \zeta_2, \zeta_3, \zeta_1^2, \zeta_2^2, \zeta_3^2, \gamma_1, \gamma_2, \mathbf{Z}_n$ , and  $\mathbf{W}_n$  depend on the ratio of the frequency, wavenumber, and material properties. The values that these variables will assume are summarised in table 2.3. All of the displacements and stresses in the material layer matrix given in equation 2.77 have been scaled by the radius squared.

## 2.8 Software Implementation of Model

A windows based software package, called Disperse, has been developed around the implementation of these wave propagation solutions. Disperse assembles the layer matrices that have been described in the previous sections in a global matrix, which is described below. Once the global matrix is assembled, valid wave propagation roots for the combined system can be found in frequency - wavenumber - attenuation space. The solutions form curves, called dispersion curves, in this three dimensional solution space. This section describes this process in more detail.

Work on Disperse was begun by Mike Lowe as part of his PhD research[10]. As part of this thesis, the author has expanded Lowe's original version, which handled multilayered isotropic plates, to incorporate cylindrical wave propagation. In addition, the program was converted from a DOS based utility to a Windows based one and numerous options have been added to make the information contained within the dispersion curves more accessible to the user. However, the main root finding and tracing routines remain the same as Lowe used. A demonstration copy of Disperse will be provided by the author upon request.

### 2.8.1 Global Matrix method

Once the wave propagation in each material layer and the boundary conditions for each interface are known, the layers can be combined to describe the entire system. The work in this thesis uses the global matrix method, which was first proposed by Knopoff in 1964[7] for use in modelling multilayered geological systems. The method has been subsequently developed by other researchers such as Randall[8] and Schmidt[61], who have increased its stability. Compared to the Thomson-Haskell transfer matrix technique[13,14], which is also commonly used, this method has the advantage that it remains stable at high frequency-thickness products. In addition, the global matrix method also allows the same intuitive base matrix to be used for real or complex wavenumber, vacuum, liquid or solid half-spaces, and modal or response solutions. The disadvantage is that the global matrix may be large and the solution therefore may be relatively slow when the systems involve many layers. However, the speed of modern computers reduces the effect of this limitation. A comparison and description of various matrix techniques can be found in [6].

In the global matrix method, a single matrix represents the complete system. The global matrix consists of  $6(n - 1)$  equations, where  $n$  is the number of layers (including each of the semi-infinite half-spaces as a layer). The equations are based, in sets of six, on satisfying the boundary conditions at each interface. The columns of the global matrix correspond to the amplitudes of the partial waves in each layer, six for each of the interior layers and three for each of the exterior (semi-infinite) layers. With this assembly of the material layer matrices, the continuity of the stresses and displacements is enforced (along the rows) and the partial waves at the top and the bottom of the layer are consistent (provided



by the column continuity). Figure 2.2 demonstrates how the global matrix is assembled for a five layer system, similar to the one displayed in figure 2.1. Multiplying the global matrix by the partial wave amplitudes simultaneously applies all of the boundary condition equations. This multiplication yields a vector that describes the displacement and stress fields of the excitation force. When no energy is being added to the system, this vector will be zero. Writing this expression as an equation provides the characteristic equation for the system, which may be written,

$$[\mathbf{G}] \{\mathbf{A}\} = 0 \quad (2.78)$$

where  $[\mathbf{G}]$  is the global matrix, and  $\{\mathbf{A}\}$  is a vector of the partial wave amplitudes. This equation is satisfied if the determinant of the global matrix is zero. The frequency, wavenumber, and attenuation values determine whether this condition is met, and need to be found via an iterative procedure that is explained below.

There are some conditions for which the global matrix will become singular other than valid wave propagation solutions [10,6]. The most common of these conditions occurs when the phase velocity ( $\omega/\xi$ ) is equal to one of the bulk velocities. In this case, the effect of the upward and downward travelling waves is indistinguishable and two of the columns become linearly dependent, causing the global matrix to become singular. Therefore, when solving for roots, the routine must be careful to avoid these spurious roots.

If one or both of the half-spaces is either a liquid or a vacuum, the matrix can be easily modified to remove the unnecessary boundary conditions and partial waves, as demonstrated for the centre core ('top' half space for a plate) in Figures 2.2(b) and 2.2(c). When the centre core is vacuum, the first three columns and rows are removed by making all of the elements zero except for the diagonal elements (1,1), (2,2), and (3,3), which are set to one. This operation removes the constraints on the displacements at the inside of the system and eliminates reference to the bulk waves that would exist in the centre core. If the center core is liquid, the constraints on the two tangential displacements are removed. In addition, the shear bulk waves are removed. This operation leaves elements that relate the amplitude of the longitudinal bulk wave to the normal displacement and normal stress at the interface of the centre core and the first layer. If the outer half-space is a vacuum or a liquid, similar modifications can be made to the constraints on the displacement at the outside surface of the cylinder and to the bulk wave amplitudes in the outer half-space.

### 2.8.2 Finding a Root

In order to find a point on a dispersion curve, a root of the characteristic equation (equation 2.78) must be found. In this case, the root corresponds to a point where the determinant of the global matrix, a complex value, is zero. The coefficients of the global matrix are dependent on the geometry of the system, the material properties, the frequency, the real wave number, and the attenuation. For a given

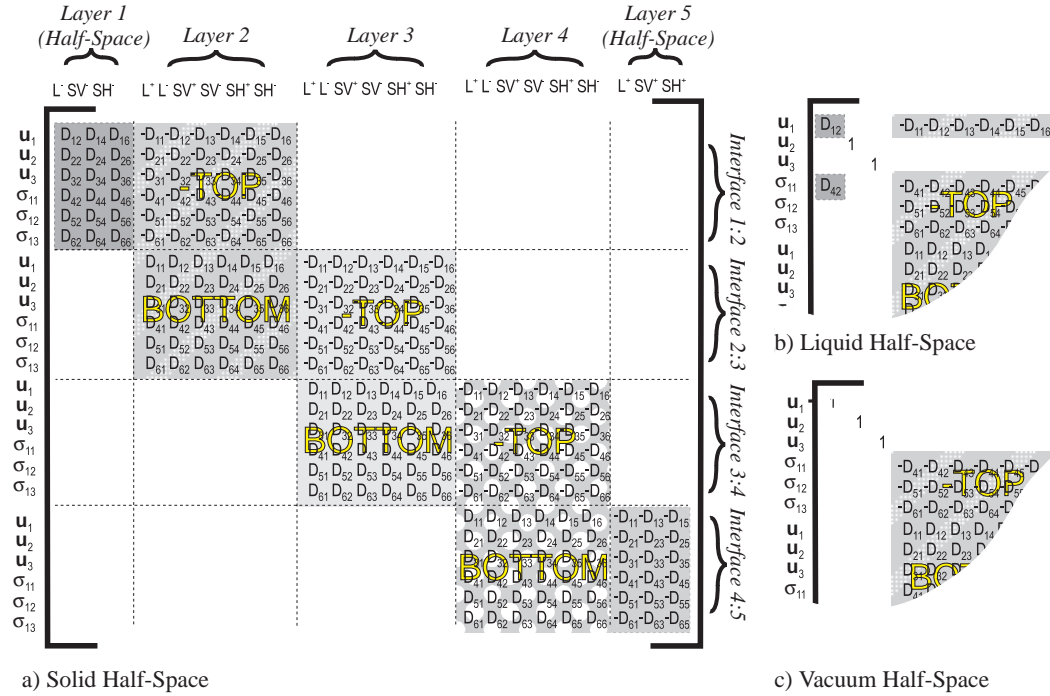


Figure 2.2: The structure of the global matrix for a (a) solid, (b) liquid, and (c) vacuum half-space, where blank spaces are zeros,  $D_{ij}$  is the layer matrix, and  $L_{+-}$ ,  $SV_{+-}$ , and  $SH_{+-}$  are the partial waves amplitudes in the various layers.

problem, the latter three properties, the frequency, real wave number, and attenuation, are varied to find valid roots.

If all of the materials are elastic and the half-spaces are both vacuum, then there is no way for energy to leave the system and so there will be no attenuation. In this case the fine search routine can be relatively simple. Since the attenuation of propagating modes will always be zero, a single one dimensional minimum search routine suffices to find the root. However, the process is more complicated when attenuation exists and a two dimensional search routine is required.

Disperse uses a robust root finding routine developed by Mike Lowe that is described in detail in reference [10]. The first step to find a root involves performing a coarse sweep, for which two of the variables are held constant while the third is varied. The routine then searches for minima in the absolute value of the determinant to use as starting points for a more detailed search. The absolute value of the determinant is used for searches because at this point the routine is only looking for local minima. Zeros of the function only occur when all three search variables (frequency, real wave number, and attenuation) take on appropriate values. If only two of the variables are correct, the zero will appear as a local minimum of the determinant. If a minimum of the characteristic equation is found, the routine begins a fine search, which then tries to converge onto a valid root.

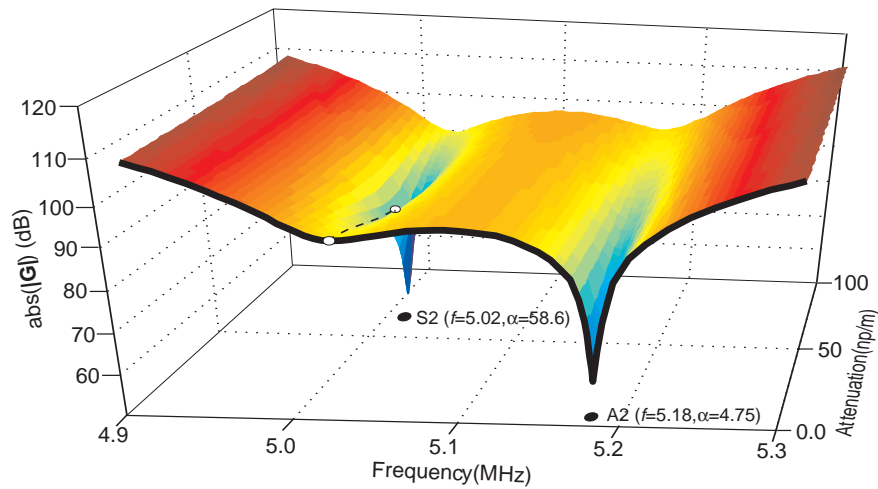


Figure 2.3: The process of finding a root involves a coarse sweep (thick line) to find an initial minimum and a fine search (dashed lines) to narrow down on a root (solid circle). The example above shows the absolute value of the determinant of the global matrix for a 1 mm steel plate immersed in water at a wave number of 4 rad/mm.

Figure 2.3 illustrates the process of finding a valid root of the characteristic equations when attenuation is present in the system. The surface corresponds to the log of the absolute value of the determinant of the global matrix when the real wave number is held at 4 rad/mm for a 1 mm steel plate immersed in water. To find a root, a coarse frequency sweep is made at zero attenuation, as shown by the thick line at the front of the surface. The two minima are identified as possible roots and are used as starting points for a fine search. The left minimum is less well defined than the right minimum because the attenuation value of the sweep is very different than the actual attenuation of the root.

Next, starting at a minimum located by the coarse sweep, the fine search uses a two dimensional iterative bisection routine to converge onto the roots (shown as the black filled circles in figure 2.3). The iteration functions in the following manner. The sweep segments that bracket the current minimum are each split in two and the function is calculated at these points. This allows a new minimum to be chosen from the middle three points. Successive bracketing continues until a preset tolerance is achieved. At this point, the routine begins to converge in attenuation. Keeping the frequency constant, the attenuation is varied in small steps until a local minimum is found. (This portion of the iteration is shown as the dashed line in figure 2.3. The white filled circles indicate local minima.) The same bracketing procedure that was used to improve the accuracy of the frequency minima is now performed in attenuation. Once the desired accuracy in attenuation is obtained, the routine repeats the search for minima in frequency and then attenuation until it determines that it has found a valid root by examining nearby phase changes[10]. This procedure will be repeated for each of the minima located by the coarse sweep. This root finding method was chosen because it is very stable (even in the regions where two modes cross) and does not require the determinant of the characteristic function, which is computationally expensive to calculate when using the global matrix method.

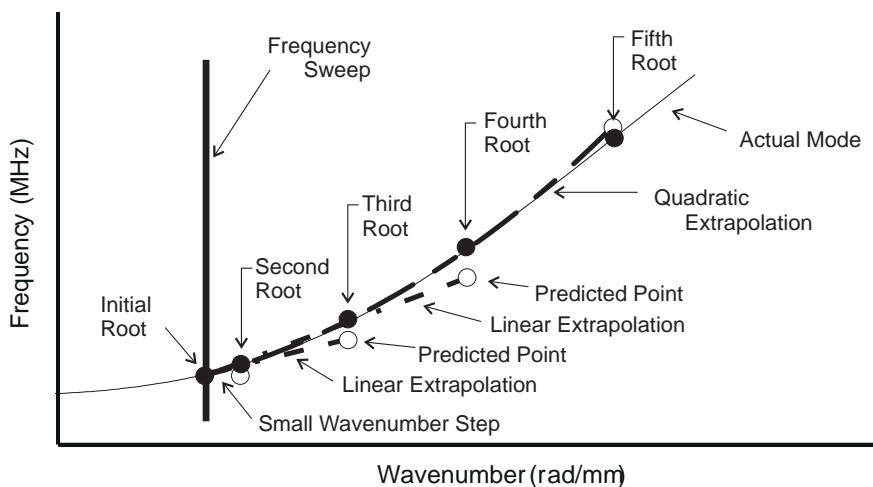


Figure 2.4: Using an extrapolating routine to trace modes dramatically improves the program's speed and reliability.

### 2.8.3 Tracing a Dispersion Curve

Although it is possible to find a lot of roots of the dispersion equation and connect the dots, there is a much more efficient and robust method that Lowe developed[6] for tracing dispersion curves. The tracing routine employed for this method uses extrapolation to provide predictions of where subsequent points on a dispersion curves will fall. Therefore, once a single point on a mode has been found, the rest of the mode may be traced much more quickly than if each point needed to be converged upon from an inaccurate starting value.

As shown in figure 2.4, the tracing routine starts from a root that was found from a coarse sweep, labelled the initial root. Next the routine takes a very small step in one of the three independent variables, in this case wave-number, and converges on a second root. These first two points are used to linearly extrapolate to and converge upon a third root, which is then used to linearly extrapolate to a fourth point. After the fourth root has been found, the routine predicts the next root by quadratically extrapolating from the three previous roots. After the seventh root, every other root is used for the quadratic extrapolation to reduce the effect of a single solution 'jumping' onto another curve as two modes pass near to each other[6]. For the case shown in figure 2.4, the wavenumber is stepped and the frequency and attenuation are extrapolated. It is also possible to step in frequency or attenuation and extrapolate values for the other two parameters. Once a mode is completely traced, another starting point is used to trace out the next mode, until the entire set of dispersion curves has been identified.

### 2.8.4 Mode Shapes

One effective method of examining the solutions of the dispersion equations is to look at the mode shape at each of the points on the mode. The mode shape displays how the displacements, stresses, or energy vary through the thickness of the system. The variation in the direction of propagation is directly related to the wavenumber and is therefore not of interest.

To calculate the mode shapes, the amplitude of one of the bulk waves is arbitrarily assumed[10]. This assumption allows the amplitudes of the other bulk waves to be found by solving a modified version of equation 2.78, which is the characteristic equation for this problem. Once all of the bulk wave amplitudes are known, the stresses and displacements for an arbitrary point in a layer can be calculated by multiplying the wave amplitude vector for that layer by the layer matrix given in equation 2.43.

In addition to the stresses and displacements, the strain energy density may be determined. The strain energy density is given by half of the sum of the stress-strain products, which in cylindrical coordinates is,

$$\begin{aligned} \text{SED} &= \frac{1}{2} \left\{ \sigma_{rr} \frac{\partial u_r}{\partial r} + \sigma_{\theta\theta} \left( \frac{1}{r} \frac{\partial u_\theta}{\partial \theta} + \frac{u_r}{r} \right) + \sigma_{zz} \left( \frac{\partial u_z}{\partial z} \right) \right\} \\ &+ \frac{1}{4} \left\{ \sigma_{rz} \left( \frac{\partial u_r}{\partial z} + \frac{\partial u_z}{\partial r} \right) + \sigma_{r\theta} \left( r \frac{\partial}{\partial r} \left( \frac{u_\theta}{r} \right) + \frac{1}{r} \frac{\partial u_r}{\partial \theta} \right) + \sigma_{\theta z} \left( \frac{\partial u_\theta}{\partial z} + \frac{1}{r} \frac{\partial u_z}{\partial \theta} \right) \right\} \quad (2.79) \end{aligned}$$

The mode shapes may be displayed in two formats, lines or grid. When the mode shape is displayed as lines, the selected stresses, displacements, and energies are plotted as they vary through the thickness of the system. Since the phase of the different components changes, each of the stresses and displacements is rotated in the complex plane so that the phase at the top of the first finite layer of the system is real and positive. When the mode shape is displayed as a grid, the normal and in-plane displacements are used to show the greatly exaggerated deformation of a super-imposed grid. The mode shape is shown over several wavelengths of the plate wave and can be animated to provide a feel for how the mode behaves. Examples of mode shapes and how they can be used to help interpret the propagation of guided waves are given in the following chapters.

## Chapter 3

# Cylindrical Wave Propagation

## Examples

This chapter discusses some sample cylindrical cases that were analysed using the wave propagation model developed in chapter 2. These cases are included to elaborate on general principles of cylindrical wave propagation, especially as it applies to leaky systems.

The detailed examples begin with the simple case that Gazis described in 1959[4], single-layered, elastic, isotropic cylinders. This case is used to illustrate several principles of dispersion curves. The first parts of the section explain different projections of the dispersion curves that will be used to display the wave propagation solutions and the system that will be used to label the curves. The following part discusses the properties of some of the modes in a cylindrical system. The final part evaluates when a hollow cylinder may be modelled as a flat plate for computational efficiency.

The following examples gradually become more complicated as surrounding liquids and solids and additional isotropic layers and transversely isotropic layers are added. The first example that discusses the significance of leaky waves considers a pipe that is filled with and surrounded by water. Different approaches of treating the fluid filled core are addressed as well as the conditions that are required for waves to leak into the surrounding fluid. The next example expands this work to analyse cylinders that are embedded in a solid medium. The final example treats an even more complicated system, a multi-layered cylinder embedded in a solid that contains material damping. The dispersion curves are very difficult to trace for this final case, however most of the low attenuation modes have been successfully identified.

All of the material constants that were used in the modelling can be found in table 3.1 at the end of the chapter.

## 3.1 Cylinders in Vacuum

This section uses two examples of cylinders in vacuum to discuss some general principles of cylindrical wave propagation. The first part of the section examines the dispersion curves for a 2 mm diameter steel bar to demonstrate some of the different views that can be used to display the dispersion curves and the system that will be used to name each of the modes. The later parts of the section use both this bar and a hollow cylinder to describe the behaviour of some commonly used modes. In addition, the hollow cylinder is used to evaluate when a simpler Cartesian model may be substituted for the exact cylindrical one.

### 3.1.1 Projections

As explained in section 2.8.3 on tracing a mode, the dispersion curves are traced in frequency – wave number – attenuation space (although for this case, an elastic steel bar in vacuum, the attenuation is always zero). These lines of solutions may be viewed in many different projections, each of which can reveal different information about the solutions. Figure 3.1 includes four common projections that are used for systems that do not have any attenuation. These are real wave number, phase velocity, group velocity, and angle of incidence for optimum generation. Another commonly used projection, attenuation, will be first used in section 3.2, which describes a cylinder that leaks energy into a surrounding fluid. A description of the significance and use of each of these five projections follows.

**Real wave number** The real wave number projection displays the relationship between the temporally and spatially varying wave characteristics of the guided mode along the direction of propagation. The wave number, which is described in section 2.6.1, is inversely related to the wavelength of the guided wave by the equation  $\lambda = 2\pi/\xi$ , where  $\lambda$  is the wavelength and  $\xi$  is the real wave number in radians per metre. The tracing routines explained in section 2.8.3 operate in real wave number – frequency space because the dispersion curves appear more linear in this projection than in any other projection that contains the same information.

**Phase Velocity** The phase velocity projection is the view that will be most frequently shown. The phase velocity of a guided wave, which describes the rate at which individual crests of the wave move, is related to the real wave number as  $v_{ph} = \omega/\xi$ , where  $\omega$  is the circular frequency and  $\xi$  is the real wave number. Because of this relation, the phase velocity shows the same information as the real wave number display and can be used interchangeably. However, the phase velocity view is more convenient to use for realistic ultrasonic testing. It is easy to compare the phase velocity to the bulk velocities in the layers to study the behaviour of leaky waves. In addition, the phase velocity projection emphasises the velocity changes due to the guided nature of the modes.

**Group Velocity** The group velocity projection displays the rate at which a guided wave packet will travel. This rate is determined by how quickly the energy of the wave will progress down the

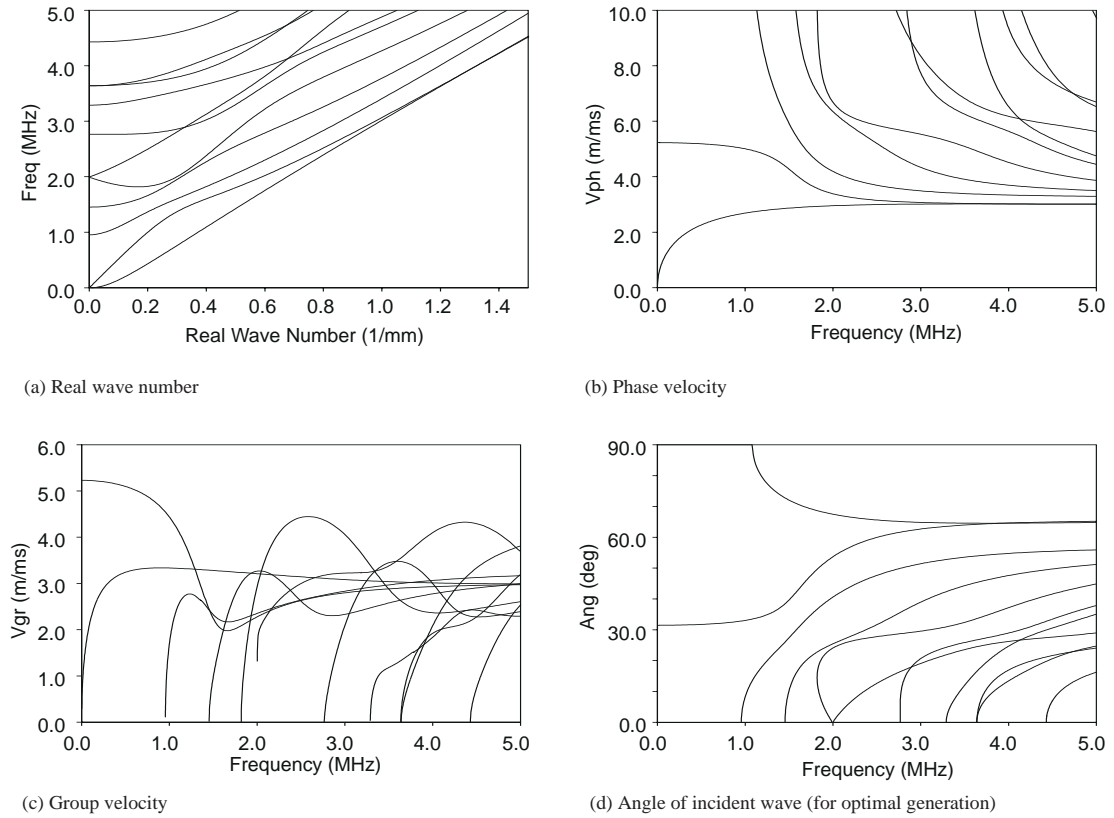


Figure 3.1: Various views of the dispersion curves for a 2 mm diameter steel bar in vacuum (zero and first circumferential order), including (a) real wave number, (b) phase velocity, (c) group velocity, and (d) angle of incident wave (in a perspex wedge) for optimal generation of modes.



structure and will always be smaller than the fastest bulk wave present in the system. The group velocity is defined in terms of the derivative of the dispersion curves such that

$$v_{gr} = \frac{\partial \omega}{\partial \xi} \quad (3.1)$$

where  $v_{gr}$  represents the group velocity,  $\omega$  the circular frequency, and  $\xi$  the real wave number, as explained in reference [39].

The group velocity can also be used to predict how much dispersion will occur for a given wave packet. Any wave that lasts for a finite time period will excite a range of frequencies, the size of which depends on the number of cycles in the wave packet, as well as the shape of the packet. Each of the frequency components in the wave packet will travel at a different group velocity. If the difference in velocities over the range of frequencies is great, there will be a lot of dispersion as the different frequency components arrive at different times. This spread will cause the signal to change shape as it propagates. However, if the group velocities are very similar over the generated frequency range, the packet will maintain the same shape during its entire propagation length. Therefore, for practical testing situations, the centre frequency should be chosen so that it corresponds to a maximum (or minimum) in group velocity, such that the predominant frequency components all travel coherently.

The definition of group velocity given in equation 3.1 is only valid for systems that do not contain attenuation. In attenuative systems, physically impossible solutions may result. For example, the group velocity may appear to tend to infinity as a mode's wavenumber tends to zero. This is clearly not accurate. Alternative definitions of the group velocity that take the attenuation into account are being explored.

**Angle of incidence** The angle of incidence plots are mainly used to assist the generation of guided waves. This view displays the angle at which an incident wave should insonify the system in order to generate a guided wave. The value is calculated by simply applying Snell's law so that the wave number components of the incident wave and the desired guided mode are constant in the direction along the interface. This wave number matching can be expressed as,

$$\text{angle} = \sin^{-1} \left( \frac{v_{inc}}{v_{ph}} \right) \quad (3.2)$$

where  $v_{inc}$  is the velocity of the incident bulk wave and  $v_{ph}$  is the phase velocity of the guided wave. In figure 3.1(d), it is assumed that a longitudinal bulk wave is incident from a Perspex wedge, whose longitudinal velocity is 2730 m/s. The portion at the upper left that is constant at 90 degrees represents the portion of a mode that cannot be generated using this angle probe since its phase velocity is less than the incident bulk velocity.

**Attenuation** The attenuation projection allows the decay of the guided wave to be examined. The model developed in chapter 2 accounts for the attenuation by incorporating a complex wavenumber, whose units are nepers per metre. An attenuation of  $\kappa$  nepers per metre means that a

wave of unit amplitude is reduced to an amplitude of  $e^{-\kappa}$  after travelling one metre. The attenuation may also be expressed in other units such as decibels per metre that may be more familiar to some readers. (Nepers can be converted to decibels by multiplying by the expression  $20 \log_{10} (e^{(1.0)}) \approx 8.6859$ .)

In a completely elastic system that is surrounded by vacuum, the attenuation will always be zero and therefore does not need to be specified. However, whenever material damping present or the system is surrounded by a liquid or solid medium, there will usually be attenuation and the attenuation must be specified in addition to the real wave number and frequency to completely describe a solution to the characteristic equation.

### 3.1.2 Naming

In order to consistently refer to different modes in cylindrical systems, I will use a modified version of the system used by Silk and Bainton[62], which tracks the modes by their type, their circumferential order, and their consecutive order. The labelling assigns each mode to one of three types,

**Longitudinal (L)** modes, which are longitudinal axially symmetric modes, (The fundamental longitudinal mode is purely extensional (displacements in the axial direction) at zero frequency.)

**Torsional (T)** modes, which are rotational modes whose displacement is primarily in the  $\hat{\theta}$  direction (These modes correspond to the 'SH' modes in a plate.), and

**Flexural (F)** modes, which are non-axially symmetric bending modes. (The fundamental flexural mode is a pure bending mode at zero frequency.)

In addition to the type of mode, a dual index system helps track the modes. The first index refers to the circumferential order of the mode, which describes the integer number of wavelengths around the circumference of the cylinder. For example, the displacements for zero order modes are constant with angle and the displacements on the top and bottom of the cylinder are 180 degrees out of phase for first order modes. Therefore, all longitudinal modes are of circumferential order 0, and all of the flexural modes have a circumferential order greater than or equal to 1. The second index is a counter variable. The fundamental modes (those modes that can propagate at zero frequency) are given the value 1 and the higher order modes are numbered consecutively. This index roughly reflects the modes of vibration within the wall of the cylinder. For example, using this convention, the third flexural mode of circumferential order 1 would be named F(1,3).

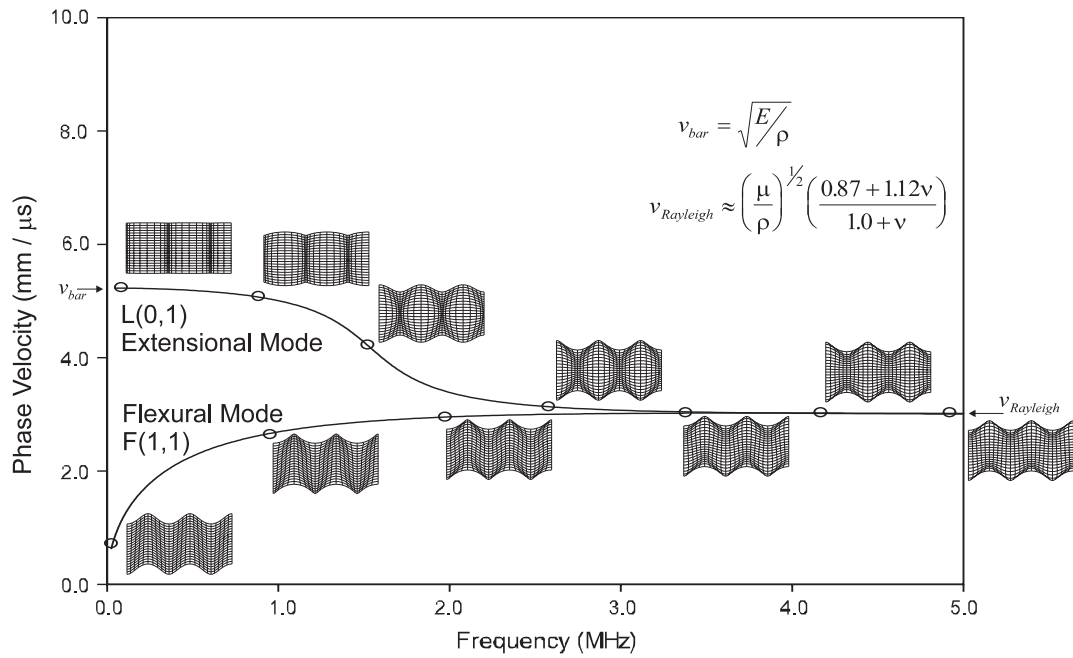
### 3.1.3 Nature of the Modes in Solid Cylinders

As explained in section 3.1.1, the dispersion curves provide a lot of information about the velocities, wave numbers, and attenuations of the solutions to the guided wave problem. However, this information does not provide a full description of how the mode behaves. In order to better understand the nature of the various guided waves and the names that are assigned to them, figure 3.2 shows the mode shapes that are associated with various modes for a 2 mm diameter steel bar. Figure 3.2(a) shows the behaviour of the fundamental longitudinal and flexural modes as the frequency changes and (b) shows the mode shapes for some of the higher order modes.

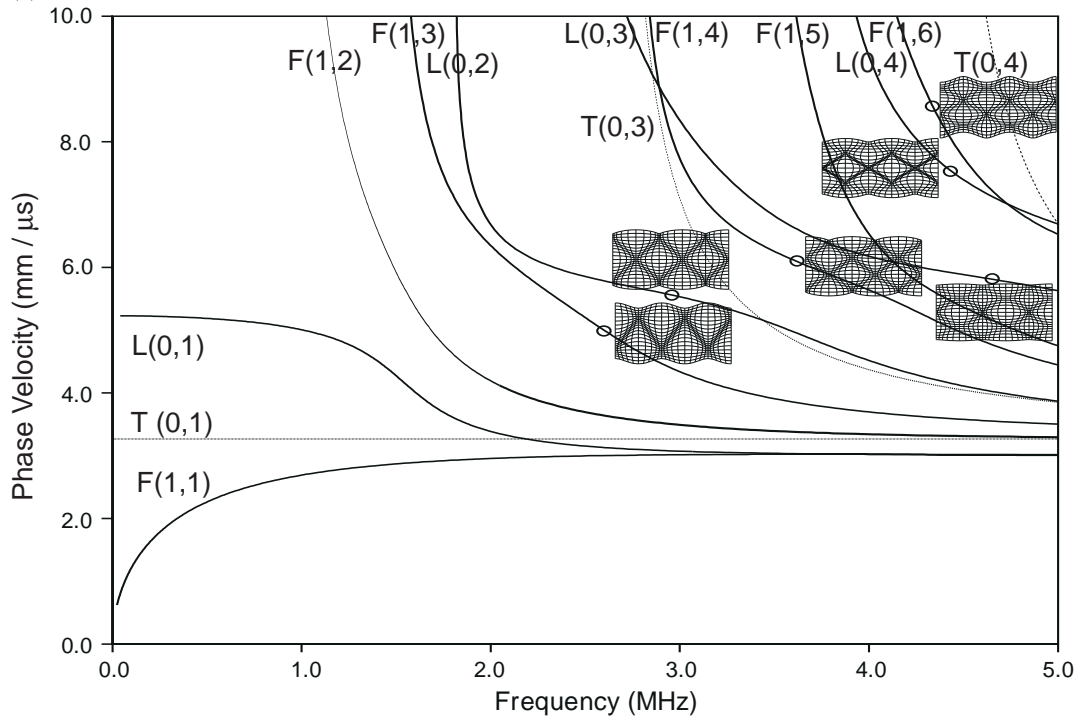
The first longitudinal mode, L(0,1), behaves as a pure extensional mode at near zero frequency. The particle motion consists of uniform axial compressions of the bar and the phase velocity at zero frequency is equal to the bar velocity,  $\sqrt{E/\rho}$ , where  $E$  is Young's Modulus and  $\rho$  is the density. This expression can be derived from a quasi-static strength of materials approach. For the steel bar used in this example, the bar velocity is 5229 m/s, which agrees with the value obtained from the model to six decimal places. As the frequency increases, the particle motion becomes more complicated. The radial component of the motion grows and the displacement is no longer constant through the thickness of the bar. As the frequency becomes very high, the mode begins to act like a Rayleigh wave on the surface of the bar. The mode is confined to the outer material of the bar to a depth of a few wavelengths and the bar acts like a semi-infinite half-space. Expressions for the bar and Rayleigh velocities are available in many wave propagation texts[39,52,63].

The fundamental flexural mode, F(1,1), begins as a pure bending, or transverse, mode at zero frequency. However, as the frequency increases, the mode takes on some extensional characteristics, just as the first longitudinal mode takes on some bending characteristics. When the frequency becomes large enough the fundamental flexural mode also begins to act like a Rayleigh wave on the surface of the bar, which to it appears to be a semi-infinite half-space. However, whereas mode L(0,1) leads to a Rayleigh wave that has the same phase all of the way around the bar, mode F(1,1) leads to a Rayleigh wave on the top surface that is 180 degrees out of phase with that on the bottom of the bar and that does not exist on the two sides of the bar.

The mode shapes for the torsional modes have not been shown because their displacement is primarily in the  $\hat{\theta}$  direction, which cannot be shown clearly by the grid mode shapes. In addition, since the fundamental torsional mode propagates at a constant phase velocity that is equivalent to the bulk shear velocity of the material, which is an unstable calculation region for the global matrix method, Disperse has difficulty calculating accurate mode shapes for this mode. However, it well known that the fundamental torsional mode corresponds to a uniform twisting of the entire bar[60]. The higher order torsional modes exhibit more complicated behaviour. The predominant motion remains a twisting of the bar. However, the angular displacement is not constant through the radius of the bar. Different locations through the radius of the bar can twist in different directions and nulls of displacement can exist.



(a) Fundamental modes



(b) Higher order modes

Figure 3.2: Phase velocity dispersion curves for a 2 mm diameter steel bar with mode shapes super-imposed on the (a) fundamental modes and (b) higher order modes.

Figure 3.2(b) displays the mode shapes for some of the higher order longitudinal and flexural modes. These mode shapes demonstrate that as the second index increases, more minima and maxima appear through the diameter of the bar. These minima correspond to higher order radial resonances or nodal diameters of the bar. Bar modes that have an even circumferential order resemble the symmetric modes of a plate, for which the displacements at the top and the bottom are in phase. On the other hand, modes that have an odd circumferential order resemble anti-symmetric plate modes, whose top and bottom displacements are out of phase.

As described in section 2.7, the wave model that is used in this thesis allows transversely isotropic materials to be modelled. This feature allows the wave propagation in systems such as a single anisotropic fibre to be accurately modelled. For most materials, the anisotropy is not very strong and its effect on the dispersion curves is slight. However, certain systems can be dramatically affected.

To examine the effect of the anisotropy of materials, figure 3.3 follows a recent paper by Nayfeh and Nagy[37], which studies the wave propagation characteristics of a carbon fibre surrounded by a silicon carbide sheath. A detailed comparison of the results obtained from the wave propagation model developed in chapter 2 and the results published by Nayfeh and Nagy is included in chapter 4; this section and section 3.3.2, which examines what happens to the wave propagation in this fibre when it is embedded in a titanium matrix (to simulate a metal matrix composite), are used to illustrate the effect of the anisotropy. In their work, Nayfeh and Nagy used material properties and geometries from a paper by Sinclair and Addison [64]. These properties are listed in table 3.2. The fibre has an overall radius of 70 microns, consisting of a 16.5 micron radius carbon core surrounded by a 53.5 micron thick cladding. The dispersion curves for the six lowest order axi-symmetric modes of the system are shown in figure 3.3 (a), which matches figure 3 in Nayfeh and Nagy's work[37]. In this figure, the dashed lines represent the dispersion curves that are generated when the materials are treated as isotropic materials and the solid lines represent the dispersion curves that are generated when the material's anisotropy is taken into account. The dispersion curves for the first order flexural modes for this system have also been calculated and are shown in figure 3.3(b). The agreement between the isotropic and anisotropic solutions is close for most modes. However, distinct, measurable, differences can be observed. For example, the phase velocity of the  $L(0,1)$  mode at low frequency increases when the anisotropy is considered.

### 3.1.4 Nature of the Modes in Hollow Cylinders

The behaviour of the modes changes when the inside of the cylinder is hollow as shown in figures 3.4 and 3.5, which show the phase velocity and group velocity curves for a 1 mm thick steel pipe that has an inner radius of 2 mm and is in vacuum. This example describes the type of system that Gazis described in 1959[4] and is validated against his solutions in section 4.2.1. Figure 3.4 includes the dispersion curves for modes of the first twenty circumferential orders, however, figure 3.5 only includes the zero and first circumferential order modes. So many modes appear in figure 3.4 because the same

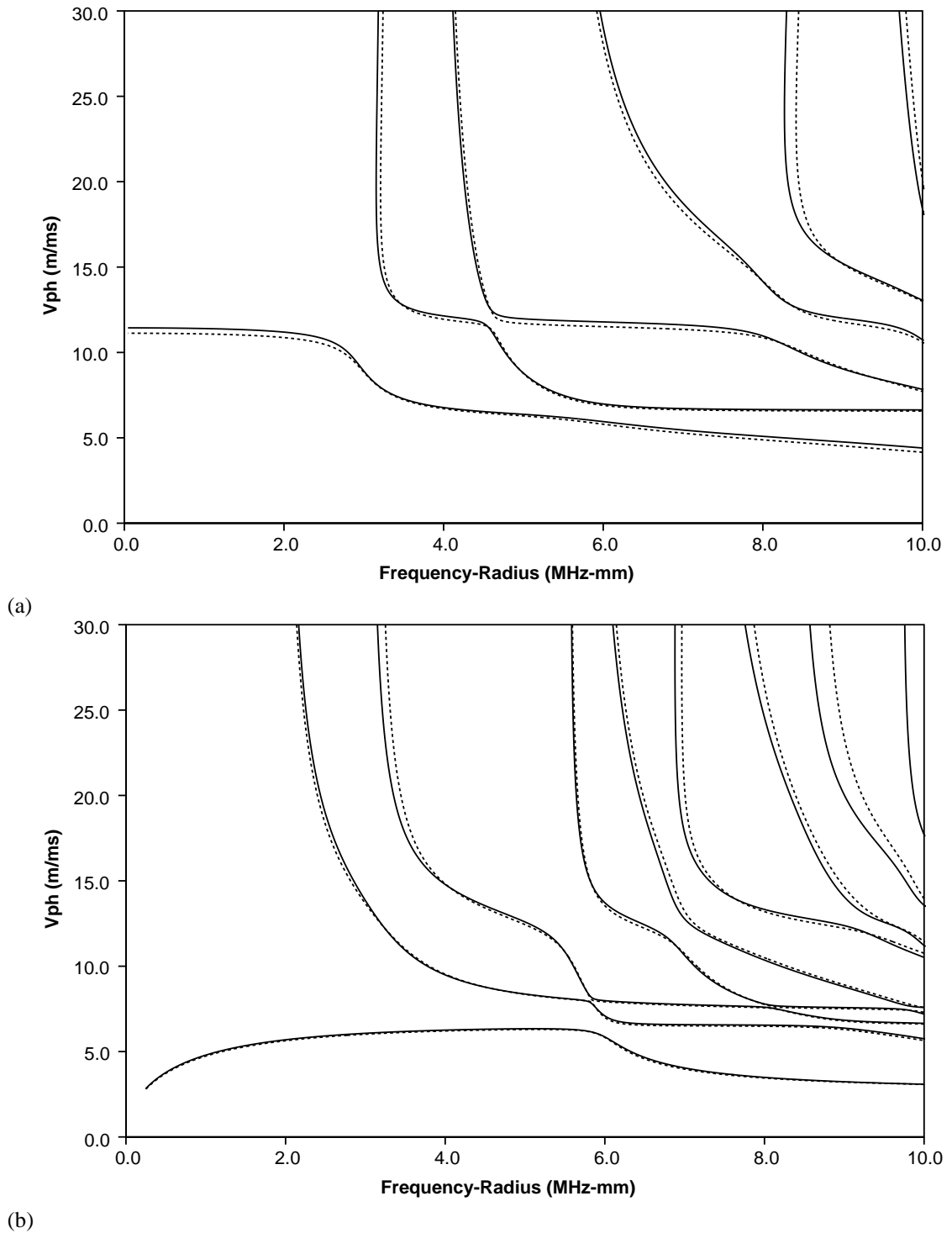


Figure 3.3: (a) The phase velocity dispersion curves for the six lowest-order axi-symmetric modes in a free SCS fibre (equivalent to figure 3 of Nayfeh and Nagy(1996)). (b) The phase velocity dispersion curves for the first circumferential order flexural modes in a free SCS fibre. The dashed lines correspond to the case when the materials are considered to be isotropic and the solid lines correspond to the solutions when the material anisotropy is included.

basic wave structure (as described by the through thickness displacement profile) can exist for multiple modes that have different numbers of wavelengths around the circumference of the pipe, each of which is orthogonal to each other. In most non-destructive testing situations, only the lower circumferential order modes (corresponding to only a few wavelengths around the circumference) are used, since practical measurement systems usually do not have enough resolution around the circumference to be able to clearly separate high circumferential orders. Therefore, the remainder of the dispersion curves in this thesis will only show low circumferential order modes. In figure 3.5, the modes have all been labelled according to the scheme discussed in section 3.1.2. The following paragraphs discuss the behaviour of these modes.

As for a bar, the fundamental longitudinal mode,  $L(0,1)$ , of a hollow cylinder begins at zero frequency, with a phase velocity equal to the bar velocity,  $\sqrt{E/\rho}$ . However, as the frequency increases, the phase velocity drops dramatically. The phase velocity and through wall displacement profile resemble those for the  $A_0$  mode in a plate. This behaviour contrasts with the behaviour of the bar described above for which the  $L(0,1)$  mode behaves more like the fundamental symmetric mode of a plate,  $S_0$ . The second longitudinal mode,  $L(0,2)$ , begins at a finite frequency and an infinite phase velocity. The mode quickly drops down to Young's velocity ( $\sqrt{E/(\rho(1-\nu^2))}$ ), where it begins to act like the  $S_0$  mode in a plate. Like  $A_0$  and  $S_0$ ,  $L(0,1)$  and  $L(0,2)$  tend to the Rayleigh velocity at high frequency.

The fundamental flexural mode,  $F(1,1)$ , begins at zero frequency, phase velocity, and wave number. At very low frequency, the  $F(1,1)$  mode represents a bending mode of the entire pipe that is similar to the  $F(1,1)$  mode of a solid bar that has the same outer radius. The  $F(1,1)$  mode in a hollow cylinder tends to increase in phase velocity and then drop back down and follow a path similar to  $L(0,1)$  in a pipe and  $A_0$  in a plate. Although the displacement profiles through the thickness of the pipe wall are very similar for both the  $F(1,1)$  mode and the  $L(0,1)$  mode in a hollow cylinder (they resemble the through-thickness displacement profile of the  $A_0$  mode in a plate), there is a major difference between the modes. The displacements at the top and bottom of the cylinder are 180 degrees out of phase for the  $F(1,1)$  mode, but they are in phase for the  $L(0,1)$  mode. Similar to the  $L(0,2)$  longitudinal mode, there is a  $F(1,2)$  mode whose displacement profile and phase velocity behaviour resembles that of  $S_0$  in a plate. This mode, which is not present in the solid cylinder, differs from the  $L(0,2)$  mode because the displacements at the top and bottom of the cylinder are out of phase.

For a hollow cylinder, the circumferential order has less effect on the high order modes than it does on the fundamental modes at low frequency. As can be seen in figure 3.5, the higher order modes of different circumferential order, such as  $L(0,4)$  and  $F(1,4)$ , nearly overlay each other. As seen later, this effect is even more pronounced as the inner radius is increased. For every mode in an equivalent Cartesian system, there will exist an infinite number of cylindrical modes corresponding to modes of different circumferential order. As the cylindrical system becomes more and more like a plate, the infinite number of cylindrical modes all overlap the dispersion curves for a plate. This trend is discussed more in section 3.1.5.

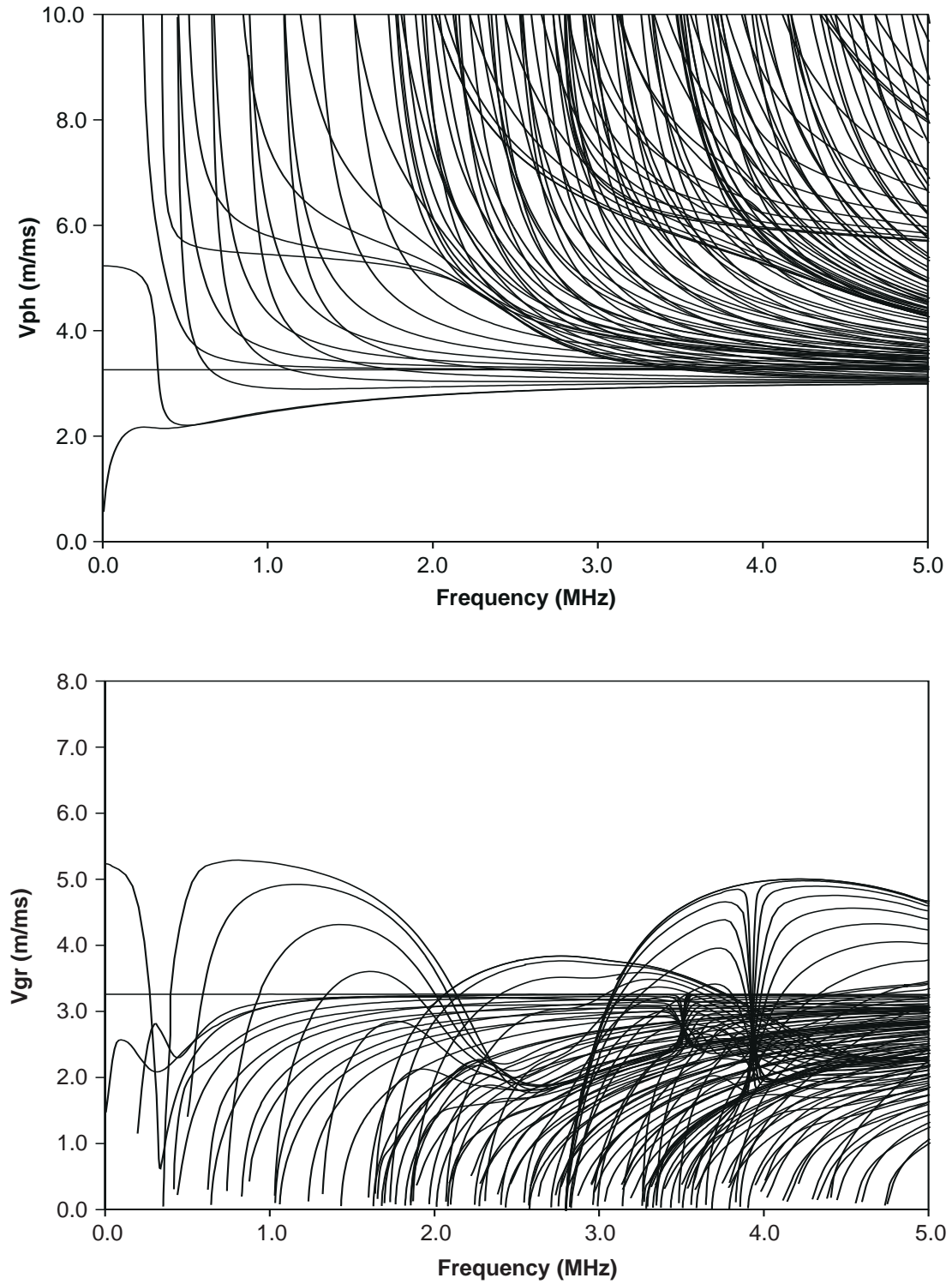


Figure 3.4: Phase velocity and group velocity dispersion curves for an empty 1 mm thick steel pipe with an inner radius of 2 mm. Modes of the lowest twenty circumferential orders have been shown.



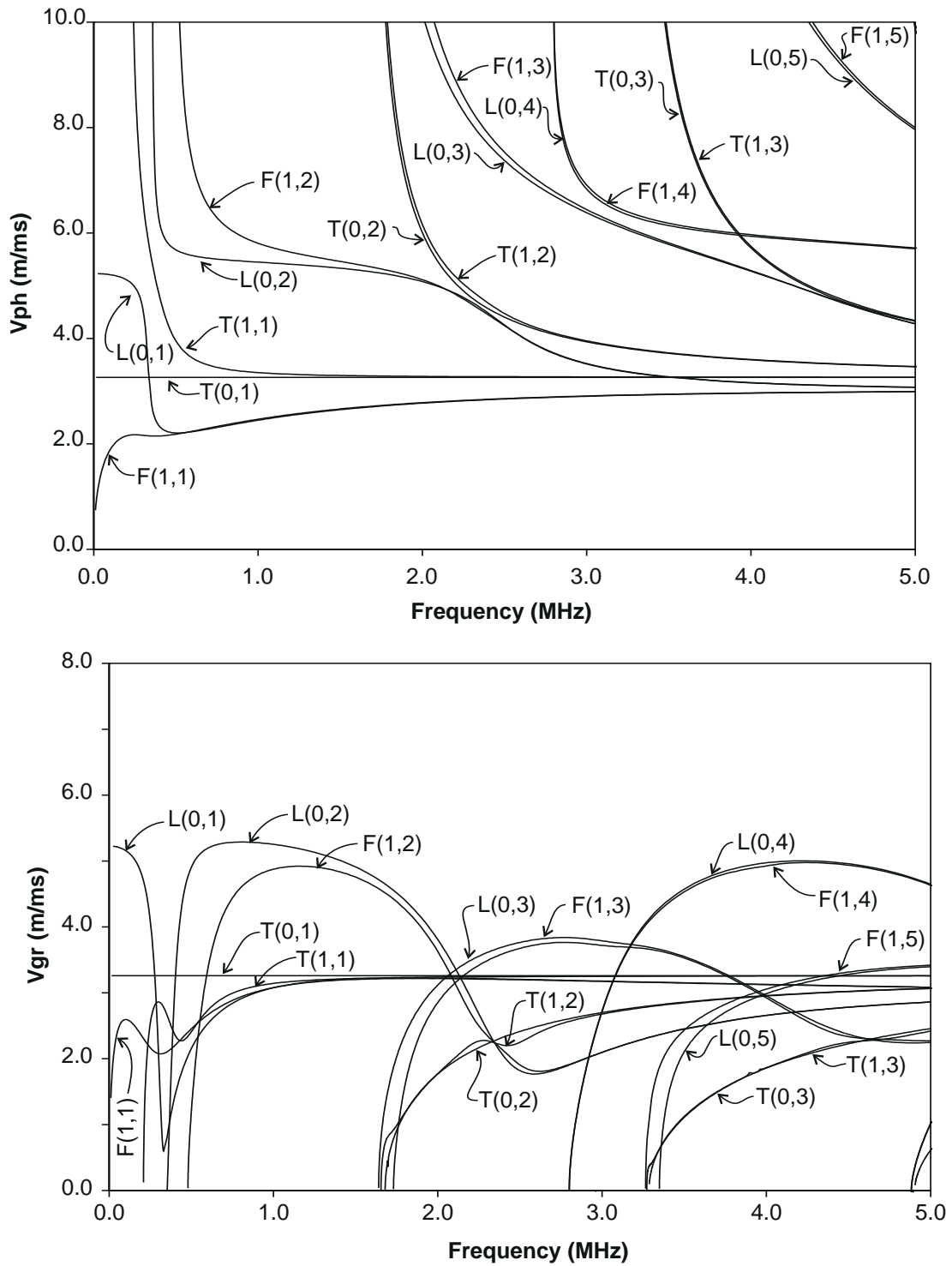


Figure 3.5: Phase velocity and group velocity dispersion curves for the zero and first circumferential order modes of an empty 1 mm thick steel pipe with an inner radius of 2 mm.

The fundamental torsional mode of circumferential order zero propagates at a constant phase velocity that is equal to the bulk velocity of the shear wave in the material. However, the higher order torsional modes show dispersion. The higher order torsional modes begin at a regular frequency-thickness spacing equal to half multiples of the shear speed. Their behaviour is more simple than the longitudinal and flexural modes and the zero order torsional modes can be expressed analytically in a similar fashion as the 'SH' modes in a plate. On the other hand, the angular displacements of the torsional modes of non-zero circumferential order are coupled to the other displacements and can only be found by the solution of the complete wave propagation solution.

### 3.1.5 Effect of Changing the Radius

Once the general behaviour of the modes of a single layered hollow cylinder is understood, the effect of changing some of the parameters can be explored. One interesting parameter to investigate is the effect of changing the ratio of the inner radius to the wall thickness. As the inner radius becomes infinitely large, the cylinder should act like a plate of the same thickness. The transition of behaviour from a system that is dominated by its cylindrical nature and a system that behaves like a plate provides an interesting subject to explore. This transition helps explain the behaviour of cylindrical waves and reveals when it is acceptable to model a cylinder as a plate to simplify the analysis.

As the ratio of the inner radius of a pipe to the wall thickness of the pipe increases the pipe begins to behave more like a plate. The trend of the dispersion curves as the radius changes from one wall thickness to 20 wall thicknesses is shown for the zero and first circumferential order modes in figure 3.6. The example models a one millimetre thick steel pipe that is filled with and surrounded by vacuum. For comparison, the dispersion curves for an equivalent one millimetre plate, which can be considered a pipe with an infinitely large radius, are shown in part (f). The effect of the curvature of the pipe is most noticeable at low frequencies, which correspond to long wavelengths. As the frequency increases and the wavelength decreases, the wave only 'sees' a local section of the pipe, which begins to appear as a plate, especially as the radius becomes larger. When the radius is 10 wall thicknesses, the difference between the pipe and the plate dispersion curves is only detectable below 0.5 MHz-mm frequency-wall thickness. Above that frequency-thickness, the cylindrical curves nearly overlay those for a plate, and the curves remain the same regardless of the circumferential order.

This example demonstrates that Cartesian dispersion curves can be used when working with high frequencies and large radius pipes to improve the speed of calculation and the stability. A rule of thumb derived from examining numerous dispersion curves indicates that the minimum frequency for which an equivalent plate case could be substituted is,

$$f_{min} = \frac{v_{long}}{r_{inner}} \quad (3.3)$$

where  $f_{min}$  is the minimum frequency in MHz,  $r_{inner}$  is the inner radius in mm,  $v_{long}$  is the bulk longi-

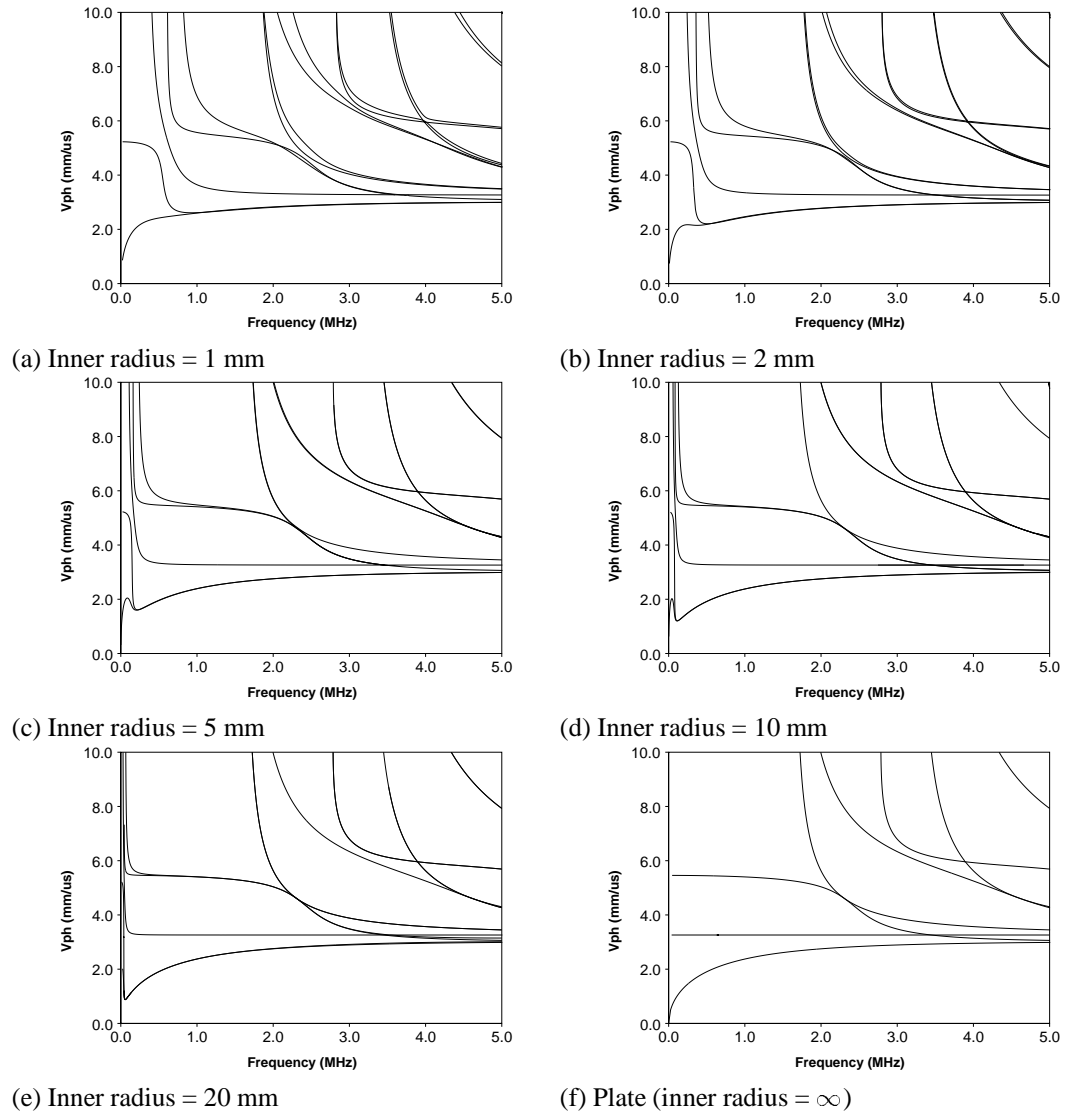


Figure 3.6: The effect of increasing the inner radius of a 1 mm thick steel pipe. As the inner radius increases, the dispersion curves begin to very closely match the dispersion curves for a plate (shown in section f), except for very low frequencies.

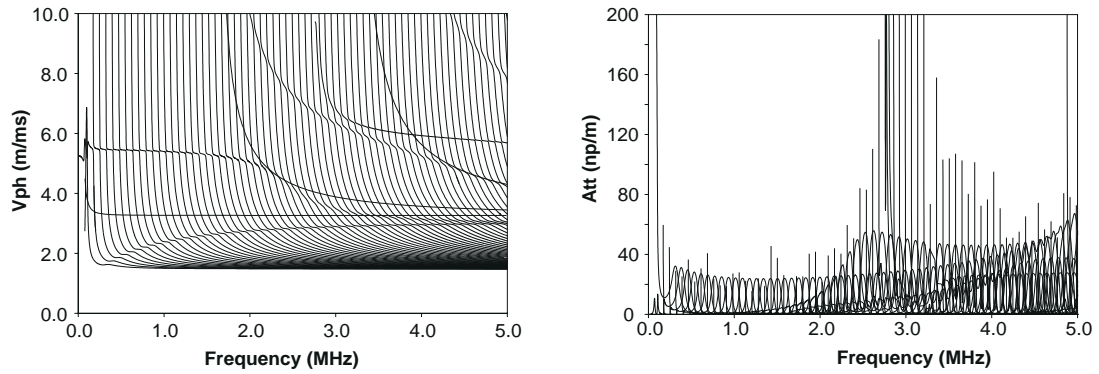
tudinal velocity in  $\text{mm}/\mu\text{s}$ . Therefore, if the target application will only use frequency–wall thicknesses above 0.25 MHz–mm, a plate case can only be substituted if the ratio of radius to the wall thickness is greater than about 20. Strictly speaking the criterion is controlled by the wavelength (which is inversely proportional to the wavenumber). Large wavelengths will ‘see’ the curvature, but short wavelengths will not. However, specifying a guideline in terms of wavelength would involve more calculations for the user and requires fore-knowledge of the dispersion curves to convert it into units that are commonly used. Therefore, the expression was simplified to its current form. The expression in equation 3.3 closely resembles the expression for the ‘ring frequency’,  $(v_{long})/(2\pi r_{inner})$ , that is used in acoustics to denote the frequency at which one wavelength of the bulk longitudinal wave extends around a thin cylindrical shell. This frequency correlates with the rapid phase velocity changes (and group velocity minima) seen in the L(0,1) and F(1,1) dispersion curves for a hollow cylinder. The criteria in equation 3.3 states that the frequency must be well above this affected region before a Cartesian system can be safely substituted for a true cylindrical model.

## 3.2 Cylinders Immersed in a Fluid

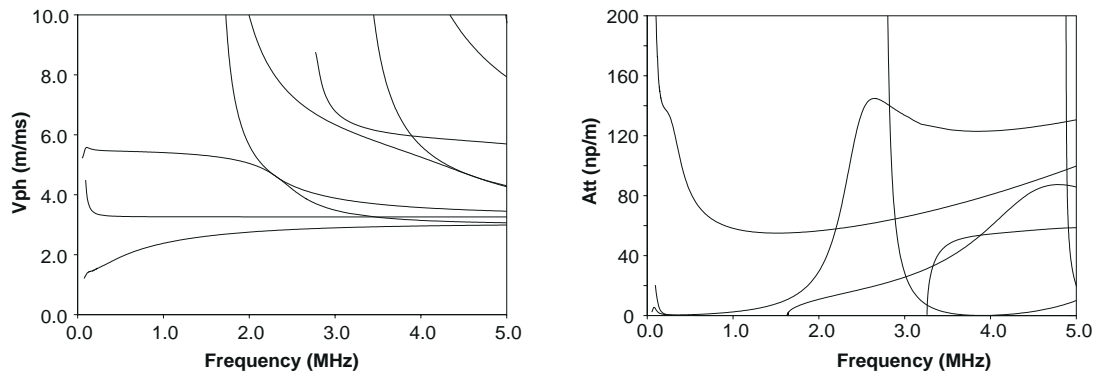
The previous cases discussed an elastic cylinder in vacuum, which is a relatively simple case to solve. When the cylinder is embedded in another material, calculating the dispersion curves becomes much more complex. When an elastic system is in vacuum, there is no mechanism for energy to be lost, so the attenuation is always zero. However, when the cylinder is surrounded by other materials, energy can leak from the structure into the surrounding liquid or solid, where it is free to propagate away in the form of bulk waves which travel to the infinite boundaries. Therefore, in addition to the frequency and phase velocity, the attenuation must be determined for each point on a dispersion curve. Since the solution routines must now search for a complex value in three dimensional space, they require many more calculations than when they only need to search for a real value in two dimensional space.

### 3.2.1 Modelling the Fluid inside the Cylinder

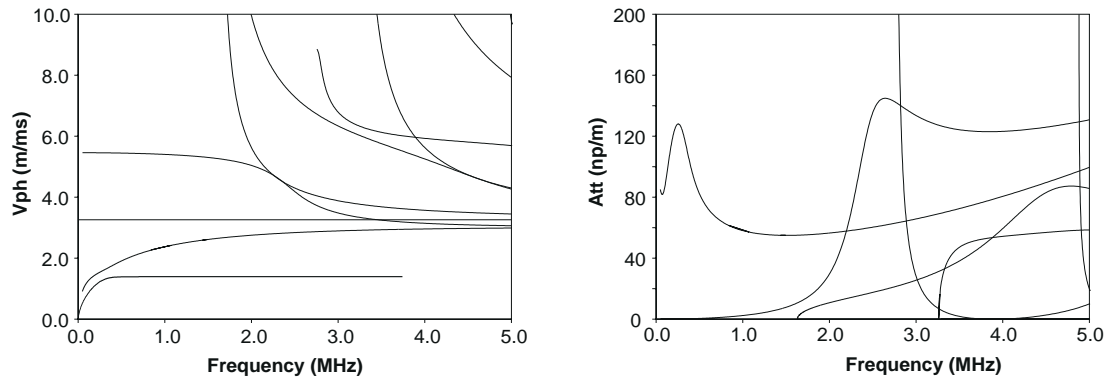
Figure 3.7 displays the dispersion curves for the zero order circumferential modes of a 1 mm thick steel pipe with an inner radius of 10 mm that is surrounded by and filled with water. The plots on the left show the phase velocity dispersion curves, comparable to those shown in figure 3.6. The plots on the right display the associated attenuation values. The three sets of dispersion curves represent subtly different cases. The first two cases model the same pipe. However, in the second case, the solution of the waves inside the pipe is modified so that there is a sink which absorbs any waves that propagate through the origin. The significance of this modification is discussed below. The third case models the pipe as a plate and is shown for comparison.



(a) 1 mm steel pipe (10 mm radius) with fluid modes shown



(b) 1 mm steel pipe (10 mm radius) with a sink in the centre of the pipe



(c) 1 mm steel plate in water

Figure 3.7: A comparison of phase velocity and attenuation dispersion curves for three cases: a water filled steel pipe immersed in water, a water filled steel pipe immersed in water with a sink in the centre, and a steel plate in water.

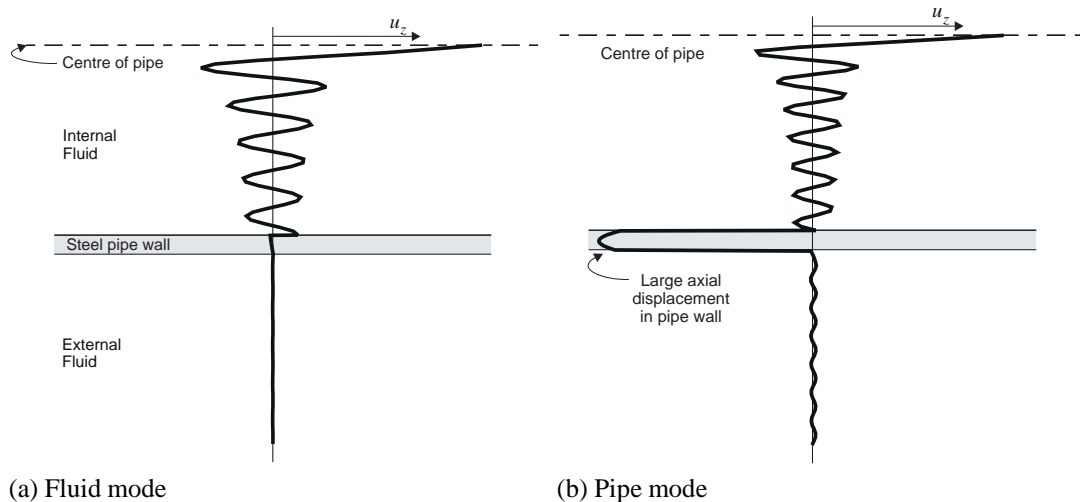


Figure 3.8: A comparison of the axial displacement for a fluid filled pipe for a mode that is (a) predominantly in the fluid and (b) predominantly in the pipe wall. The top of the graph represents the fluid filled core, the middle section the steel wall of the pipe, and the bottom section the first 10 mm of the surrounding fluid

The top set of dispersion curves in figure 3.7 models the fluid filled steel pipe as it actually exists. The dispersion curves contain fluid modes, whose energy and motion is concentrated in the water. These modes appear as the tight, regularly spaced curves. They tend to have low attenuation values and their group velocity (not shown) tends to be less than the bulk velocity of water. When the phase velocity and frequency of the fluid modes correspond with a point on the dispersion curves for the unloaded steel pipe, the energy of the fluid modes couples into the steel where a fast wave may propagate. However, at these points, there will also be significant attenuation because the energy of the wave, which is principally located in the steel, can easily leak into the surrounding water on the outside of the pipe where it is lost. Figure 3.8 displays the axial displacement for two points very near each other on the same mode. At the point shown in figure 3.8(a) it is behaving as fluid mode and at the point shown in figure 3.8(b) it is behaving as pipe mode. The top portion of the graph represents the centre of the system. The displacement becomes very large towards the centre as the waves that are leaking from the steel pipe into the centre of the pipe are focused. The middle section of the graph represents the wall of the steel pipe. When the mode is behaving as primarily as a fluid mode, there is very little displacement in the steel. However, there is a considerable amount of axial displacement when the mode deviates from its path and behaves primarily as a pipe mode. The bottom section of the graph represents the first 10 mm of the surrounding fluid. The wave that is seen in this section in figure 3.8(b) corresponds to the leaky wave that causes attenuation. Since the fluid layers are considered to be ideal liquids that do not support shear, the torsional modes of the system propagate solely in the steel wall of the pipe. Since there is no coupling of the torsional displacement component, there is no leakage and no therefore no attenuation.

The middle set of dispersion curves in figure 3.7 represents the same system as the top set of dispersion curves except that a sink has been placed at the centre of the system by modifying the representation liquid core. This modification involves changing the Bessel function that is used in the material layer

matrix for the liquid core from a standard Bessel function (which represents standing waves generated across the core of the pipe) to a Hankel function of the second kind (which represent a bulk wave propagating towards the centre of the pipe and being absorbed). The numerical sink caused by the usage of the Hankel function absorbs energy that is propagating inwardly from the steel pipe and prevents the fluid modes from forming. The attenuation values are much larger for this case as opposed to the previous case because energy is lost in both the sink and as it leaks into the fluid outside of the pipe.

Strictly speaking, this substitution does not represent the actual system and is not valid. However, there is valuable information in the second set of dispersion curves that is lost in the more accurate first set. Some ultrasonic tests are designed to propagate energy down the fluid inside a pipe and these tests must use the first set of dispersion curves. However, other ultrasonic tests are performed by sending waves down the walls of the pipe. This choice is usually made because the testing procedure is searching for defects in the pipe or because it is difficult to gain access to the inside of the pipe. Using this testing arrangement, it is important to know how quickly the test signal will be attenuated. As described in section 2.6.1, when the pipe is only partially filled with a fluid, the attenuation can be much higher than the values predicted by the model for a fully filled pipe. In the partially filled case, the bulk waves in the fluid core, which form a portion of the total guided wave, will be reflected off of the surface of the fluid and will no longer propagate at the correct incidence angle to continue to contribute to the energy of the mode. This scattering causes additional attenuation, which can be approximated by inserting a numerical sink in the centre of the pipe. Another effect, which will only appear in transient problems, can also cause the observed attenuation to be larger than the values predicted by the model for a completely filled pipe. When energy leaks from the wall of the steel pipe into the centre, it propagates through fluid core and is reabsorbed on the other side. Although the energy is not lost from the mode, the reabsorption of energy will be delayed by the propagation time through the fluid core. For a harmonic solution, this delay has no effect on the amplitude of the propagating wave. However, for a transient solution, such as an experiment, this delay has a noticeable effect. Instead of consisting of a single signal, a transmitted wave packet will consist of a series of successively smaller signals, the spacing of which corresponds to the transmission time across the fluid core. Because of this effect and the transfer of energy into the trailing signals, the peak amplitude of the largest transmitted signal will be smaller than would be estimated from the attenuation value alone. By incorporating a sink in the centre of the pipe, which absorbs the energy that would be lost to the successive peaks, the attenuation values may better represent what actually happens in practice.

The third set of dispersion curves in figure 3.7 displays the phase velocity and attenuation curves for a 1 mm steel plate in water. Comparison between the last two sets of curves shows that the behaviour of a large radius pipe at high frequency is very similar to that of a plate, confirming that the similarity seen in figure 3.6 also holds for leaky systems. (Please note that the Scholte wave, which appears for the plate case as the mode whose phase velocity asymptotically approaches the compressional wave speed of water, could not be traced for the pipe case.)

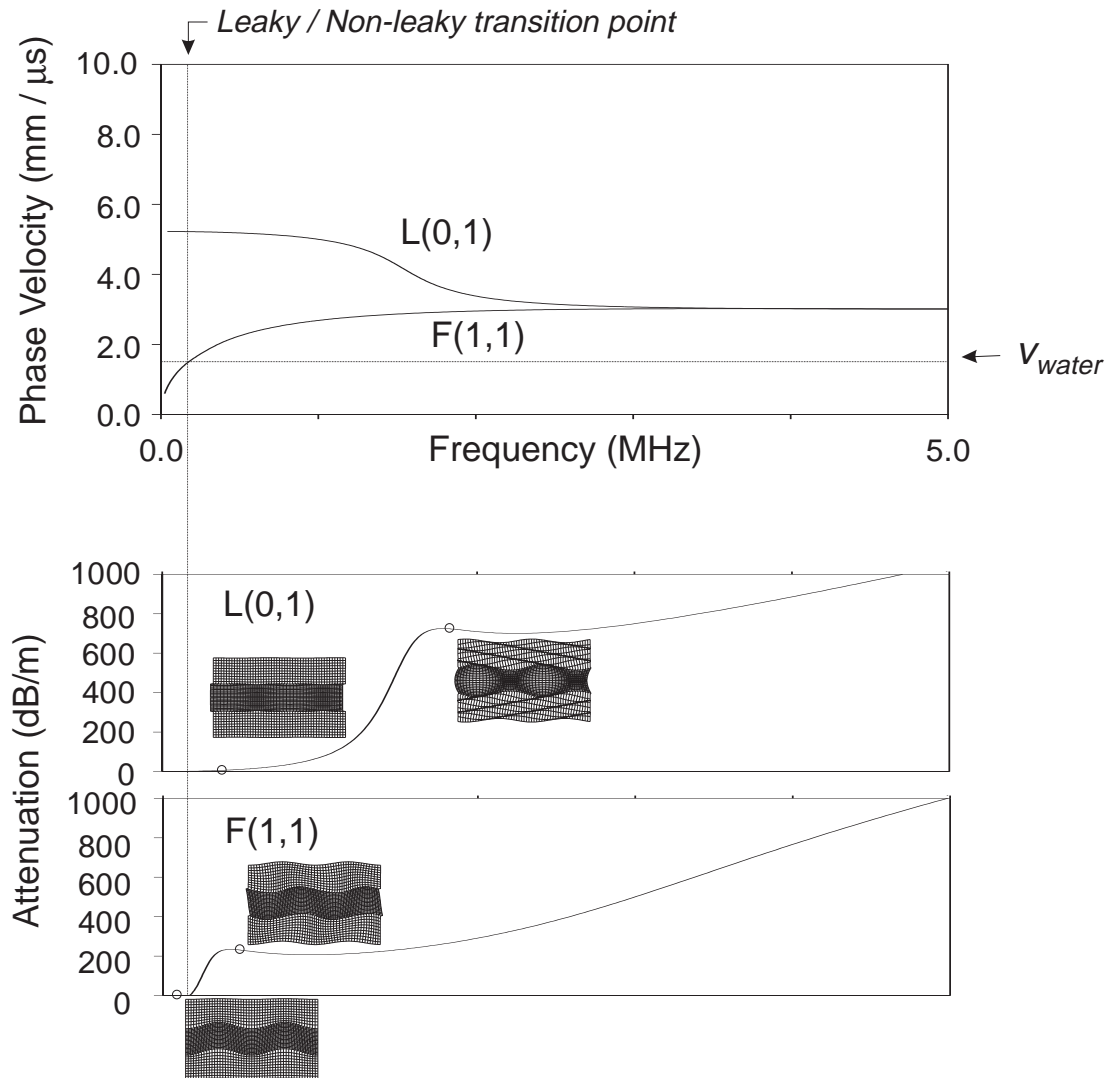


Figure 3.9: Phase velocity dispersion curves for a 2 mm diameter steel bar immersed in water with mode shapes super-imposed on the fundamental modes.

### 3.2.2 Leakage into the Surrounding Medium

Much of the variation in attenuation in figure 3.7 can be attributed to the changing amount of radial displacement on the surface of the cylinder. The radial displacement permits the energy to be coupled from the guided wave into the surrounding liquid. Figure 3.9 demonstrates this effect for a 1 mm radius bar immersed in water for the fundamental longitudinal and flexural modes. The top graph shows the phase velocity curves for these two modes and the bottom graphs show the related attenuation values. Four grid mode shapes display the nature of the mode at the circled points. The centre section of the grid mode shapes represents a cross section through the centre of the bar and the outer sections represent the first two millimetres of the infinitely large surrounding fluid.



L(0,1), the fundamental longitudinal bar mode, is very lightly attenuated at low frequencies since the majority of the motion is in the axial and not the radial direction. However, as the frequency increases, the attenuation also increases dramatically as the mode's radial displacement at the surface increases. As the frequency continues to increase, the attenuation approaches the attenuation value for a leaky Rayleigh wave, which is linear with frequency.

The fundamental flexural mode has significant radial displacement components at the surface of the bar across a wide frequency range. Correspondingly, the attenuation values remain relatively high. However, when the phase velocity of the F(1,1) mode drops below the bulk velocity of water, the attenuation becomes zero although there is still significant radial displacement.

This 'non-leaky' mode can be explained by figure 3.10. As the guided wave travels down the bar, the radial displacements at the surface of the bar couple energy into the surrounding fluid. This motion will create a bulk wave in the fluid, which then carries energy away from the system. The wavelength of a bulk wave in the fluid is known, since bulk waves only travel at one speed and the frequency is known. The wavelength of the guided wave is calculated from the dispersion curves. Since the projection of the wave along the interface must match for the guided wave and the bulk wave, the leakage angle,  $\theta_{leak}$ , can be determined to be,

$$\begin{aligned}\theta_{leak} &= \sin^{-1} \left( \frac{\lambda_{water}}{\lambda_{steel}} \right) \\ &= \sin^{-1} \left( \frac{v_{water}/f}{v_{ph}/f} \right) \\ &= \sin^{-1} \left( \frac{v_{water}}{v_{ph}} \right)\end{aligned}\tag{3.4}$$

where  $\lambda$  is the wavelength,  $v_{water}$  is the bulk velocity of the water,  $v_{ph}$  is the phase velocity of the guided wave, and  $f$  is the frequency. If the phase velocity,  $v_{ph}$ , is less than the bulk velocity in the surrounding medium, then equation 3.4 implies that the leakage angle,  $\theta_{leak}$  would be imaginary. Physically, the imaginary angle means that instead of creating a wave that propagates away from the bar, the displacements die away exponentially and the energy is trapped against the bar. Therefore, in general, a mode will not leak if its phase velocity is less than the bulk velocity of any waves that can exist in the surrounding liquid. This principle is also known as the coincidence principle or the phase matching condition.

### 3.3 Cylinders Embedded in a Solid

When the system is surrounded by a liquid, the energy leaks via a bulk compressional wave. However, when the system is surrounded by a solid material, energy can be carried away from the system by both shear and compressional (longitudinal) bulk waves. In addition, since the tangential displacements and stresses couple into the surrounding solid as well as the normal displacements, the attenuation values tend to be much higher and the minima in attenuation do not usually reach down to zero attenuation.

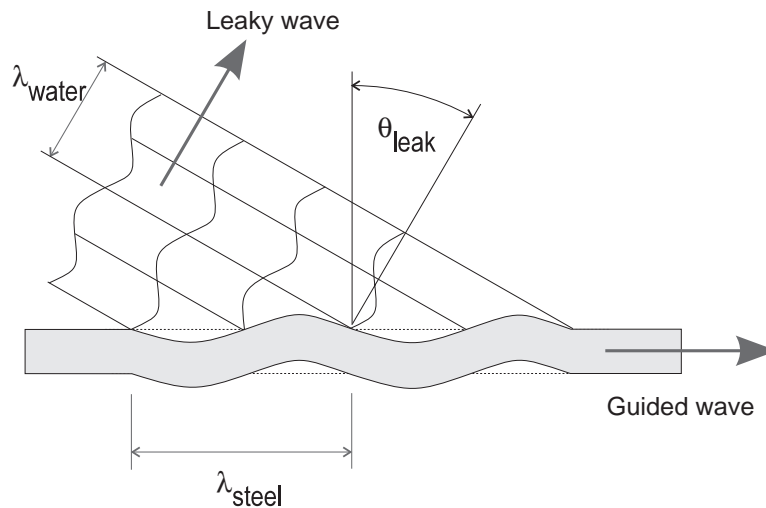


Figure 3.10: As a guided wave travels down a bar, it couples energy into the surrounding fluid, creating a leaky bulk wave at a characteristic angle.

An example of a system that is surrounded by a solid is given in figure 3.11. The system represents an empty 1 mm thick steel pipe with a 10 mm inner radius that is surrounded by a soft stone (mudstone).

Comparing the attenuation curves with those for a filled pipe in water in figure 3.7 reveals some dramatic differences. First, the attenuation values are much larger, so much larger than the liquid loaded case that different scales had to be used. The increased attenuation is mainly due to two factors. The density and impedance of the surrounding material are much higher for the mudstone than for the water. Therefore, the guided wave that is propagating in the steel bar couples much more strongly to the leaky bulk waves that are generated in the mudstone than to those generated in the water. This effect can be evaluated in terms of the reflection coefficients at the boundary between two layers. If the impedances are similar, a large portion of the energy will be transmitted across the boundary. However, most of the energy will be reflected if the impedances are very dissimilar. Applying this interpretation for guided waves indicates that more energy will leak from the steel bar into the surrounding material when the impedances are more closely matched. The second reason why the attenuation is lower for the fluid immersion case is that when a bar is surrounded by a liquid, only the radial displacements can couple from the solid bar into the surrounding liquid. However, when the bar is surrounded by a solid material, the circumferential displacements ( $\hat{\theta}$ ) and the axial displacements ( $z$ ) also couple the two layers together. This additional coupling increases the attenuation. For this reason, all of the torsional modes shown in the immersed case experience no attenuation (since the  $\hat{\theta}$  displacement at the surface of the pipe does not couple into the surrounding fluid), however, the torsional modes do experience attenuation in the embedded case. When surrounded by a solid material, the theta displacement couples into the surrounding medium, a bulk wave will be produced, and attenuation will be present.

The second major difference between the dispersion curves for the immersed and embedded cases is that not all of the modes are plotted as continuous curves in the embedded case. For example, the

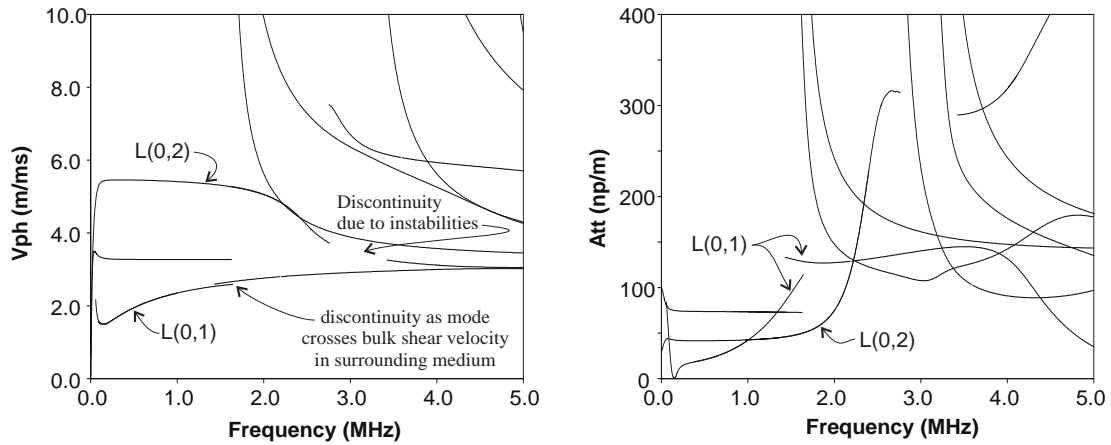


Figure 3.11: Phase velocity and attenuation dispersion curves for an empty 1 mm thick steel pipe with a 10 mm inner radius that is surrounded by soft stone (mudstone).

L(0,1) mode in the embedded pipe is not continuous when it crosses the bulk longitudinal velocity of the surrounding mudstone,  $2.6 \text{ mm}/\mu\text{s}$ . At this point, there is a jump in attenuation and frequency. The cause of this jump is that at a phase velocity above the bulk longitudinal velocity of the surrounding solid, the pipe is leaking both shear and longitudinal waves. However, below the bulk longitudinal velocity, the pipe is only leaking shear waves, which leads to the discontinuity. The two portions of the curve should in fact be linked mathematically. However, the linking section of the curve would be unsuitable for non-destructive testing and cannot be traced using the global matrix method (which cannot trace modes very near any of the bulk wave velocities) so effort has not been expended to find these links. In addition, there is a gap in the L(0,2) mode around 3 MHz. In reality this mode should continue, however, numerical instabilities around the shear bulk velocity in steel do not allow it to be traced any farther for the moment. These instabilities are mainly due to a mathematical singularity inherent in the global matrix method and rounding errors in the complex Bessel function routines.

### 3.3.1 Different Types of Leakage

The different types of mode leakage for a solid cylinder embedded in a solid are shown in figures 3.12 and 3.13. Figure 3.12 shows the phase velocity dispersion curves for a 1 mm radius steel bar embedded in a light stiff stone (density =  $2200 \text{ kg}/\text{m}^3$ , Young's modulus =  $60 \text{ GPa}$ , and Poisson's ratio = 0.25, as shown in table 3.1). The existence of non-leaky portions of modes that have no attenuation makes a significant difference between these curves and those in figure 3.11. Two straight lines are shown on the phase velocity diagram which correspond to the longitudinal and shear bulk velocities in the surrounding rock. These bulk velocities divide the graph into regions with modes that are non-leaky, leak only shear, and leak both shear and longitudinal waves. The points marked (a), (b), and (c) correspond to the points for which the mode shapes are shown in figure 3.13. Point (a) is in the non-leaky region, below both the shear and longitudinal bulk velocities. Point (b) is the region where only bulk shear waves can leak

and point (c) is in the region above the longitudinal bulk velocity where both shear and longitudinal modes leak into the surrounding solid. The mode shapes in figure 3.13 demonstrate this effect. The centre part of the grid represents the cross section of the bar and the outer section of the grid represents the first two millimetres of the surrounding rock. In the non-leaky section shown in figure 3.13(a), the displacement in the surrounding solid dies away exponentially as described in the previous section. In figure 3.13(b) only a shear wave leaks from the bar into the surrounding solid. The displacement field in the surrounding solid shows a single leaky wave. However, the displacement field is much more complicated for figure 3.13(c) because the leaky shear and longitudinal bulk waves overlap at different leakage angles.

### 3.3.2 Multi-layered Cylinders Embedded in a Solid

The final examples in this chapter take advantage of the multi-layered nature of this solution to the wave propagation problem.

#### **Multi-layered isotropic materials with material damping**

The first system that is considered is the same as the example shown in figure 3.11, however a 0.5 mm layer of grout has been added to the inside of the pipe to simulate a scaled down version of a mains water pipe. In addition, material damping is considered for both the grout and the mudstone (see table 3.1 for the material properties used). The attenuation due to the material damping is super-imposed on the attenuation due to leakage. The dispersion curves are shown in figure 3.14.

It is immediately obvious in figure 3.14 that many of the modes are incomplete. The complexity of the system and the high losses associated with it render many of the regions insoluble. Many of the instabilities have been improved by using appropriate scaling factors in the equations, however, these instabilities have not been completely conquered and still cause problems as seen in this example. Another feature of figure 3.14 is that the modes are shifted to the left, compared to the previous dispersion curves. Since this system is thicker than the previous one because the grout lining adds to the steel wall, the frequencies at which through thickness resonances occur decrease.

The L(0,1) mode shows interesting behaviour. At low frequencies, it travels at a phase velocity similar to the shear bulk velocity in the steel. However, as the frequency increases, its phase velocity lowers to the shear bulk velocity of the grout liner. This behaviour is consistent with the practice that the longer wavelengths associated with low frequencies 'look' farther into the system and are predominantly influenced by the steel layer while the short wavelengths and high frequencies are predominantly affected by the grout lining.

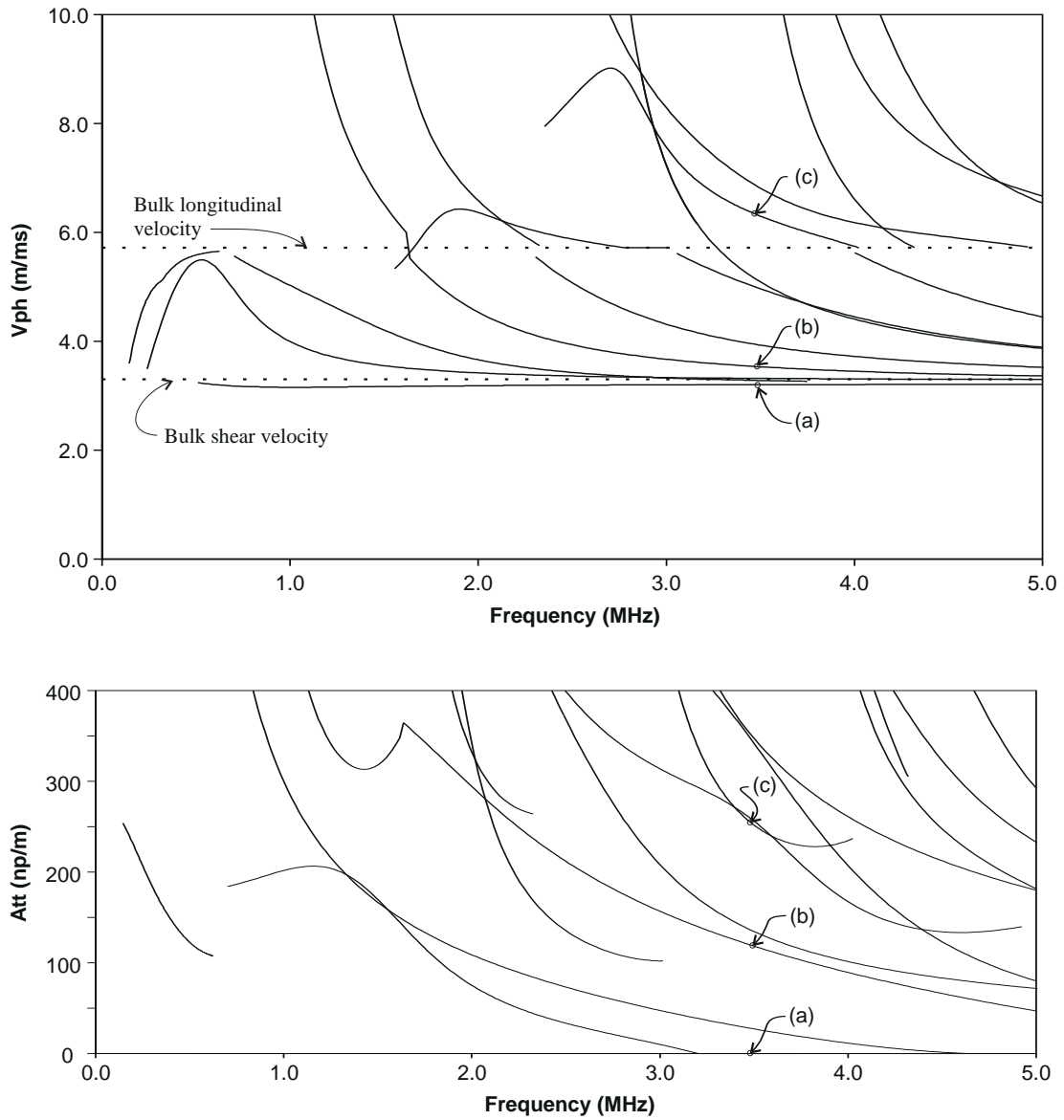


Figure 3.12: Phase velocity and attenuation dispersion curves for the zero and first circumferential order modes of a 1 mm radius steel bar embedded in a stiff material. The arrows and labels correspond to the positions for which the mode shapes are given in the next figure. The straight dotted lines correspond to the bulk velocities in the surrounding solid and divide the dispersion curves into different leaky regimes.

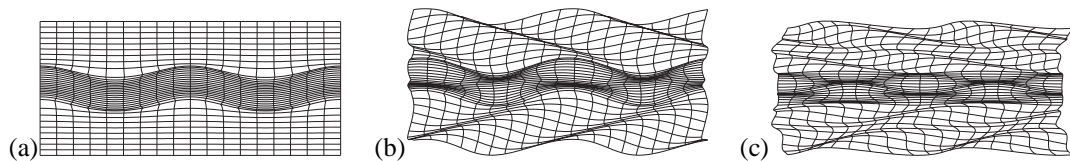


Figure 3.13: Mode shapes for a steel bar embedded in a stiff material in (a) a non-leaky region, (b) a region where only shear waves leak, and (c) a region where both shear and longitudinal bulk waves leak into the surrounding solid.

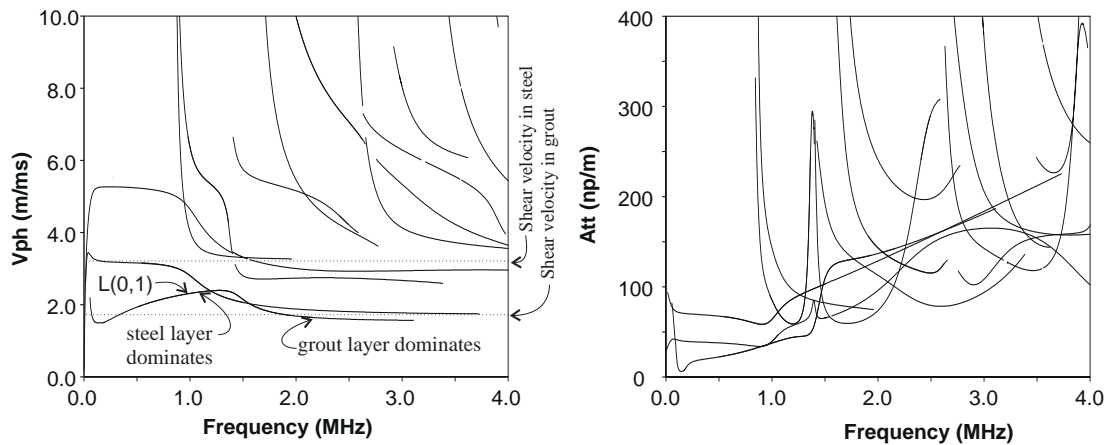


Figure 3.14: Phase velocity and attenuation dispersion curves (zero circumferential order modes) for a 1 mm thick steel pipe with a 10 mm inner radius that is lined with lossy grout and is surrounded by lossy soft stone (mudstone).

### Multi-layered transversely isotropic materials

Guided waves that are propagating in layered transversely isotropic materials will leak into the surrounding half-space just like their isotropic counterparts. This effect can be seen in figure 3.15, which shows the phase velocity dispersion curves for the axi-symmetric modes of a single Carbon - Silicone carbide fibre that is embedded in a titanium matrix. In this figure, the width of the solid lines indicates the relative attenuation of the mode, with the thin lines being highly attenuated and the thick lines being less highly attenuated.

As done in figure 6 in Nayfeh and Nagy's work [37], these results can be compared to the dispersion curves for the free fibre (figure 3.3) to examine the changes that are caused by embedding the fibre. Figure 3.16 shows this comparison. The dispersion curves for the free fibre are shown as dashed lines superimposed on the same dispersion curves for the embedded system that are in figure 3.15. There are some distinctive changes. As discussed by Nayfeh and Nagy[37] and Simmons et al.[34], the phase velocity of the fundamental longitudinal mode tends to zero instead of the finite bar velocity. This behaviour is caused by the loading of the axial displacement of the mode. As the frequency decreases, the wavelength of the guided mode becomes much larger than the fixed radius of the fibre. Soon the fibre diameter becomes negligible (in wave propagation terms) and can no longer support a true guided mode, since most of the energy is contained within the surrounding matrix. This singularity does not appear for liquid loaded structures that are only coupled through the radial displacement and stresses since the radial displacement of the fundamental longitudinal mode tends to zero as the frequency decreases.

It is assumed the fibre and the titanium matrix are perfectly bonded, which causes the attenuation to be very high, as can be seen in figure 3.17, the attenuation values for the axi-symmetric modes. The attenuation in figure 3.17 has been normalised by scaling by the radius of the fibre. Thus, the attenuation values shown indicate the amount of attenuation that will occur when the guided wave propagates a distance along the axis of the fibre that is equal to the length of its radius. Figure 3.17 shows that

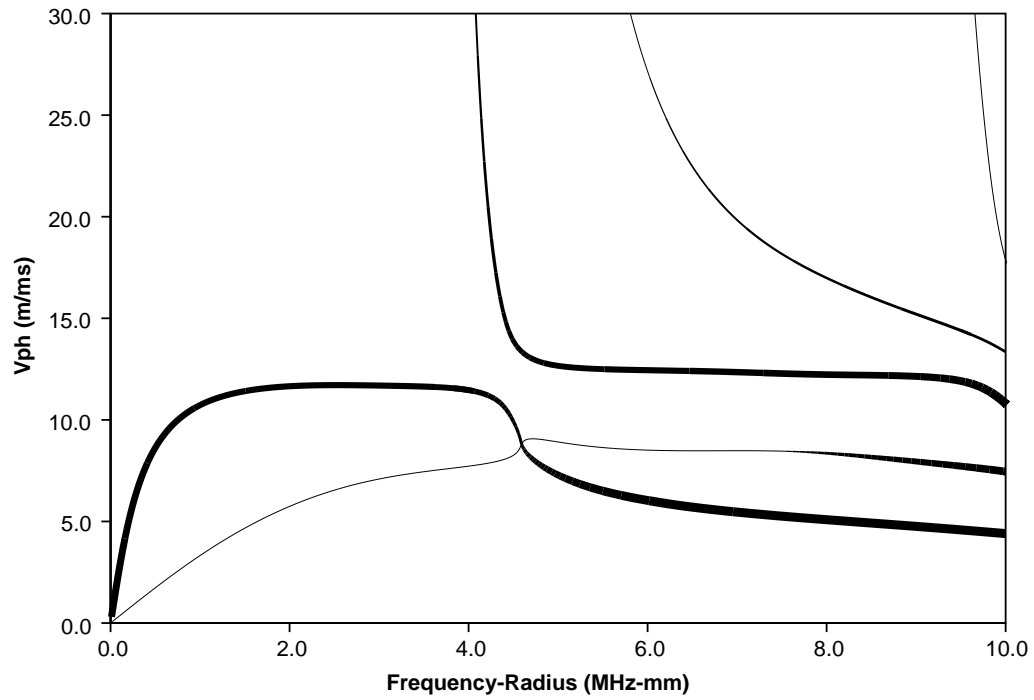


Figure 3.15: Phase velocity dispersion curves for the axi-symmetric modes of a 70 micron SCS fibre embedded in a titanium matrix. The width of the lines indicates the relative attenuation of the points on the mode (thicker lines correspond to lower attenuation values).

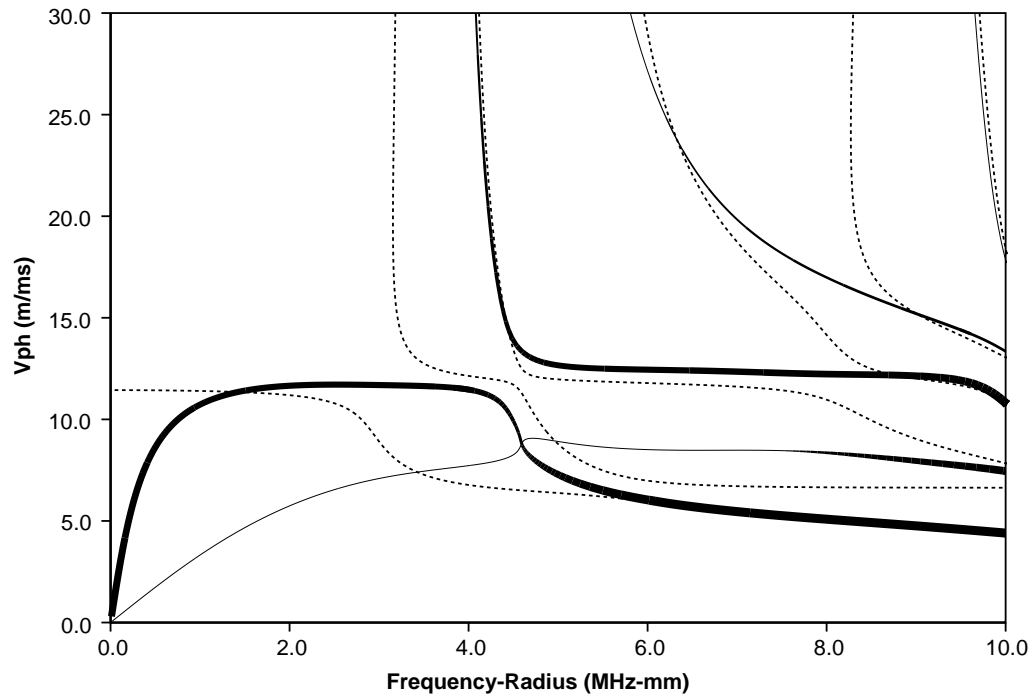


Figure 3.16: Phase velocity dispersion curves for 70 micron SCS fibre embedded in a titanium matrix (solid lines) overlaid on the dispersion curves for the free system (dashed lines).

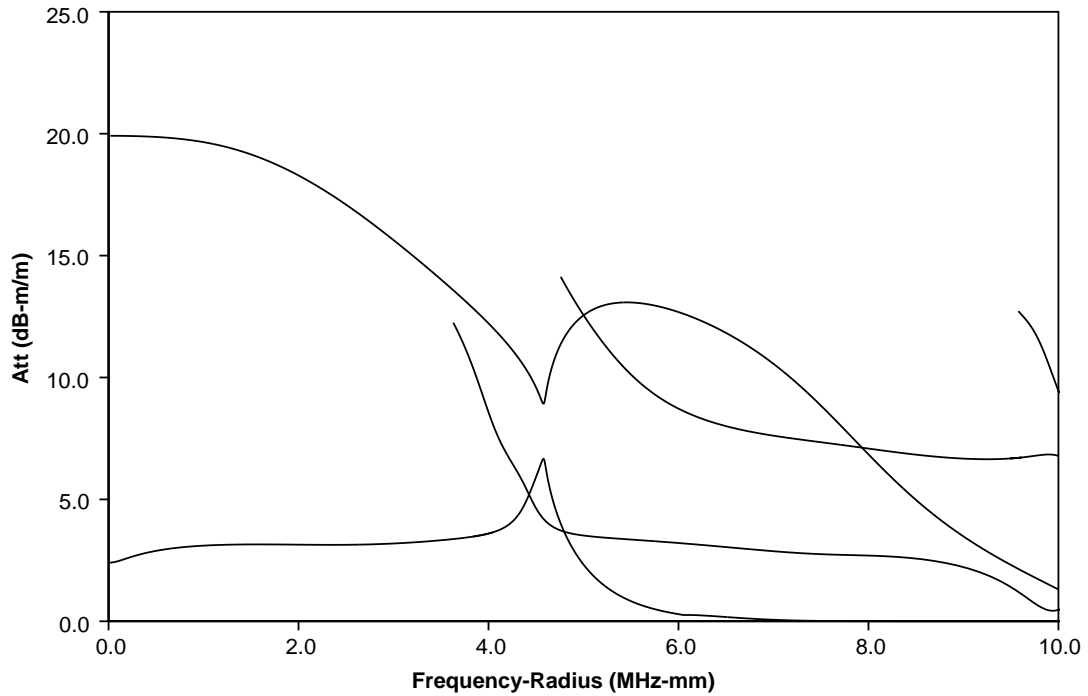


Figure 3.17: Attenuation dispersion curves for the axi-symmetric modes of a 70 micron SCS fibre embedded in a titanium matrix.

the normalised attenuation is over 6 dB for most of the modes that can exist in this system. In practice, perfect bonding between the fibre and the matrix may not occur. An intermediate layer that has degraded properties can be inserted between the outside of the fibre and the surrounding metal to simulate an imperfect bond. Inserting this degraded layer allows the modes of the cylinder to decouple from the surrounding matrix and dramatically reduces the observed attenuation. This case is discussed later and shown in figure 3.21.

Figure 3.18 shows the dispersion curves for the first circumferential order modes for the same embedded fibre system. An interesting feature of these dispersion curves is the separation of the fundamental first order mode  $F(1,1)$  into two parts. Three points have been marked (a), (b), and (c) on the two low phase velocity modes in figure 3.18. The mode shapes at these points are shown in figure 3.19 so that the behaviour of these portions can be more closely examined. The low phase velocity mode that contains point (c) represents a mode that propagates along the interface between the silicone carbide sheath and the surrounding titanium matrix. In the high frequency range, the attenuation of this mode increases linearly with frequency, in the same way that the attenuation of a leaky Rayleigh wave will increase linearly with frequency. The other low phase velocity mode represents a guided wave whose energy is concentrated in the fibre. As the frequency increases, the attenuation of this mode decreases. For example, the attenuation at the point marked (a) is over 8 dB for each radial length that the mode propagates, however the attenuation at the point marked (b) is less than  $1.0e^{-7}$  dB per radial length, eight orders of magnitude less. At point (b), the mode can be considered to be non-leaky, guided in the



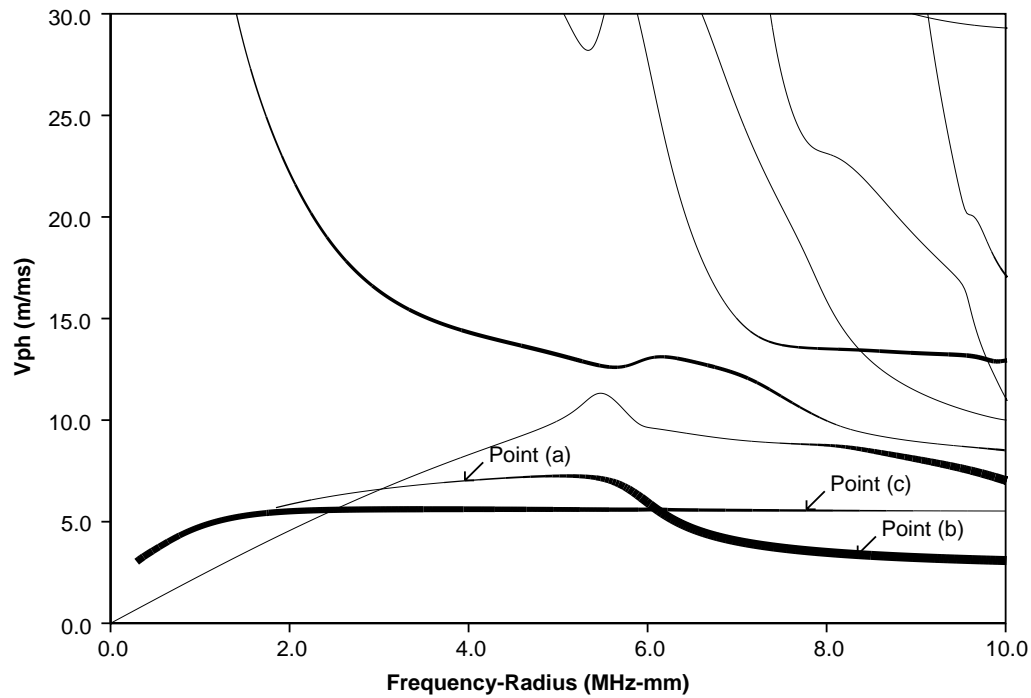


Figure 3.18: Phase velocity dispersion curves for the first circumferential order modes of a 70 micron SCS fibre embedded in a titanium matrix. The line thickness indicates the amount of attenuation present (thin lines indicate high attenuation). The mode shapes for the points marked (a), (b), and (c) are shown in the following figure.

carbon core, which is surrounded by the faster silicone carbide (SiC) sheath. Because the phase velocity of the guided wave is less than the bulk velocities of the silicone carbide, there are no bulk waves excited in the SiC sheath that would provide for leakage from the wave in the carbon core. However, although no bulk waves are created in the SiC sheath, there are still displacements in the sheath. The amplitude of the displacements is greatest at the interface between the carbon and the SiC sheath and decays exponentially with the radius. This exponentially decaying field can be thought of as 'tails' of the non-leaky guided wave. The 'tails' reach through the entire thickness of the SiC sheath and cause there to be displacements at the interface between the SiC sheath and the titanium matrix. Since the phase velocity of the guided wave is greater than the shear velocity of titanium, a leaky wave can be formed in the infinite titanium matrix. This effect accounts for the small amount of attenuation observed at point (b). As the frequency increases, the amplitude of the 'tails' decays more rapidly and there is less observed attenuation.

Many of the higher order modes are very highly attenuated by the leakage into the surrounding metal. This high leakage dramatically affects the shape of the phase velocity dispersion curves as can be seen by studying figure 3.20, which overlays the dispersion curves for the embedded case (figure 3.18) and the free case (figure 3.3(b)), which is shown as dotted lines.

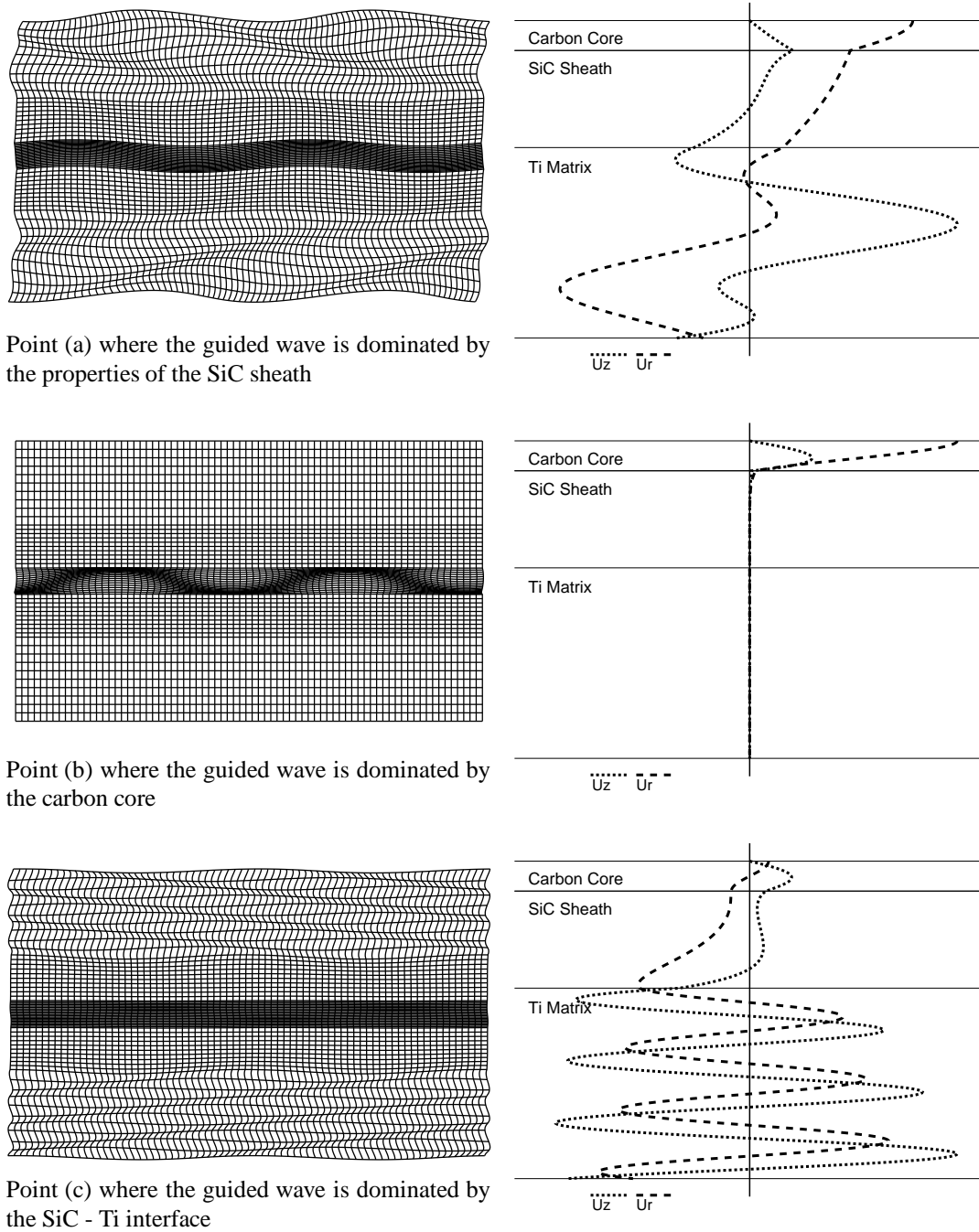


Figure 3.19: A comparison of the grid and line mode shapes for the three points marked on the dispersion curves for an embedded SCS fibre that are shown in the previous figure.

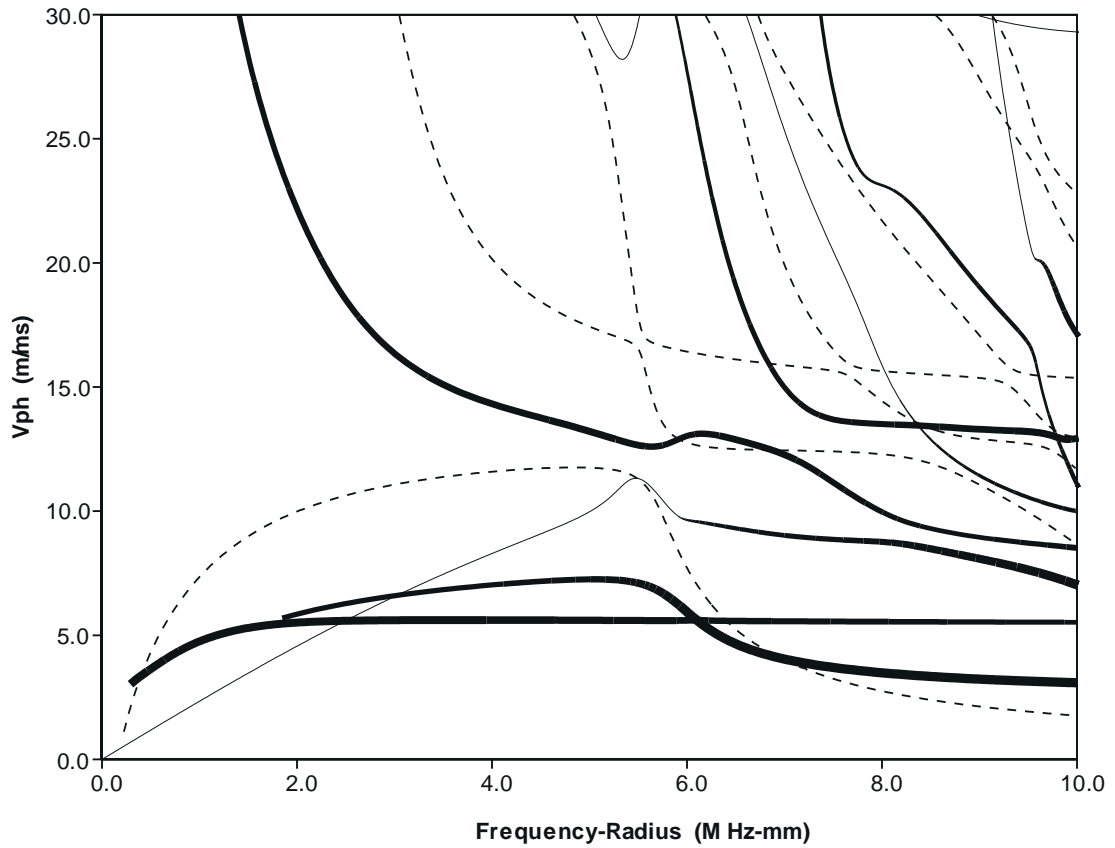


Figure 3.20: Phase velocity dispersion curves for the first circumferential order modes of a 70 micron SCS fibre embedded in a titanium matrix. The dashed lines represent the phase velocity curves for the free fibre and the solid lines correspond to the embedded case (with the thickness dictated by the attenuation of the embedded mode).

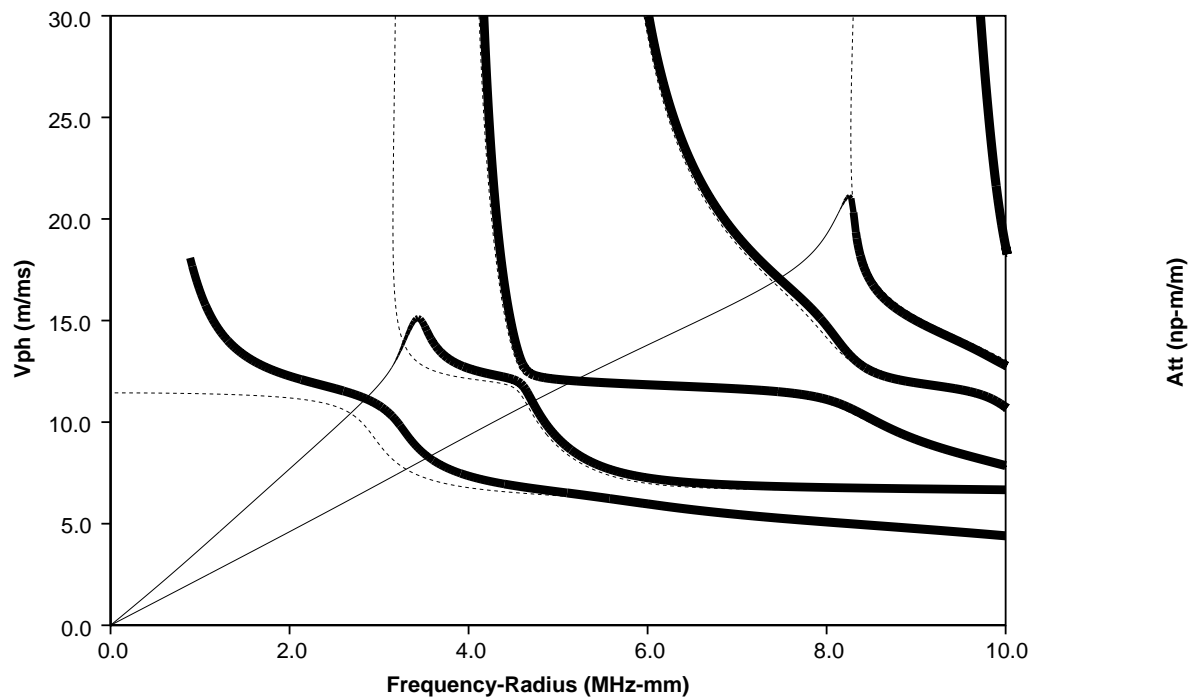


Figure 3.21: Phase velocity dispersion curves for the axi-symmetric modes of an embedded SCS fibre when an imperfect bond exists between the fibre and the surrounding titanium matrix. For comparison, the free case is shown as dashed lines.

The modelling in the previous example assumes that the bond between the SCS fibre and the surrounding titanium matrix is perfect. However, in reality, this bond will not be perfect. An imperfect bond can be simulated by introducing a thin additional layer between the fibre and the surrounding material. The stiffness of this additional layer controls how well the two materials are bonded. An example of this technique is shown in figure 3.21. To create the dispersion curves in this figure, a one micron thick degraded layer was introduced at the SiC-Ti interface. The density was set to be the same as the surrounding material, however, the stiffnesses were divided by sixty-four. In comparison to the perfectly bonded case in figure 3.16, the attenuations are much lower and the phase velocity dispersion curves much more closely resembles the free fibre case.

### 3.4 Summary of Cylindrical Examples

This chapter has examined several different examples of guided wave propagation in cylindrical systems. The general nature of the different types of guided waves has been discussed, as well as the effect of immersing the structure in a fluid or embedding it in a solid. The following chapter uses several of the examples developed in this chapter and some new examples to validate the wave propagation model.

Table 3.1: Material constants used for isotropic materials in the wave propagation modelling.

Material	Density ( $g/cm^3$ )	$v_l$ (m/s)	$v_s$ (m/s)	Young's Modulus (GPa)	Poisson's Ratio	$\alpha_l$ ( $np/\lambda$ )	$\alpha_s$ ( $np/\lambda$ )
Steel	7.932	5960	3260	217	0.29	0.0	0.0
Perspex	1.18	2730	1430	6.327	0.31	0.0	0.0
Water	1.0	1483	-	-	-	0.0	-
Mudstone	2.5	2592	1497	14	0.25	0.03	0.08
Grout	1.6	2810	1700	11.2	0.21	0.043	0.1
Stiff Stone	2.2	5720	3300	60.0	0.25	0.0	0.0

Table 3.2: Material constants used for transversely isotropic materials in the wave propagation modelling.

Material	Density ( $g/cm^3$ )	$C_{11}$ (GPa)	$C_{12}$ (GPa)	$C_{13}$ (GPa)	$C_{33}$ (GPa)	$C_{44}$ (GPa)
isotropic carbon	1.65	42.1	18.0	18.0	42.1	12.0
isotropic silicone carbide	3.10	425.8	90.9	90.9	425.8	167.5
anisotropic carbon	1.65	42.1	18.4	17.1	44.2	11.7
anisotropic silicone carbide	3.10	404.8	95.4	86.6	446.3	170.2
isotropic titanium	4.43	158.7	71.3	71.3	158.7	43.7
nylon reinforced rubber	1.014	0.0196143	0.00749677	0.0113867	0.573065	0.00574575

## Chapter 4

# Validation of Cylindrical Wave Propagation Model

The previous chapter discussed the wave propagation solutions for some cylindrical systems, so that cylindrical wave propagation could be better understood. This chapter examines various cylindrical wave propagation solutions in more detail for the purpose of validating the wave propagation model that was developed in chapter 2.

The validation cases fall into several categories, asymptotic limits for which there are exact solutions, cases which have been published in the literature, the internal consistency of the solutions, and comparison to results from independent finite element modelling and experiments. Each of these areas will be addressed in the following sections. The first section validates the model against asymptotic limits for which there are known analytical solutions. For example, the phase velocity of the first longitudinal mode in an isotropic bar is known analytically. The second section compares the results of the model to published results for the free case, the axi-symmetric loaded case, and the first order flexural loaded case. The third area looks for internal consistencies. For example the solution should be the same if each layer is divided into a number of sub-layers. The final area of validation compares the obtained solutions to the wave propagation that has been observed in finite element modelling, which represents an independent method of examining the wave propagation characteristics. In addition, the results from a limited number of experiments are included. In general, the cases which leak energy into a fluid provide the most complete validation because they incorporate two different material types. Cases where energy leaks into solid materials are generally more difficult to trace than those that leak into a fluid. However, cases that involve leakage into a solid only verify that the layer matrix for a solid material is correct. Therefore, many of the examples in this chapter will concentrate on fluid loaded case and the free case, so that both the liquid and solid layer matrices can be validated.

Excellent agreement is obtained between the wave propagation model and all of the validation criteria that follow, which provides a great deal of confidence in the model.

## 4.1 Validation against Asymptotic Limits

The first validation criteria that will be considered are the comparisons to known asymptotic values, such as the bar velocity.

**Bar velocity** The phase velocity of the fundamental longitudinal mode of a free isotropic bar should approach the static limit (called the bar velocity) which is given by  $\sqrt{E/\rho}$ , where  $E$  is the Young's modulus and  $\rho$  is the density of the material[65,52]. For steel, whose young's modulus is usually around 216 GPa and whose density is around  $7932 \text{ kg/cm}^3$ , the bar velocity should be 5218.38 m/s. When calculated using Disperse, the phase velocity of the fundamental longitudinal mode is  $5218.38 \text{ m/s} \pm 0.02 \text{ m/s}$  when either a single layer is used or when three layers with identical material properties, but different thicknesses are combined together. The bounds of  $\pm 0.02 \text{ m/s}$  is controlled by the precision of the mathematical routines used to calculate the solutions as well as the tolerance used in the iterative root finding routines. The value given was measured by observing small oscillations in the phase velocity dispersion curves.

**Rayleigh Velocity** The well known Rayleigh velocity for the propagation of a surface wave on the surface of a semi-infinite half-space can be used to validate the solutions at the high frequency limit. We know that the Rayleigh velocity for a steel half space ( $\rho = 7932 \text{ kg/cm}^3$ ,  $c_1 = 5960$ ,  $c_2 = 3260$ ) is approximately 3016.47 m/s. This value can be calculated by solving the third order equation[60],

$$T^3 - 8T^2 + (24 - 16R)T - 16(1 - R) = 0 \quad (4.1)$$

where  $T = (c_r/c_2)^2$ ,  $R = (c_2/c_1)^2$ ,  $c_1$  is the bulk longitudinal velocity,  $c_2$  is the bulk shear velocity, and  $c_r$  is the Rayleigh velocity, or by using the Cartesian wave propagation solutions in Disperse. This value can be compared to the high frequency asymptote of a steel pipe, since as the frequency increases, the wall of the pipe begins to look more and more like a flat semi-infinite half-space to waves that are propagating on it. For a steel pipe whose inner radius is 10 mm and whose wall thickness is 1 mm, the two lowest longitudinal modes converge on the Rayleigh velocity from above and below. At 35 MHz, the highest frequency for which the solution remained stable, the phase velocities of these two modes are  $3016.02 \text{ m/s} \pm 0.02 \text{ m/s}$  and  $3016.96 \text{ m/s} \pm 0.02 \text{ m/s}$ . If these modes converge on their average, the predicted value for the Rayleigh velocity will be  $3016.49 \text{ m/s} \pm 0.02 \text{ m/s}$ , which agrees with the analytically calculated value. The high frequency asymptote of the fundamental modes in a bar could also be used to approximate the Rayleigh velocity, however since the curvature of the surface of the

bar is greater than a large radius pipe, much higher frequencies will need to be used. At 150 MHz, the highest frequency that could be reliably calculated for this system, the phase velocity of a steel bar with a 1 mm radius is 3015.3 m/s and still steadily rising. A curve can be fitted to the high frequency portion of the curve to get an approximation of the phase velocity at infinite frequency, which should be equal to the Rayleigh velocity. Using the least squares method to fit a function of the type  $a - b/x$  to the high frequency portion of the L(0,1) mode (80-150 MHz) yields an approximate Rayleigh velocity of 3016.43 m/s, which agrees well the analytically calculated value of 3016.47 m/s.

**Stoneley Waves** Stoneley waves, which propagate along the interface between two solids without loss [66], can also be used to validate the wave propagation model. Stoneley waves can only propagate when the two materials satisfy certain criteria that were identified by Scholte in 1946[67]. One such permissible combination is an interface between a steel half-space and a titanium half-space<sup>†</sup>. The Stoneley wave, which travels at a phase velocity slightly lower than the bulk velocities, propagates at 3251.17 m/s for this material combination, as calculated by the previously validated Cartesian routines in Disperse [10].

At the high frequency limit, a titanium bar embedded in a semi-infinite steel half-space should demonstrate this same behaviour. When a one millimetre titanium bar is embedded in steel, the mode that will become the Stoneley wave has a phase velocity of 3251.28 m/s at 150 MHz, which is approaching the Cartesian limit. If a least squares fit method is applied to fit the function  $a + b/f$  (where  $a$  and  $b$  are constants and  $f$  is the frequency) to the 80-150 MHz section of this mode, an approximation for the phase velocity of this mode at its high frequency limit is obtained as 3251.14, which agrees well with the Cartesian case.

**Large radius comparison with plate** As the radius of a pipe increases, its dispersion curves begin to resemble the dispersion curves of a flat plate more and more closely. This feature was shown in figure 3.6 which examines the dispersion curves of a hollow pipe as the radius to wall thickness ratio is changed. This behaviour provides additional validation of the wave propagation model as it approaches an asymptotic limit. This comparison can also be extended to leaky modes. Figure 4.1 compares the zero and first circumferential order modes of a vacuum filled steel pipe immersed in water to the dispersion curves for a plate that is water loaded on one of its sides. The pipe has an inner radius to wall thickness ratio of 20.0 and all of the modes including torsional and shear horizontal modes have been shown. The solid lines represent the solutions for the plate case, the tightly dashed lines are the axi-symmetric modes, and the loosely dashed lines are the first order flexural modes. In the high frequency - high wavenumber region there is good agreement between the two sets of curves, indicating that they will converge on the same solution as the inner radius becomes infinite. However, as expected, the solutions do differ at locations where the wavelengths are long (generally low frequencies and low wavenumbers),

<sup>†</sup>The properties for titanium were taken to be  $\rho = 4460 \text{ kg/cm}^3$ ,  $c_1 = 6060 \text{ m/s}$ , and  $c_2 = 3260 \text{ m/s}$ , and the material properties for steel were taken to be  $\rho = 7932 \text{ kg/cm}^3$ ,  $c_1 = 5960 \text{ m/s}$ , and  $c_2 = 3260 \text{ m/s}$ .



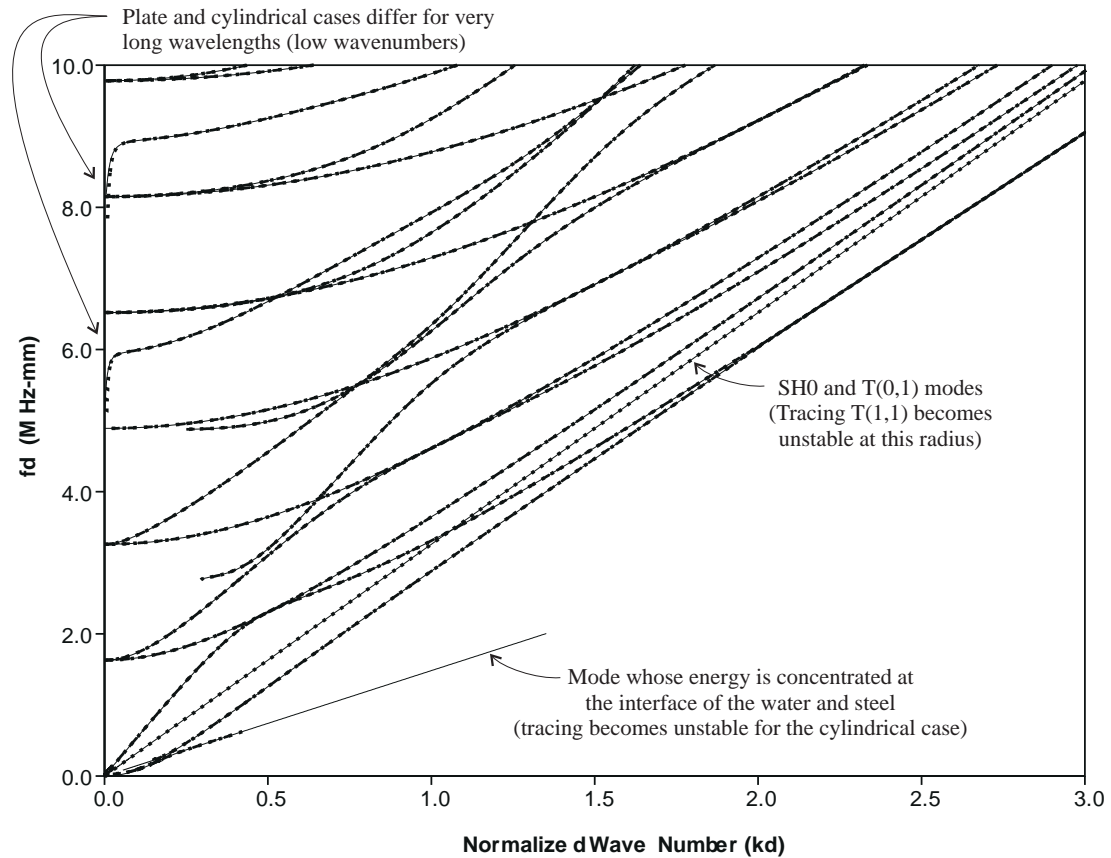


Figure 4.1: A comparison between the wave number dispersion curves for a large radius steel pipe immersed in water and a steel plate that is water loaded on one side. (Solid lines = plate, tightly dashed lines = axi-symmetric modes, loosely dashed line = first order flexural modes)

as discussed in the derivation of a guideline (equation 3.3) for when the pipe and plate cases will differ significantly. Equation 3.3 implies that there will not be good agreement between the plate and pipe case below 0.3 MHz-mm, but at frequencies higher than this value, there may be better agreement. Figure 4.2 zooms in on the low frequency - low wavenumber region of the plot in 4.1. In this figure, it can be seen that the fundamental SH mode in the pipe and the fundamental zero order torsional mode in the pipe behave the same, since in both cases they propagate non-dispersively at the shear velocity of the medium. However, in other modes, there are large differences between the plate case and the pipe case. Differences between the pipe and plate cases in figure 4.1 can also be seen at very low wavenumbers, near the cut-off frequencies of certain modes. This is expected because at these locations the wavelength is very long ( $\text{wavelength} = 2\pi/\xi$ ) and so the modes 'see' the curvature of the pipe. A third noticeable difference is that for a few modes, the plate case was more stable and able to trace modes over a wider range. The greater stability for the plate case is due to the use of exponentials in the solution as opposed to the Bessel functions that are required for the cylindrical model and are less stable with large arguments.

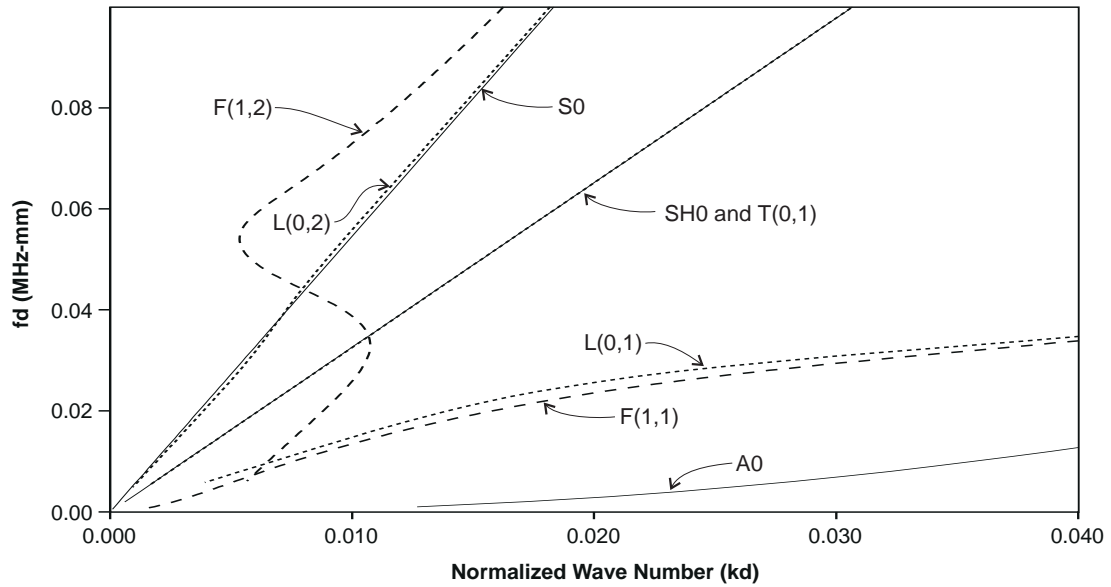


Figure 4.2: The low frequency, low wavenumber region of the wave number dispersion curves for a large radius steel pipe immersed in water and a steel plate that is water loaded on one side. (Solid lines = plate, tightly dashed lines = axi-symmetric modes, loosely dashed line = first order flexural modes)

In addition to the wave number dispersion curves, the attenuation dispersion curves for this large radius case can be compared to the plate case, as shown in figure 4.3. As in the previous figures, the solid lines represent the plate case, the tightly dashed lines are the axi-symmetric modes and the loosely dashed lines are the first order flexural modes. The attenuation for the two cases is quite similar for most of the modes, however at around 6 MHz-mm, the attenuation of the fundamental modes does vary significantly between the two cases; the dispersion curves for the axi-symmetric and first order flexural modes nearly exactly overlay each other, however the curves for the plate case are far away. This difference can be explained by understanding what is happening to the fundamental modes in this region of the dispersion curves. In this region, the fundamental modes are changing from modes that affect the entire wall thickness roughly equally to modes that are tending toward Rayleigh waves. The first flexural mode is tending towards a Rayleigh wave on the inner, unloaded surface and the first longitudinal mode is tending towards a leaky Rayleigh wave on the outer fluid loaded surface. In the transition region, the attenuation is very sensitive to the distribution of the displacement of the mode, since only one side of the pipe is surrounded by water and leaks energy. Therefore, this area will be much more sensitive to very small differences between the pipe and plate case than a simple wavelength analysis would indicate. Although the dispersion curves in figures, 4.1, 4.2, and 4.3 have been created using the isotropic model, the same results are obtained when the dispersion curves are calculated using isotropic constants in the transversely isotropic model.

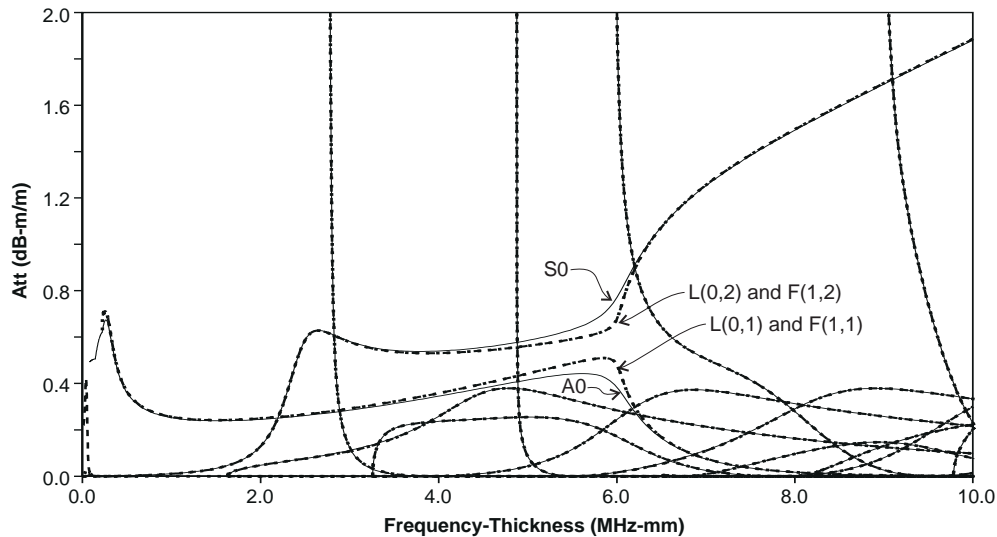


Figure 4.3: A comparison between the attenuation dispersion curves for a large radius steel pipe immersed in water and a steel plate that is loaded with water on one side. (Solid lines = plate, tightly dashed lines = axi-symmetric modes, loosely dashed line = first order flexural modes)

## 4.2 Validation against Published Literature on Cylindrical Wave Propagation

As highlighted in section 2.2, there has been a great deal of work on isotropic cylinders in vacuum as well as a significant amount of work on cylinders that are embedded in other media. This section compares some of these published results to the results obtained from the cylindrical wave propagation model developed in this thesis.

The first results that will be used for comparison are the results published by Gazis in 1959[24] for the axi-symmetric and flexural modes of an homogeneous hollow isotropic cylinder. Results obtained by Nagy[31] and Nayfeh and Nagy[37] will be used to validate the transversely isotropic and isotropic model for systems that are immersed in water and embedded in a solid half-space. Finally the leakage of flexural modes in a transversely isotropic cylinder that is immersed in water will be validated against results obtained by Berliner and Solecki [32]. Each of these publications uses a different method to solve the wave propagation problem, therefore their combination forms a good set against which to validate the model.

### 4.2.1 Gazis

Gazis' 1959 derivation of the wave propagation solutions for a hollow cylinder [4] forms the basis of the wave propagation solution developed in this thesis for isotropic materials. To ensure that our solution, which uses the general purpose cylindrical wave propagation solution, matches the results that Gazis

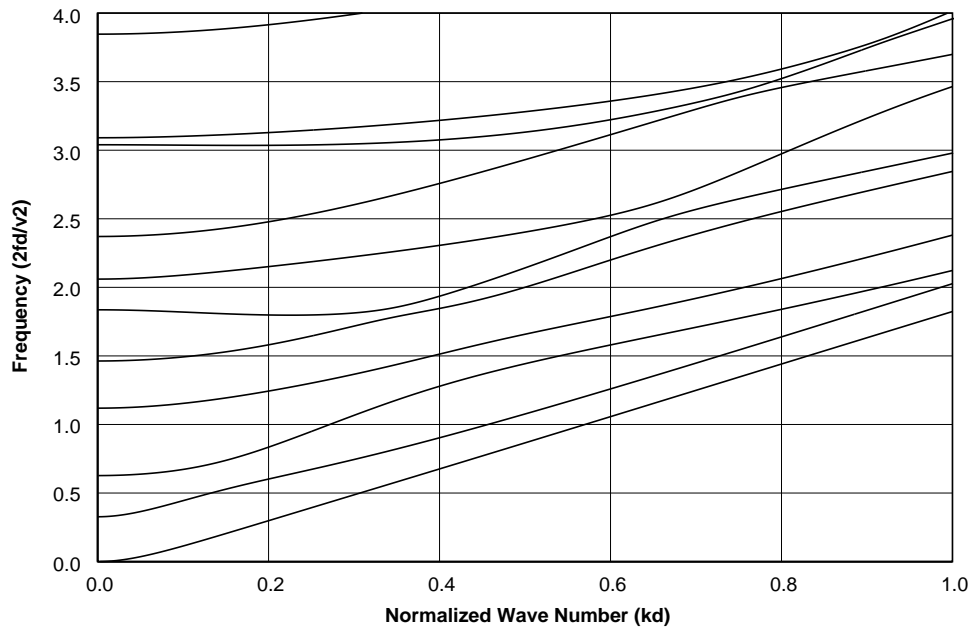


Figure 4.4: The normalised frequency ( $fd/(2v_2)$ ) versus the normalised wavenumber ( $kd$ ) for the first circumferential order modes of a hollow cylinder consisting of a single isotropic layer which has a Poisson's ratio of 0.30 and a thickness ( $d$ ) to mean radius ratio of 1.0. (equivalent to (Gazis 1959) fig. 4)

found, three of his figures have been recreated and compared to the dispersion curves that he shows. These figures are described below.

Figure 4.4 uses Disperse to reproduce the results shown in figure 4 of Gazis[24]. The dispersion curves in this figure show the first circumferential order modes of a hollow cylinder consisting of a single isotropic layer which has a Poisson's ratio of 0.30 and a thickness to mean radius ratio of 1.0. Since the frequency axis has been normalised by multiplying by the thickness and dividing by the shear velocity, the solution only depends on the Poisson's ratio. The solutions are independent of the density and the shear velocity. The wavenumber axis has been normalised by multiplying by the thickness. These normalisations are the same as Gazis uses. By comparing figure 4.4 with figure 4 of Gazis' paper, it is revealed that Gazis' solutions and the solutions calculated by the wave model explained in this thesis are the same to the tolerance that can be read from the published graphs.

Figure 4.5 recreates figure 5 of Gazis[24], which is the same case as the previous figure except that the ratio of the thickness to the mean radius has changed. Again the solutions found by Gazis and those found by the wave model developed in this thesis are equivalent to the tolerance that can be read from the published graphs.

Figure 4.6 recreates figure 7 of Gazis[24], which shows the detail of the three lowest first circumferential order and second circumferential order modes of a large radius hollow cylinder, with a Poisson's ratio

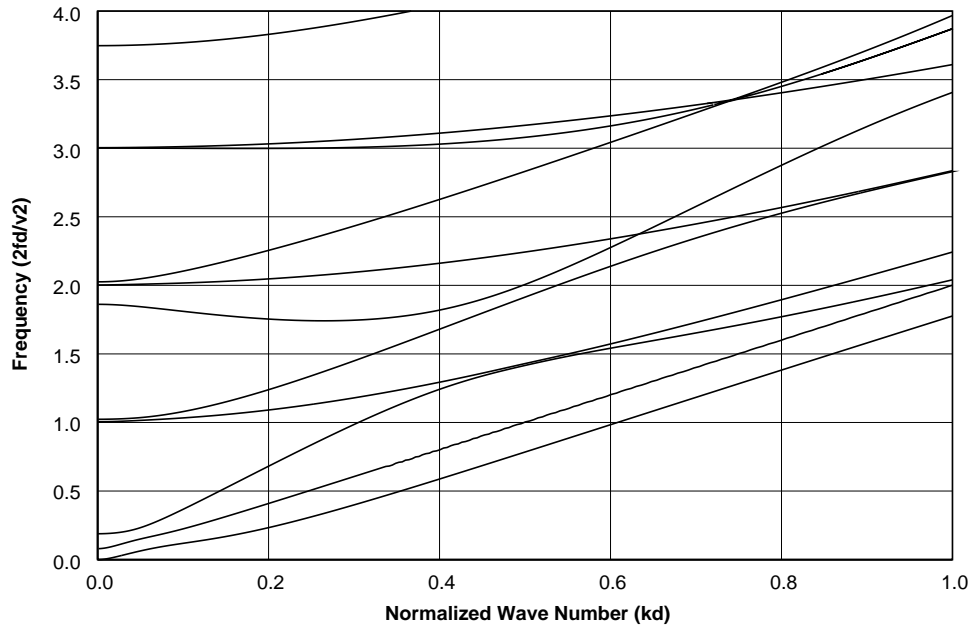


Figure 4.5: The normalised frequency ( $fd/(2v_2)$ ) versus the normalised wavenumber ( $kd$ ) for the first circumferential order modes of a hollow cylinder consisting of a single isotropic layer which has a Poisson's ratio of 0.30 and a thickness ( $d$ ) to mean radius ratio of  $1/4$ . (equivalent to (Gazis 1959) fig. 5)

of 0.30 and a thickness ( $d$ ) to mean radius ratio of  $1/30$ . For a cylinder with such a large radius to thickness ratio, the first and second order solutions only vary significantly in this region near the origin. The solutions found by Gazis and those found by the wave model developed in this thesis are the same (except that Gazis reverses the line types for the first and second circumferential order non-fundamental modes).

#### 4.2.2 Nagy and Nayfeh

Nagy has derived expressions for axi-symmetric wave propagation in transversely isotropic rods that are immersed in a liquid[31], which can be used to validate the model developed in chapter 2. Working with Nayfeh, Nagy expanded his wave propagation solution to handle multiple layers and leakage into solid materials[37] by using the transfer matrix method. To help validate the wave propagation model developed in this thesis, the results obtained from Disperse will be compared to the results presented in these two papers. In Nagy's derivation, the wave displacements are found by solving Christoffel's equation for transversely isotropic materials. Since this approach differs from the derivative of potentials method that Mirsky[5] uses (and which the transversely isotropic derivation in this thesis is based upon), these solutions provide valuable independent validation information.

For easier comparison between the solutions, Nagy's analytical solution for a single layer transversely isotropic rod in a liquid[31] was implemented in software. This implementation is used in the following

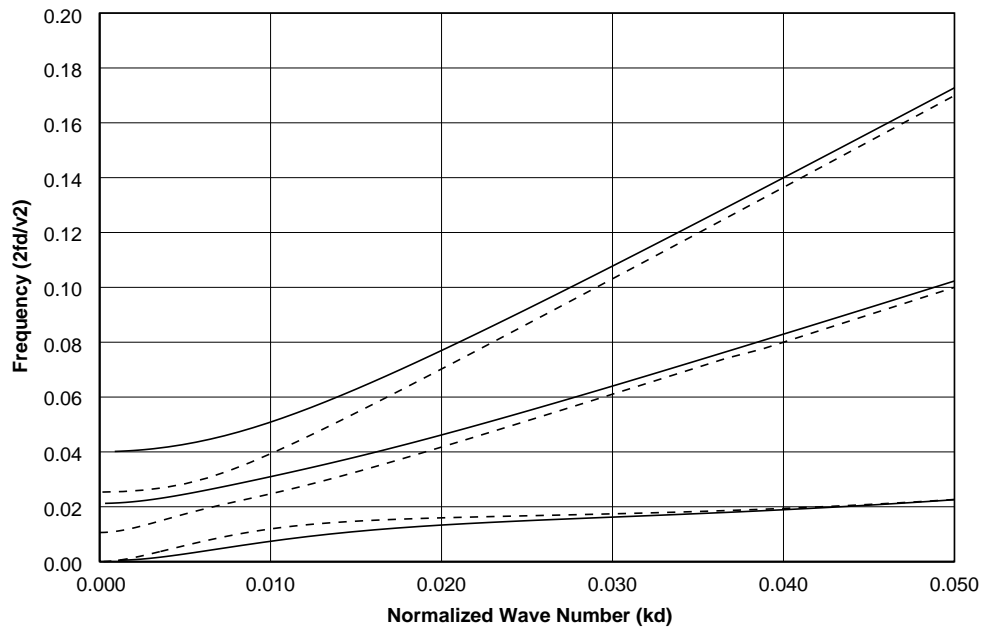


Figure 4.6: Detail of the three lowest first circumferential order (dashed) and second circumferential order (solid) modes near the zero frequency - wavenumber origin for a hollow cylinder consisting of a single isotropic layer which has a Poisson's ratio of 0.30 and a thickness ( $d$ ) to mean radius ratio of 1/30. (equivalent to (Gazis 1959) fig. 7)

figures for comparison. Figure 4.7 shows the dispersion curves for a 1 mm radius steel bar immersed in water. Three sets of dispersion curves are overlaid on this figure. Solid lines represent the solutions obtained with the isotropic model that is developed in chapter 2. The tightly dashed lines, which lie directly under the solid lines, represent the solutions when isotropic material properties were inserted into the transversely isotropic model (also developed chapter 2). The third set of lines (loosely dashed) are the results using the analytical solution of Nagy. All three of the solutions lie on top of each other within the precision of the solution routines. Similarly, figure 4.8 shows the overlay of two sets of dispersion curves for a 1 mm radius uni-directional graphite epoxy rod immersed in water. In this figure, the solid line represent the solution obtained with the transversely isotropic model developed in this thesis and the dashed lines represent the analytical solution of Nagy. Again, the two solutions lie on top of each other.

A 1996 paper by Nayfeh and Nagy[37] expanded on the analytical solution for a transversely isotropic rod that Nagy derived so that waves in multilayered rods which leak into solid materials could be modelled using a transfer matrix method. In this paper, Nayfeh and Nagy apply their wave propagation model to a typical metal matrix composite problem, a Carbon - Silicone carbide (SCS) fibre that is embedded in a solid titanium matrix. Their results can be compared to the zero circumferential order (axi-symmetric) results presented for this same case in sections 3.1.3 and 3.3.2 (figures 3.3(a), 3.15, and 3.21) for validation of the axi-symmetric leaky modes. Figure 3.3(a) mimics figure 3 of Nayfeh and Nagy[37], the dispersion curves for a free SCS fibre overlaid on the curves for a free SCS fibre when

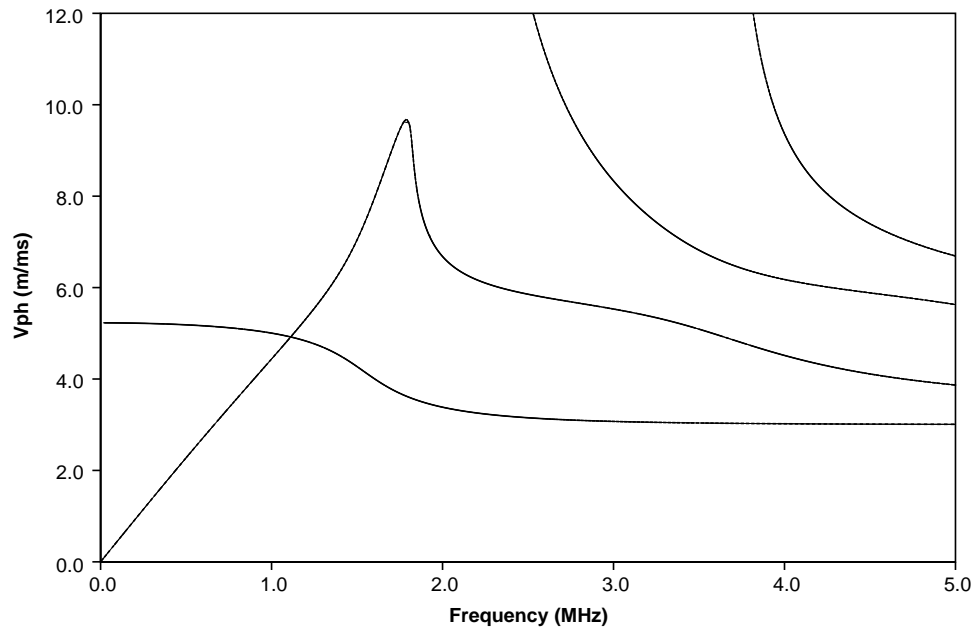


Figure 4.7: Phase velocity dispersion curves for a 1 mm radius steel bar in water. Three sets of solutions have been overlaid; solid lines = isotropic solution, tight dashed lines = anisotropic solution, loosely dashed lines = Nagy's analytical solution. The dashed lines cannot be seen because all three curves overlay each other very well.

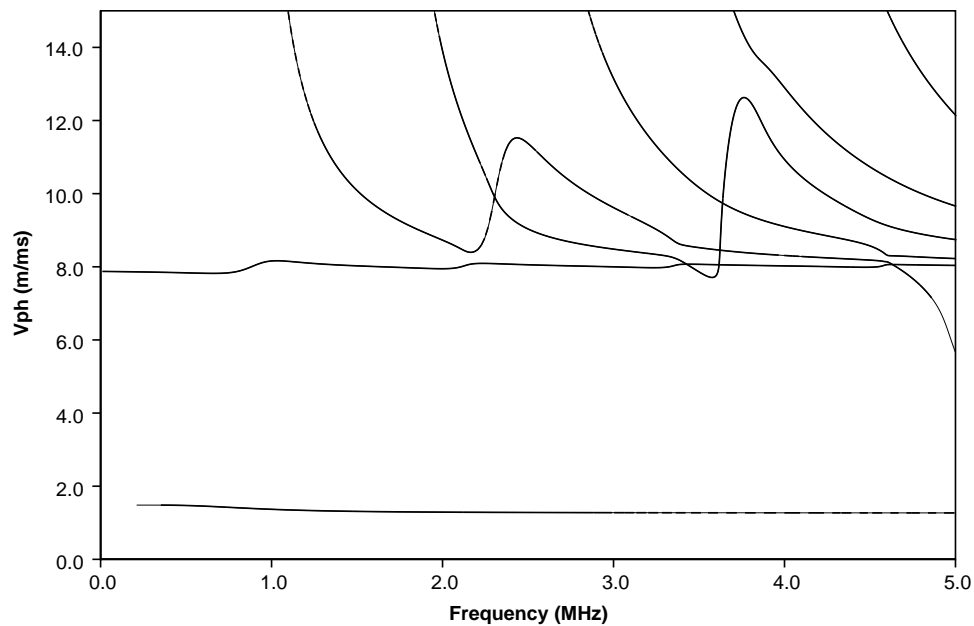


Figure 4.8: Phase velocity dispersion curves for a 1 mm radius graphite reinforced epoxy rod immersed in water. Two sets of solutions, which lie directly on top of each other, have been plotted; solid lines for the anisotropic solution and loosely dashed lines for Nagy's analytical solution.

isotropic properties are assumed for the constituents of the fibre. No difference can be detected between Nayfeh and Nagy's results and the results obtained in this thesis. The quoted values for low-frequency asymptotic value of the phase velocity of the lowest-order axi-symmetric mode (11 126 m/s for the isotropic fibre and 11 440 m/s for the transversely isotropic one) agree with results obtained in figure 3.3(a) to all five quoted significant digits. There is also excellent visual agreement between the solutions for a perfectly bonded embedded SCS fibre that is shown in figure 3.15 and figure 6 in Nayfeh and Nagy. For the third case, an embedded fibre with an imperfect bond to the surrounding matrix, there is a slight difference. This difference is due to different methods of modelling the imperfect boundary. Nayfeh and Nagy use a finite interfacial stiffness model [68–70] to model the imperfect fibre-matrix boundary, however the results in figure 3.21 were calculated by inserting a thin layer, which has degraded properties, between the outside of the fibre and the surrounding matrix. Because these two different methods were used, precisely comparable results cannot be obtained. However, the resulting dispersion curves are very similar.

### 4.2.3 Berliner and Solecki

A third group of cases will be used to validate the flexural (non-axi-symmetric) modes in a cylinder. For comparison, we will use the recent papers by Berliner and Solecki [32,36], which discuss the first circumferential order modes in a nylon reinforced rubber cylinder whose thickness to inner radius ratio was 1:4. Three cases are examined, a hollow cylinder, a fluid filled cylinder, and a fluid filled cylinder that is immersed in a fluid. The method that Berliner and Solecki have used to solve the wave propagation problem in cylindrical transversely isotropic materials is based on the same paper by Mirsky[5] as the wave propagation model in chapter 2.

Using the material properties given in the appendix of reference [36] (and repeated in table 3.2), the three cases that Berliner and Solecki considered were repeated with the wave model developed in this thesis. To compare results, figure 4.9 mimics figure 4 of Berliner and Solecki. In these figures, the dashed lines represent the solution when the transversely isotropic cylinder is hollow inside and outside. The solid lines represent the case when the cylinder is filled with water. Both the axes have been normalised by the thickness of the cylinder. The frequency axis has also been normalised by dividing by the shear velocity in the cylinder. There is good agreement between the solutions obtained by Berliner and Solecki and the solutions obtained by the model developed here. There are two additional modes shown in figure 4.9 that are not shown in figure 4 of Berliner and Solecki, since they have chosen to only show the lowest 3 flexural modes, instead of all of the modes in the frequency - wavenumber range.

There is also good agreement for the third case, a fluid filled cylinder that is also immersed in water. Figure 4.10 can be compared to figure 5 of Berliner and Solecki to study this case. In both figures, the solid lines represent the solutions for the filled and immersed cylinders, while the dashed lines represent the solution to the fluid filled case. Except for the better resolution of the curves and the



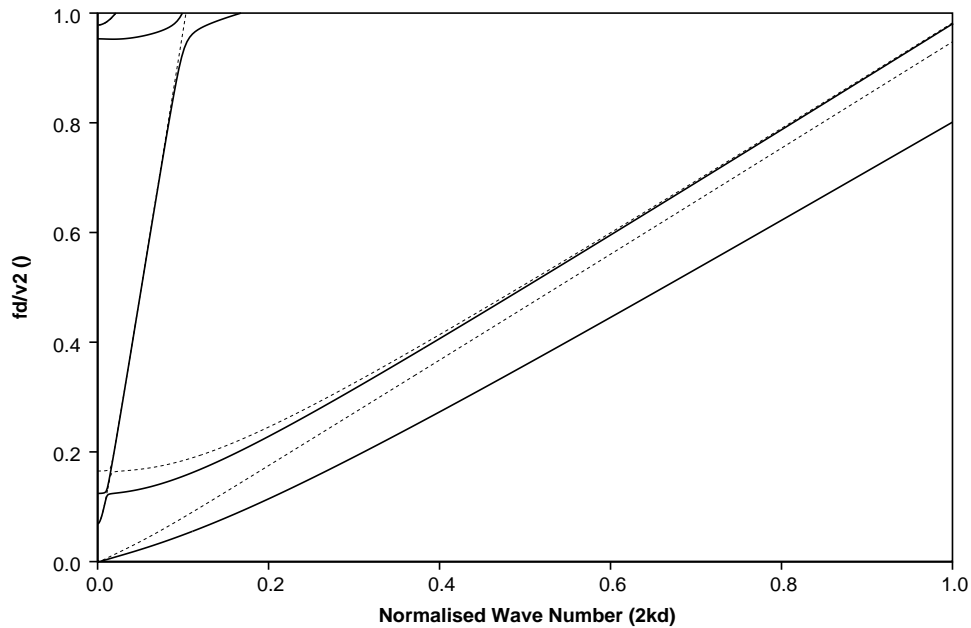


Figure 4.9: Comparison of dispersion curves for a hollow (dashed lines) and fluid filled (solid lines) transversely isotropic cylinders (equivalent to Berliner and Solecki figure 4).

additional modes that are included in figure 4.10 the solutions agree to the precision that can be read from published figure.

### 4.3 Internal Consistency of Solutions

This section examines the internal consistency of the wave propagation solutions. A primary criterion for internal consistency is that different, but equivalent systems should yield the same results. For example, the same result should be found when an individual layer is replaced by a series of layers of identical material properties whose total thickness is the same as the original layer. The solutions should be consistent whether the isotropic solution is used or whether the transversely isotropic solution is used with isotropic stiffness constants. The mode shapes also provide an effective method of checking the internal consistency of the solutions. When multiple layers are added (or transversely isotropic ones replace equivalent isotropic ones), the mode shapes should stay constant. In addition, for cases when there is no attenuation, the energy velocity should be equal to the group velocity[71]. These internal consistency checks frequently provide an effective and quick method of locating problems in the wave propagation model.

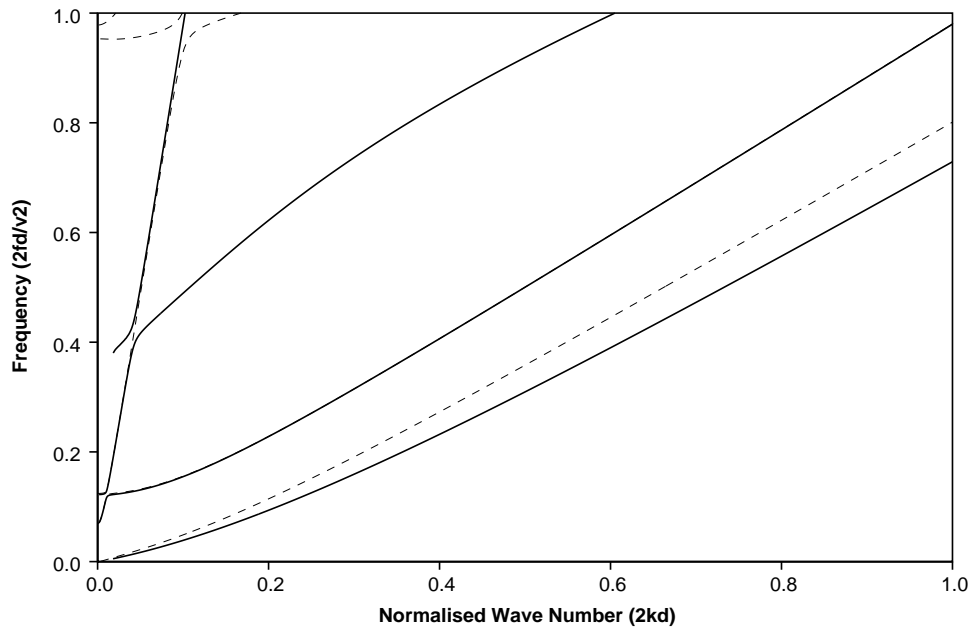


Figure 4.10: Comparison of dispersion curves for fluid filled (dashed lines) and fluid filled immersed (solid) transversely isotropic cylinders (equivalent to Berliner and Solecki figure 5).

### 4.3.1 Multiple Layers

The wave model that was developed in chapter 2 allows arbitrary multi-layered cylindrical systems to be modelled. The only limit on the number of layers that can be modelled is the size of the global matrix and the time that it will take to calculate its determinant. This sub-section uses the multi-layered nature of the model to validate itself. Individual layers are replaced by a series of thinner layers whose total thickness is the same as the initial layer and whose material properties are the same. For isotropic materials, some of these new layers are defined as transversely isotropic layers with isotropic stiffness constants to cross validate the two solution types.

The first system that will be shown for this validation is an isotropic version of a water immersed SCS fibre, which consists of a 16.5 micron carbon core surrounded by a 53.5 micron thick silicone carbide sheath. This system provides a good validation case for several reasons. First, the case has already been discussed in previous validation cases, since Nayfeh and Nagy have published literature on this case. More importantly, however, this system is chosen because it has the potential to detect a wide range of problems. The inner core, the internal layers, and the surrounding material are all handled slightly differently when the global matrix is formed, therefore all three types of solutions should be included for validation. Two different solid materials are included, which ensures that the scaling of stresses and displacements is not material dependent. A fluid layer is included to ensure that the fluid layer matrix is consistent with the solid layer matrices. The material properties that were used for the modelling of this case are in tables 3.1 and 3.2. Please note that the anisotropic stiffness constants for the isotropic

materials are slightly different than those given in Nayfeh and Nagy so that they exactly match the wave speeds that were used in the isotropic portion of the model.

Figure 4.11 shows the real wavenumber and attenuation dispersion curves for the SCS fibre described above immersed in water. The thinner solid lines represent the solution when each of the constituents is modelled as a single layer. The dashed lines represent the solution when the carbon core is modelled as two layers, one 6.5 microns thick and one 10 microns thick, and the silicone carbide sheath is modelled as three layers, 30, 25, and 8.5 microns thick. All of the phase velocity dispersion curves have been truncated to show only the portions with attenuations less than 3 dB-m/m (attenuation normalised to the fibre thickness). As can be seen by the figure, the dispersion curves lie on top of each other. The maximum differences detected are within the tolerance of the solution.

The following figure, figure 4.12, displays the dispersion curves for the same system. However, in this figure, the solid lines represent the solution when half of the six constituent layers are actually defined as transversely isotropic materials. All of the dispersion curves have been truncated to only show the portions with less than 3 dB of normalised attenuation. Once again the two sets of solutions are identical within the precision to which the curves have been traced.

### 4.3.2 Mode Shape Consistency

When using the global matrix method, it is relatively simple to implement a routine that will display the distribution of various displacements and stresses through the thickness of the system. The display of this 'mode shape' provides a lot of information about the wave propagation solutions that the dispersion curves alone cannot convey. In addition, the mode shapes provide an effective means of validating whether the wave propagation solutions are correct. An initial simple validation involves evaluating if the mode shapes change as layers are divided into sub - layers which have the same total thickness, even if the anisotropic layer matrices are combined with the isotropic ones. In addition, more sophisticated calculations of energy density and energy velocity can be calculated by integrating products of components of the mode shapes. When there is no attenuation, the energy velocity should be equal to the group velocity[71], which is calculated as a derivative of the wavenumber dispersion curves. If these two values match, the solution is probably valid.

**Mode Shape Consistency For Multi-layered Systems** The previous section searched for differences in the phase velocity and attenuation dispersion curves between the solutions obtained when an immersed SCS fibre was defined as three isotropic layers and when it was broken into a series of six sub-layers which combined the isotropic and anisotropic model formulation. The same validation process can be extended to the mode shapes, which describe how various properties of the mode change through the thickness of the system. Throughout the solution range, there is good agreement between the mode shapes of the single and multiple layer systems. The comparison for two example locations,

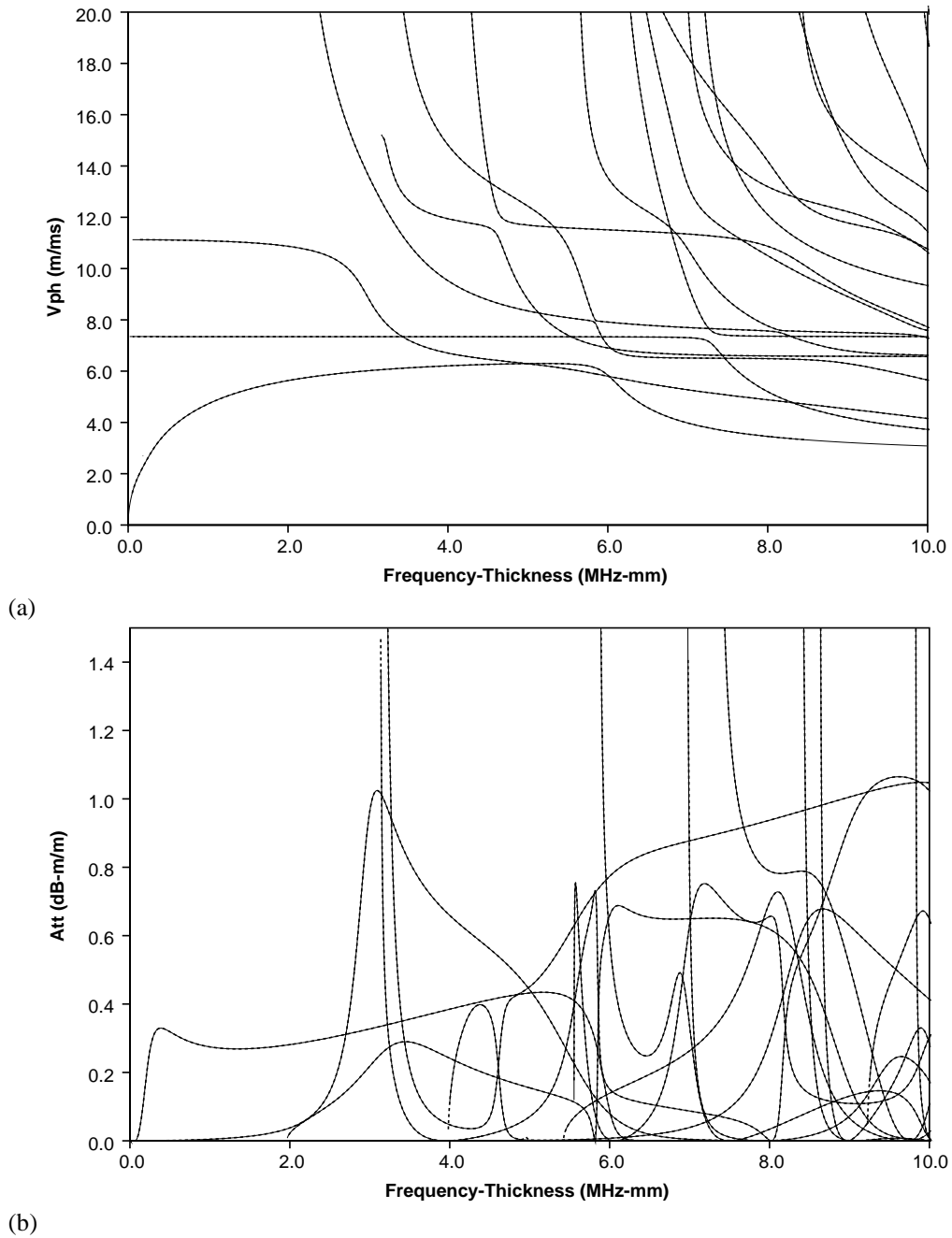


Figure 4.11: Comparison of dispersion curves for an immersed SCS fibre when each constituent layer is modelled as a single layer (thin solid lines) and when each constituent layer is divided into sub layers (thicker dashed lines). As expected, the agreement between the two solutions is excellent.

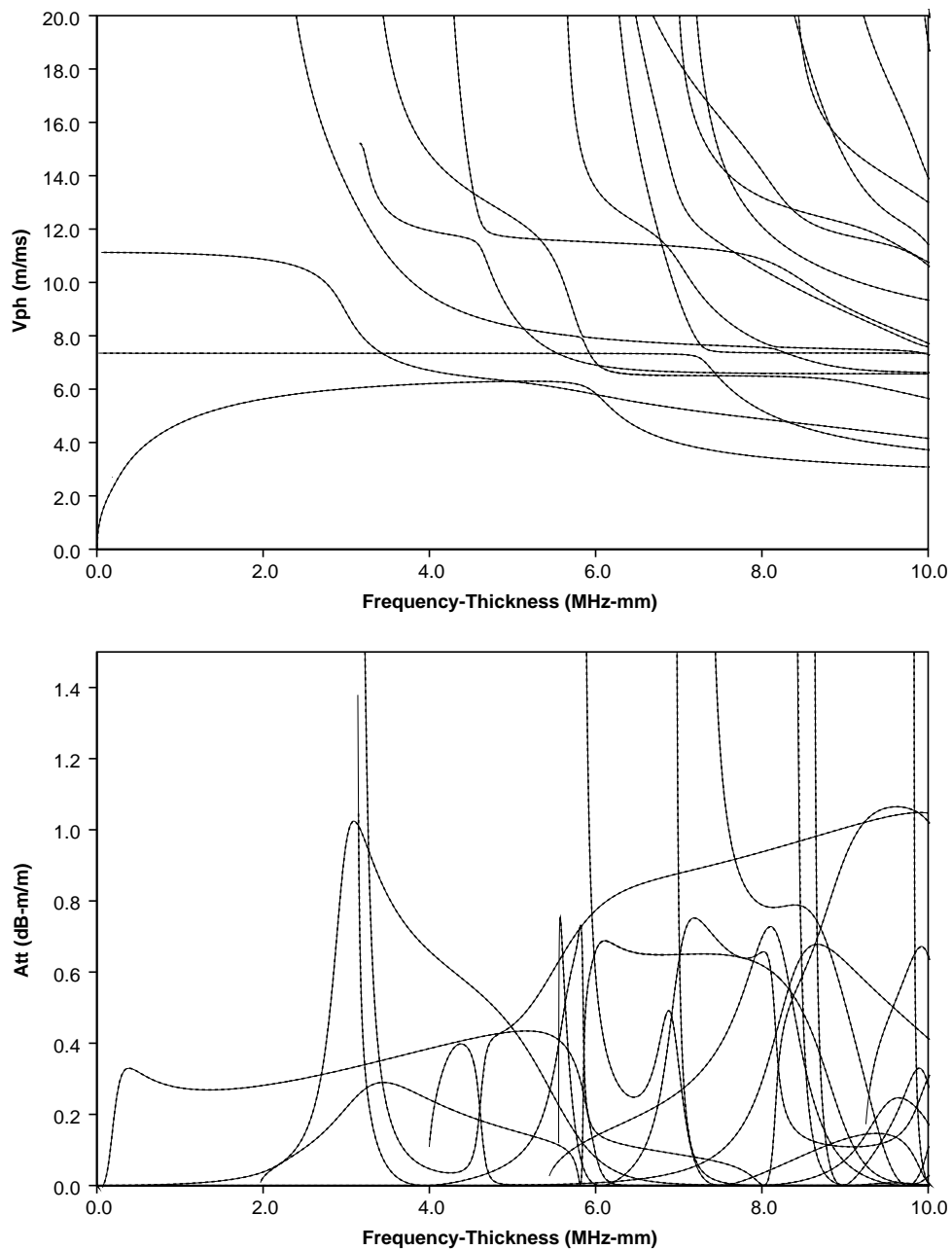


Figure 4.12: Comparison of dispersion curves for an immersed SCS fibre when all of the layers use the isotropic model (thicker dashed lines) and when half of the sub-layers use the transversely isotropic model.

marked (a) and (b) on the dispersion curves in figure 4.13, are shown in figure 4.14. Point (a) is on the longitudinal mode, L(0,3), at 8.4 MHz-mm (120 MHz) and point (b) is on the flexural mode, F(1,2), at 4.2 MHz-mm (60MHz). In this figure, the thin solid lines represent the mode shape components when the system is treated as three isotropic layers and the dashed lines correspond to the components when the system consists of a combination of six isotropic and anisotropic layers. The radial and axial displacements are shown for both points, however the circumferential displacement is only shown for the flexural mode, since it is identically zero for the axi-symmetric mode on which point (a) lies. The consistency of the stresses and strains that are not shown in figure 4.14 can be evaluated by examining the consistency of the strain energy density, which is calculated as the dot product of the strains and stresses (see equation 2.79). There is good agreement between the mode shapes that were calculated using the two different, but equivalent, systems. No discontinuities can be detected at the boundaries between an isotropic layer and an anisotropic layer that has equivalent material properties. Small differences between the two sets of mode shapes can be attributed to quite small inaccuracies that are introduced into the wave propagation solutions when the value for the desired frequency is interpolated between two known roots. In addition to agreeing with each other, the mode shapes seem logical. For example, the radial displacement component is continuous through all of the material changes, as specified in the boundary conditions. The axial component is continuous across solid-solid boundaries, but can be discontinuous at solid-liquid boundaries. The circumferential displacement is identically zero for the longitudinal mode (for which the torsional modes are decoupled), but exists for the flexural mode (for which the circumferential motion is coupled to the radial and axial motion). In the fluid, which cannot support shear, the circumferential motion becomes zero. In Cartesian systems, one would expect the strain energy density to increase in the fluid as radial distance increases for leaky modes such as this one. However, for a cylindrical system, this effect is counteracted by the spread in the energy over a larger circumference as the radius increases. This effect acts as  $1/r$ , and can cause the strain energy density to decrease even as the total energy increases, as in these cases.

**Energy Density Calculation** The energy that is contained in a mode as it propagates can be divided into two types, potential energy and kinetic energy [39]. For a propagating mode, the potential energy is called the strain energy (SE) and is calculated as half the integral of the strain dotted with the stress over the area normal to the propagation distance (S),

$$\mathbf{SE} = \frac{1}{2} \int_{\mathbf{S}} \boldsymbol{\epsilon} \cdot \boldsymbol{\sigma}, \quad (4.2)$$

which for a cylinder can be expanded as (see equation 2.79),

$$\begin{aligned} \mathbf{SE} = & \int_{r=0}^{r=\infty} \int_{\theta=0}^{\theta=2\pi} \frac{1}{2} \left\{ \sigma_{rr} \frac{\partial u_r}{\partial r} + \sigma_{\theta\theta} \left( \frac{1}{r} \frac{\partial u_\theta}{\partial \theta} + \frac{u_r}{r} \right) + \sigma_{zz} \left( \frac{\partial u_z}{\partial z} \right) \right\} \\ & + \frac{1}{4} \left\{ \sigma_{rz} \left( \frac{\partial u_r}{\partial z} + \frac{\partial u_z}{\partial r} \right) + \sigma_{r\theta} \left( r \frac{\partial}{\partial r} \left( \frac{u_\theta}{r} \right) + \frac{1}{r} \frac{\partial u_r}{\partial \theta} \right) + \sigma_{\theta z} \left( \frac{\partial u_\theta}{\partial z} + \frac{1}{r} \frac{\partial u_z}{\partial \theta} \right) \right\} d\theta dr. \quad (4.3) \end{aligned}$$

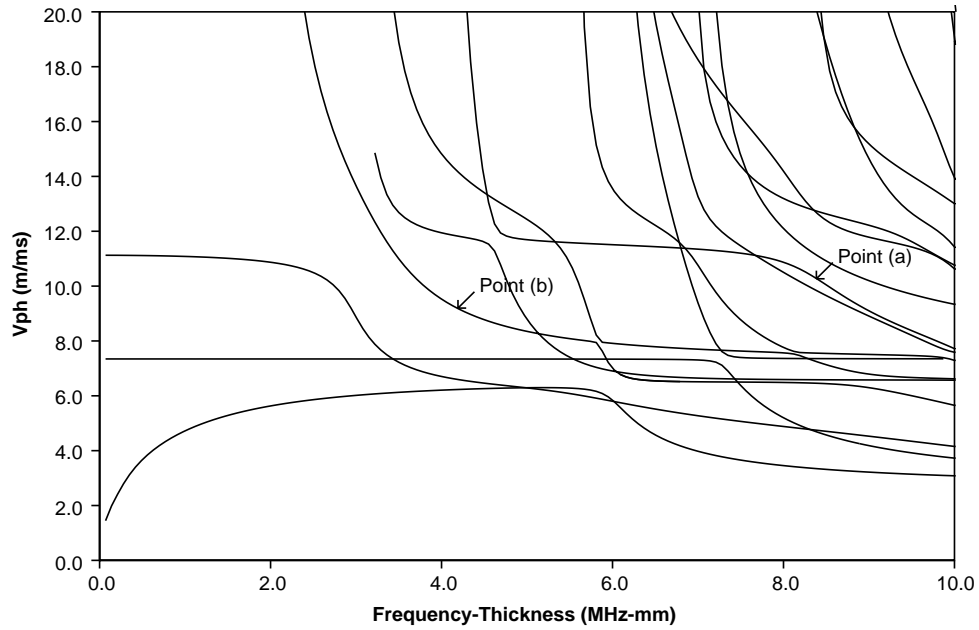


Figure 4.13: Dispersion curves for an immersed SCS fibre showing the locations used for the mode shape calculations in the following figures.

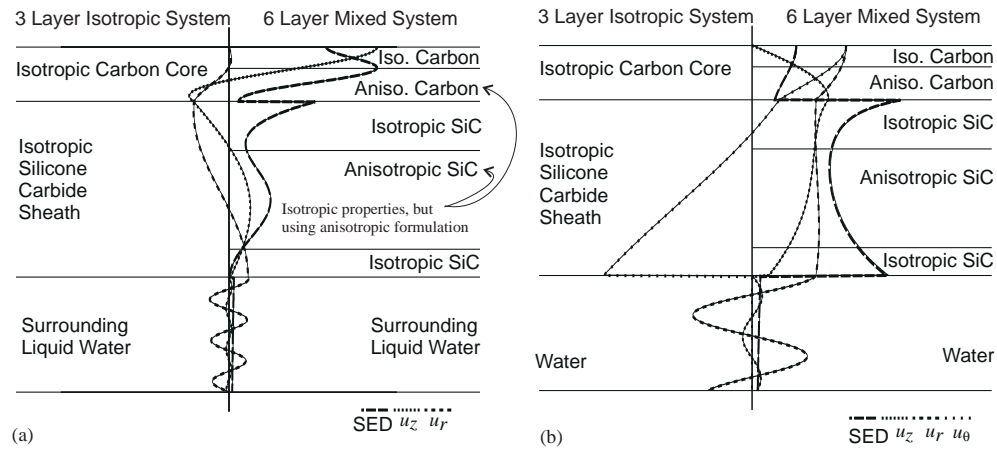


Figure 4.14: Comparison of the mode shapes for an immersed SCS fibre when the system is defined as 3 isotropic layers (solid lines) and when the system is defined with the same materials but as a combination of isotropic and anisotropic layers (dashed lines) for two points on the dispersion curves, (a) the L(0,3) mode at 8.4 MHz-mm and (b) the F(1,2) mode at 4.2 MHz-mm.

The kinetic energy (KE) can be expressed as

$$\mathbf{KE} = \frac{\rho}{2} \int_{\mathbf{S}} v \cdot v, \quad (4.4)$$

where  $v$  is the velocity. For a cylinder, this expression can be expanded as,

$$\mathbf{KE} = \frac{\rho}{2} \int_{r=0}^{r=\infty} \int_{\theta=0}^{\theta=2\pi} [v_r^2 + v_\theta^2 + v_z^2] d\theta dr. \quad (4.5)$$

During a cycle, energy will be converted between these two forms of energy, however the total energy stored should always be same. In addition, the total kinetic energy integrated over a cycle should be equal to the total strain energy integrated over a cycle [39]. This balance can provide a further validation of whether the mode shapes, and by extension the dispersion curves, are valid.

The balance between the kinetic and strain energy only strictly holds when the mode shape is integrated through the entire thickness. When the system is surrounded by vacuum, this is a relatively simple procedure, since there will be no energy contained in the vacuum half-space and the limits of integration become finite. However, it is more difficult for leaky systems which contain energy in the surrounding infinite half-space. Therefore, the validation cases presented in this section are limited to free cases. The first case is a solid aluminium cylinder, that has been divided into isotropic and anisotropic sub layers. Using forty integration points per layer for a three layer mixed system, the maximum error for all of the zero and first circumferential order modes below 5.0 MHz-mm frequency-thickness is about 0.1 percent, where the error has been measured as one minus the ratio of the strain energy to the kinetic energy,  $1 - \mathbf{SE}/\mathbf{KE}$ . This error is mainly due to the crude method of integration through the thickness. If the total number of integration points is increased from 120 to 280 by using a seven layer system with 40 points per layer, the maximum error falls to less than one one-hundredth of a percent (0.0001), with an average error less than  $2.0e-5$ , however the calculation takes a significantly longer time. The strain energy to kinetic energy ratios for these two cases are shown in figure 4.15. From this figure, it can be clearly seen that the error increases at higher frequencies as the mode shape changes more rapidly and the integration routine become less accurate. Similar good agreements are also obtained for multi-layered structures with layers of different properties, such as a free SCS fibre.

To put these differences into perspective, if one of the strains, for example  $\sigma_{zz}$ , in the three layer bar case is halved, the maximum error is over 40 percent and the average error is over 10 percent. The very small difference observed between the total strain energy and the total kinetic energy shows that the calculated mode shapes are internally consistent, and therefore, the wave propagation solutions are most likely valid.

**Energy Velocity Calculation** The previous section examined the energy that is stored in the structure as the mode passes. The energy that flows through the structure can also be evaluated [39]. This quantity of energy, which is called the power flow, can be divided by the stored energy to determine the energy



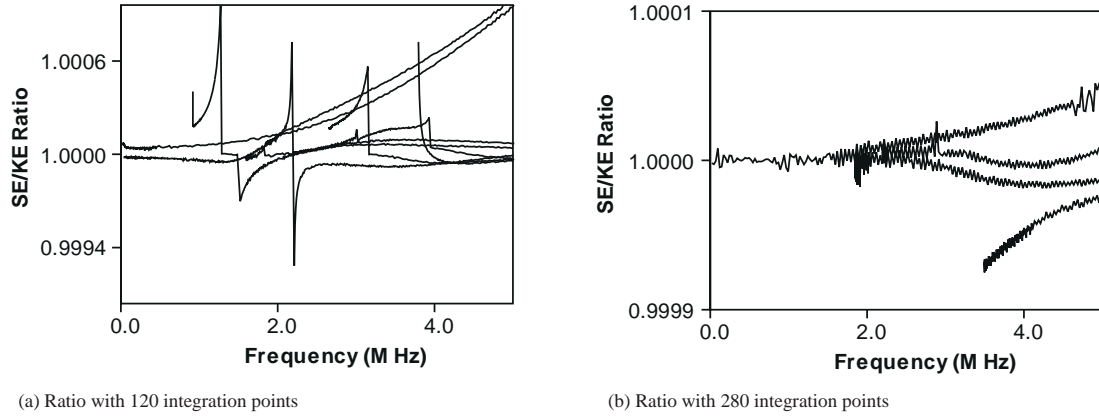


Figure 4.15: The ratio of the strain energy to the kinetic energy for a (a) 3 layer system with 120 integration points (zero and first order modes) and a (b) 7 layer system with 280 points (zero order modes only).

velocity, which is how fast the energy propagates along the structure. For a mode in a free isotropic system, the energy velocity is exactly equal to the group velocity, which is calculated as a derivative of the wavenumber dispersion curves[71,39]. Since there are two relatively independent methods of calculating the energy velocity for a free isotropic system, one that relies on the mode shapes and one that relies on the derivative of the dispersion curves, the internal consistency of the solutions can be effectively checked.

The power flow is expressed as the dot product of the velocity and stress vectors,

$$P = v \cdot \sigma, \quad (4.6)$$

where  $v$  is the velocity and  $\sigma$  is the stress. Therefore, the power flow in the axial direction,  $\hat{z}$  is,

$$P_z = v_z \sigma_{zz} + v_r \sigma_{rz}. \quad (4.7)$$

To obtain the total power flow, the previous expression can be integrated through the cross section perpendicular to the propagation direction and averaged over a cycle to give the average total power flow,  $\langle \mathbf{P} \rangle$ ,

$$\langle \mathbf{P} \rangle = \int_{r=0}^{r=\infty} \int_{\theta=0}^{\theta=2\pi} [v_z^* \sigma_{zz} + v_z \sigma_{zz}^* + v_r^* \sigma_{rz} + v_r \sigma_{rz}^*] d\theta dr, \quad (4.8)$$

where the \* superscript refers to the complex conjugate of the quantity. (The averaging over a time cycle is performed by the use of the complex conjugate of some of terms in the expression.) The velocity of the energy that is carried by a mode can be obtained by dividing this power flow by the sum of the strain energy and the kinetic energy that is stored as the mode passes.

It is well known that for an unattenuated mode in an isotropic structure, the energy velocity is equal to the group velocity[39]. The group velocity is calculated as a derivative of the dispersion curves of a

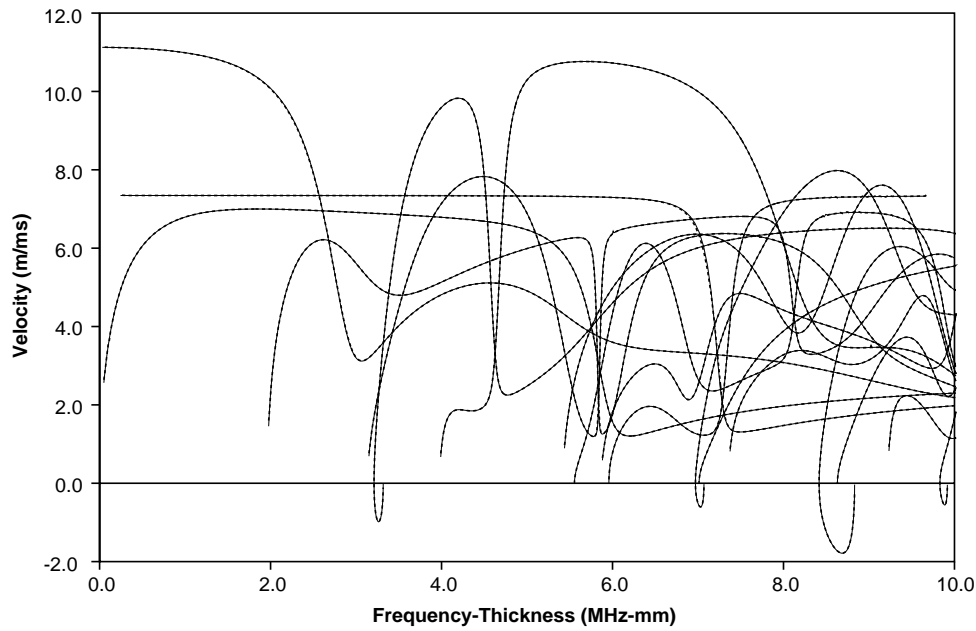


Figure 4.16: A comparison between the group velocity (dashed lines) and energy velocity (solid lines) dispersion curves for a free isotropic SCS fibre. The average difference between the two cases is less than 0.1 percent.

mode,

$$v_{gr} = \frac{\partial \omega}{\partial \xi}, \quad (4.9)$$

where  $\omega$  is the circular frequency and  $\xi$  is the wavenumber in the direction of propagation. The derivation of this expression, which can be found in reference [39] and other texts on guided waves, is based on the creation of a modulated wave by taking two waves with slightly differing values of frequency and wavenumber.

Figure 4.16 compares the group velocity and the energy velocity dispersion curves for a free isotropic SCS fibre, that consisted of 2 carbon layers and 3 silicone carbide layers, some of which were calculated by the isotropic model and some by the transversely isotropic model. The agreement between the two sets of curves is good. Although the maximum difference is as high as 2 percent the average error is less than 0.1 percent. These error values are due to noise in the numerical differentiation routines which calculate the derivative,  $\partial \omega / \partial \xi$ . When the energy and group velocities are compared for the multi-layered aluminium bar, the average error is also below 0.1 percent. This high level of agreement further confirms that the wave propagation model solutions are valid.

The correlation between the group velocity and the energy velocity is only valid when there is no attenuation in the system. Therefore, this comparison cannot be used to validate the model in leaky systems. However, if the model is correct, the calculated energy velocity should be physically possible. The group velocity and energy velocity cases for two leaky cases, an SCS fibre immersed in water and an SCS fibre

embedded in a titanium matrix are considered in figures 4.17 and 4.18. As can be seen in figure 4.17, for most of the modes in the immersed system, the group velocity closely approximates the energy velocity. However, there are large discrepancies when the imaginary part of the wavenumber (the attenuation) is much greater than the real part of the wavenumber ( $\omega/v_{ph}$ ). In this high attenuation region, the group velocity dispersion curves become very erratic, jumping from very high positive group velocities to very low negative group velocities. Therefore, these regions were truncated for the plotting of the figure. The energy velocity calculation does not have this limitation and could be reliably calculated for all of the regions of dispersion curves. Figure 4.17 shows that in the areas dominated by the attenuation where the group velocity calculation breaks down, the energy velocity is dying away to zero. This behaviour agrees with physical expectations of the system, since these regions correspond to the non-propagating modes of a free plate, and the velocity of a non-propagating mode is by definition zero. For the embedded fibre case, the attenuation is very high for all of the modes, and the correlation between the group velocity and the energy velocity dispersion curves completely breaks down. The group velocity curves are not physically consistent. Many modes supposedly propagate faster than fastest bulk velocity in the material, which is not feasible. However, the energy velocity curves for this system are all physically reasonable. The energy velocity is never larger the longitudinal bulk velocity in the silicone carbide and the energy velocity tends to zero for the 'non-propagating' sections of the modes. In addition, the energy velocity agrees well with our understanding of the various modes. Modes which are primarily confined to the carbon have lower energy velocities than modes which are dominated by the faster silicone carbide sheath. The physically reasonable properties of the energy velocities of leaky modes helps validate the model.

## 4.4 Agreement with Finite Element Results

All of the solutions which have been considered up to this point in this thesis have been concerned with the modal wave propagation problem. The solution is exact and describes harmonic wave propagation in infinitely long structures. Instead of using this quick, exact method, a finite element technique can be employed to study the wave propagation characteristics of a system. Using this technique, the system is broken down into a finite number of small elements, which each obey the basic equations of motion. Therefore, the system can be modelled without invoking the more complicated wave field solutions that are used for guided waves. In addition, systems with local changes in geometry, such as defects, can be easily studied. Since the finite element solutions are found in an independent manner, they can be used to validate the infinite wave propagation solutions developed in chapter 2. The finite element results presented in this chapter were obtained using FINEL, a software package developed by Denis Hitchings in the Aeronautical Department of Imperial College[72]. More information on the finite element methods used to study wave propagation can be found later in chapter 5. This chapter simply uses the results to validate the wave propagation solutions.

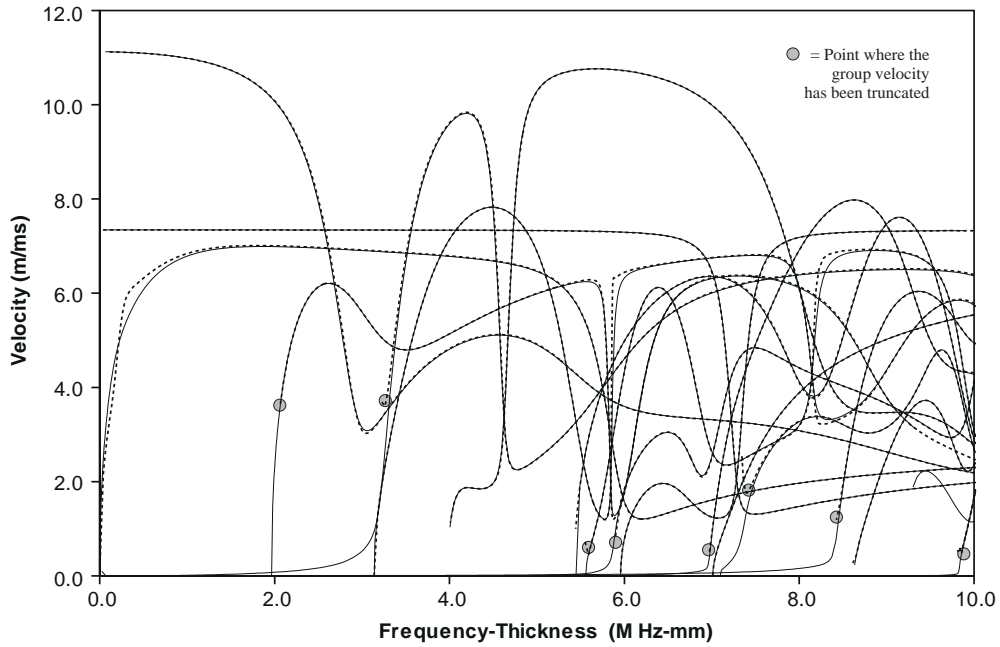


Figure 4.17: A comparison between the group velocity (dashed lines) and energy velocity (solid lines) dispersion curves for an immersed isotropic SCS fibre. As expected, the differences become apparent when the attenuation becomes very large. In many cases the group velocity curves had to be truncated at points where the attenuation of the mode starts to become excessive.

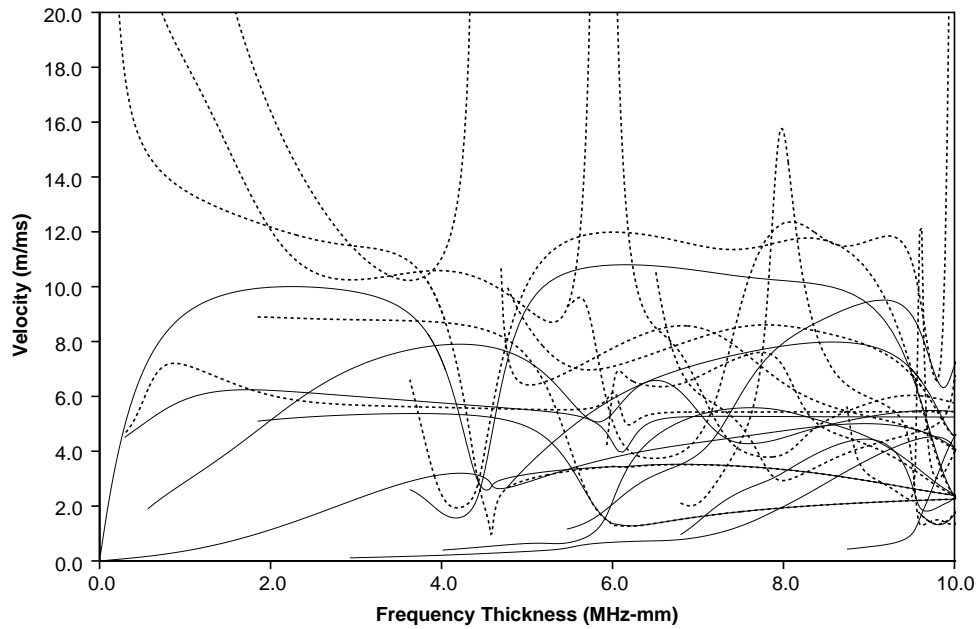


Figure 4.18: A comparison between the group velocity (dashed lines) and energy velocity (solid lines) dispersion curves for an isotropic SCS fibre embedded in a titanium matrix. Because of the high attenuation associated with most of the modes in this system, there is very little agreement between the two sets of curves.

Several types of comparisons can be made between the infinite wave propagation solutions and the finite element results. The first method extracts the frequency dependent phase velocity from finite element predictions of time traces at two different points along the direction of propagation and compares the velocity to the phase velocity calculated by the infinite wave propagation model. In addition, the attenuation due to leakage can be extracted from two finite element simulated traces and the results compared to the infinite wave model. The second method uses the modal wave propagation solution of chapter 2 to predict a time signal for a given tone burst after a simulated propagation of a certain distance. This time trace is then compared to the time traces that are generated by finite element modelling. The close agreement between the finite element solutions and the infinite modal solutions will be used in later chapters to efficiently extract more information about the behaviour of each of the modes.

#### 4.4.1 Phase Velocity Extraction

Throughout this thesis it is assumed that guided waves propagate as,

$$e^{i(\xi z - \omega t)}, \quad (4.10)$$

where  $\omega$  is the circular frequency,  $\xi$  the wavenumber in the direction of propagation,  $z$  the axial position, and  $t$  the time. This expression can be rewritten as

$$e^{i\xi_r(z - \frac{\omega}{\xi_r}t)} e^{\xi_i z} = e^{i\xi_r(z - v_{ph}t)} e^{\xi_i z}, \quad (4.11)$$

where  $\xi_r$  is the real part of the wavenumber,  $\xi_i$  is the imaginary part of the wavenumber, and  $v_{ph} = \omega/\xi_r$  is the phase velocity, which specifies the rate at which the phase of the guided wave changes. The phase spectrum technique [73,74] provides a relatively simple method of determining the frequency dependent phase velocity of guided waves that are propagating in a structure. The phase spectrum method relies on Fourier transforming two different signals that have propagated different distances and comparing the differences in the phases of the resulting frequency components. The phase velocity is calculated by dividing the product of the frequency and the distance travelled by the phase shift.

The main limitation of the phase spectrum method is that only a single wave packet can be present in the signals that are used for the analysis. The phase spectrum of multiple wave packets will overlap and confuse the analysis. However, this limitation does not affect the results that are obtained from finite element modelling since the model can be constructed so that it is large enough that outgoing and reflected signals are well separated in time. The outgoing wave packet can easily be sampled at two points along the plate and used for reliable analysis provided that the generated mode is pure. Chapter 5 describes the techniques that have been used to ensure a pure mode is excited in the structure. Another limitation of the phase spectrum method is that the approximate number of cycles that have passed must be known.

The results of the phase velocity extraction can be seen in figure 4.19. The system that is being studied consists of a free, thick-walled, steel pipe, whose wall thickness is 1 mm and whose inner radius is 0.5 mm. A ten cycle Gaussian windowed tone burst centred on 0.855 MHz was used to excite the fundamental axi-symmetric mode. The dashed lines indicate the phase velocity that is extracted from the finite element results and the thinner solid lines represent the solutions obtained from the wave propagation model of chapter 2. For the lowest frequencies shown, random error in the sampling can be seen in the finite element results. This error appears because there is only a very small amount of energy contained in these frequencies in the finite element model. This error could be removed by performing additional finite element runs at different centre frequencies. Above this error region, there is very good agreement for the low frequency results for the two methods. As the frequency increases, the agreement remains good, but small differences can be seen between phase velocity results for the two methods. These small differences could be due to several effects, including the lumping of the mass at the finite element nodes (through the diagonalisation of the mass matrix) or the discretisation used for the time marching. However, the largest differences are probably caused by the well known fact that the finite element techniques tend to be more stiff than real systems[75]. The finite element model cannot represent a continuously varying displacement profile through the thickness of the structure. Instead, it must break the displacement profile into a number of discrete segments. Since the actual mode shape cannot be modelled precisely by the finite element model, the material acts as though it is stiffer. The results in figure 4.19 have been calculated with eight elements through the thickness, which is twice the number that is needed for pure stability concerns[12]. If only four nodes are used, the difference between the two phase velocity curves roughly doubles, which still provides good agreement between the finite element modelling and wave propagation modelling results.

Verifying that the phase velocities of the finite element model and the wave propagation model agree is equivalent to verifying that predictions of the shape of a signal after it has propagated a certain distance agree. This prediction that can be done for both types of models. However, the modal wave propagation solutions that are derived in chapter 2 provide the solution for a mode at a single frequency. This type of solution implies that the time signal is infinitely long, containing only a single harmonic frequency. Such a time trace is not particularly useful for most non-destructive testing applications, which look for reflections from various defects. A more suitable time trace from a testing perspective is a modulated tone burst that contains a range of frequencies centred around a central frequency. In order to model such a signal using the modal solution, the tone burst must first be transformed into the frequency domain using the well known Fourier transform. Once in the frequency domain, each harmonic can be treated separately, as dictated by the modal solution, and a modified time trace can be retrieved via an inverse Fourier transform. In this manner, the propagation of a tone burst can be modelled by simulating the propagation of all of the individual frequency components contained within it. This modal solution can then be compared to the propagation that is simulated by finite element modelling. Good agreement between the two methods provides strong validation of the individual solutions.

Figure 4.20 compares the predicted time signals for the fundamental longitudinal mode of a 1 mm thick steel pipe with an inner radius of 0.5 mm for a 10 cycle Gaussian windowed tone burst with a centre

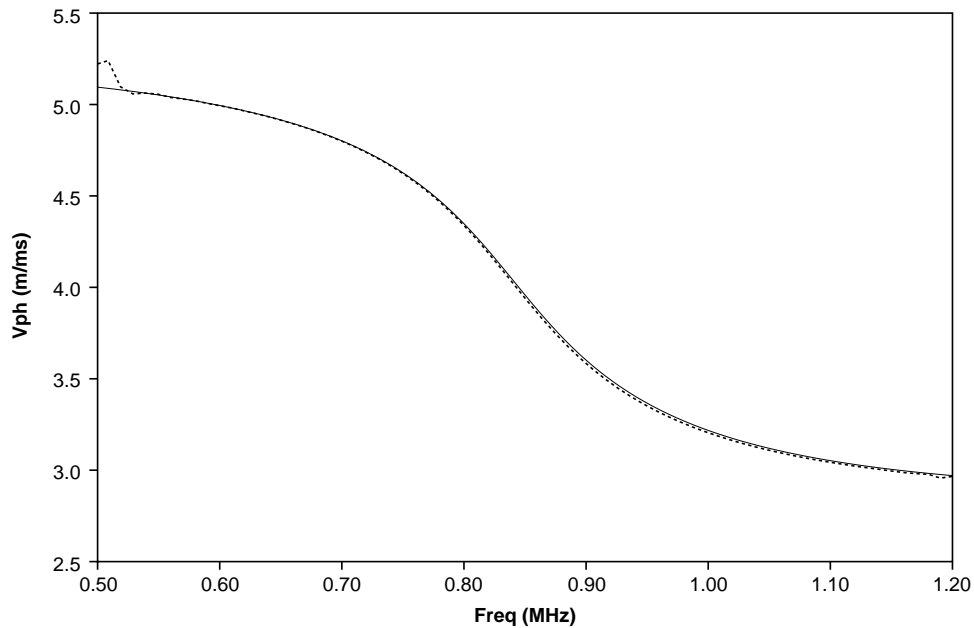


Figure 4.19: A comparison between the phase velocity as calculated for by finite element modelling (dashed lines) and the wave propagation model (solid lines) for the fundamental axi-symmetric mode of a 1 mm thick steel pipe with an inner radius of 0.5 mm.

frequency of 0.885 MHz. Two propagation distances are shown, 30 and 50 mm from the source. The solid lines represent the predictions of the wave propagation model and the dashed lines represent the finite element predictions. There is good agreement between the two types of predictions except for the middle portion of the signal that has propagated 50 mm, which is dominated by the interference between two frequency components and is extremely sensitive to minute differences.

The phase spectrum method could also be applied to non axi-symmetric modes to extract the phase velocity. However, because the finite element program does not allow the phase of the circumferential component of the displacement to be set independently from the phase of the radial and axial components, a single pure mode cannot be generated effectively. Components of other modes that are also generated corrupt the signal and cause error in the phase spectrum method. However, for some modes there is still good agreement between the two techniques, as can be seen in figure 4.21, which compares the phase velocity curves of the third flexural mode of first circumferential order of a 1 mm thick steel pipe with an inner radius of 0.5 mm as calculated by the finite element technique and as calculated by the infinite wave propagation model. The more stiff nature of the finite element model remains a large source of error.

Systems that leak energy into the surrounding medium can also be validated against finite element studies. However, the leakage complicates the generation of the finite element model and the interpretation of the results. Great care must be taken to not contaminate the results with bulk waves that are not part of the guided wave solution, but will propagate in the portion of the finite element model that repre-

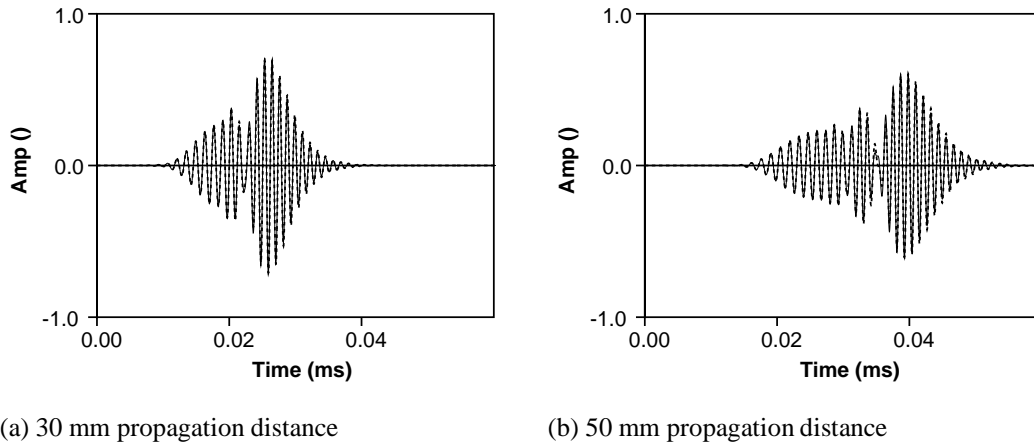


Figure 4.20: Comparison of predicted time traces for the (a) 30 mm and (b) 50 mm propagation distance of the fundamental longitudinal mode of a 1 mm thick steel pipe with an inner radius of 0.5 mm, as calculated by the wave propagation model solution (solid lines) and finite element solution (dashed lines). The input signal consisted of a 10 cycle Gaussian windowed tone burst with a centre frequency of 0.885 MHz.

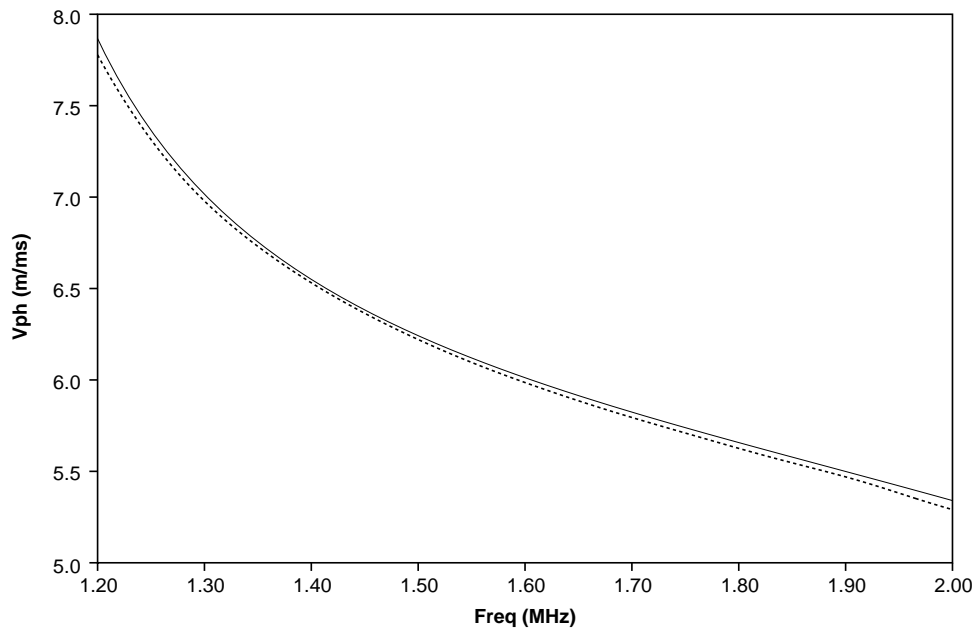


Figure 4.21: A comparison between the phase velocity as calculated by finite element modelling (dashed lines) and the wave propagation model (solid lines) for the third, first circumferential order, flexural mode of a 1 mm thick steel pipe with an inner radius of 0.5 mm.



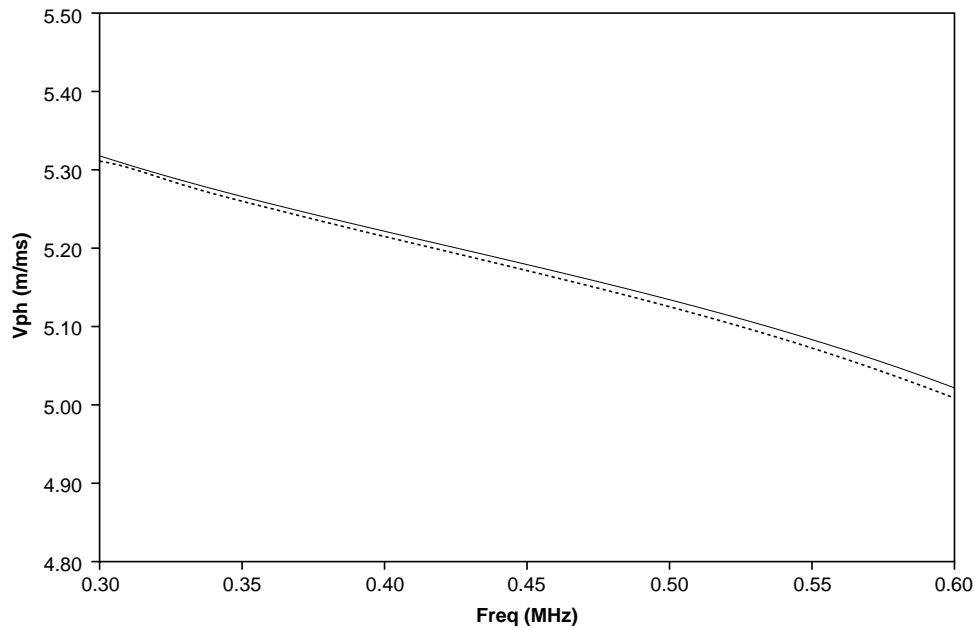


Figure 4.22: A comparison between the phase velocity as calculated by finite element modelling (dashed lines) and the wave propagation model (solid lines) for the fundamental longitudinal mode of a 1 mm thick steel pipe with an inner radius of 0.5 mm that is surrounded by grout.

sents the surrounding medium. Details of the technique that has been used to model leaky guided wave propagation in a finite element model can be found in section 5.3.

Figure 4.22 shows the agreement of the wave propagation solutions (solid lines) and the finite element modelling (dashed lines) for a portion of the fundamental longitudinal mode of a 1 mm thick steel pipe with an inner radius of 0.5 mm that is surrounded by grout. The dashed lines were calculated by applying the phase spectrum method to a 10 cycle Gaussian windowed tone burst centred on 0.45 MHz that propagated through a finite element model with three elements per millimetre. There is good agreement between the two methods. The maximum error between the two solutions in the region shown is 0.25 percent.

#### 4.4.2 Attenuation Extraction

For systems that leak energy into the surrounding medium, such as the one used for figure 4.22, the attenuation, as calculated by the wave propagation model and as calculated by the finite element modelling, can also be compared to validate the solutions. Two methods of extracting the attenuation from the finite element model are explained below. The first method simply measures the decay in the amplitude of the signal as the wave passes through a series of points along the direction of propagation. The second method resembles the phase spectrum method. The frequency spectra of two different time traces (that were sampled at different propagation distances) are divided and the frequency dependent attenuation is extracted.

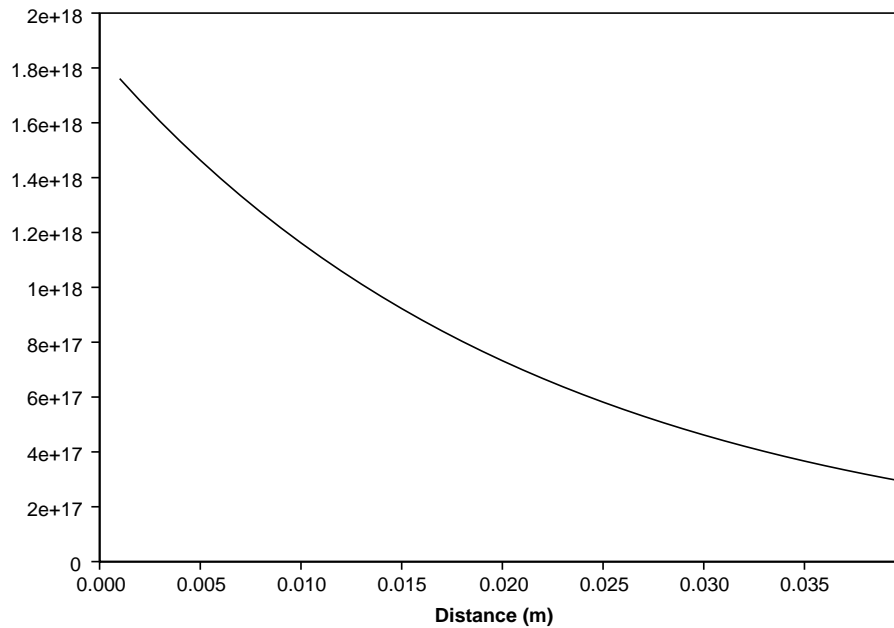


Figure 4.23: A plot of the decay of the maximum amplitude of the frequency spectrum of the fundamental longitudinal mode as it propagates in a 1 mm thick steel pipe with an inner radius of 0.5 mm that is surrounded by grout.

#### Measurement of Signal Decay

A simple method of determining the attenuation of the wave that is propagating in a finite element model involves measuring the decay in the amplitude of the signal as the wave passes through a series of points along the direction of propagation. An exponential decay can be fitted to the amplitude of the successive points and this value can be compared to the predicted attenuation. The maximum amplitude of the Fourier transform of the signal is used to specify the amplitude of the signal so that the results are not affected by aliasing or dispersion of the mode. Figure 4.23 shows the decay of the maximum signal amplitude of the fundamental longitudinal mode of an embedded 1 mm thick steel pipe with inner radius of 0.5 mm for a 10 cycle Gaussian windowed tone burst centred on 0.45 MHz. Using a commercial spreadsheet package to fit an exponential decay to this curve yields the equation

$$Amp = 2(10^{18})e^{-46.156z}, \quad (4.12)$$

where  $z$  is the distance (in metres) along the direction of propagation. The value of the attenuation that can be extracted from equation 4.12 is  $46.156 \text{ np/m}$  ( $400.9 \text{ dB/m}$ ). The wave propagation model predicts that the attenuation of the L(0,1) mode at 0.45 MHz is  $47.41 \text{ np/m}$  ( $411.8 \text{ dB/m}$ ). These two values compare reasonably well (within three percent).

### Frequency Spectrum Method

The signal decay method that is discussed above has some disadvantages. Its primary limitation is that it only yields the attenuation at a single frequency, the frequency that contains the largest amount of energy. The phase spectrum method that was used above to determine the phase velocity of a propagating wave can be easily adapted to also provide information on the frequency dependent attenuation of a propagating wave. As before, the frequency spectra of two different time traces that were sampled at different propagation distances will be used. However, instead of subtracting the phase of the frequency components of the two signals, one frequency spectrum will be divided by the other. The resulting value can be converted into an attenuation value, provided that the propagation distance between the two sample points is known.

This frequency spectrum operation was performed on the results from the embedded steel pipe that was used in figure 4.22 to produce the attenuation values that are shown as short dashes in figure 4.24. The solid line in figure 4.24 represents the attenuation values that were calculated by the wave propagation model. The agreement between these two solutions is reasonable, differing by at most five percent. At happened above, most of this difference can be attributed to the artificially stiffer nature of the finite element model. For comparison purposes, a third line of long dashes as been added to figure 4.24. This line represents the attenuation values that are obtained by the wave propagation model when the elastic stiffness (Young's modulus) of the steel is increased by five percent. The much better agreement of this solution with the finite element results confirms that the finite element model is behaving as a more stiff system. The additional stiffness is not considerable (only 5 percent), although it causes a relatively large shift in the observed attenuation.

Except for the more stiff nature of the Finite Element model, the agreement is excellent between the results obtained by the finite element modelling and the results obtained by the wave propagation model. This excellent agreement provides good validation of the wave propagation model from an independent technique. This validation has been shown for longitudinal and flexural modes in a free system and for the fundamental longitudinal mode in a leaky system. The limitations that control why more varied cylindrical systems cannot be modelled with finite elements is explained in section 5.6.3. In addition, future chapters, such as chapter 6 include more cases that demonstrate the agreement between the wave propagation model and finite element modelling.

## 4.5 Experimental Verification of Leakage Rate Along a Bar

The previous validation cases in this chapter have been based on analytical or numerical solutions of wave propagation. This final section compares the wave propagation solutions to the results from some simple experimental tests to confirm if the wave propagation solutions are feasible. This section helps to validate the leakage rates of flexural modes, which could not be modelled using the finite element method.

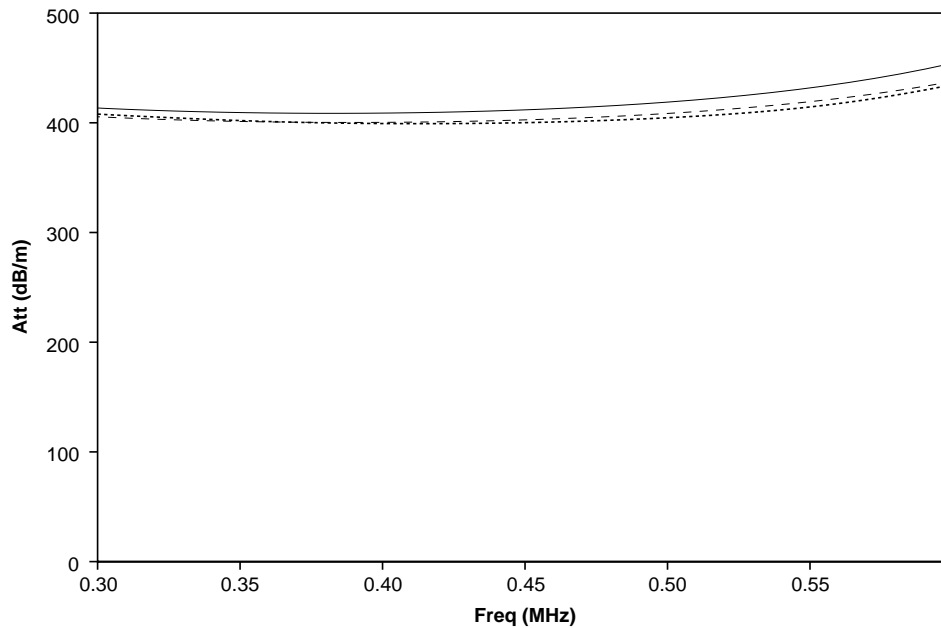


Figure 4.24: A comparison of the attenuation of the fundamental longitudinal mode of a 1 mm thick steel pipe with an inner radius of 0.5 mm that is surrounded by grout as calculated by finite element modelling (short dashes), the wave propagation model (solid lines), and the wave propagation model with the stiffness of the steel increased by five percent (long dashes).

All of the experimental confirmation work that is presented in this section was performed on a half inch (12.7 mm) diameter steel bar immersed in water. Three simple experimental configurations were used for the validation work. The first two configurations were used to generate the fundamental longitudinal and flexural modes at low frequencies. Since only three modes with reasonable attenuations, the fundamental longitudinal, flexural, and torsional modes, exist below 150 kHz, simple pulse-echo tests can be used to determine the leakage rates. Once a wave is generated in the bar, the decrease in amplitude of the received signal that occurs when the bar is immersed can be used to determine the attenuation caused by the water loading. A slightly more complicated technique must be used to determine the leakage of the higher order modes. At higher frequencies, more modes can exist in the bar, and so a technique must be used that can separate out the amplitudes of the different propagating modes. For these tests, the bar was immersed in water and signals were sampled at various points along its length. These signals were used to perform a 2-D FFT[76], which is explained in section 5.4 and provides the amplitude of a mode at a particular frequency and wavenumber. The decline in the amplitude of a mode with distance along the plate was used to determine the attenuation rate. The wave number and attenuation dispersion curves for zero, first, and second circumferential order modes, of the half inch (12.7 mm) diameter steel bar that was used for these experiments are shown in figure 4.25. The circles in figure 4.25 represent the points for which experimental data was obtained and the labels indicate the equivalent points on the dispersion curves.

Diagrams describing the experimental configurations and the sample time traces that were used to determine the leakage rates of the fundamental modes are shown in figures 4.26 and 4.27. In both cases, a 10 cycle Hanning windowed tone burst centred on 120 kHz was used to excite the waves. For the longitudinal case shown in figure 4.26, a commercially available one inch diameter wide band plane wave immersion transducer with a center frequency of 250 kHz was used. Three subsequent reflections of the L(0,1) mode from the opposite end of the bar can be clearly seen. These reflections are labelled (1), (2), and (3) in figure 4.26(c). In order to determine the leakage rate, the ratio of the amplitude of the third reflection to the first reflection was calculated for both the slightly immersed and the completely immersed cases. The larger decay of the completely immersed case is attributed to the leakage of energy into the surrounding water where its energy would be lost. This conclusion assumes that the received signal is not contaminated by reflections from the boundary of the water and that the change in the reflection coefficient from the end of the bar does not change significantly when it is in air or immersed in water (the change would be about 6 percent for each reflection if the L(0,1) mode was a bulk longitudinal wave – see equation 6.4). The ratio of the amplitudes of the reflections was used so that slight variations in coupling between subsequent tests would not affect the results. The decay ratios can be converted into an attenuation rate by dividing the ratio of two decays by the additional distance travelled by the wave when it is more fully immersed in water. In this case, the two decays are 0.752 and 0.375. Since the wave travels the length of the bar four times between the first and third reflections from the far end, the additional immersed distance travelled by the wave is four times the change in the amount of the bar that is immersed (four times 0.290 metres = 1.16 metres). These values equate to an attenuation of 0.6 np/m (5.2 dB/m), which is in the same range as the attenuation calculated by the wave propagation model, 0.54 np/m (4.7 dB/m). The experimental attenuation values can be made more accurate if the procedure compensates for the reduced size of the reflection from the end of the bar opposite the transducer that would occur when it is immersed. Assuming that the reflection coefficient of the L(0,1) mode in this frequency range is similar to that of a bulk longitudinal wave in steel, two reflections from an immersed end would cause the resulting signal amplitude to be 88 percent the size of the signal would occur if the end was in air. This calibration procedure reduces the value obtained for the experimental data from 0.6 np/m to 0.53 np/m, which agrees very well with the modal wave propagation solutions. The attenuation of this mode at this frequency (120 kHz) is so low because most of the motion of the mode is parallel to the axis of the bar and therefore does not couple well into the surrounding water, where its energy would be lost.

The attenuation of the fundamental flexural mode at 120 kHz is much greater than the attenuation of the fundamental longitudinal mode. Therefore, a slightly different technique has been used to extract the attenuation values from the signals shown in figure 4.27. In order to preferentially excite F(1,1), a pair of 0.5 mm thick PZT crystals were bonded to the end of the bar using a low viscosity epoxy and then driven out of phase. Since the attenuation of F(1,1) is so large at this frequency, only half of the bar was immersed for any of the experiments so that the amplitude of the first reflection of the F(1,1) mode would always be much greater than the amplitude of the L(0,1) mode. In addition, since the elements which generated and received the wave packets were permanently attached, the coupling

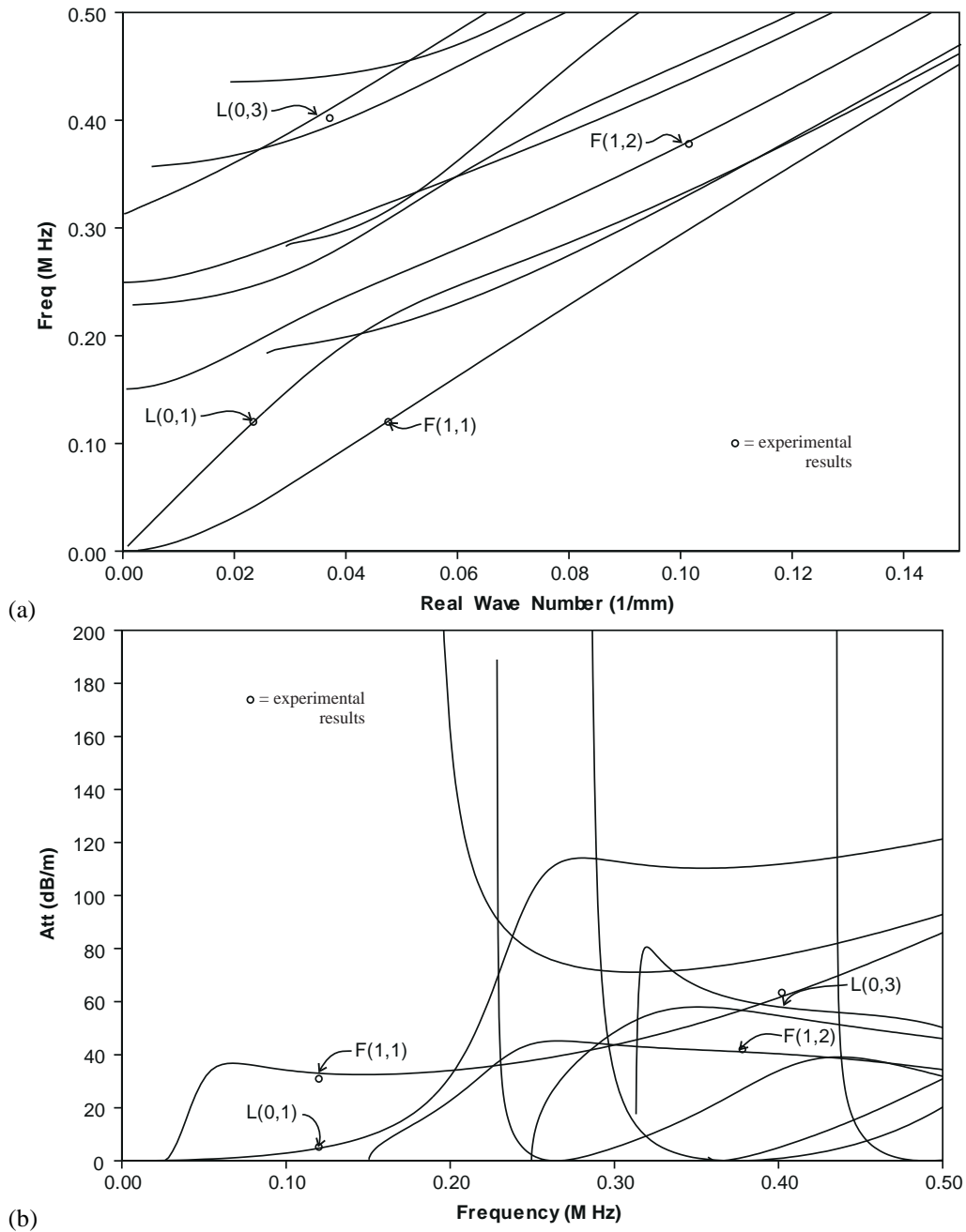
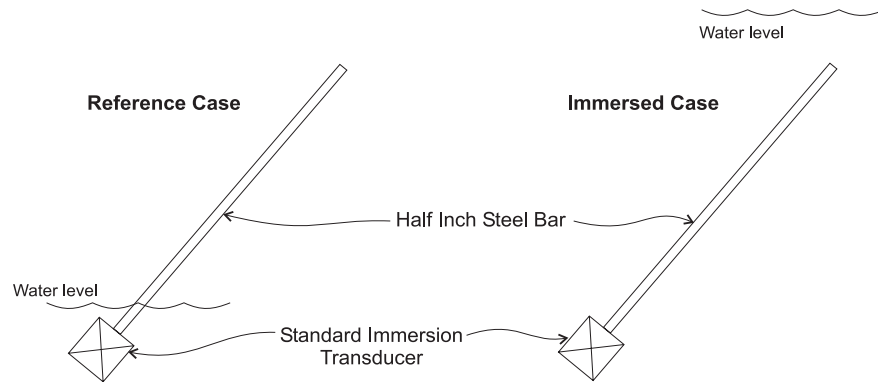
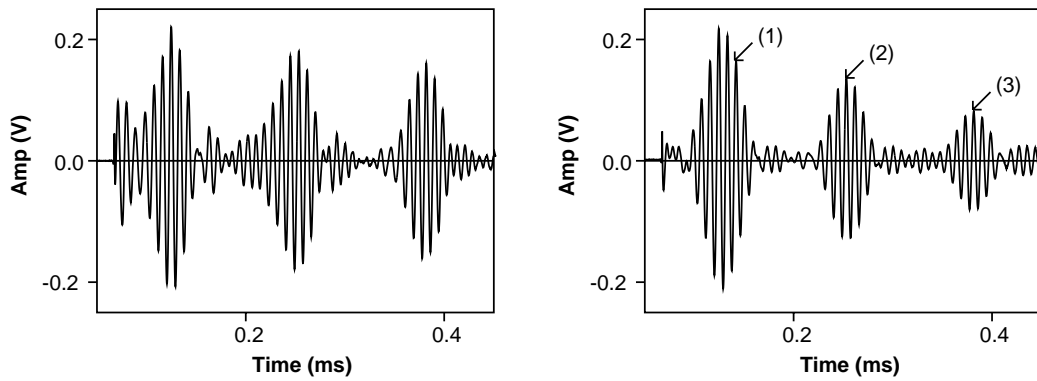


Figure 4.25: The (a) wave number and (b) attenuation dispersion curves for zero, first, and second circumferential order modes, of a half inch (12.7 mm) diameter steel bar. The circles represent the experimental data that was obtained and the labels indicate the equivalent points on the dispersion curves. The dispersion curves were cropped to only show locations with moderate attenuations.

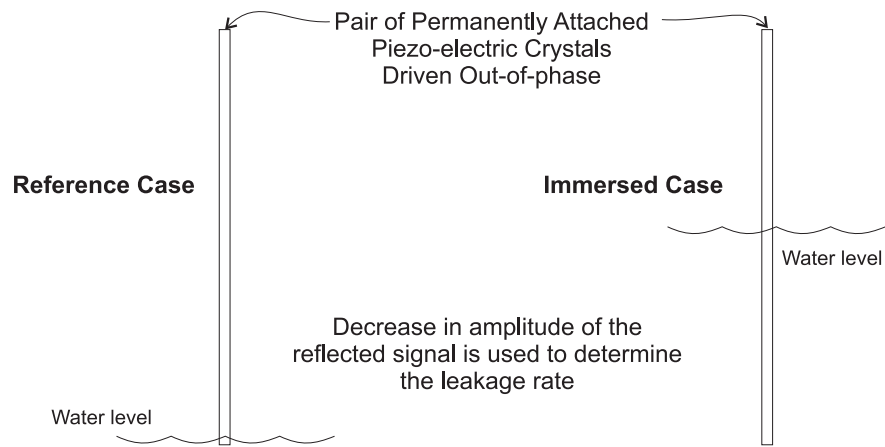


(a) The experimental configuration for generating the fundamental longitudinal mode  $L(0,1)$

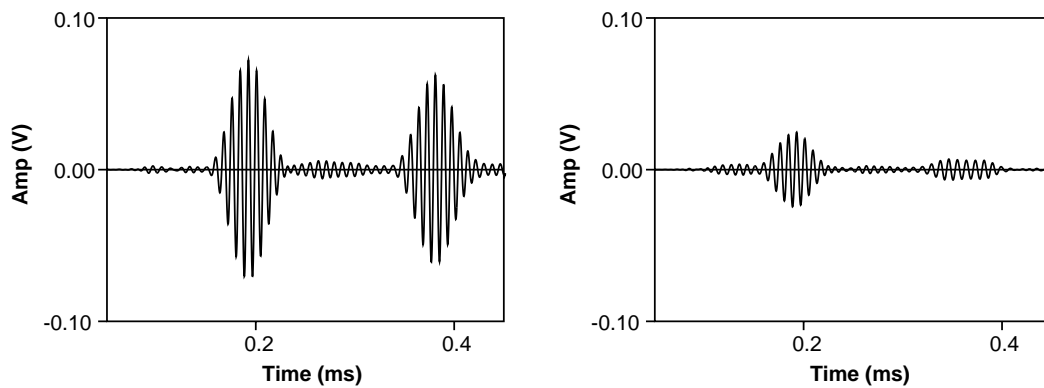


(b) Time trace with 14 mm of the bar immersed      (c) Time trace with 304 mm of the bar immersed

Figure 4.26: The (a) experimental configuration and (b,c) time traces that were used to experimentally determine the leakage rate of the fundamental longitudinal mode,  $L(0,1)$ , in a half inch steel bar.



(a) The experimental configuration for generating the fundamental flexural mode  $F(1,1)$



(b) Time trace with 10 mm of the bar immersed      (c) Time trace with 160 mm of the bar immersed

Figure 4.27: The (a) experimental configuration and (b,c) time traces that were used to experimentally determine the leakage rate of the fundamental flexural mode,  $F(1,1)$ , in a half inch steel bar.

between subsequent tests could be considered consistent. Therefore the amplitudes of the reflected signals can be used directly, without having to normalise the amplitudes of later reflections by the amplitude of the first reflection. Noting that the peak to peak amplitude of the first reflection declines from 0.142 V to 0.049 V when the amount of the bar that is immersed in water is increased from 10 mm to 160 mm (an additional propagation distance of 300 mm for the reflected signal), the attenuation can be calculated to be around 3.6 np/m (31 dB/m). This attenuation value falls within a reasonable range of the value calculated by the wave propagation model, which is 3.8 np/m (33 dB/m).

Extracting the attenuation values of the fundamental longitudinal and flexural modes of the bar involved relatively simple procedures, since only one flexural mode and one longitudinal mode could propagate at the frequency used. By using an appropriate source, an axi-symmetric one for the longitudinal case and an a-symmetric one for the flexural case, allows most of the energy to be directed into the desired mode. However, at higher frequencies, many more modes can exist. Therefore, the received signals will be the composite of several modes that interfere with each other. In order to separate the amplitudes



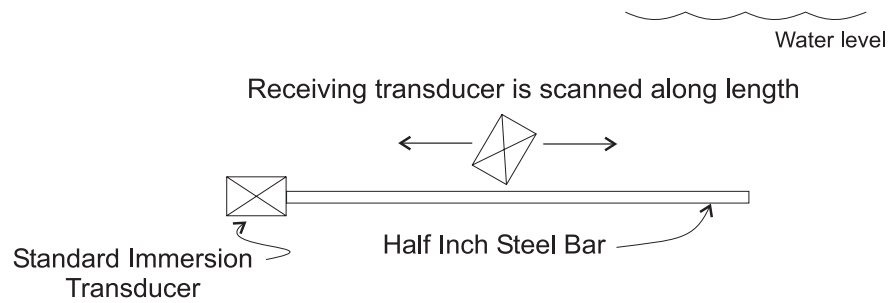


Figure 4.28: The experimental configuration used to collect the signals that were used for the two dimensional Fourier transform.

of the different modes, a technique such as a two dimensional Fourier transform (2-D FFT) needs to be employed[76]. The 2-D FFT, which is explained in section 5.4, first performs a Fourier transform in time and then a second Fourier transform in space to determine the amplitude of the waves that are propagating at a specified frequency and wavenumber. Figure 4.28 shows the experimental configuration that was used to collect data for a 2-D FFT for the half inch steel bar used in the previous experiments. One transducer was used to generate waves in the bar. The excitation signal consisted of a 10 cycle Hanning windowed tone burst centred on 400 kHz. A second transducer was scanned along the axis of the bar, sampling waveforms every 0.5 mm and the data was used to calculate the 2-D FFT that is shown in figure 4.29(a). Two frequency - wavenumber points were chosen to analyse, one near the F(1,2) mode and one near the L(0,3) mode. These points were chosen because the peak in the 2-D FFT was primarily composed of only mode. Figure 4.29(b) shows a typical cross section of many of the peaks. The irregular nature of the peaks indicates that the spatial resolution was not great enough to separate the signals from the different modes. However, the peaks used to measure the attenuation of the F(1,2) and L(0,3) modes appear to be mainly composed of a single mode. In order to determine the attenuation, the range from which the 2-D FFT was calculated was offset down the axis of the bar. The amplitude at a fixed frequency and wavenumber was plotted for each offset and an exponential curve was fitted to the decay, which was used to calculate the attenuation. The decay curves along with fitted exponential decays for the two modes considered are shown in figure 4.30. The oscillatory nature of the decay reflects the interference in the 2-D FFT of the primary mode being studied with other modes. In order to remove this interference, the signal would have to be sampled over a much longer distance, which would allow the 2-D FFT to better separate the wavenumbers of the propagating waves. In addition, the signals should be sampled from positions all around the bar so that the different circumferential orders of modes could be separated. Unfortunately, the facilities available at the time of testing did not allow these improvements to be made in the resolution of the 2-D FFT. However, even with the 'contaminated' results, the extracted attenuations agree favourably with the wave propagation predictions. For the F(1,2) mode, the fitted attenuation was 4.7 np/m (41 dB/m), while the wave propagation solution predicted 4.73 np/m (41 dB/m). For the L(0,3) mode, the attenuation extracted from the 2-D FFT was 7.2 np/m (63 dB/m). This compares to 6.65 np/m (58 dp/m) that is predicted by the wave propagation model.

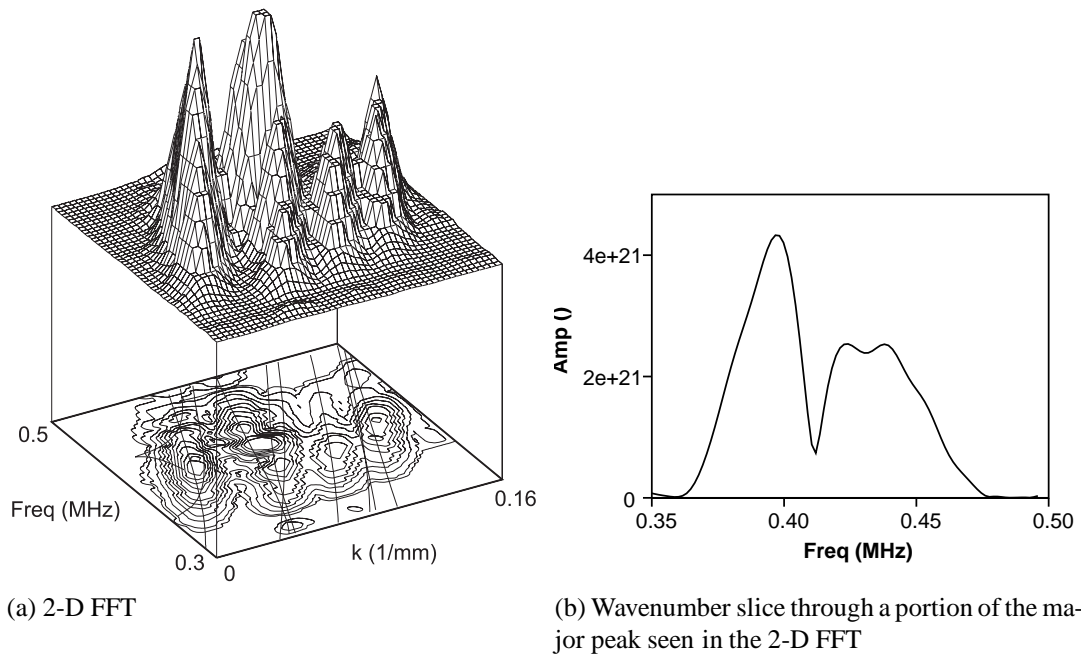


Figure 4.29: The (a) two dimensional transform obtained from a half inch diameter steel bar immersed in water along with (b) an example of a slice through the largest peak, whose irregularity indicates that the peak is composed of multiple modes.

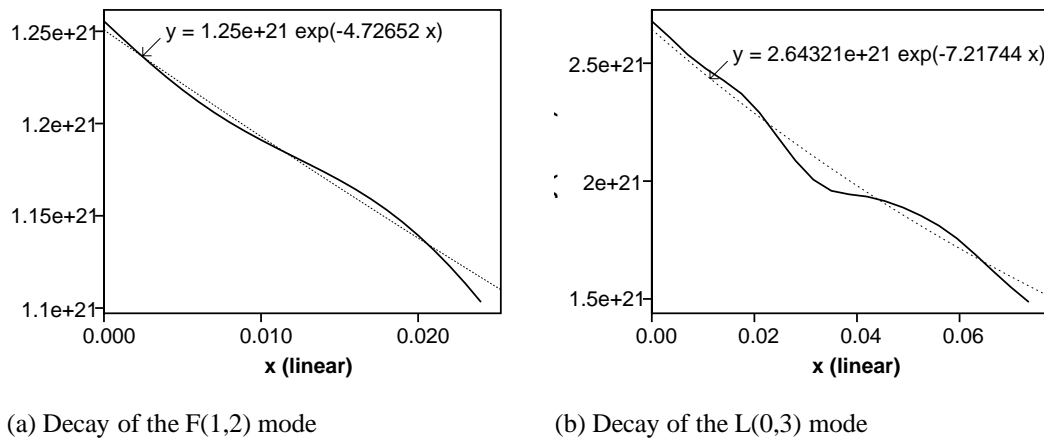


Figure 4.30: Plots of the rate of decay of the (a) F(1,2) and (b) L(0,3) modes in a half inch diameter steel bar immersed in water. The dashed lines represent exponential decays that were fitted to the decays obtained from the 2-D FFT.

The agreement obtained between the wave propagation model and the crude experiments described helps confirm that the solutions calculated by the model are reasonable. The comparisons of the leakage of flexural modes in a bar helps validate the wave propagation solutions for this series of modes, which could not be validated using independent solutions such as finite element modelling.

## 4.6 Summary of Validation

In this chapter, the wave propagation model developed in chapter 2 has been validated against asymptotic limits for which there are exact solutions, published results for cylindrical wave propagation, the internal consistency of the solutions, agreement with finite results, and agreement with some simple experiments. Taken together, these validations provide strong evidence that the wave propagation solutions are correct, for both the free and leaky cases.

## **Chapter 5**

# **Finite Element Techniques Used in Combination with the Wave Propagation Model**

The previous chapters in this thesis have discussed wave propagation in cylindrical systems in terms of the modal properties of the system. The solutions to the modal problem provide a great deal of information on how guided waves will propagate, however, they cannot provide all of the information that is needed to create an effective non-destructive testing technique for a certain system. The boundary conditions that are specified for the wave propagation model require that the system does not vary in the direction of propagation. For example, a cylinder must be infinitely long and must always consist of the same homogeneous layers. However, in most non-destructive testing applications, the goal is to find some sort of defect, which from a modelling point of view is a change in material properties or geometry. Therefore, in order to completely understand how the system will behave, an additional modelling method is needed to determine the effects of this interaction.

Time domain finite element modelling provides an effective means of gaining additional information about the way that waves will propagate in a given system. Instead of breaking the wave propagation into a collection of potential functions which influence the displacement field everywhere, the finite element technique decomposes the problem into a collection of small elements, which each follow basic equations of motion. The elements are only linked to their neighbours and must be finite in number. This technique provides an effective means to model systems which have many discontinuities. Combining finite element modelling with the modal solutions yields more information about the wave propagation characteristics of a particular system than can be extracted than from either of the two methods individually.

The author of this thesis was not involved in the development of FINEL [72], the finite element program that was used to obtain the results presented in this thesis. Instead, his contribution to the field involves the pre and post processing techniques that have been developed to help study guided waves. The concepts behind some of these techniques (namely the 2-D FFT and exact mode shapes) were originally developed by David Alleyne[12,76] and then expanded by the author of this thesis to handle the modelling of ultrasonic wave propagation of embedded cylindrical systems. Other techniques, such as through-thickness mode extraction, were developed by the author.

This chapter begins by explaining why finite element modelling is advantageous, reviewing the requirements of the finite element technique that is used, and examining some methods that can be used to model wave propagation in leaky systems. The next section of the chapter looks at two ways that the amplitudes of propagating guided waves can be extracted from multi-mode displacement fields in a finite element model. First, the two dimensional Fourier transform, a well established method[76], is reviewed. Then a through thickness mode extraction technique, which is based on a mode orthogonality principle, is developed. In the final section, these techniques are used to analyse the purity of the modes that are generated in the finite element model. Two methods are discussed that can be used to generate single pure guided modes in a finite element model.

## 5.1 Why Finite Element Modelling

As discussed above, the modal solutions can only model structures that do not vary along the direction of propagation. However, finite element modelling allows us to model the interaction with local changes, such as simulated defects. This section discusses the advantages of each of the techniques and the advantages of combining the two techniques together.

The modal solutions that are developed in chapter 2 have several advantages over their finite element counterparts. In comparison to the finite element solutions, the modal solutions can be calculated very quickly. Even for quite complicated systems, the time it takes to calculate the dispersion curves is measured in minutes, while the finite element analysis is measured in hours. Since the modal solutions describe fields that are continuous and describe the waves along the entire length of the system, propagated signals can be predicted in seconds once the dispersion curves have been calculated. On the other hand, the finite element solution must march through time to arrive at a prediction for a propagated solution. Even after this time intensive procedure, only a small portion of the solution space is revealed by the finite element analysis. On the other hand, the modal model searches the entire solution space. The modal solutions also have the advantage that they are exact. The solutions that are obtained provide frequency, wavenumber, and attenuation roots that exactly solve the constitutive equations. Each of the modes is clearly separated from the others. However, this is not the case for the finite element solutions. In finite element analysis of wave propagation it is common to use four noded elements, for which the displacements and stresses vary linearly between the corners. This approximation of the actual mode

shape as a series of short line segments adds a small amount of error into the finite element solutions, causing them to be too stiff[75]. In addition, for the finite element case, it is often not easy to completely separate the various modes. Methods, such as the two dimensional Fourier transform that is discussed below, can be used to separate the amplitudes of overlapping propagating modes, however the precision to which the frequency and wavenumber of a mode can be determined depends on how the wave propagation is monitored. Without an understanding of which waves can exist in a system, the finite element results will often be extremely difficult to interpret.

Although the modal solutions have many advantages, they cannot model defects, since they require that the system does not vary in the direction of propagation. Therefore, another technique is required. The main advantage of finite element modelling is its flexibility in modelling local geometric changes. By breaking the problem into small elements that each follow the basic equations of motion, the interaction with defects (modelled as local changes in geometry) can be predicted without requiring any particular knowledge of the behaviour of the propagating wave modes. This allows many different types of defects to be modelled without extensive derivation of analytical reflection coefficients.

The real advantage comes from combining the techniques together. The modal solutions can be used to determine which waves can exist and identify modes that are likely to provide effective testing. Then, these potential modes can be generated in the finite element model and allowed to interact with simulated defects. Post-processing can convert the information from the finite element models back into modal information such as the reflection coefficients for the various modes. This interaction between the two techniques also helps validate that the solutions are correct, since any discrepancy between the finite element techniques and the complementary analytical modal solutions can be quickly identified.

The ability to effectively merge the two techniques relies on two important properties of guided ultrasonic waves that propagate in finite structures; they are orthogonal to each other and they behave in a linear fashion. Since the modes are orthogonal, the combination of modes that produces a given displacement field is unique and the finite element simulated displacement fields can be unambiguously translated into their modal components. Likewise, a combination of modes can be converted into a unique displacement field in the finite element model. The linear behaviour of the guided wave modes allows each mode to be studied separately and then later combined using the superposition principle to understand the entire system. This information is used both as a design and a calibration tool. Knowing how the various modes behave allows the optimum mode and frequency to be chosen for the testing requirements. In addition, the sensitivity of the experimental setup can be predicted quickly and inexpensively. These predictions can also provide a guideline to confirm when all of the experimental equipment is functioning correctly, since the modelling serves as a controlled virtual experiment. The number of finite element calculations needed to thoroughly analyze the system can be reduced by generating an input signal that has a wide frequency bandwidth. Once the response of the system over a wide frequency band is known, the response of the system to an input signal that contains a subset of that frequency band can be calculated immediately without re-running a finite element calculation. This knowledge can be used to quickly design effective non-destructive testing techniques that use guided ultrasonic waves.

## 5.2 Review of Finite Element Techniques used for Guided Wave Propagation

This section provides a quick overview of the finite element method that is used for the work in this thesis. It concentrates on how the method is used and the conditions that are required for the method to be stable as opposed to the operation of the method itself, since the author of this thesis was not involved in the development of the finite element modelling, but only in the development of the processing of the input and output of the data. Later sections will discuss some pre and post processing methods that have been developed to facilitate the generation and analysis of guided waves.

All of the finite element studies included in this thesis use a software program called FINEL that was developed in the Aeronautical Department of Imperial College by Denis Hitchings [72]. The Imperial College NDT Lab has been using this program for many years. Several modifications have been made to simplify the processing of the wave propagation modelling. In order to accommodate large models and avoid the inversion of a large stiffness matrix, an explicit time marching algorithm is used and the mass has been lumped to diagonalize the mass matrix and band the stiffness matrix, which simplifies the estimation of the acceleration and allows the model to march forward on an element by element basis. This technique minimizes memory usage and generally reduces the overall processing time. For more information on how this method works and why it was chosen to model ultrasonic wave propagation please refer to the PhD thesis published by David Alleyne [12], or one of the general texts on finite element modelling, such as reference [75].

The cost (in time and resources) of a finite element prediction depends on the size of the model and the density of the finite element mesh as well as the time step used for the time marching and the amount of time that needs to be predicted. The density of the nodes in the mesh and an adequate time step are controlled by stability concerns. The overall dimensions of the model and the time period over which it needs to be calculated depend on the type of system that is being modelled and the properties of the modes that will be present.

Numerical accuracy requires that there are at least 8 elements per wavelength for the shortest wavelength that will be present in the system. Alleyne [12] quotes an error estimation formula by Harker [77] that predicts that the velocity error will be less than 0.5 percent if this criterion of 8 elements per wavelength is followed. If there are less elements per wavelength, the error quickly increases as the displacements vary rapidly over the length of an element. However, if there are too many elements per wavelength, the computation costs increase, the time step must be made smaller (see below), and the rounding error will increase. Since this criterion of elements per wavelength applies to the shortest wavelength that can exist, it is controlled by the slowest wave that can propagate. In practice, this criterion is satisfied by making the element size one eighth of the Rayleigh velocity of the slowest material divided by the highest frequency that contains significant energy.

Although the slowest wave controls the size of the elements, the fastest wave controls the size of the time step and the stability of the solution. The largest time step that would be possible, as given by Blake [78], is the element size divided by the fastest bulk wave. Physically this indicates that no wave can propagate so fast that it moves more than one element in a given time step. When this condition is satisfied, the growth of a disturbance should be bounded and the model is generally stable. In practice, the time step is set to be 80 percent of this theoretical maximum value.

The overall dimensions of the finite element model depend on the type of system being modelled. In general, the model is designed so that the reflections from various features are well separated in time. This separation dramatically simplifies the interpretation of the data and the extraction of the amplitudes of the propagating waves. When calculating the required size, the behaviour of all of the modes that can exist at the given frequency must be considered. Enough distance must be allowed for reflections of both the slowest and the fastest mode to be well separated.

A wave is launched in the finite element model by applying a time varying displacement or force to a series of nodes, which are usually located on one of the free surfaces of the model. The resulting wave is allowed to propagate and the displacements at a series of points are stored for later processing. For numerical efficiency, most of the modelling is performed in two dimensions. A plane strain condition is frequently assumed for flat plates. This assumption implies that the plate is infinitely thick and that the elements in the model represent the cross section through the thickness of the plate and along the direction of propagation of the guided wave. Similarly, axi-symmetric conditions are often assumed for cylindrical structures. Under these conditions, the elements in the model represent a cross section through the radius and along the axis of the structure. The formulation of the stresses simulate the rotation of this cross section around the centre axis of the structure. Although this forces the geometry of the structure to be axi-symmetric, non-axi-symmetric wave propagation can still be modelled. However, the conversion from one circumferential order mode to a mode of a different circumferential order cannot be modelled. In order to model mode conversion between different circumferential orders, the finite element model would need to be truly three dimensional, which quickly causes the model to become unfeasibly large for all but a few cases.

The technique outlined in this section has proven robust for modelling plates in vacuum[12,10,79,80]. The following section discusses how it was adapted to accommodate leakage.

### **5.3 Extension of the Finite Element Techniques to Model Leakage**

Whenever guided waves are propagating in systems that are in vacuum, the energy in the system will remain constant if all of the materials are elastic. However, if the system is immersed or embedded in another material, energy can leak into the surrounding material and be lost from the system as it propagates towards the infinitely far away boundaries. Modelling this leakage causes some difficulties



for finite element modelling. By dividing a wave propagation problem into a finite number of small elements, the finite element method provides an efficient method of modelling rapidly changing geometries. However, the elements cannot be infinitely large and there must be boundaries. The waves that are generated in the surrounding material can be reflected off the boundaries of the model and return to the system, where they contaminate the results. This contamination must be eliminated to match the modal wave propagation solutions and the realistic physical case, for which the leaky waves tend to be scattered or attenuated so heavily that they cannot be reflected back towards the embedded system.

There are several methods that could be used to eliminate the reflections from the boundaries of the model, from sophisticated to simple. Because only a few cases needed to be studied in this thesis, a simple method, which did not require extensive modification of the finite element program was chosen. However, if leakage needed to be frequently modelled, one of the more sophisticated methods described below would be more suitable.

The most elegant method of handling leakage would be to implement absorbing (or radiating) boundaries [72,81–84], a special boundary condition that eliminates any reflections from the boundary of the model by matching impedances. Unfortunately, this is a difficult procedure for most of the embedded cases that are considered in this thesis. In order to predict what stresses should be applied to match impedances, the routines generally assume that there is only one incident wave, which is planar and incident at a single angle. However, because each of the modes propagates over a range of phase velocities, there will be a range of leakage angles that approach the boundaries. In addition, there will be both shear and longitudinal modes incident on the boundary. These conditions dramatically complicate the implementation of absorbing boundaries in finite element models.

Another possible method of eliminating the reflections from the boundaries would be to attenuate the waves that leak into the portion of the model that is simulating the surrounding medium. By adding an adequate amount of material damping the amplitudes of the reflections could be small enough that they do not affect the results. However, at the moment of writing this thesis, viscous materials are not supported in the wave propagation portion of FINEL.

A third method requires running the finite element model twice, once with free boundaries and once with rigidly supported boundaries[85]. Since the reflections from the boundaries will be 180 degrees out of phase, combining the two cases allows the first reflection from the boundary to be masked. This technique allows the model to be smaller and improves the display of the displacement fields in the leaky region.

A fourth method relies on using large amounts of computer resources. It simply makes the region that represents the surrounding material large enough that any reflections from its boundaries will occur late enough in time that they are separated from the reflections from the defects that are being studied. This is the method that is used for most of the results that are shown in this thesis since only a few cases need to be evaluated and most of these involve low frequencies which allow a coarse mesh to be used. In

general, the thickness of the surrounding layer has to be 30 times as thick as the internal layer in which the wave propagation is being modelled. Even when the input signal and the geometry of the model are optimised to ensure that the minimum amount of time and elements need to be used, the average finite element calculation used for this thesis still involves 100,000 elements and takes seven hours on a UNIX workstation that was considered to be fast in 1996.

## 5.4 Separation of Propagating Modes - Review of the 2-D FFT

In order to relate the finite element results to the modal wave propagation solution, a method must be developed to determine the amplitude of the propagating modes in the finite element model. If only one mode is present, a simple technique that looks at the maximum amplitude of a displacement component at a node (or the maximum amplitude of the Fourier transform of this signal) can be used. However, when multiple modes overlap in a signal, a more sophisticated technique is required. A second dimension, in addition to the time dimension, must be used to separate the modes. This thesis uses two techniques to perform this extraction. The first of these techniques is the two dimensional Fourier transform (2-D FFT) technique, a well established technique that has already been documented in the literature[76,12]. It has already been used extensively for finite element studies of Lamb wave modes[12,10,79,80]. Its concept is summarized in this section, since it is very relevant to the analysis of the work presented. The second technique, which was developed by the author of this thesis and is presented in the following section, extracts the amplitude of the modes by analysing the through thickness displacement profile.

In the wave propagation models developed in this thesis, guided ultrasonic waves are sinusoidal in both time and space, the wave fields being governed by a complex exponential such as,  $e^{i(kz - \omega t)}$ , where  $k$  is the wavenumber,  $z$  is the distance in the direction of propagation,  $\omega$  is the circular frequency, and  $t$  is the time. Therefore, a two dimensional Fourier transform, which involves both time and space, may be used to resolve the amplitudes of the propagating guided wave modes, even though several modes can exist at any frequency.

As shown schematically in Figure 5.1, the two dimensional transform requires time histories from multiple (typically 64) equally spaced points in space. The desired portion of each signal is gated in time and transformed into the frequency domain. For each frequency, the responses at all of the monitoring points are collected, the collection is windowed, and a second transform is performed to convert the spatial information into the wavenumber domain. In the frequency-wavenumber domain, each of the modes that is present appears as a peak in amplitude. The heights of the peaks can be used to quantify the amount of energy present in each mode as seen in the monitoring region. The width of the peaks in the frequency domain is controlled by the frequency bandwidth of the input signal and the width of the peaks in the wavenumber domain (as seen in 2-D FFT plot) is controlled by the length of the monitoring region. Since a short monitoring region is unable to differentiate between similar wavenumbers, the

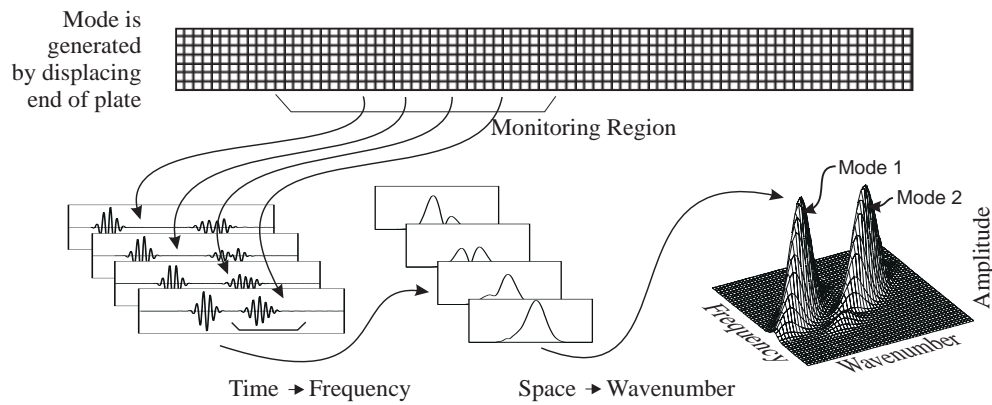


Figure 5.1: A schematic diagram showing how the two-dimensional transform technique[3] determines the amplitude of propagating Lamb wave modes by first transforming time into the frequency domain and then space into the wavenumber domain.

peaks will spread over a wide wavenumber range. As the length of the monitoring region increases, the width of the peaks (in the wavenumber domain) will decrease until the monitoring region is infinitely long and the peaks contain only one wavenumber for each frequency component.

## 5.5 Through Thickness Mode Extraction

This section discusses a second method of extracting the amplitude of separate guided wave modes that are propagating in a finite element model that contains multiple modes. This second technique, referred to as through thickness mode extraction (or simply mode extraction) in this thesis, determines which modes are propagating in a structure given the displacements sampled through its thickness. This contrasts with the 2-D FFT technique, which samples points along the direction of propagation. This section begins by giving a quick overview of the process. Then it discusses its advantages, details of how it works, and some sample results. This mode extraction technique was developed by the author of this thesis, however it is based on a well known orthogonality relationship of guided waves and uses techniques that are relatively common in certain areas of normal mode theory. The novelty of this work derives from the application of the techniques to evaluate time marching displacement based finite element results.

### 5.5.1 Overview of Mode Extraction

The guided wave modes that propagate in a structure are orthogonal to each other[39]. The orthogonality relationship, which is shown below, depends on an integral through the thickness of the structure. The extraction technique developed in this section uses this relationship to determine the unique set of guided wave modes that are present. First, the displacement field of the finite element simulation is sampled at

nodes along a line through the thickness of the structure, perpendicular to the direction of propagation. Then the time histories at each of these nodes is converted into the frequency domain using either a Fourier or wavelet transform. Once in the frequency domain, the displacement profiles at points through the thickness of the model are converted into a series of frequency dependent mode shapes. For each frequency, the analytical mode shapes from the modal model are used to decompose the mode shape derived from the finite element model into the contributions made by each mode. This procedure yields a unique distribution of propagating modes. Unfortunately, the orthogonality relationships that the mode extraction routine uses to determine the contributions of various modes cannot distinguish between forward and backward travelling waves. Therefore, within the time being analysed, the monitoring location can only contain modes that are travelling in one direction. This limitation does not apply to the 2-D FFT technique.

### 5.5.2 Benefits of Using Mode Extraction

When extracting the amplitudes of individual modes from a multi-mode signal, the mode extraction routine has several benefits compared to the two dimensional Fourier transform technique. A major advantage of mode extraction compared to a 2-D FFT is that the mode extraction routines sample the displacement field at a single location along the direction of propagation, as compared to the 2-D FFT method which requires sampling over a region along the direction of propagation. Because of this difference, the finite element model can be much shorter when mode extraction is used since space does not have to be left for the monitoring region. This is especially important for leaky systems, for which the model length must be minimised to allow the models to be reasonably sized. In addition, when attenuation is present, sampling at a single location along the direction of propagation is preferable to sampling over a region in which the amplitude of the modes is changing. The implications of performing a 2-D FFT on signals that contain decaying modes is not fully understood. It is likely that the Fourier transform would need to be replaced by another type of transform, such as Prony's method, which fits complex exponentials to data[86–88]. The mode extraction technique also has the advantage that its results are not smeared in wavenumber in the same way as the two dimensional FFT. The 2-D FFT represents the amplitude of each mode as a region in frequency-wavenumber space that surround the location of the propagating modes. If the monitoring region is not long enough, the regions from separate modes will overlap and complicate the interpretation of the mode amplitudes. However, the mode extraction routine represents the amplitude of each mode as a distinct, unambiguous, line. When wavelet transforms (which can provide frequency versus time graphs) are used with the mode extraction routines, plots of the mode amplitudes with time can be created, which aids the interpretation of the results.

The main disadvantage of the mode extraction routine described in this section is that it is difficult to use on experimental results. The technique requires that the displacement profile is known through the thickness of a structure. Because the technique cannot distinguish between modes that travel in opposite directions, the displacement profile cannot be measured at a free boundary of the structure (where

reflections cause modes to be travelling in both directions). However, this is the only location where displacements can be conveniently measured experimentally. To use information about the displacement at the edge of the structure would require that the ratio of the incoming to the outgoing mode amplitudes is known beforehand (via finite element studies or some other method). Therefore, the technique is essentially limited to finite element simulations. Another disadvantage is the need to calculate the dispersion curves and mode shapes for all of the modes that may be propagating in the structure. The technique requires this information to be able to interpret the finite element results. On the other hand, the 2-D FFT technique provides information about the frequency and wavenumbers that are present independently of any information about the modes that can propagate.

### 5.5.3 Solution Algorithm

The mode extraction process relies on the fact that the guided modes are orthogonal to each other[60]. This orthogonality demonstrates that the energy that is propagating in one mode cannot transfer to another mode unless there is some change in a boundary condition, such as a defect. The orthogonality of the modes also implies that if a composite field is separated into its component modes, the separation will be unique (there is only one possible combination of modes that can make up any given field, just as a Fourier transform will map a time trace into a unique set of frequencies)[38,40]. This section first discusses the Cartesian case and then explains the modifications that are necessary to apply it to cylindrical structures.

The orthogonality relationship for a flat, elastic plate in vacuum is given by Auld in his two volume textbook on acoustic wave fields [39,60]. It is,

$$\langle O \rangle = \int_{-h/2}^{h/2} (\mathbf{v}_m(y) \cdot \sigma_n^*(y) + \mathbf{v}_n^*(y) \cdot \sigma_m(y)) \cdot \hat{z} dy = 0 \quad (5.1)$$

for  $m \neq n$  and  $m \neq -n$

where  $\mathbf{v}$  is the particle velocity vector,  $\sigma$  is the stress tensor, the  $m$  and  $n$  subscripts distinguish the  $m^{th}$  and  $n^{th}$  modes with the  $-n$  indicating the  $n^{th}$  mode with a negative wavenumber (travelling in the opposite direction), the  $*$  superscript represents the complex conjugate,  $\hat{z}$  is the direction of propagation,  $y$  is the direction through the thickness of the plate, and  $h$  is the total thickness of the plate[60]. This relationship is similar to the calculation of the average power flow in a propagating wave, which is simply given as, [39]

$$\langle P_m \rangle = -\frac{1}{2} \int_S (\mathbf{v}_m^*(y) \cdot \sigma_m(y)) \cdot \hat{z} dS, \quad (5.2)$$

where  $S$  is the cross section of the plate or cylinder.

If both the displacement and the stress fields of a propagating multi-mode signal are known, the orthogonality relationship of equation 5.1 can be directly applied to determine the amplitude and phase of the individual modes that combine to produce the composite signal. This application of the orthogonality

relationship works in the following manner. The displacement field is sampled at several points through the thickness of a plate in which a multi-mode signal is propagating. The number of points sampled through the thickness of the plate is usually set to be the minimum number of points that would be necessary for wave propagation in a finite element model of the system to be stable. Then, the time history of the displacement and stress profile for each of the sample points is Fourier transformed to obtain the frequency dependence. For each frequency, the points through the thickness of the plate are used to compile a displacement and stress profile that is specific to that frequency and represents combination of all of the modes that may be propagating in the structure. These displacement and stress profiles are then used for the  $m$  'modes' in equation 5.1. (The orthogonality relationship works in the same manner whether the displacement profile is from a single mode or from the combination of several modes.) The analytical mode shapes (obtained from the modal wave propagation model) for the modes that can propagate at each frequency are used as the  $n$  modes in equation 5.1. To ensure consistency across different frequencies and modes, the analytical mode shapes are scaled so that their total strain energy is always the same. Applying the orthogonality relationship of equation 5.1, which involves integrating through the thickness of the plate, extracts the amplitude of each mode from the composite mode shape. As shown in equation 5.1, whenever the relationship is applied to two different modes the result is zero. However, when mode  $m$  and mode  $n$  in equation 5.1 are the same mode, the result corresponds to the amount of power in a mode. This behaviour also applies when one of the modes is a composite of several modes. For this case, the result of applying the orthogonality relationship yields the amount of mode  $n$  contained in the composite 'mode'  $m$ , which represents the displacement and stress profile in a multi-mode signal. This feature has been frequently used by researchers such as Torvik[89] to decompose the field reflected from the end of a plate into its modal components. Applying the orthogonality relationship for each frequency and each analytical mode quickly provides information about the distribution of the energy of the modes.

To test this mode extraction technique, the modal wave propagation solutions were used to simulate the displacement and stress fields for two different propagating modes (A0 and A1 at around 3.0 MHz-mm frequency thickness) in a 1 mm steel plate. The displacement and stress fields were then added together to obtain the composite field. The mode extraction explained above was performed and the extracted amplitude and phase of the frequency components of the two modes matched the values that were used to create the simulated composite field. When the amplitude scaled and phase adjusted mode shapes of both of the extracted modes was subtracted from the composite displacement profile, the total amplitude of the resulting residue displacements was less than 0.1 percent of the total amplitude of the original displacements. This result indicates that the amplitudes were correctly extracted, since this small amount of error can be attributed to the numerical integration routines and can be dramatically reduced by applying the orthogonality relationship a second time to the residue that remained once the amplitudes of the extracted modes has been subtracted.

However, some difficulties emerge when finite element results are used for the composite signal from which modes are to be extracted. As mentioned before, the finite element model is more 'stiff' than

an actual plate, which is modelled by the modal wave propagation solutions. Therefore, the mode shapes are different and the two systems are not strictly orthogonal. However, a larger source of error comes from inaccuracies in the stress field of the finite element model. Finite element modelling using displacement elements enforces that the displacements are continuous at the nodes, but there are no constraints on the continuity of the stresses across elements[75]. Unless the element can exactly model required stress distributions, which very rarely happens for guided waves, there will be discontinuities in the stresses. In addition, the stresses, which are calculated on an element by element basis, will likely contain errors. In practice, these errors cause the through thickness stress profile to be 'jagged', even when the stresses are shown at the Gauss points, where they should be the most accurate[75]. These errors in the stresses are large enough to render the mode orthogonality relationship useless in the form just presented. The errors in the stress field can be reduced (but not removed) by using a finer mesh. However, the disadvantages of needing to use a finer mesh override any benefits that can be obtained by using this mode extraction technique.

Since the stress field in the finite element model cannot be accurately known, the mode extraction method must be adjusted so that this information is not needed. Examining the orthogonality relationship in equation 5.1 reveals that the relationship consists of the integration of two terms. The first term,  $\mathbf{v}_m(y) \cdot \sigma_n^*(y)$ , multiplies the composite velocity field of the finite element model by the complex conjugate of the stress field of the mode that is being extracted. Both of these components can be calculated in a stable fashion. The finite element model supplies information on the velocity profile of the field, which can be obtained by differentiating the displacement field (multiplying by  $-i\omega$ , since the only time dependence is in the term  $e^{i(\xi z - \omega t)}$ ). The constraints that the displacements must be continuous at node boundaries allows this quantity to be relatively stable. The stress profile is taken from the exact modal wave propagation solutions. The second term in equation 5.1,  $\mathbf{v}_n^*(y) \cdot \sigma_m(y)$ , requires knowledge of the stress field in the finite element model and therefore cannot be accurately calculated. Using only the first term (and ignoring the second) provides a pragmatic (although not mathematically rigorous) solution to mode extraction. However, to be able to ignore the second half of the orthogonality relationship and still extract the correct amplitudes, several modifications must be made to the mode extraction routines.

When only the first half of the mode orthogonality relationship is used, an iterative procedure must be employed to extract the mode amplitudes. The iterative procedure is required because the correct amplitudes cannot be directly calculated as they were for the case when the full orthogonality relationship was used. Instead, each iterative loop provides increasingly accurate estimations of the amplitudes. The procedure progresses in the following manner. First, the frequency dependent displacement profile of the finite element model is calculated in the same manner as described above for the full orthogonality relationship. Then, the iterative loop begins. The first half of the mode orthogonality relationship of equation 5.1,

$$\langle Q \rangle = \int_S (\mathbf{v}_m(y) \cdot \sigma_n^*(y)) \cdot \hat{z} dS, \quad (5.3)$$

is applied to the displacement profile of the finite element model (represented by 'mode'  $m$  in the equation) and each of the analytical modes that can exist at the frequency under consideration (represented

by mode  $n$ ). Each of the 'amplitudes' obtained by this operation is then normalized by the 'amplitude' of the analytical mode shape, which is calculated by applying equation 5.3 to the analytical mode and itself. This division provides an estimate of the amplitude (and phase) of each mode in the composite signal. The mode that has the largest apparent amplitude is used for the next step in procedure. Its analytical mode shape (scaled and phase rotated according to the predicted amplitude) is subtracted from the composite displacement profile obtained from the finite element model. The iterative loop then repeats itself using the new displacement profile. This process stops when the residue of the remaining displacement profile falls below a set tolerance (in comparison to the amplitude of the initial displacement profile). After the amplitudes are calculated at a particular frequency, the process must be repeated for the other frequencies of interest. This iterative technique works well and can usually separate several propagating modes in only a few iterations. The amplitudes that it extracts appear to be stable and unique. For example, when a multi-mode signal in a lossless finite element model is sampled at several points that correspond to different propagation differences, the same mode amplitudes are obtained for each point. In addition, energy conservation concerns and comparisons with the 2-D FFT technique, which are discussed in section 5.5.4, indicate that the amplitudes that are extracted using this through thickness mode extraction technique are correct.

This mode extraction process also works for cylindrical systems. The orthogonality relationship for modes in a free cylinder is very similar to that for a free plate, except that there is an additional integration around the circumference of the cylinder in addition to across its radius[90]. This extra integration applies the orthogonality relationship to the entire cross section of the cylinder, exploiting the fact that modes of different circumferential order are orthogonal to each other. The orthogonality relationship for cylindrical systems can be expressed as,

$$\langle O \rangle = \int_a^b \int_0^{2\pi} (\mathbf{v}_m(r, \theta) \cdot \sigma_n^*(r, \theta) + \mathbf{v}_n^*(r, \theta) \cdot \sigma_m(r, \theta)) \cdot \hat{z} \, d\theta \, dr = 0 \quad (5.4)$$

for  $m \neq n$  and  $m \neq -n$

where  $a$  and  $b$  are the inside and outside radii of the cylinder and  $r$ ,  $\theta$ , and  $z$  are global coordinates. Since the cylindrical finite element models that are used in this thesis all contain axi-symmetric elements, only one circumferential order can ever be present. Therefore, all of the modes present in the model have the same circumferential behaviour and the integration around the circumference is not needed to separate different order modes. For zero order modes, the circumferential integration simply appears as an extra  $r$  term, such that the orthogonality relationship becomes  $\int_a^b (\dots) r \, dr$ . As happened for the plate case, an iterative technique that uses half of the orthogonality relationship must be used to extract the amplitudes of propagating modes when finite element results are being used. This half orthogonality relationship for zero circumferential order cylindrical modes is,

$$\langle Q \rangle = \int_a^b (\mathbf{v}_m(r, \theta) \cdot \sigma_n^*(r, \theta)) \cdot \hat{z} \, r \, dr. \quad (5.5)$$



When the guided wave is leaking energy into an infinite surrounding material, the orthogonality relation does not strictly apply. Auld explains that the orthogonality relationship does not hold when there are losses in the system since it was derived from the complex reciprocity relationship[60]. Therefore, the mode extraction routine may have some difficulties with leaky systems. However, the finite element techniques used in this thesis only allow fundamental modes at low frequencies to be modelled in leaky systems. Therefore, in the cases considered here, there is only one mode present in cylinders and two in plates, so separating the modes is not a difficult problem. In practice, when the orthogonality relation is applied over the finite layer of the structure, the mode extraction routine that is described above has no difficulties in reliably extracting the amplitudes of this limited number of modes.

#### 5.5.4 Results

In order to examine how well the through thickness mode extraction routine works, this subsection examines an example of determining reflection coefficients and compares the mode extraction routine to the 2-D FFT technique. The details of how the reflection coefficients are calculated are given in chapter 6, however, they are summarized here for completeness. In order to determine the reflection coefficients from a feature such as the end of the plate, the amplitudes of the individual propagating modes must be determined both before and after the interaction with the feature. The amplitudes of the modes are usually determined by using the mode extraction technique developed in this section or by the 2-D FFT technique that was reviewed earlier. Dividing the amplitudes of the modes present after the interaction with the feature by the amplitude of the incident mode, the reflection coefficients can be calculated. Depending on the method used to determine the amplitudes of the modes, the reflection coefficients may be in terms of displacement amplitudes or energy contained in the mode. Various conversions can be applied to convert between these different measurements provided that the properties of the modes are well known.

The example developed in this section examines the reflection of the A0 mode from the end of a 1 mm steel plate. The input signal consists of a 15 cycle Gaussian windowed tone burst centred on 10 MHz. When this incident wave reflects off the perfectly symmetric end of the plate, it mode converts into other anti-symmetric modes. For this system, there are five propagating anti-symmetric modes at 10 MHz into which the energy of the incident mode is partitioned. A finite element simulated time trace for this system, which was modelled as 40 by 1000 four-noded plain-strain elements excited using the pure mode method described in the next section, is shown in figure 5.2. The simulated plate, which was 25 mm long, had its displacement monitored 17.5 mm from the end of the plate. In the trace in figure 5.2, the incident wave can be seen passing the monitoring point as well as the reflected modes. The signals that tend to trail behind the main reflected signal correspond to the slowly propagating cut-off modes. As seen in the group velocity dispersion curves in figure 5.3, the velocity of the modes decreases rapidly as they approach their cut-off frequencies. Therefore, when excited near their cut-off frequency, modes will arrive much later than other modes.

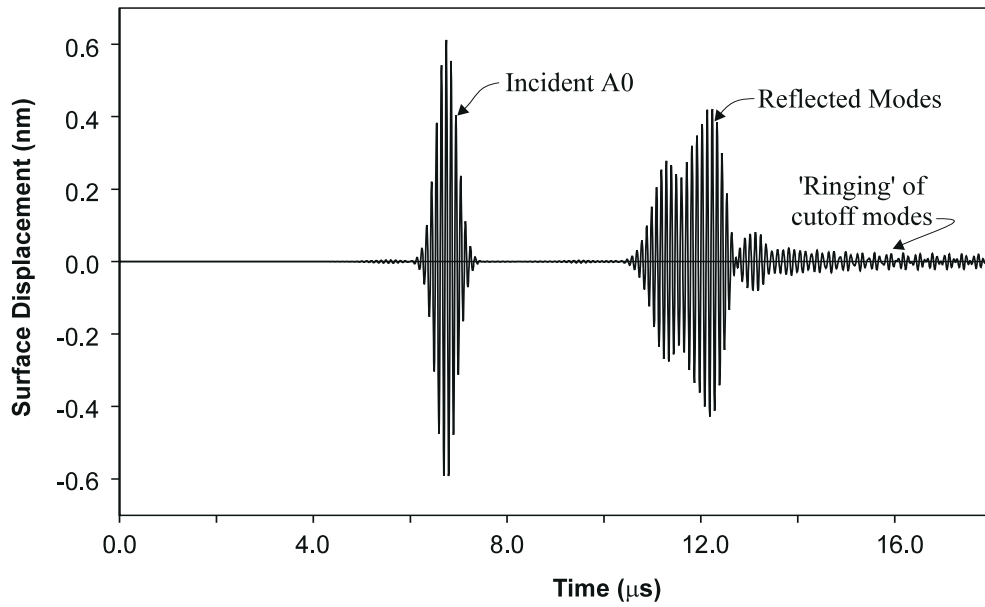


Figure 5.2: An example time trace from the finite element model of the A0 mode reflecting from the end of a 1 mm steel plate.

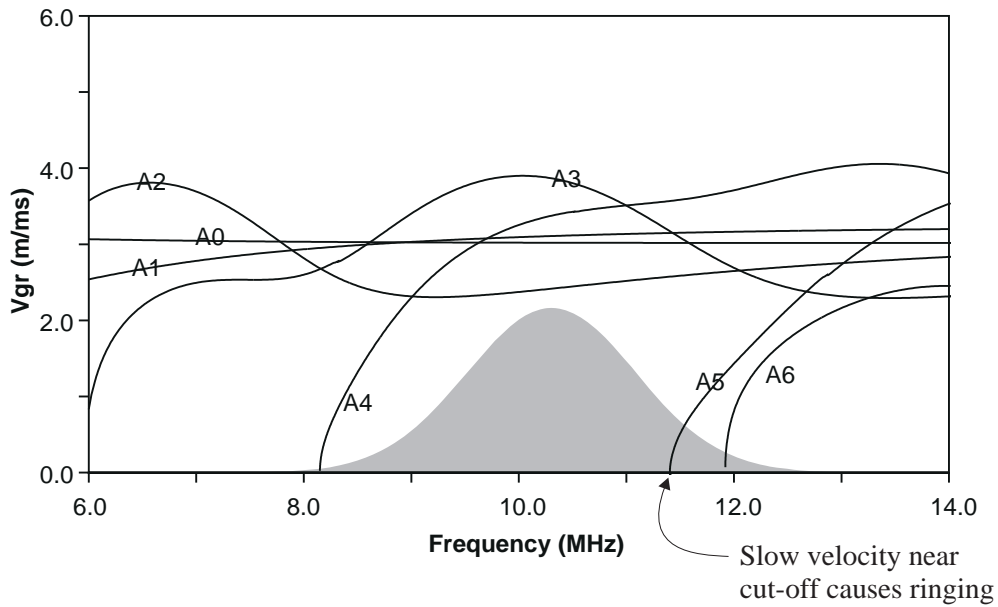


Figure 5.3: Group velocity dispersion curves for the anti-symmetric modes of a 1 mm steel plate. The frequency profile of a 15 cycle Gaussian windowed toneburst is shown as the greyed shape in the background.

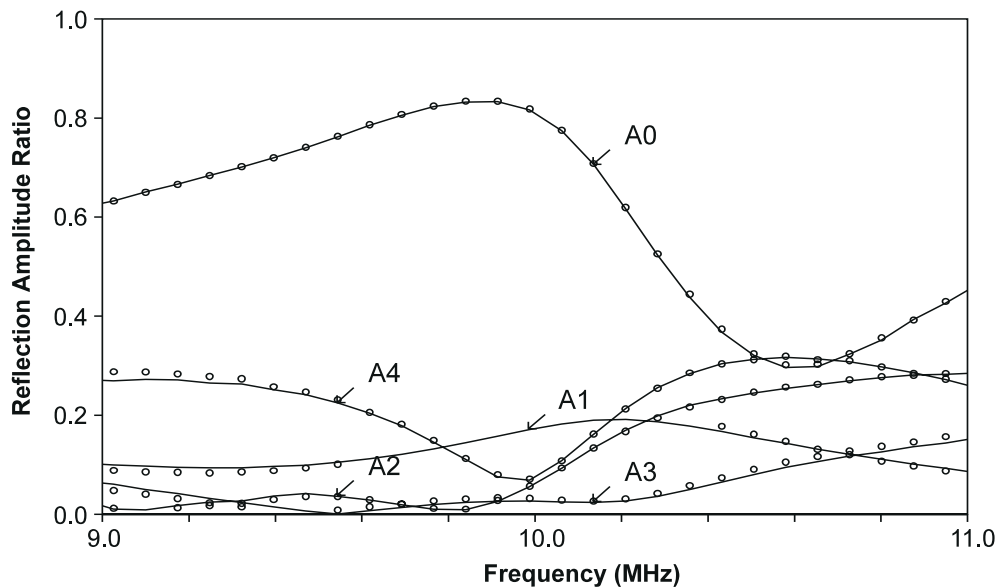


Figure 5.4: The amplitude reflection coefficients (in terms of out-of-plane surface displacement) for the A0 mode incident on the edge of a 1 mm steel plate. The lines represent results obtained from the mode extraction technique and the circles represent results obtained using the 2-D FFT technique.

Figure 5.4 demonstrates the partition of energy between the various modes upon reflection from the end of the plate. It shows the reflection coefficients in terms of the out-of-plane surface displacements. The lines represent the solution obtained using the mode extraction routine, which required that a line of nodes be monitored through the thickness of the plate. The circles represent the solution obtained via a two dimensional Fourier transform, which required that nodes be monitored along the direction of propagation. For all of the modes, there is good agreement between the results from the two types of solutions. The main difference is that a portion of the 2-D FFT data for the A1 mode is missing. The missing data corresponds to locations where the peak extraction routines are not able to distinguish the amplitude of the A1 mode from the amplitude of the nearby (in frequency-wavenumber space) A0 mode in the 2-D FFT, even when the propagating waves were sampled over 100 wavelengths of propagation distance.

Since there are no loss mechanisms in the finite element model and since all of the energy will be reflected from the end of the model, the total power contained in the reflected modes should balance with total power of the incident mode. In order to compare the mode extraction and 2-D FFT routines, this balance was calculated for the centre frequency of the input signal for the reflection coefficients that were obtained with each method. Before this summation of energy could be performed, the reflection coefficients were converted into energy reflection coefficients by using the wave propagation model to relate the observed surface out-of-plane displacement to the total power contained in a mode. When the energy reflection coefficients derived from the mode extraction routine were summed, the total was 100.3 percent of the energy of the incident mode. On the other hand, the total energy reflected as calculated by the 2-D FFT method came out to be 102.7 percent of the input energy (note that mode

extraction data was substituted for the missing 2-D FFT data for the A1 mode). This agreement is excellent for the mode extraction data and good for the 2-D FFT data, whose error is primarily caused by an overestimate of the amplitude of the A3 mode due to interaction with the A4 mode in the 2-D FFT surface.

### 5.5.5 Mode Extraction Conclusions

Determining which modes are propagating in a structure by analysing the through thickness profile of the displacements has proven to be an effective method of evaluating finite element results. This (through thickness) mode extraction technique has several advantages over the equivalent two dimensional Fourier transform technique. Its greatest advantage is that all the data is taken from a single location along the direction of propagation (and multiple points through the thickness at that location). Therefore, finite element models that use this technique can be much 'shorter' than models which must leave a considerable length along the direction of propagation for the monitoring zone. This is especially important for leaky systems, for which the model length is very critical. In addition, sampling at a single point along the direction of propagation simplifies the analysis of the leaky modes since the modes' amplitude does not vary over the region that is being analyzed. Another significant advantage of the through thickness mode extraction technique is that it does not smear the amplitudes of the modes over a range of wavenumbers. The amplitude of each mode is extracted as a single line, corresponding to the frequency and wavenumbers of the mode. This allows the propagating waves to be immediately related to the dispersion curves. However, the 2-D FFT routine produces peaks which can overlap and are difficult to correlate to the dispersion curves in a robust, automated method. Therefore, much more human intervention is required to obtain reliable results when 2-D FFT data is used, especially when one wants to convert the reflection coefficients from one unit, such as out of plane displacements, into another unit, such as energy. This difference exists because the mode extraction technique separates modes by their orthogonality, whereas the 2-D FFT method relies on differences in wavenumber. The through thickness mode extraction technique has some additional advantages. Since the 2-D FFT technique only looks at a single position through the thickness of the structure, it is unable to determine the amplitude of a mode if it has no displacements at that position. The mode extraction routine on the other hand examines the displacements throughout the structure and therefore can always determine which modes are propagating. The mode extraction technique provides information on the total amplitude of each mode, which can easily be converted into an energy or displacement at a particular location in the structure in a stable manner. Because the mode extraction does not rely on the amplitude of a particular displacement component that could be near zero even if the energy in that mode is very large, the amplitudes obtained from the mode extraction routines tend to be more stable than the amplitudes obtained from 2-D Fourier transform techniques. An additional advantage of the through thickness mode extraction routine is that the finite element output files can be much smaller than those needed for a 2-D FFT since fewer nodes need to be monitored. This reduces the required resources and time taken for processing the data.

There are, however, some disadvantages to the through thickness mode extraction technique. The primary disadvantage is that the technique cannot be used on experimental data because the required displacement profile cannot be obtained. Therefore, the method is limited to finite element simulations. Another major disadvantage is the method's reliance on accurate dispersion curves. The method can only detect propagating modes for which it has modal wave propagation solutions. If additional modes are present in the finite element model, they will not be identified by the extraction routine. Their presence will simply cause a large residue to be left. In addition, the technique has difficulties converging at frequencies near the cut-off frequencies of propagating modes. This difficulty can be attributed to the effect of the 'ringing'. Near their frequency cut-offs, modes propagate at a very slow energy velocity, which causes their signals to be spread over a long time region. Since there is no attenuation present in the finite element model, their amplitude will not decrease with time. Therefore, there appears to be a 'ringing' trailing the main signal. Since the finite element model is relatively limited in size, all of the ringing cannot be sampled and the analysis routines must artificially reduce the amplitude to zero after a certain time. Truncating the signal distorts the frequency spectrum of the monitored points and consequently contaminates the displacement field used for input into the mode extraction routines. When the field is not correct, the modes cannot be correctly extracted. The distortion generally appears as ripples in the reflection amplitude plots that occur near the cutoff frequencies are attributed to the side lobes surrounding the incorrectly sampled frequencies. This problem could be greatly reduced by incorporating a small amount of attenuation into the finite element model. This addition would cause the 'ringing' portions of the signal to be attenuated with time so that they could be completely sampled. However, the finite element program that was used does not currently support attenuating materials for acoustic wave time marching. Another weakness of the method is its inability to separate modes that are travelling in different directions.

## 5.6 Pure Mode Excitation

The previous sections have discussed ways that the displacement fields in a finite element model can be expressed in terms of the modal wave propagation solutions. This section examines the opposite problem: how to control which guided waves are excited in a finite element model. Generally, this procedure occurs before mode extraction since the modal wave propagation solutions are usually known and the finite element model is being used to gain more information about the modes. Mode extraction techniques are then used to relate the finite element results back to the modal solutions. However, in this thesis, the mode extraction techniques were presented first because they are needed to analyse effectiveness of the excitation methods.

Precisely controlling which guided waves are excited is important because it allows the effects of the various modes to be studied separately, which greatly simplifies the analysis of a complex system. Since the modes behave in a linear fashion, the behaviour of the individual modes can be later combined to model the complete system.

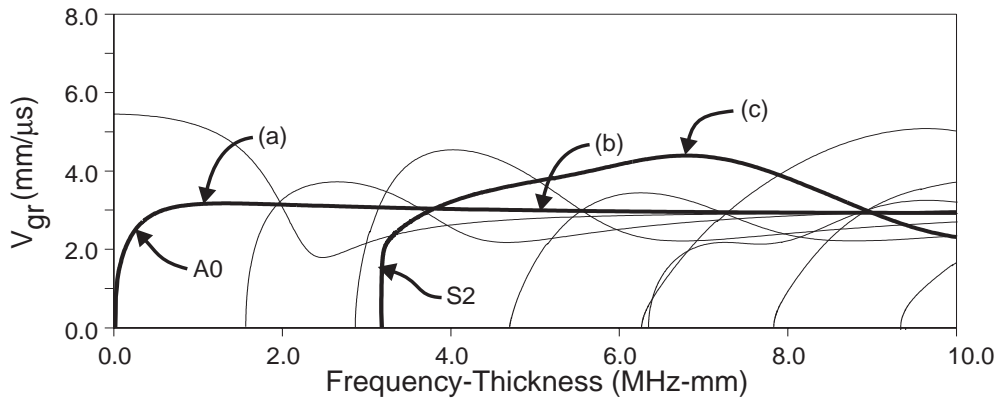


Figure 5.5: The group velocity dispersion curves for an aluminum plate. The three points marked (a), (b), and (c) correspond to the locations where modes are generated in the examples.

This section explores two methods to excite a single "pure mode" by applying a time-varying displacement profile of the desired mode at the end of the plate. Since the modes of a plate are orthogonal at any frequency, if the applied displacement profile properly matches the displacement profile of the mode, only the desired mode will be generated [89]. The simpler of the two methods to produce a pure mode will be referred to as "centre mode shapes". This technique, which assumes that the mode shape is constant over the frequency bandwidth of the input signal, works well to preferentially excite fundamental modes at low frequency-thicknesses. However, there are other locations on the dispersion curves where a more sophisticated technique, such as the one referred to as "exact mode shapes" in this thesis, is required. The exact mode shape technique accounts for the change in the displacement profile of the mode as the frequency changes and therefore concentrates the energy in the chosen mode throughout the excitation frequency range.

This section discusses the procedures that are used to generate pure modes in finite element models and compares the results from the two types of generation. Three different input signals, generated at separate locations on the dispersion curves, will be used to evaluate the two techniques. These locations are shown in figure 5.5, which shows the group velocity dispersion curves for an aluminum plate. The first two points, (a) and (b), are on the A0 mode at 1.0 and 5.0 MHz-mm respectively. The third location, marked (c), is on the S2 mode at its maximum group velocity, which occurs near 6.8 MHz-mm.

The centre mode shapes and exact mode shape techniques that are discussed in this chapter were conceived by David Alleyne[12]. His original work was expanded by the author of this thesis to include multiple layers, cylindrical geometries, and leakage into a surrounding material. In addition, the author has fine tuned the method to provide for the pure generation of high order modes and has incorporated it into the general purpose wave propagation modelling software, Disperse. Integration of the routines into Disperse involved calculating the displacement profiles (mode shapes) using the global matrix method instead of analytical solutions for a single layered plate in vacuum, which were previously used. As explained in subsection 5.6.4, this change also required that all of the mode shapes were treated as complex quantities, so that leaky guided wave propagation could be properly modelled.

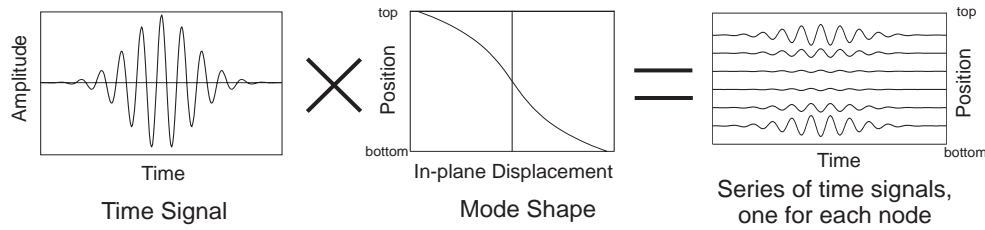


Figure 5.6: A schematic view of how the centre mode shape technique scales the input signal by the displacement profile at the desired centre frequency.

### 5.6.1 Centre Mode Shapes

The "centre mode shape" technique represents a first attempt to generate a pure mode by prescribing a displacement profile at the boundary of a finite element mesh[12]. For the technique to work, the displacement profile of the desired mode must be known. The mode shape, which specifies the stress and displacement profiles through the thickness of the plate, is a part of the modal information for a plate that can be extracted from the wave propagation solutions.

The displacement profiles in the two directions in the plane of the model are calculated at the centre frequency of the chosen input signal. Then the input time signal at each node at the end of the finite element mesh is simply scaled according to the amplitude of the displacement at that location in the mode shape profile. The process is applied in both displacement directions, and a phase difference is introduced between the two components as appropriate. (This phase shift is fixed at 90 degrees for an elastic plate in vacuum.) The scaling operates in the time domain and produces a series of inputs to be used by the Finite Element model. This process is shown schematically in figure 5.6 for the A0 mode at low frequency. Since guided wave modes are orthogonal to each other, if the displacement profile is correct for a single mode, only that mode is excited [89].

This technique works well to generate some modes. For example, figure 5.7 shows the 2-D FFT results and a sample time history when the A0 mode is generated at 1.0 MHz-mm (point (a) in figure 5.5), using a 12 cycle Gaussian windowed tone-burst. The dispersion curves for the system, which were originally shown in the frequency-group velocity domain in figure 5.5, have been converted into the frequency- wavenumber domain and overlaid on the contour plot below the two dimensional transform to help identify the modes that are generated. The jagged edges on the contours are an artifact of the interpolation of the surface plot; in reality, the contours are smooth. Only one peak appears in the 2-D FFT plot revealing the presence of only one mode. Consequently, the sample time trace from a monitoring point on the surface of the plate is clean and easy to interpret.

However, when the frequency of the input signal is increased or the number of cycles in the input signal is reduced, this basic strategy is problematic. Figure 5.8 displays the results when the A0 mode is generated at 5.0 MHz-mm (point (b) in figure 5.5), using a 2 cycle Gaussian windowed tone-burst. In addition to the desired A0 mode, the A1, A2, and A3 modes are also generated, as evidenced by the humps in

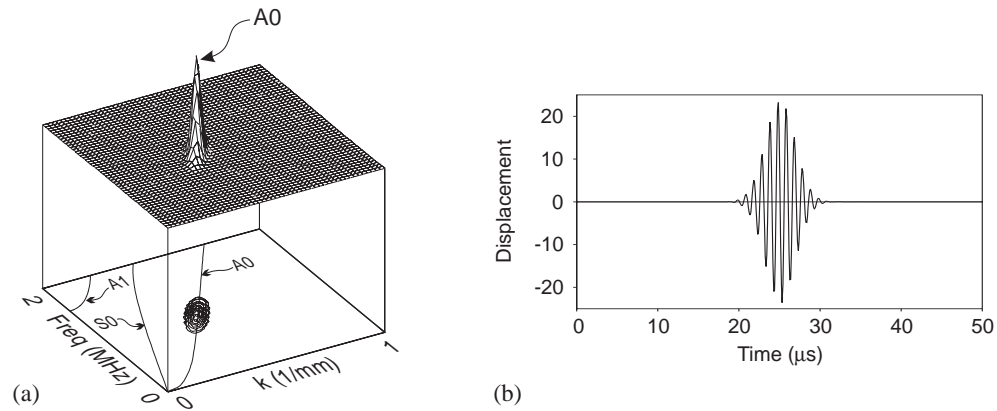


Figure 5.7: The (a) 2-D FFT and (b) sample time history for the generation of the A0 mode at 1.0 MHz using the centre mode shape technique and a 12 cycle Gaussian windowed tone-burst.

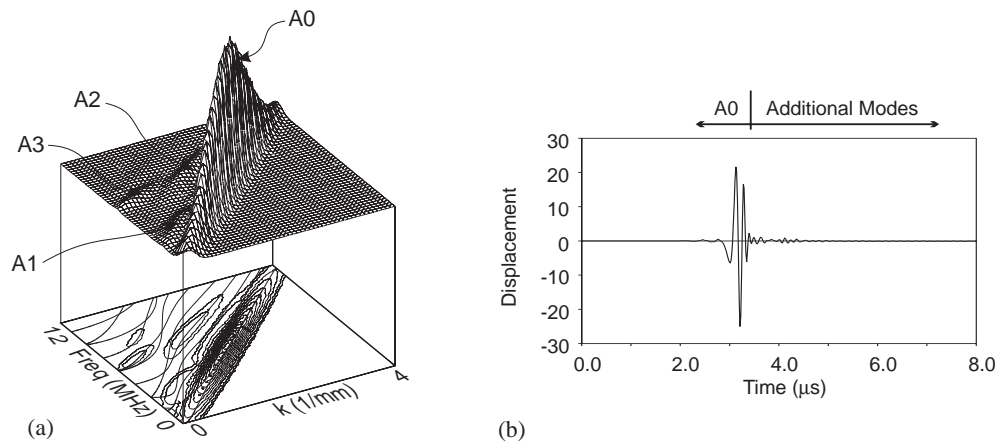


Figure 5.8: The (a) 2-D FFT and (b) sample time history for the generation of the A0 mode at 5.0 MHz-mm using centre mode shapes and a 2 cycle Gaussian windowed tone-burst.

the 2-D FFT plot. The presence of these modes also contaminates the sample time history that is shown in part (b) of the figure. The small ripples that occur later in time than the main signal correspond to these undesired modes. Even in these small amounts, the additional modes would complicate the interpretation of signals that have been reflected from simulated defects. For example, their presence could easily mask an echo from a small defect.

Another example when the centre mode shape technique fails to produce a pure mode is when higher order modes are being generated. For example, figure 5.9 shows the results obtained when centre mode shapes are used to generate the S2 mode at its maximum group velocity, at 6.8 MHz-mm (point (c) in figure 5.5), using a 10 cycle Gaussian windowed tone-burst. Both the S3 and S1 modes are easily identified in the two-dimensional transform. These modes also appear in the time domain signal, occurring later in time than the main S2 signal.



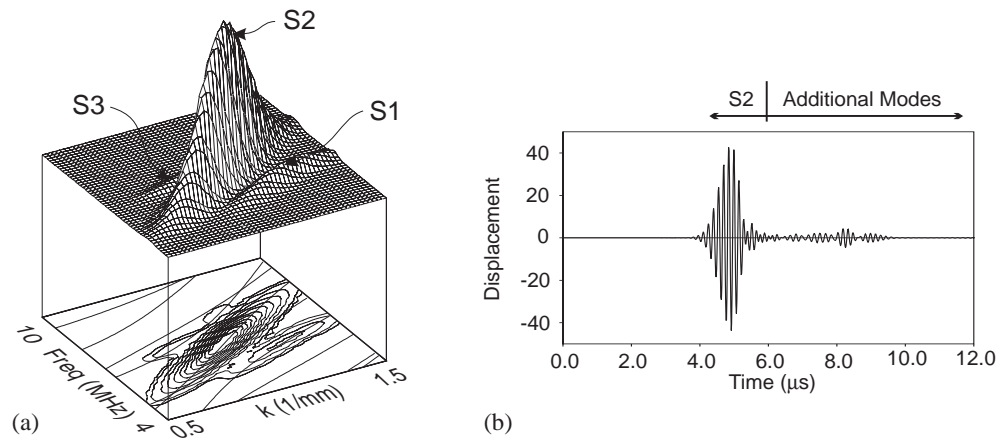


Figure 5.9: The (a) 2-D FFT and (b) sample time history for the generation of the S2 mode at its maximum group velocity using centre mode shapes and a 10 cycle Gaussian windowed tone-burst.

The generation of additional modes in these two cases can be attributed to the fact that the input displacement profiles do not match the mode at all of the frequency components that are present in the excitation signal. Implicit in the direct scaling of a single time history is the assumption that the mode shapes are constant for all frequencies. However, in reality, the mode shapes change with frequency. Therefore, the centre mode shapes technique will impose an incorrect mode shape at all frequencies where the mode shapes are different from that at the centre frequency of the input signal. The residual components at these frequencies generate additional undesired modes.

### 5.6.2 Exact Mode Shapes

The generation of additional modes can be eliminated if the input signal accounts for the frequency dependent changes in mode shapes. These changes can be accounted for by operating in the frequency domain, using a technique called "exact mode shapes". This technique operates by combining the frequency dependent displacement profiles of a mode with the frequency spectrum of the desired input signal [12].

The first step of the process involves choosing the desired waveform, for example a 10 cycle Gaussian windowed tone burst centred at a particular frequency, and calculating its frequency spectrum using a Fourier transform. The displacement profiles of the desired mode are then calculated for every frequency component at which there is significant amplitude ( $> 0.1$  percent of the maximum amplitude of the frequency response). The amplitudes of the displacements are scaled so that the total strain energy held in the mode is the same for every frequency in the bandwidth of the excitation signal.

The second step multiplies the frequency spectrum of the input signal and the frequency dependent displacement profiles. For each node through the thickness of the finite element mesh, the multiplication process steps through all of the significant frequency components in the input signal. The value of each

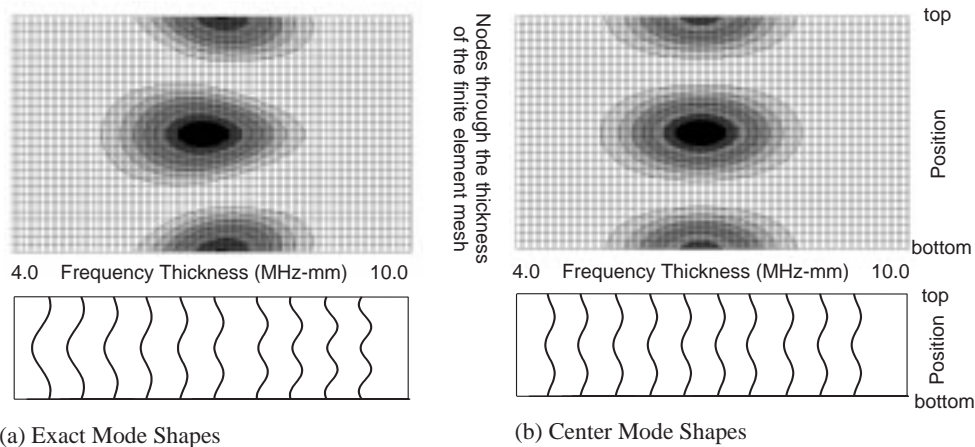


Figure 5.10: A contour view and profile of the displacements in the direction of propagation of the S2 mode as a function of frequency-thickness and position through the thickness of the plate using (a) exact mode shapes and (b) centre mode shapes. The amplitudes shown in the contour view account for generation by a 10 cycle Gaussian windowed tone-burst at 6.8 MHz-mm.

frequency component in the signal is multiplied by the value of the mode shape displacement at that location in the thickness of the plate and at that frequency. The result can be considered to be a matrix whose rows contain the significant frequency components, whose columns contain the nodes through the thickness of the plate, and whose values are the displacement. A contour view of the amplitude of this matrix can be seen in figure 5.10, which plots the magnitude of the displacement in the direction of propagation of the S2 mode (i.e. the in-plane displacement) at its maximum group velocity in an aluminium plate (point (c) in figure 5.5) as a function of frequency-thickness at 30 positions through the plate. For comparison, figure 5.10b shows the same matrix as it would look when the centre mode shapes technique is used. Below each of the contour plots, and sharing the frequency-thickness axis, is a strip showing the displacements in the direction of propagation of the S2 mode that were used for these calculations. (Please note that the displacement profiles shown in the strip have not been windowed by the frequency profile of the input signal, however the values in the contour plot have been.) There is a significant change in the displacement of the S2 mode around its maximum group velocity, which will cause the frequency spectra applied to the various nodes to vary also.

The final step that is used for the exact mode shapes technique converts the scaled frequency spectra into time histories using inverse Fourier transforms. The resulting time histories are then applied to the end nodes of a finite element mesh. As the finite element model marches forward in time, a pure mode is generated.

The benefit of using exact mode shapes can be seen in figure 5.11 and figure 5.12, which show the results of applying exact mode shapes to the two cases with which the centre mode shapes technique had difficulties (see figures 5.8 5.9). For both of the cases, A0 generated over a wide frequency bandwidth and S2 generated at its maximum group velocity, the 2-D FFT results indicate the presence of only one generated mode. The time traces are also much simpler to interpret than they were for the centre mode

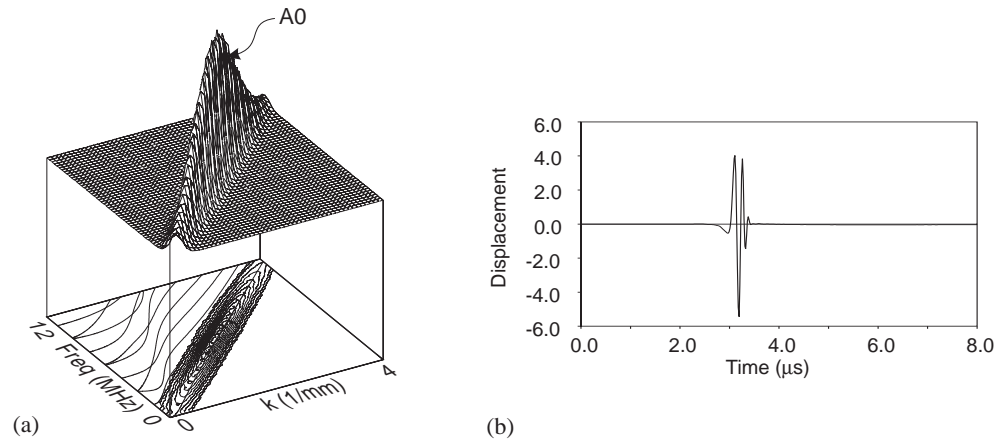


Figure 5.11: The (a)2-D FFT and (b)sample time history for the generation of the A0 mode at 5.0 MHz-mm using exact mode shapes and a 2 cycle Gaussian windowed tone-burst.

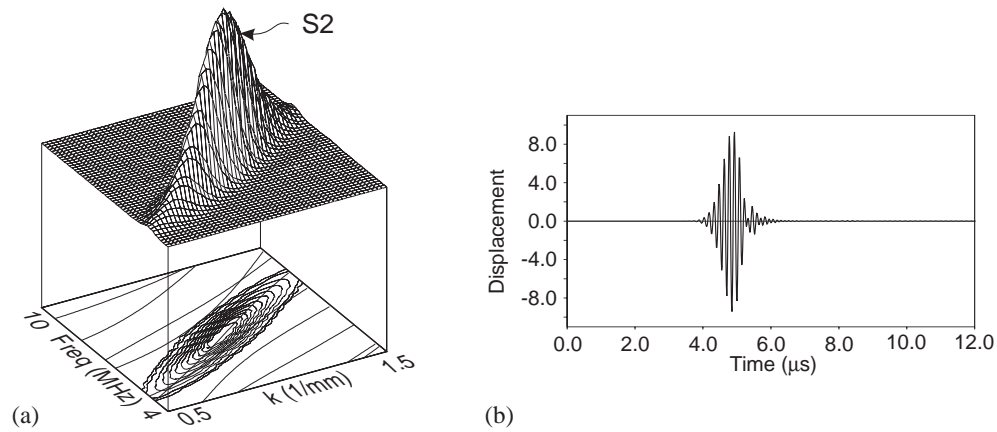


Figure 5.12: The (a)2-D FFT and (b)sample time history for the generation of the S2 mode at its maximum group velocity using exact mode shapes and a 10 cycle Gaussian windowed tone-burst.

shapes cases. The effect of dispersion can be seen for both cases; the low frequency components of the A0 mode arrive first and the tone burst envelope of the S2 mode has increased in duration, decreased in amplitude, and changed shape as various frequency components interfere. However, the influence of secondary modes is not evident as it was for the other generation method.

### 5.6.3 Cylindrical Example of Exact Mode Shapes

The exact mode shapes technique works equally well for cylindrical systems as it does for Cartesian ones, since the modes in a cylinder are also orthogonal to each other. However, some slight changes must be incorporated into the exact mode shapes technique to deal with cylindrical systems.

Instead of treating the system as plane strain, the constraints are adjusted so that the system behaves in an axi-symmetric manner. This constraint condition allows the complete cylinder to be modelled using

two dimensional elements, instead of constructing a large three dimensional model. Unfortunately, this constraint also means that the non-axi-symmetric features cannot be modelled and that there can be no conversion between modes of different circumferential order. Except for a few cases, high order flexural modes cannot be modelled. Pure flexural modes cannot be generated because the finite element program that was used, FINEL, assumes that all of the displacement components (radial, axial, and circumferential) that are prescribed as input to the model obey the same phase relationship around the circumference of the cylinder. However, for the flexural modes of a cylinder, the circumferential displacement is ninety degrees out of phase with respect to the radial and axial displacements. For example, for the first circumferential order, if the radial component reaches its maximum at zero degrees (a cosine relationship), the circumferential component reaches its maximum at ninety degrees (a sine relationship). Therefore, a pure flexural mode cannot be generated in the finite element model. However, if one of the displacement components completely dominates the displacement profile of the mode and there are not many modes possible, a relatively pure mode can be generated by correctly forcing the displacement profile in the dominant direction and allowing the other directions to find their own equilibrium. A pure mode could be generated using a full three-dimensional mesh, however, the mesh can quickly become prohibitively large even for simple cases and leaky cases with a full three dimensional model are out of the question. Another implication of the axi-symmetric constraint is that the solution becomes unstable at zero radius. Therefore, when solid bars are being modelled, a small hole (typically one percent of the bar radius) is placed down the middle of the bar to avoid the region of instability. Constraining the radial displacement around this small hole to be identically zero for the longitudinal modes helps remove any possible effects that the hole may create. There is good agreement between the modal wave propagation solutions and the finite element results that are obtained when this small hole and radial constraint are present. Therefore it is believed that this adjustment has little effect on the solutions. A final change that must be made for pure mode generation in cylindrical systems using FINEL concerns the orientation of the mesh. For Cartesian systems, the plate is usually oriented so that it is horizontal. However, the axi-symmetric constraint requires that the system be symmetric about the y-axis. Therefore, all of the mesh generation routines must be modified so that the system is vertical.

An example of the effect of using exact mode shapes for cylindrical systems can be seen in figure 5.13, which shows the effect of generating the L(0,2) mode in a steel bar at its maximum group velocity (around 2.5 MHz-mm frequency radius product - see figure 3.2) with a 15 cycle Gaussian windowed tone burst (monitoring axial displacements). Figure 5.13(a) shows the results when the centre mode shape technique is used to generate the mode. Significant amounts of the L(0,1) and the L(0,3) modes are also generated. These modes appear as the smaller, slower tone bursts that follow the main signal in the simulated time trace. Figure 5.13(b) shows the results when the exact mode shapes technique is used. Using this technique, neither the 2-D FFT nor the simulated time trace show significant quantities of undesired modes.

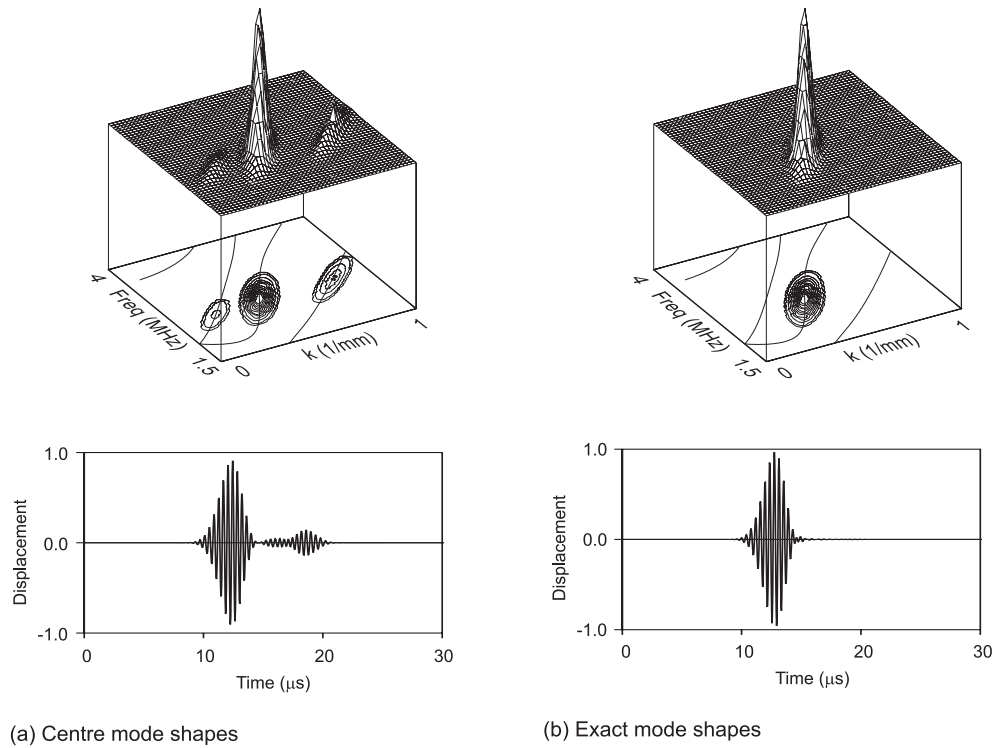


Figure 5.13: The 2-D FFTs and sample time histories for the generation of the L(0,2) mode in a steel bar at its maximum group velocity (around 2.5 MHz-mm frequency-radius) using (a) centre mode shape and (b) exact mode shapes, both with a 15 cycle Gaussian windowed tone burst.

### 5.6.4 Leaky Example of Exact Mode Shapes

Some changes to the pure mode generation techniques are also required in order to handle systems that leak energy into a surrounding medium. The attenuation present in leaky modes creates a phase difference between different points in the mode shape that was not present for the non-attenuative, free case[10]. Since the centre mode shapes technique enforces a fixed phase difference between the in and out-of-plane displacements, this technique cannot properly describe leaky systems, for which the phase between the displacement components changes through the thickness of each layer. Therefore exact mode shapes will be used exclusively. The phase differences continue into the surrounding material where they appear as a time shift if the frequency dependent mode shape information is inverse Fourier transformed into the time domain. The resulting time shift allows the propagating wave to obey causality, such that the leaky guided wave in the internal layers creates a bulk wave in the surrounding medium, which then propagates away from the structure.

Leaky problems involve the generation of waves in the surrounding material in addition to the internal layers. The waves in the surrounding material are bulk waves that have leaked out of the structure. These bulk waves can be set up by either forcing the edge of the surrounding material with an appropriate displacement or by propagating a wave in the internal layers and allowing the leaky waves to establish themselves. Although the second option of forcing only the internal layers is much simpler to implement, forcing the edge of the surrounding material in addition to the internal layers has several advantages. Since the mode shape is formed by both the displacement in the surrounding material and the displacement in the internal layers, marginally better mode selectivity can be gained by forcing throughout the entire cross section of the model. However, this effect is only really noticed for high order modes. The more dominant effect of only forcing in the internal layers is mainly cosmetic. When the displacements at the edges of the surrounding material are not constrained (by enforcing what they should be), a surface wave is generated on this free edge. This surface wave interferes with the leaky bulk wave and causes the displacement field to look distorted when a snap shot of the entire field is viewed. The effect of forcing only the internal layers as compared to forcing the entire cross section is shown in figure 5.14, which shows displacement snap shots of the L(0,2) mode of a steel bar (with a small hole down the centre) embedded in grout for the two different loading conditions. For both of the snap shots, the first twenty elements on the left represent the 1 mm radius of the steel bar and the elements to the right of those represent the grout. The wave was generated at the bottom of the model and propagates towards the top. The reflection of waves from the right boundary was removed by running the case twice, once with free boundaries and once with fixed boundaries, and then adding the results together. The large amplitude surface wave that is generated along the bottom of the model in figure 5.14(a), can exist because the displacements on the boundary are not forced to obey the mode shape of the leaky guided wave. This wave does not appear when the edge of both the steel bar and the surrounding grout is constrained.

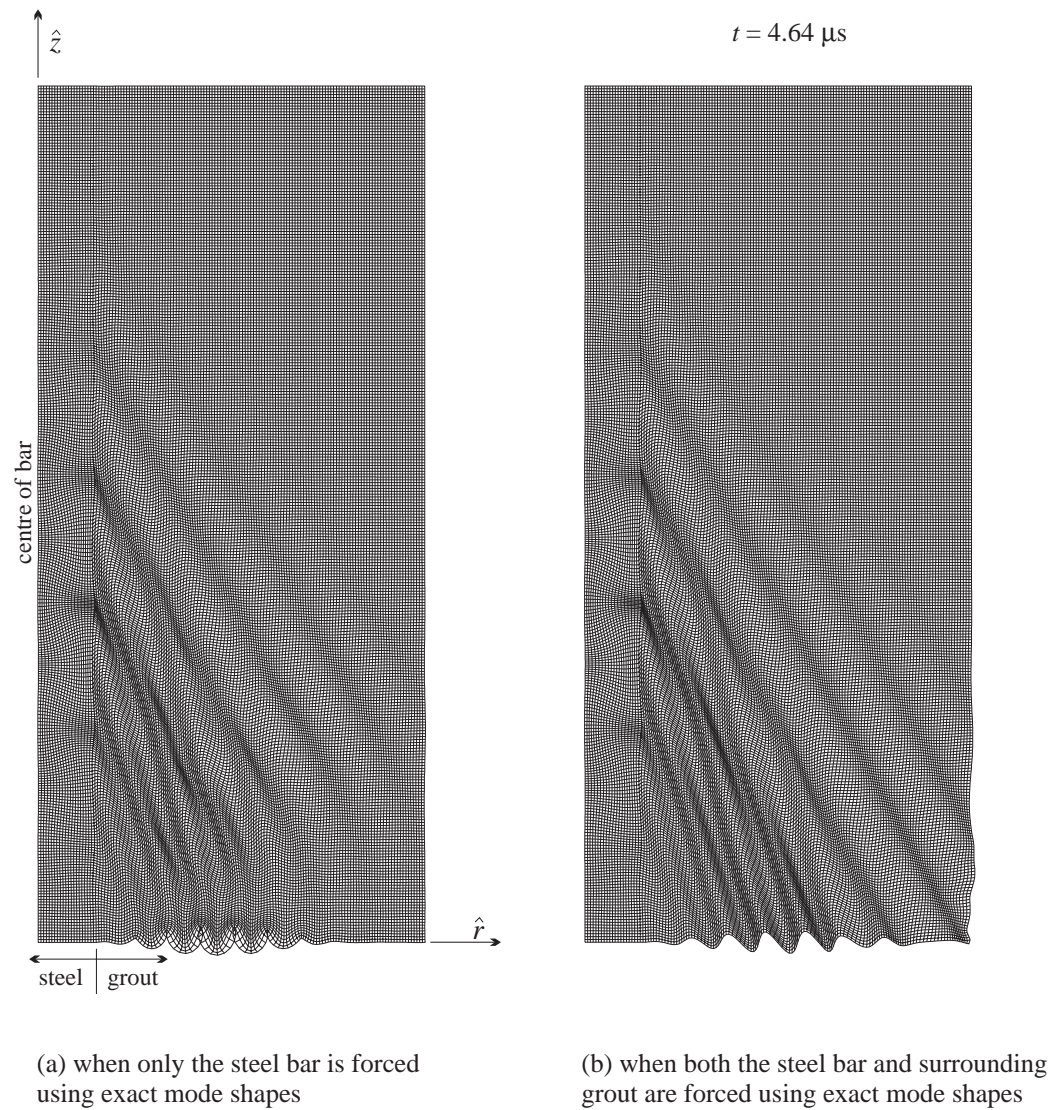


Figure 5.14: Snap shots (in time) of the displacement field as a 10 cycle Gaussian windowed tone burst of the L(0,2) mode of an embedded steel bar propagates, when (a) only the nodes in the steel bar are forced and (b) when both the nodes of the steel bar and the surrounding grout are forced.

For the cases considered, it has been possible to generate a pure mode even when leakage is present. This is encouraging because the leaky modes are not strictly orthogonal to each other unless their extent from zero radius to infinite radius is considered. As discussed in chapter 4, the close agreement between the attenuation values extracted from the finite element results and the wave propagation model validates the two techniques: a pure mode can be generated by using exact mode shapes and its propagation characteristics match those predicted by independent analytical modelling.

### 5.6.5 Summary of Pure Mode Excitation

Attempting to generate a mode without considering its changes in mode shape can lead to the generation of undesired modes. The presence of additional modes complicates the analysis of guided wave behaviour. However, a technique presented in this chapter, exact mode shapes, can create a pure mode excitation for finite element models by accounting for changes in the mode shape that occur with frequency.

Accounting for the frequency dependent changes in mode shapes has an especially important effect on two types of cases: when wide frequency bandwidths (i.e. a few cycles) are used and when higher order modes are being modelled. The wide frequency bandwidth case benefits because the displacement profiles can change significantly over the frequency range and other modes can be generated when there are large discrepancies between the actual and imposed mode shapes. The high order mode case benefits because there are usually many other possible modes in the frequency range being studied, so any small errors in the profiles will cause complicated multi-mode signals to be generated.

Although in experiments, an exact displacement profile cannot be specified through the thickness of plate in order to generate a pure mode, various other techniques, such as incident angle or interdigital transducers, can be combined with time gating to ensure that a single mode is received. The results of finite element models that use pure mode excitation predict how the modes that are generated will react so that an optimum test procedure can be developed quickly and inexpensively.

The techniques for combining the modal wave propagation solution and the complementary finite element model solutions that were developed in this chapter, will be applied in the following chapter to examine the reflection coefficients from embedded defects in bars. These reflection coefficients are then used in chapter 7.



## **Chapter 6**

# **Finite Element Determination of Reflection Coefficients**

When designing a non-destructive testing strategy that relies on detecting the reflection of guided ultrasonic modes from defects, it is important to know how the various modes will interact with the defects. Since the modal wave propagation solutions do not provide this information, alternative methods, such as finite element modelling, must be used. This chapter examines how finite element modelling can be combined with the modal wave propagation solutions to determine how guided ultrasonic waves will reflect off simulated defects and how much energy will be transferred between the modes.

Finite element modelling has been used extensively to model the interaction of lamb waves with simulated defects both within the Imperial College NDT Laboratory [12,10] and in other non-destructive testing laboratories[91–94]. The first section of this chapter highlights the methods that have been used in this previous work via an example. The following section extends the previous work to examine the reflection coefficients for the fundamental modes of embedded systems. Comparisons are drawn between the reflection behaviour of the free and leaky systems. Later sections extend the previous work to examine the reflection coefficients of high order cylindrical modes, such as the ones proposed in chapter 7 for testing post tensioned bridges.

### **6.1 Review of Techniques for Low Frequency Free Systems**

The reflection of the fundamental modes of a plate from a defect will be used to illustrate the principles of determining reflection coefficients from finite element results. This basic procedure is straight forward and has been discussed by many other authors in the field, including those in references [12,10,80].

The reflection and transmission coefficients simply display the ratio of each mode that will be reflected or transmitted. The ratio is typically displayed as either an amplitude or as an energy ratio. Provided that the nature of the mode is known, one type of coefficient can be converted into the other, as described later. Since guided ultrasonic waves behave in a linear fashion, the reflection coefficients are determined by simply dividing the amplitudes of the modes that have been reflected off of a simulated defect by the amplitude of the incident mode. The amplitudes of the propagating waves can be determined by several means. If there is only one non-dispersive mode, the peak amplitude of the appropriate portion of the signal can be used. However, if the mode is dispersive, the shape of the pulse will change shape as it travels. Therefore, simply using the peak amplitude will cause the results to be incorrect. In this case, it is better to Fourier transform each relevant portion of the signal and use the amplitude of a particular frequency component for the analysis. When there are multiple overlapping modes or frequency dependent reflection coefficients are required, a more sophisticated method of extracting the mode amplitudes is suggested. Such methods include a 2-D FFT or the mode extraction technique described in the previous chapter. This method of determining the reflection coefficients relies on there being only one mode incident on the simulated defect. If multiple modes are incident, much more complicated analysis routines would be necessary. Fortunately, by controlling the excitation and accommodating the frequency dependent nature of the mode shapes, single pure incident modes can be generated as described in section 5.6. Transmission coefficients are obtained in the same manner as reflection coefficients, except that the signal is monitored at a location beyond the simulated defect.

An example of the interaction of the S0 mode with a defect is shown in figure 6.1, which shows snapshots of the greatly exaggerated displacement field in a finite element simulated 1 mm steel plate with a defect that extends halfway through its thickness. The S0 mode is generated at the left end of the plate and it propagates towards the defect that is near the middle of the plate. Upon interaction with the defect, the mode is partially reflected and partially transmitted. In addition, the A0 mode, which travels more slowly, is also generated at the defect and propagates in both directions. A monitoring region, which is shown on the figure, is used to sample the displacement field for input into the mode extraction routine. The sampled time trace from one of these points (for a longer model) is shown in figure 6.2, in which the incident mode can be seen passing as well as the reflection from the defect and re-reflections that occur as the reflected waves are reflected off the left edge of the model. The reflection coefficients obtained from this case are shown in figure 6.3, along with the transmission coefficients that were calculated by monitoring a region to the right of the simulated defect. The solid lines represent transmission coefficients and the dashed lines represent reflection coefficients.

The reflection and transmission coefficients that are shown in figure 6.3 represent the amplitude of the respective modes that will be reflected / transmitted. Although the amplitude reflection coefficients are very useful, it is often helpful to know the proportion of power that is distributed into the various modes, so that conservation of energy can be used to validate the model. The ratio of the reflected / transmitted power to the input power will be referred to as energy reflection coefficients in this thesis. The energy reflection coefficients are calculated from the amplitude reflection coefficients in the following

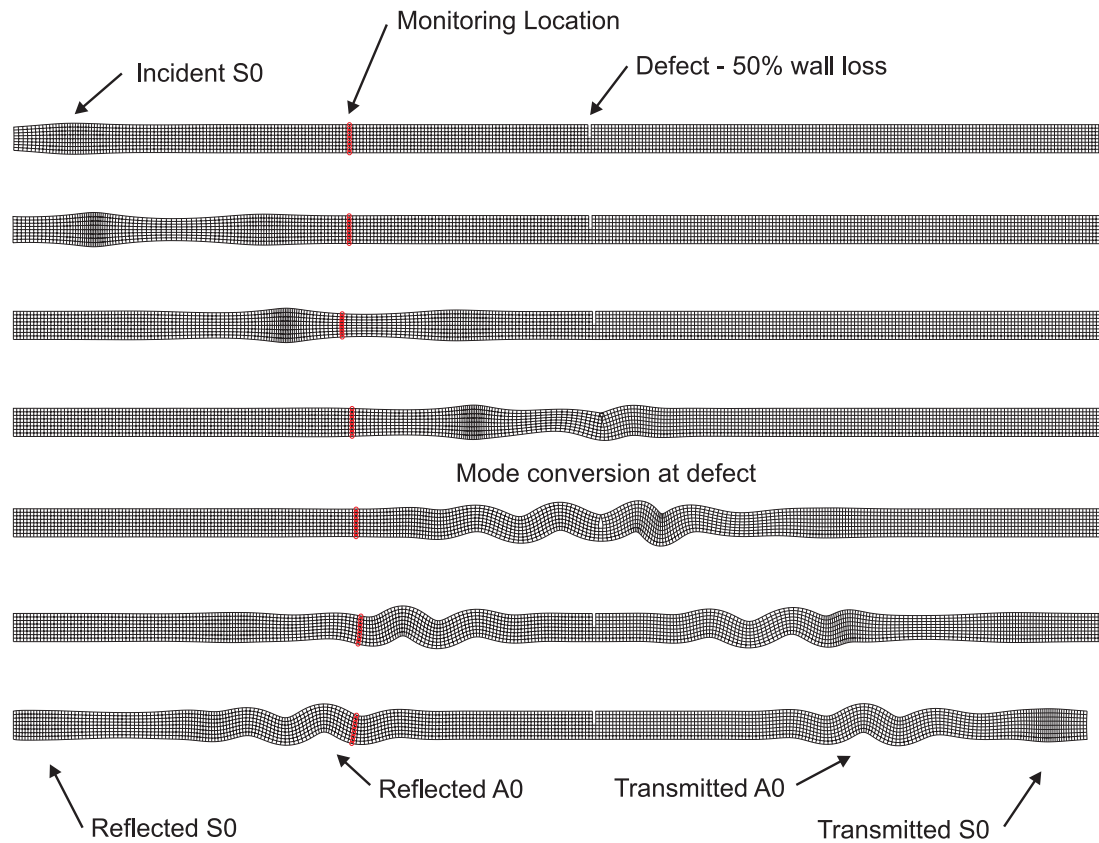


Figure 6.1: Series of snap-shots of the S0 mode in a steel plate reflecting from a 50 percent loss of section. The circles represent nodes whose displacements were monitored.

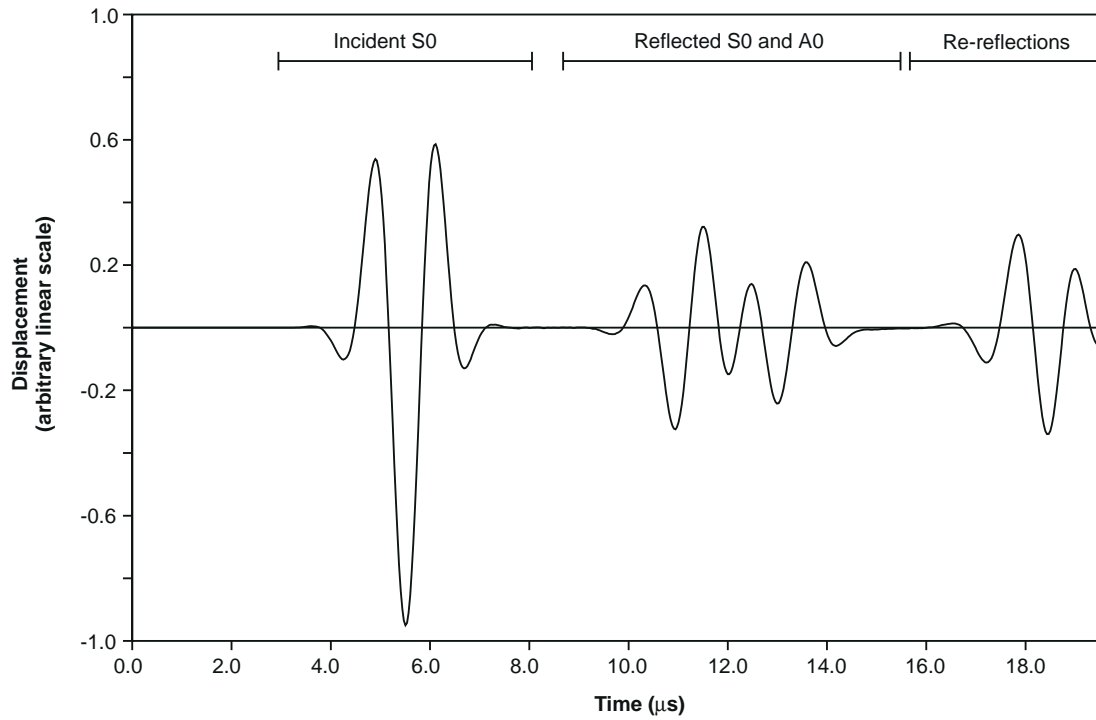


Figure 6.2: A sample time trace from the top monitoring location shown in the previous figure.

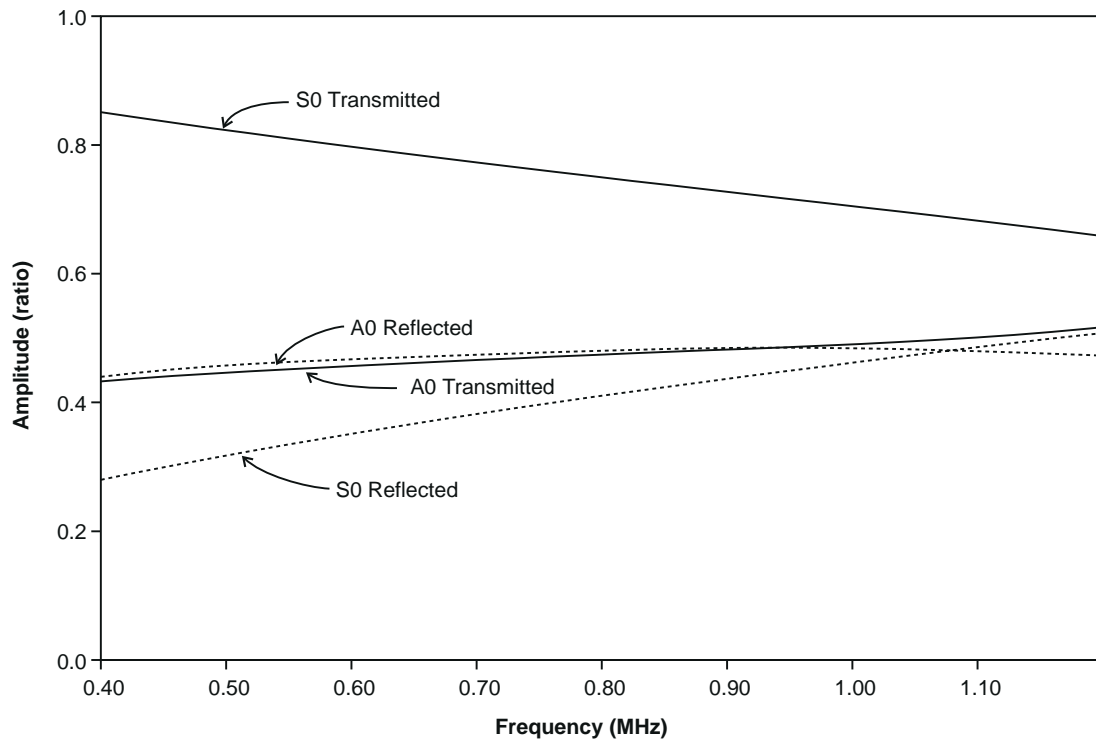


Figure 6.3: Amplitude reflection coefficients for the S0 mode in a 1 mm steel plate impinging on a notch that extends half way through the thickness.

manner[80]. The time averaged power in a mode is given by the expression [60],

$$\langle \mathbf{P} \rangle = \frac{1}{2} \int_{-\infty}^{\infty} (\mathbf{v}(y) \cdot \sigma^*(y)) \cdot \hat{z} dy \quad (6.1)$$

where  $\hat{z}$  is a unit vector in the direction of propagation,  $y$  is the through thickness direction,  $\mathbf{v}$  is the particle velocity vector, and  $\sigma^*$  is the complex conjugate of the stress vector. As can be seen in equation 6.1, the power is a product of the velocity and stress vectors. Since the amplitude of each of these vectors is linearly proportional to the displacement, the energy carried in a mode will be proportional to the square of the displacement. In addition, there will be a scaling factor,  $E_n$ , that relates the square of the displacement of mode  $n$  (at a specific point) to the power in the mode[80]. When the amplitude of the mode is only known at a specific location, such as the surface, and a specific direction, such as the out-of-plane displacement,  $y$ , Disperse determines the appropriate scaling factors by calculating the mode shape and dividing the power of the mode (calculated using equation 6.1) by the square of the appropriate displacement amplitude. This technique is used when the modes are extracted using a technique such as the 2-D FFT. However, the through thickness mode extraction technique does not provide the displacement amplitude at a particular point in the structure. Instead, it yields an overall amplitude of the propagating mode, which can be related to actual displacements by multiplying it by the mode shape of the mode. In this case, the scaling factors,  $E_n$ , are simply proportional to the energy velocity of the mode (which is equivalent to the group velocity when there is no attenuation[71,60]).

Figure 6.4 shows the energy reflection coefficients corresponding to the amplitude reflection coefficients in figure 6.3. The line marked 'Energy Sum' represents the summation of the energy reflection and transmission coefficients. When there are no loss mechanisms, this energy sum should be unity for all frequencies. For the case shown, the power of the various modes sums to  $1.000 \pm 0.003$ , which corresponds to less than 0.5 percent of error. For more complicated cases, i.e. those that contain more modes, the error generally increases, but remains less than two percent for all of the non-leaky cases tried to date, unless the mode extraction routine had problems converging on a solution.

## 6.2 Extension to Leaky Systems

In a leaky system, the amplitude of the wave decreases as energy leaks into the surrounding medium. Therefore if the same procedure that is used on vacuum loaded systems is used on a leaky system, the amplitude of the reflection coefficients would appear to depend on the distance between the defect and the monitoring location. However, it is much better to have reflection coefficients that do not depend on the location of the monitoring. To obtain location independent reflection coefficients, the attenuation effects can be removed by using data from the modal wave propagation solutions, which predict the rate at which each mode leaks energy.

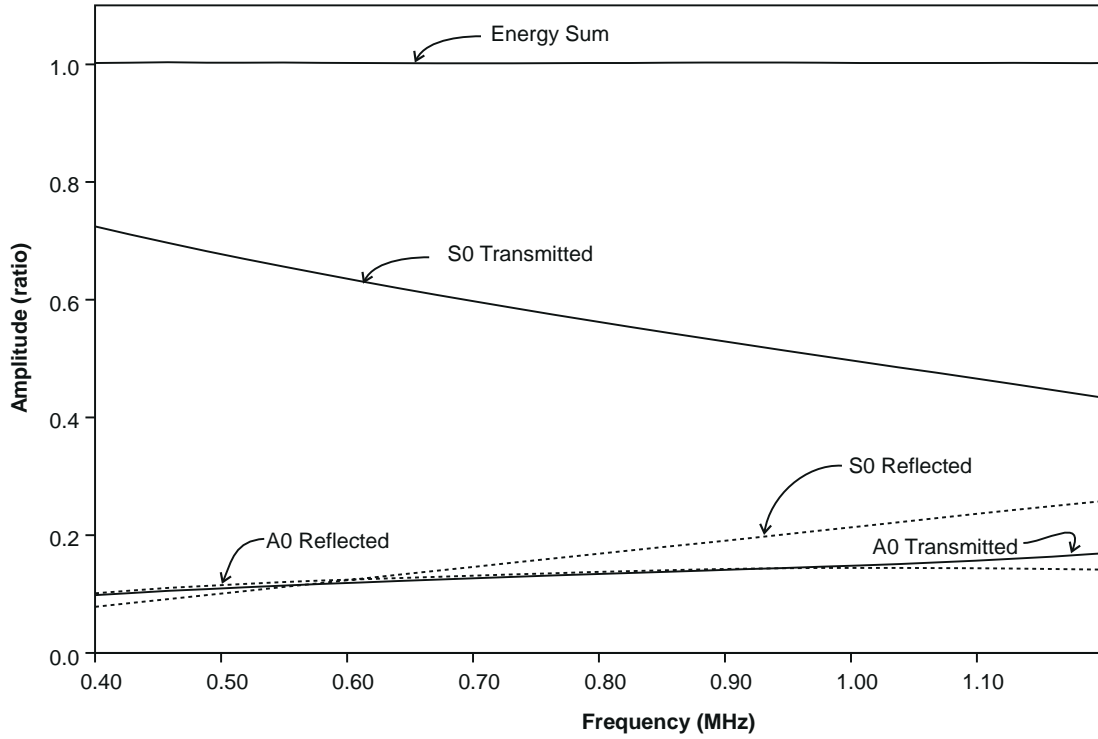


Figure 6.4: Energy reflection coefficients for the S0 mode in a 1 mm steel plate impinging on a notch that extends half way through the thickness.

Removing the attenuation is not a difficult task, provided that the attenuation rate and the distance that the mode has travelled are known. The procedure used to process the results presented in this chapter begins by determining the amplitude of each of the modes propagating before the incident mode impinges on the defect and the amplitudes of the modes that are present after interaction with the defect. The mode extraction technique described in chapter 5 is used. Therefore, care must be taken that signals from waves travelling in opposite directions do not overlap. The amplitudes of the modes after interaction with the defect are then adjusted to remove the attenuation due to leakage. The wave propagation model predicts that the modes will attenuate as

$$e^{-\kappa z}, \quad (6.2)$$

where  $\kappa$  is the frequency dependent attenuation (in np/m) that changes for each mode and  $z$  is the location (in m) along the direction of propagation. Therefore the amplitude of the modes that have interacted with the defect are adjusted, such that,

$$A'_i = A_i (e^{\kappa_0 z_0} e^{\kappa_i z_1}) \quad (6.3)$$

where  $A_i$  is the unadjusted amplitude of the mode at the frequency of interest,  $A'_i$  is the adjusted amplitude of the mode,  $\kappa_0$  is the attenuation of the incident mode,  $z_0$  is the distance from the location where the incident mode is monitored to the defect,  $\kappa_i$  is the attenuation of the reflected or transmitted

mode, and  $z_1$  is the distance from the defect to the location where the reflected or transmitted mode is monitored. After this adjustment is performed, the reflection coefficients can be determined in the same manner as the reflection coefficients for a free system.

However, directly using this method to remove attenuation effects causes some minor difficulties. As discussed before in sections 4.4.1 and 5.1, the attenuation that is derived from the finite element model is slightly different than the attenuation values provided by the wave propagation model. This difference is caused by the slightly stiffer nature of the finite element model, since it models the displacement field as a series of linear segments. Although this discrepancy is very small in percentage terms, it does make a significant difference in the calculation of the reflection coefficients. For example, even for the short model used in section 6.3 in which a low attenuation mode is propagating, the size of the reflected signal for a complete loss in section is about 4.5 percent after the mode has propagated 23 mm to the defect and back, even though almost all of the energy of the guided wave is reflected back down the bar. When only half of the bar's radius is lost, the reflection is about 3 percent of the size of the input signal, as can be seen in the sample time trace shown in figure 6.5. Therefore, the attenuation compensation that was used accounts for a difference of about 40 dB, but the difference in reflection amplitude was only 3 dB. Any errors in the attenuation values used to remove the effect of the attenuation are therefore dramatically amplified. To overcome this problem, the incident wave is sampled at two locations along the direction of propagation before it impinges on any simulated defects. The amplitude of the mode is calculated by mode extraction for each of these points and the results are used to calculate the attenuation of the mode as it propagates in the finite element model. The attenuation for the incident mode that is determined by the modal wave propagation solution is then replaced by the attenuation present in the finite element model. Making this adjustment significantly reduces the errors. For example, when there is no defect in the bar, one hundred percent transmission would be expected. However, when the attenuation is removed, it appears that 104 percent of the L(0,1) mode is transmitted. This error can be better than halved (making it appear that 101 percent of the mode is transmitted) if new attenuation values extracted from the finite element model over a 9 mm region are used instead. Even with this correction, it is estimated that the error in the extracted reflection coefficients could still be as high as five percent. The error is especially likely to be present for small reflections, whose amplitude can often be of the same order of magnitude as the rounding 'noise' present in the finite element model, once they have propagated even a short distance.

In addition to compensating for the decay of the guided wave, the bulk waves that are created in the surrounding material must be carefully considered when calculating the reflection coefficients for leaky systems. Reflections from the edge of the mesh that represents the surrounding material can easily contaminate the finite element results since the size of these reflections can be larger than the reflections of the guided wave that is being studied. These reflections can be removed using one of the techniques discussed in section 5.3. However, if the reflection cannot be completely eliminated, then the model must be made large enough so that the reflected signals arrive at the monitoring location after all of the important signals. This allows the part of the signal corresponding to the reflection from the edge of the surrounding material to be gated in time, provided that the location of the reflected waves is known.

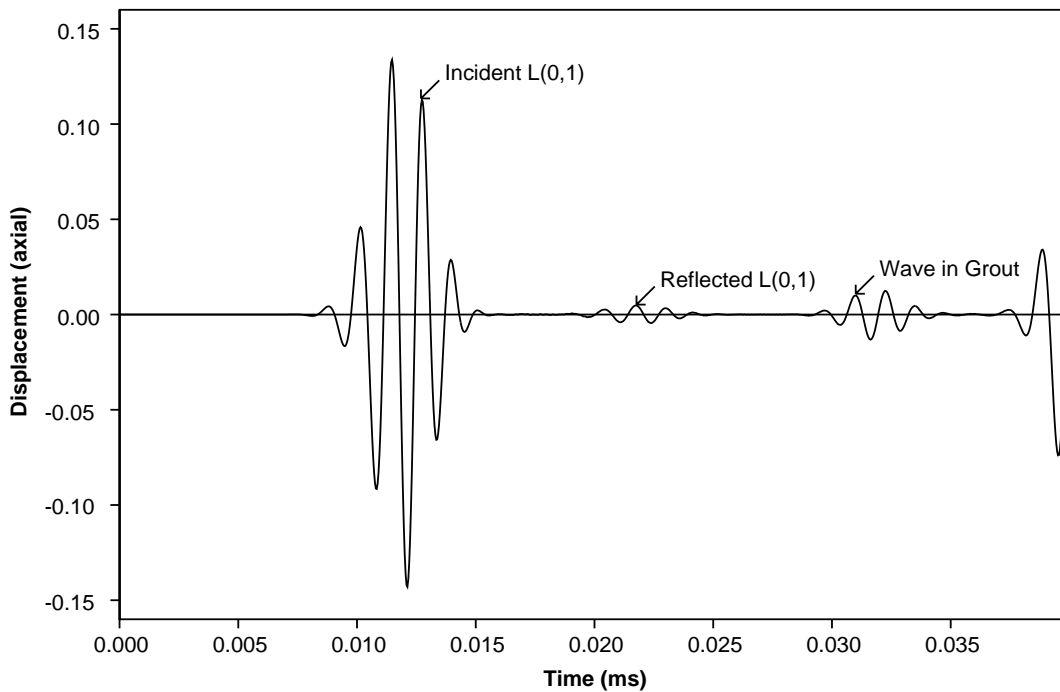


Figure 6.5: Time trace of the axial displacement at the centre of an embedded steel bar with a notch that extends half way through the thickness of the bar. The trace shows the incident wave passing, the reflected wave returning and unwanted reflections from the outer boundary of the embedding grout.

### 6.3 Reflection Coefficients for L(0,1) in an Embedded Steel Bar

The reflection coefficients for many free systems are relatively well known. However, the reflection coefficients for embedded systems are much less understood. Unfortunately, the systems that motivated this thesis require that the interaction of leaky guided waves with defects is understood. There are several questions which need to be addressed. For equivalent notch depths, are the reflection coefficients for the embedded system similar to those for the free case? How sensitive are the reflection coefficients to the orientation of the notch / defect? How sensitive are leaky guided ultrasonic waves to defects in the surrounding material? How much of the energy is transmitted and reflected at the point where a system changes from being free to embedded. The following section attempts to answer these questions in the context of the L(0,1) mode in a bar at a frequency-radius below the cut-off frequency of the L(0,2) mode. Later chapters will examine how these reflection coefficients affect the testing strategies for various systems.

The system was modelled using four-noded axi-symmetric elements, one sixth of a millimetre square. The radius of the steel bar was set to be one millimetre and the radius of the surrounding material (cement grout) was set to be 32 mm (when modelling an embedded system). The material properties were the same as those used in chapter 3. The model was 90 mm long, with an axi-symmetric notch located 55 mm from the excitation point. The bar was actually modelled as a very thick walled cylinder, with



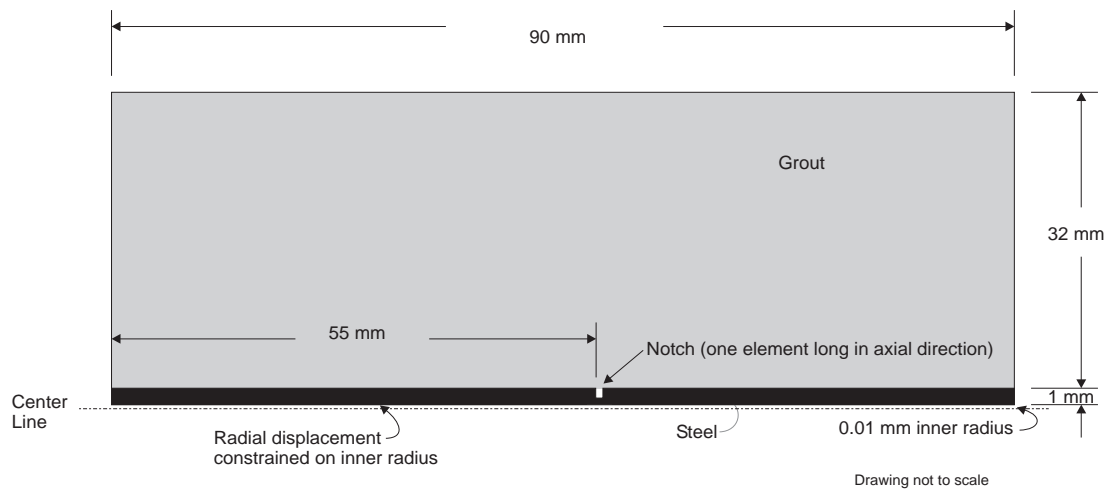


Figure 6.6: A schematic of the geometry used in for the modelling of the L(0,1) mode in an embedded steel bar.

a radius of 1 mm and an inner diameter of 0.01 mm to avoid numerical difficulties that can arise from calculations at zero radius. The radial displacements at the inner edge were fixed at zero displacement to improve stability and simulate the axi-symmetric nature of the longitudinal modes of a solid bar. This geometry is summarised in figure 6.6. The displacements corresponding to a six cycle Gaussian windowed tone-burst with a centre frequency of 0.75 MHz were applied to the end nodes that represented the steel bar (but not to the nodes that represented the surrounding grout) and the wave was allowed to propagate. The radial and axial displacements were monitored 31.5, 22.5, and 67.5 mm from the excitation end of the model, so that reflection, calibration, and transmission signals could be sampled. The pure mode excitation technique of section 5.6 was used to generate all of the input signals and the through thickness mode extraction technique of section 5.5 was used to process all of the results. Since everything in the model is axi-symmetric, there can be no mode conversion between modes of different circumferential order. In addition, since only one propagating axi-symmetric mode can exist in a steel bar below about 1.8 MHz-mm, there is no mode conversion to other modes. The finite element model took about 7 hours to complete each embedded case on a DEC Alpha workstation that was considered to be fast in 1996.

### 6.3.1 Comparison Between Free and Embedded Systems

The first question that will be addressed is how similar are the reflection coefficients of an embedded system to the comparable free system. Seven cases were modelled for both the free and the embedded cases for which the depth of a square notch on the outside of bar was increased from zero to 100 percent of the radius of the bar. The reflection and transmission coefficients for 0.70 MHz are shown in figure 6.7. In general, the reflection / transmission coefficients are quite similar, however, there are some interesting differences between the two cases.

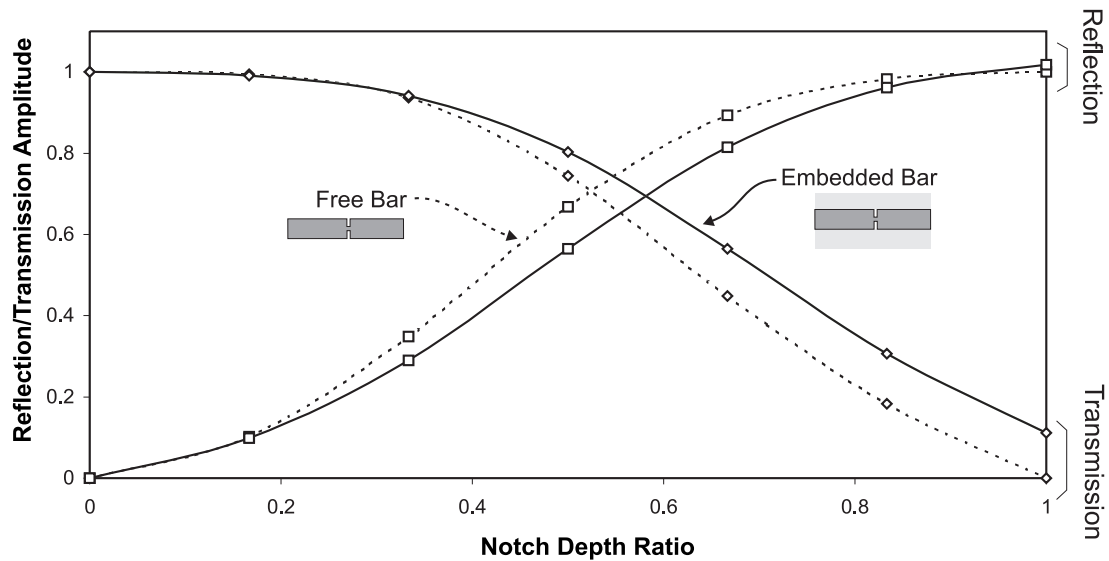


Figure 6.7: Comparison of the reflection and transmission coefficients for a free and embedded 1 mm radius steel bar.

One major difference is that even when the notch extends through the entire thickness of the steel bar, there is still energy transmitted for the embedded case. The amplitude of this transmitted wave is about eleven percent the amplitude of the incident wave (once the attenuation due to leakage has been extracted), and therefore accounts for approximately one percent of the energy of the mode. This energy is carried around the notch by the surrounding grout, which can couple displacements on one side of the vacuum filled notch to the other side of the notch.

Surprisingly, the amplitude of the mode that is reflected from an embedded notch that extends through the entire thickness of the bar is shown as  $103.5 \pm 5$  percent of the amplitude of the incident wave. (The error limits were estimated by examining the numerical 'noise' present in the finite element results after the attenuation effects were removed using the procedure discussed in section 6.2.) Most likely, this value for the reflection coefficient is too large. However, it is possible that observed reflection coefficient could be greater than 100 percent because of residual effects of the processing that is performed to remove the effects of the attenuation. As the mode travels down the bar, energy is being continually transferred into bulk waves that propagate energy away from the bar. During the processing of the results, this energy loss is removed from the observed reflection coefficients to make the reflection coefficients independent of location. This procedure implies that the energy in the leaked bulk waves is 'lost' from the system and no longer influences the mode's propagation. However, this assumption is not entirely correct. For example, the previous paragraph discussed how energy can be transferred from a steel bar through the grout and into a second bar, even when the bar is completely severed. Similarly, a portion of the bulk wave that is carried in the grout can be reflected and generate a reflected guided wave in the initial embedded bar. This reflection will contribute to the guided wave that is directly reflected from the end of the bar. Therefore, because of the processing, the reflection coefficient could appear to be larger than 100 percent.

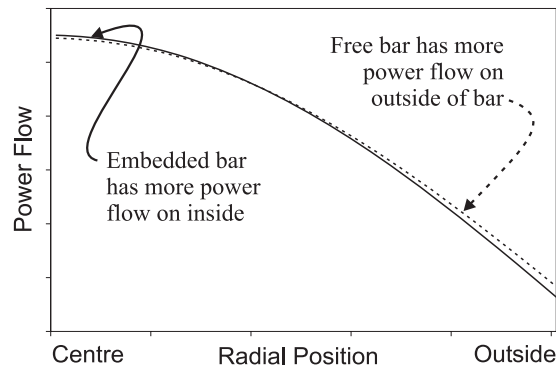


Figure 6.8: Comparison of the profile of the power flow of the L(0,1) mode at 0.70 MHz through the radius of a 1 mm steel bar when it is free and when it is embedded in grout.

Another difference that can be observed between the two cases is the notch depth at which the transmission and reflection coefficients cross (indicating that half of the energy is reflected and half is transmitted). The crossing point for the free case corresponds to a notch that is about five percent less deep than for the embedded case. This change can be explained by examining the radial profiles of the power flow of the L(0,1) mode at this frequency, which are shown in figure 6.8. When the bar is embedded in grout, the power is more concentrated in the centre of the bar than when the bar is in vacuum. Therefore, one would expect that for the reflection to be the same magnitude, the notch would have to be deeper (as measured from the outside of the bar) for the embedded case than for the free case, which is what is observed in the finite element modelling.

The previous figure (figure 6.7) shows the reflection coefficients at 0.70 MHz-mm frequency-radius product. The primary reason that this frequency-radius was chosen is that it corresponds to a section of the L(0,1) mode that does not suffer from great attenuation or dispersion. Therefore it is an attractive frequency-radius at which to perform non-destructive tests. Since the centre frequency of the tone-bursts used in the finite element models was 0.75 MHz-mm, a lot of energy is present at 0.70 MHz-mm, so the solutions are stable. The results shown for this frequency-radius are comparable to those for many surrounding frequency-radii. Figure 6.9 compares the reflection coefficients at this frequency-radius to those at 0.85 MHz-mm and 0.55 MHz-mm. The behaviour for all three frequency-radii is very much the same, however, the point at which the reflection and transmission coefficients cross changes (because the power flow distribution changes) and the transmission through a notch that extends through the entire radius of the bar changes (because the power flow distribution and the wavelength change). Future figures will only show the results for 0.70 MHz-mm, which are indicative of nearby frequency-radii.

### 6.3.2 Grout Filled Square Notches

The finite element models discussed above consider the notch to be completely empty (vacuum filled). For the types of applications that are considered in later chapters, this is a reasonable assumption. How-

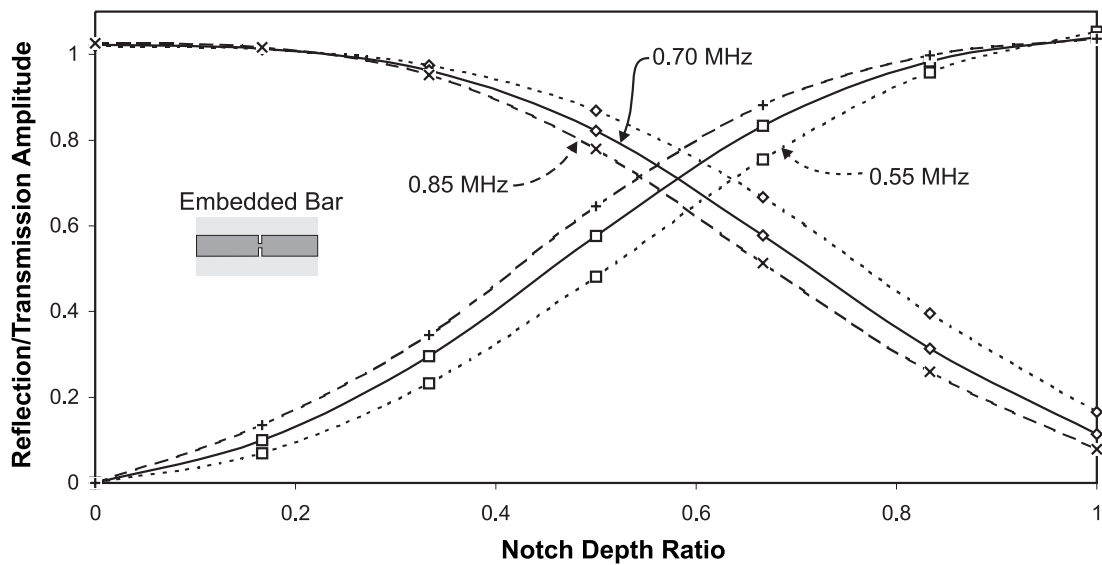


Figure 6.9: Comparison of the reflection and transmission coefficients at different frequencies for an embedded bar.

ever, it is interesting to observe how the system behaves when the notch is filled with grout, to understand how small the reflected signal could become. In addition, the grout filled notch cases can be used to further compare the free and embedded reflection cases. Figure 6.10 illustrates the reflection and transmission coefficients at 0.70 MHz when the notches are filled with grout. For comparison, the solid lines show the coefficients for an embedded bar with an empty notch that were shown in figure 6.7. The long dashed lines represent the case of an embedded bar with a grout filled notch and the short dashed lines represent a free bar with a grout filled notch. As expected, the reflection from the filled notch is much less than from an empty notch and the transmission is much greater. For example, when the notch extends completely through the thickness of the bar, the reflection in the embedded steel bar is only 72 percent compared to over 100 percent for the empty notch. Similarly, the transmission increases from 11 percent to 68 percent when the notch is filled. Converting these figures into energies reveals that when the notch becomes filled, roughly half of the energy is reflected and half is transmitted, as opposed to nearly all of it being reflected. This change in reflection coefficient can be roughly correlated to the standard formula for the amplitude reflection coefficient of a bulk wave as it passes from one material to another. This formula is,

$$R = \frac{Z - Z_0}{Z + Z_0}, \quad (6.4)$$

where  $R$  is the reflection coefficient and  $Z = \rho v$  is the impedance of the grout, which is the product of the density and the bulk velocity of interest, and  $Z_0$  is the impedance of the steel. For the longitudinal bulk waves of the steel-grout combination, the impedances are  $47 \cdot 10^6 \text{ kg}/(\text{m}^2 \text{ s})$  for steel and  $4.5 \cdot 10^6 \text{ kg}/(\text{m}^2 \text{ s})$ . Therefore the reflection from the steel-grout interface would be about 82 percent, but would be 100 percent for a steel-vacuum interface.

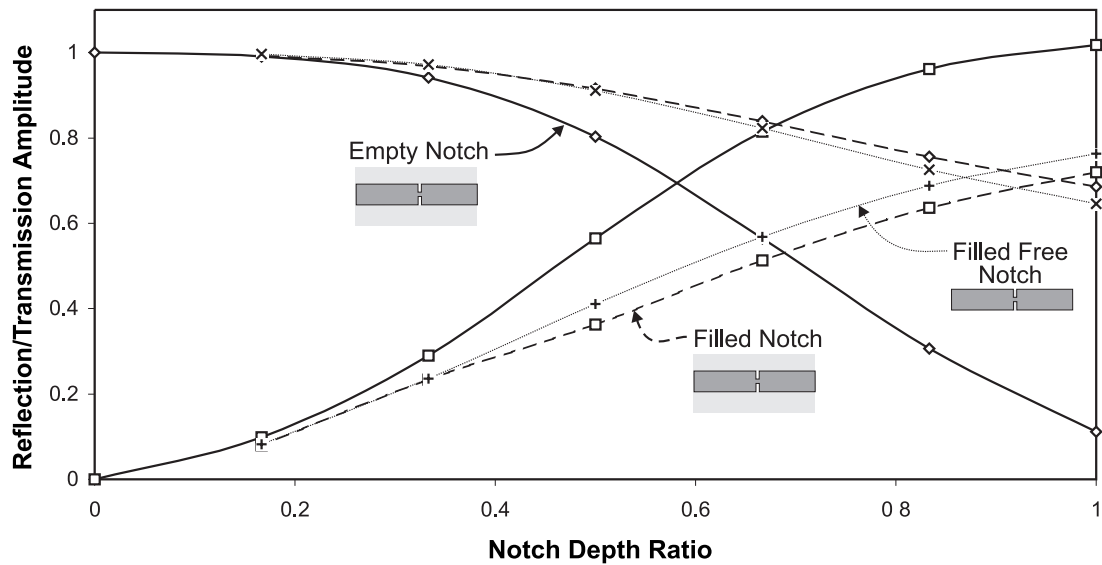


Figure 6.10: Comparison of the reflection and transmission coefficients for a vacuum filled versus a grout filled defect for an embedded bar.

When the notch in the free bar is filled with grout, its reflection coefficients follow the same trend as the reflection coefficients of the embedded bar. As expected the reflections are much smaller and the transmissions are greater than for the cases when the notch was empty. Seventy-six percent of the mode is reflected when the notch extends through the entire radius of the bar. Although this corresponds to about a five percent maximum difference between the reflection coefficients obtained for the embedded cases and the free cases, the results could generally be interchanged for most applications. There is also a reasonable correlation with the reflection coefficient for a planar bulk longitudinal wave.

### 6.3.3 Orientation of the Notch

The previous finite element cases all considered square notches whose sides were perpendicular to the direction of travel of the guided wave. However, in practice, corrosion may occur at any orientation and often does not resemble a square notch. Therefore, this section considers the effect of changing the orientation of the notch so that it is oriented at an angle of 45 degrees to the direction of propagation. It also examines a crude approximation of the leading edge of a corrosion patch. This provides a first step towards understanding the behaviour of the guided wave as it interacts with real corrosion.

If the L(0,1) mode is thought of as a bulk wave instead of the guided wave that it is, the reflection from a diagonal notch can be considered intuitively. When the notch is perpendicular the direction of propagation, the energy will be directed in the exactly opposite direction. However, when the notch is at a 45 degree angle, the energy can be deflected at right angles to the direction from which it came, as shown in figure 6.11(a). If the bar is in vacuum, when the energy reaches the outside of the bar it will be redirected towards the notch and then back in the direction from which it came. Therefore, one



Figure 6.11: A schematic diagram showing how energy would be redirected by (a) a diagonal notch and (b) a corrosion step if the L(0,1) mode behaved as a bulk wave.

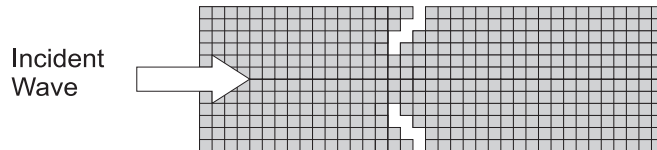


Figure 6.12: A portion of the finite element mesh used to create a diagonal notch extending through two thirds of the radius of the bar.

would not expect a very large difference in the reflection coefficients for the two different orientations. However, when the bar is embedded in grout, not all of the energy will be redirected towards the notch once it encounters the outside of the bar. Therefore, one would expect that the reflection coefficient would be affected to a certain degree. To determine if this simplistic model holds for the guided L(0,1) mode, several finite element cases were run. For these cases, an axi-symmetric, outwardly oriented diagonal notch was created in the bar. This notch was created by removing elements from the mesh, as shown in figure 6.12. Since the element size is so small in comparison to the wavelength of the mode, this square sided, diagonal notch should act in a very similar manner to a notch that has true diagonal sides.

Figure 6.13 shows the reflection and transmission coefficients for a free bar, when the notch is oriented perpendicular to and at a 45 degree angle to the direction of propagation. The coefficients for the two cases are very similar. The small differences between the cases are most likely due to interference between waves of slightly different phases, which are generated at the beginning and end of the diagonal notch section. The equivalent embedded cases are shown in figure 6.14. When the notch is not very deep, the diagonal notch very much resembles a square notch and so the differences are not great. However, as the depth of the notch increases, the difference between the two types of notches increases. The greatest difference can be seen for the reflection from a defect that extends through the entire cross section of the steel bar. For this case, the amplitude reflection coefficient reduces from over 100 percent for the square notch case to around 86 percent for the diagonal notch. This difference reveals that the diagonal orientation of the notch tends to reflect energy into the surrounding medium and that predictions based on the reflection coefficients of a free bar cannot be substituted for those of an embedded bar when the notch is not perpendicular to the direction of propagation.

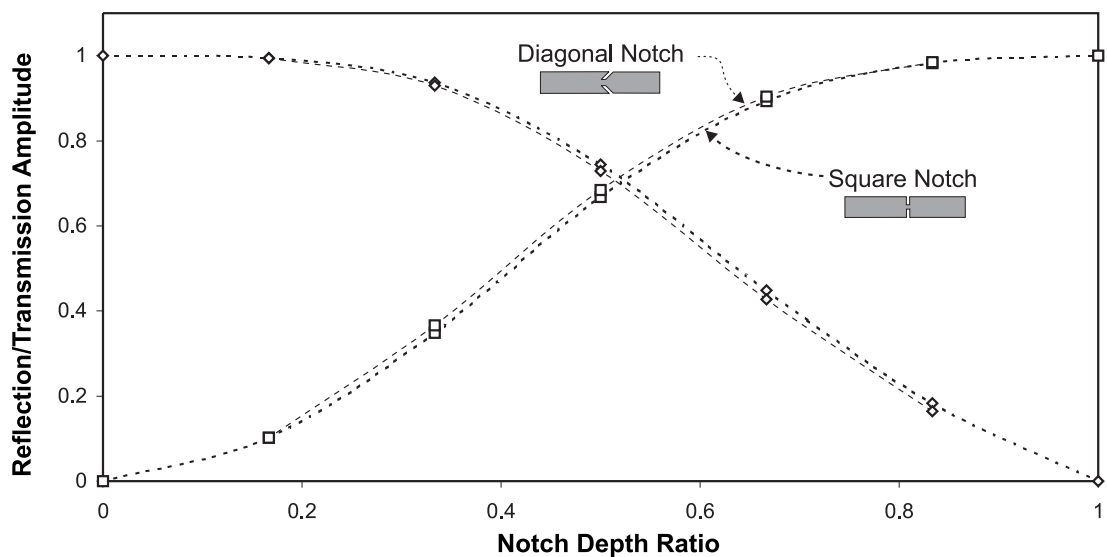


Figure 6.13: Comparison of the reflection and transmission coefficients for different notch orientations in a free bar.

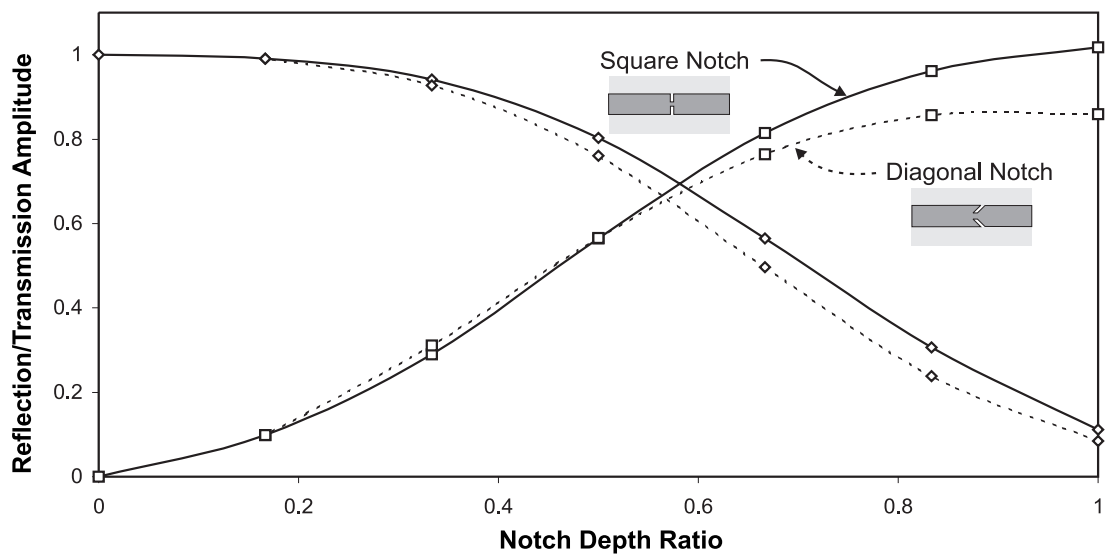


Figure 6.14: Comparison of the reflection and transmission coefficients for different notch orientations in an embedded bar.

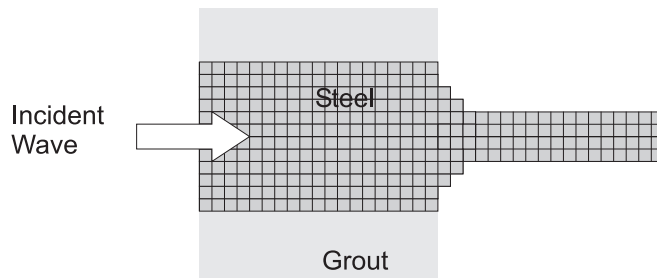


Figure 6.15: A portion of the finite element mesh used to create a corrosion patch extending through two thirds of the radius of the bar.

The angle of the diagonal notch shown in figure 6.12 is not very likely to occur in actual testing situations. When there is generalised corrosion of a steel bar embedded in grout, it usually occurs at a voided region, where the alkaline grout is not present to provide protection. The profile of this corrosion would be much more 'dish-like' than the diagonal notch described above. In addition, the leading edge of the corrosion patch would be angled in the opposite direction, tending to reflect waves toward the centre of the bar instead of the outside of the bar, as shown in figure 6.11(b). Several finite element models were run to simulate this more common type of defect. Only the beginning of the patch was modelled to reduce the model size and eliminate effects of the length of the corrosion patch (interference between reflections from the beginning and end of the patch can cause the observed reflection coefficient to fluctuate as the length of the patch changes). Figure 6.15 shows a portion of the mesh that was used to model this type of defect. Figure 6.16 shows the reflection coefficients that were obtained from the finite element calculations. The solid line represents the reflection coefficient for the square notch and the dashed line represents the reflection from the corrosion patch. Especially for deep notches, the reflection coefficients for these two cases are much more similar than for the diagonal notch that was considered. The differences observed between the two cases for small notches can be attributed to the reflection from the end of the grout (the beginning of the voided region) that occurs for the corrosion patch case.

The results from the previous four cases are summarised in Table 6.1. The values of the reflection coefficients are given for the free and embedded cases for defects that extend completely through the steel bar and defects that correspond to a 50 percent loss of radius. As explained above, for a free bar that has an empty notch, the reflection coefficient is mainly a function of defect depth and not orientation. However, for the embedded case, certain notch orientations have a significant effect. The reflection coefficients for a grout filled square notch are similar for both the free and the embedded cases.

### 6.3.4 Defects in the Surrounding Grout

When performing non-destructive tests, false calls need to be avoided whenever possible, otherwise the testing procedure becomes impractical to use. Since leaky guided waves propagate in both the central



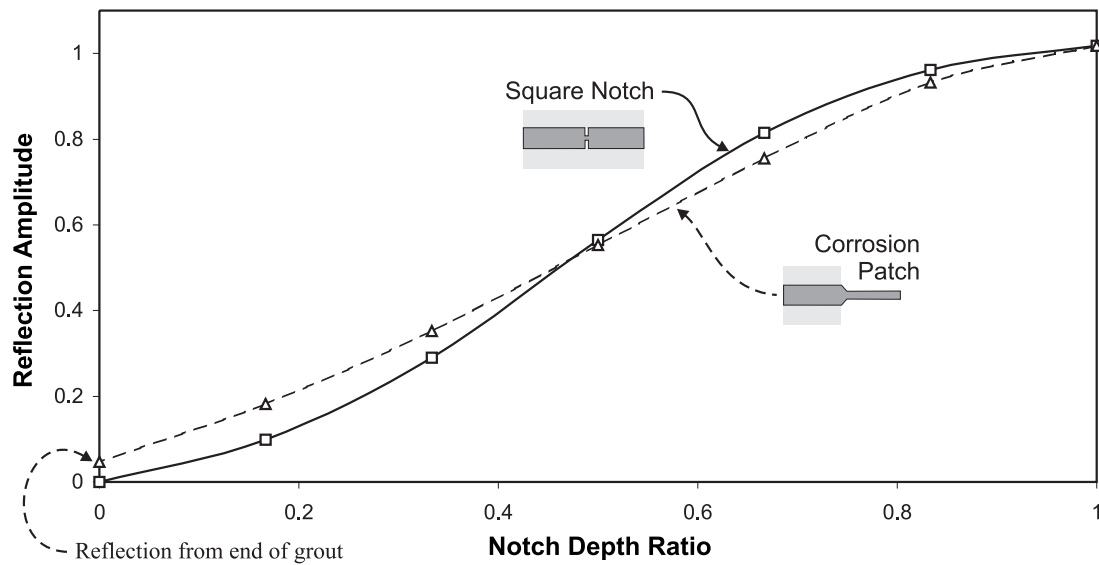






Figure 6.16: Comparison of the reflection coefficients for a square notch and a corrosion patch in an embedded bar.

Table 6.1: Summary of the reflection coefficients for four different types of notches in a steel bar.

	Complete Break		50% loss of radius	
	Free	Embedded	Free	Embedded
 Square Notch	100%	102%	67%	56%
 Diagonal Notch	100%	86%	68%	57%
 Corrosion Patch	100%	102%	69%	55%
 Filled Notch	76%	72%	41%	36%

 = Wavelength

structure (the steel bar in this case) and in the surrounding medium (grout), there is some concern that the waves will reflect off defects in the grout although there has been no damage to the steel bar. To examine this concern, a finite element run was conducted in which a one millimetre deep square notch was placed in the portion of the grout next to the steel bar. At 0.7 MHz-mm frequency-radius, the amplitude reflection coefficient from this defect was seven percent and the transmission coefficient was determined to be about 100 percent. Of the frequencies examined, the largest reflection was at about 0.55 MHz-mm. However, this reflection was still less than 10 percent of the amplitude of the incident wave (one percent of its energy). This size of reflection corresponds to a square notch in the steel bar whose depth is less than 15 percent of the radius. Provided that the testing procedure is looking for significant section loss, a reflection of this size from a defect in the grout would probably not be detected. However, since the modes attenuate quickly as they propagate, care must be taken to ensure that a small defect near the transducer is not mistaken for a large one farther away.

### 6.3.5 Transition between Leaky and Free Systems

All of the previous examples in this chapter have assumed that the system consists of the same geometry for its entire length, for example, it is always a free bar or always an embedded bar. However, in reality, there will often be transitions between these two extremes. For example, at the anchorages of post tensioned bridges, the steel tendons protrude from the end of the grout. To produce a wave in the embedded section of the tendon, a wave is first generated in the free section and then it enters the embedded section. Since the wave in a free bar has different properties than a wave in an embedded bar, a portion of the wave will be reflected as the new boundary conditions are matched. It is important to know the size of this reflection. The reflected wave will reverberate in the free (unattenuated) section of the bar, transmitting a certain amount of its energy into the embedded section each time it reaches the interface. While this wave is reverberating in the free section of the bar, the transmitted part of the guided wave is travelling in an embedded section of bar, leaking energy into the surrounding grout as it travels towards a potential defect. If the amplitude of the reverberations is greater than the size of the received reflection from an embedded defect, the defect will not be reliably detected. Therefore, it is important to quantify the size of the reflection from the boundary between two systems and relate this to the amplitude of the reverberations.

A finite element model was run to determine the size of the reflection that will occur when the bar enters the grout. Fifty five (55) millimetres of a 1 mm radius steel bar was allowed to be free and a 35 millimetre length was embedded in grout. A wave was generated at the free end of the simulated bar and the resulting reflection and transmission was measured. The reflection coefficients of the opposite case, the transition from an embedded section to a free section, were also calculated. Figure 6.17 shows the reflection coefficients for these two cases. This figure shows that the reflection upon entry to the grout was about 3 percent of the amplitude of the incident wave, at 0.7 MHz. Likewise, the transmission into the grout was calculated as  $100 \pm 2$  percent, once the attenuation effects were removed. (The error range

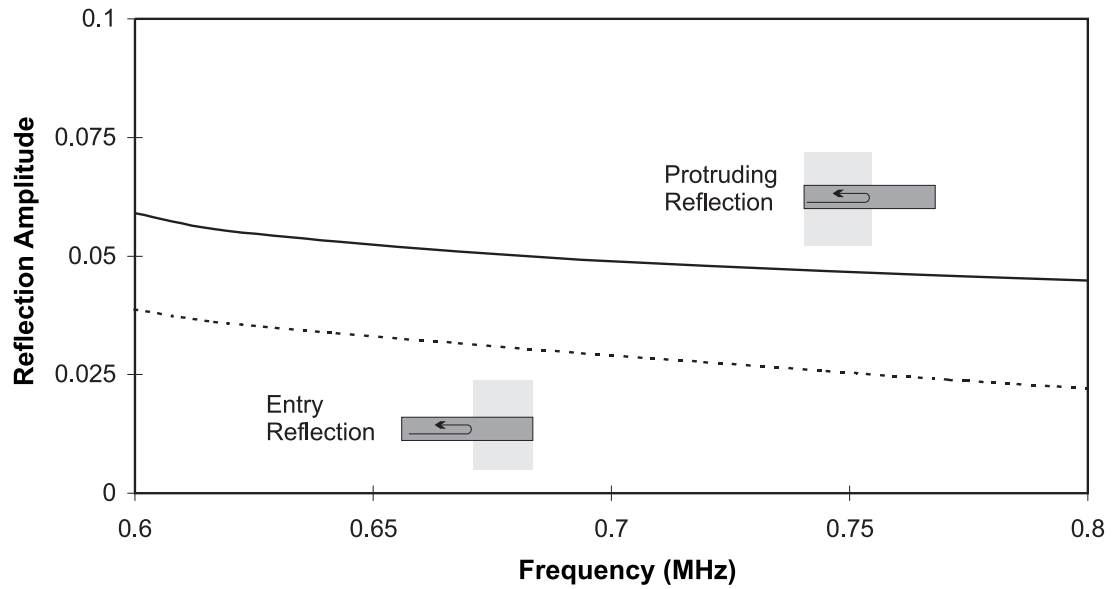


Figure 6.17: The reflection coefficients for the L(0,1) mode in a steel bar as it transitions from an embedded section to a free section and visa versa.

for this case is smaller than for the previous fully embedded cases since much of the model consists of a free bar whose errors are not magnified by the attenuation removal processing.) It is quite encouraging that so much of the energy was transmitted into the embedded section. For example, upon the second reflection at the point of entry, the amplitude of the reflected signal will only be 0.09 percent of the original wave. However, it should be noted that the attenuation of the L(0,1) mode at this frequency is  $60 \text{ np/m}$ . Therefore a complete reflection only 30 mm into the grout will also appear as a signal that is  $3 \pm 0.2$  percent of the input.

By knowing the size of the reflection from the point where the bar enters the grout, the decay of the reverberations can be easily quantified. Each time that the guided wave reaches the boundary between the free and embedded section, the amplitude of the reverberations will decrease. The drops occur every time that the reverberating guided wave propagates  $2d$  distance, where  $d$  is the length of the protruding end of the embedded bar, as shown in figure 6.18. If this decay is considered to be continuous (as opposed to being composed of a series of steps), it can be expressed as a simple power law relationship,

$$\text{Amplitude} = rc^{x/2d}, \quad (6.5)$$

where  $rc$  is the reflection coefficient (0.03 in this case) and the value  $x/2d$  represents the number of reverberations in the free end, which is  $d$  metres long, that occur while the wave travels  $x$  metres. The decay represented by equation 6.5 can be expressed in dB as,

$$\text{Amplitude (in dB)} = \frac{10x}{d} \log(rc). \quad (6.6)$$

This decay is shown in figure 6.19. The stepped solid lines represent the actual decay in the amplitude of the reverberations in the free end of a bar that protrudes two different lengths (10 mm in figure

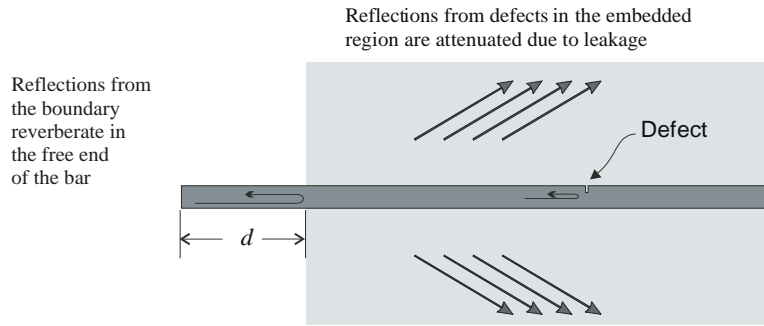


Figure 6.18: A schematic view of the geometry used to evaluate the size of the reverberations in the protruding end of an embedded bar.

6.19(a) and 50 mm in figure 6.19(b)) assuming that 3 percent of the signal is reflected from the free / embedded boundary. The dashed lines that follow the stepped solid lines represent the decay expressed in equation 6.6. The other dashed lines are included for comparison. They show the rate at which the signal which enters the embedded section of the bar would decay (assuming an attenuation of 530 dB/m, which corresponds to the L(0,1) mode at 0.7 MHz in a 2 mm diameter embedded steel bar). For the case shown in figure 6.19(a) (10 mm protruding), the attenuation of the mode in the embedded section is less than the equivalent attenuation of the reverberations. Therefore, the signal from the reflection from a defect in the embedded section should be larger than the signal reverberating in the free end of the bar (assuming a 100 percent reflection from the defect). Therefore, the reflection could be detected (provided that several other factors, such as the sensitivity of the equipment and the size of the reflection from the defect, do not prevent its detection). However, for the case shown in figure 6.19(b) (50 mm protruding), the equivalent attenuation of the reverberations is less than the attenuation of the wave in the embedded section. Therefore, any reflections from a defect in the embedded section will be obscured by the reverberations.

It is possible to predict when the reverberating signal will obscure reflections from defects in embedded bars (assuming that 100 percent of the embedded guided wave is reflected from the defect). The expression in equation 6.6 can be normalised by the propagation distance and converted into an equivalent attenuation in units of dB/m. By assuming that the mode in the embedded section and the mode in the free section travel at the same speed (which they usually nearly do), this 'attenuation' can be directly compared to the attenuation of the mode propagating in the embedded section. This comparison allows a maximum attenuation of the propagating mode to be specified for a given length of protruding end. If the attenuation is higher than this value, given as,

$$\text{Maximum Attenuation (in dB/m)} = \frac{10}{d} \log(rc), \quad (6.7)$$

the reverberations will obscure any reflections from defects in the embedded section. Likewise, for a given attenuation of a propagating mode,  $\kappa$ , the length of the protruding end of an embedded bar must

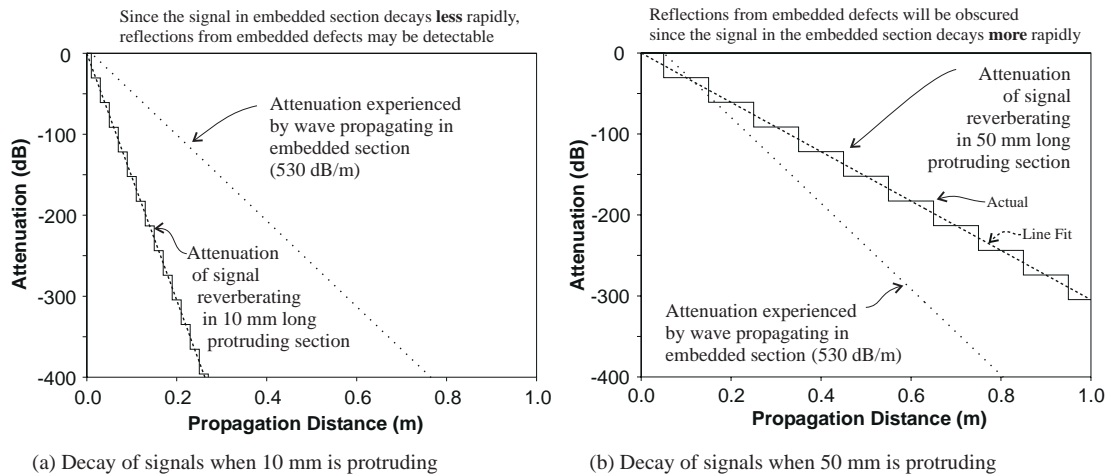


Figure 6.19: Plots of the decay in amplitude of a signal propagating in an embedded section of bar (with an attenuation of 530 dB/m) and the decay in amplitude of the reverberations in the free end of a bar that protrudes from the embedding material 10 mm (in part (a)) and 50 mm (in part (b)). The plots assume that 3 percent of the wave is reflected from the free / embedded boundary.

be less than the value given by the expression,

$$\text{Maximum length of protruding end (in m)} = \frac{10}{\kappa} \log(rc). \quad (6.8)$$

These relationships are shown in figure 6.20. The shaded portion of the figure indicates the where the reverberations are sure to obscure the reflection from the embedded defects when the reflection coefficient at the transition between the free and embedded systems ( $rc$ ) is 3 percent. If the reflection coefficient increases to 5 percent, this shaded area would expand to the solid line that is labelled  $rc = 0.05$ . The dotted lines illustrate two cases. For the L(0,1) mode at .7 MHz in a 2 mm diameter embedded steel bar, which has an attenuation of 530 dB/m, the length of the protruding end must be less than 28 mm or the reverberations will obscure any reflection from an embedded defect. Similarly, for the 50 mm long protruding end shown in figure 6.19(b), the maximum attenuation of the mode propagating in the embedded section must be less than 305 dB/m.

When using figure 6.20 and equations 6.7 and 6.8 to predict the size of the reverberating signal, two issues should be noted. First, the criteria in equations 6.7 and 6.8 can only be used to exclude possible attenuation–protruding length combinations. Satisfying the criteria does not mean that a reflection from a defect in the embedded section of the bar will be detectable. For example, if 100 percent of the embedded mode is not reflected, the reflected signal will be smaller than the value used to determine the criteria in equations 6.7 and 6.8. Therefore, the reflection may be obscured even though the criteria are satisfied. The second issue concerns the location of the defect. The criteria in equations 6.7 and 6.8 are not affected by the location of the defect. There is a set decay rate of the reverberations and there is a set decay rate of the embedded guided wave. Therefore, regardless of propagation distance, one signal will always be larger than the other. However, for experimental data, the location of the defect will have an

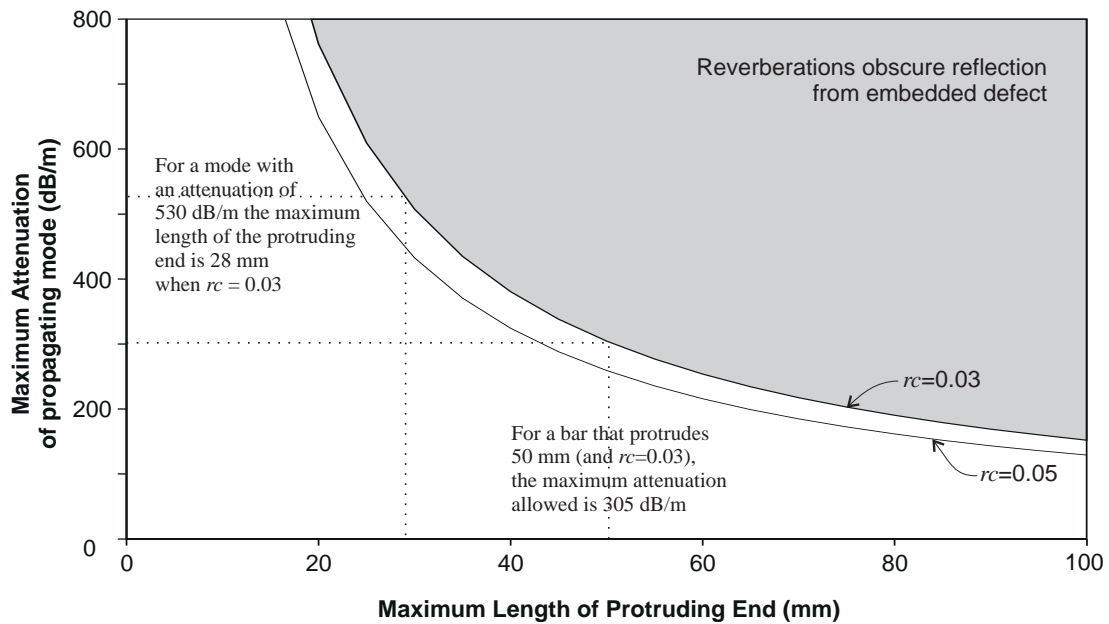


Figure 6.20: A diagram relating the maximum length of the protruding end of an embedded bar to the maximum attenuation that the mode in the embedded section can experience for the amplitude of the embedded signal to remain larger than the reverberations.

effect. The criteria in equations 6.7 and 6.8 assume that a defect can be detected if its amplitude is 0 dB greater than the amplitude of the reverberations. However, for a defect to be detected, its amplitude usually needs to be at least 6 dB greater than any other effect such as the reverberations. Even if the criteria in equations 6.7 and 6.8 are satisfied, the defect will need to be a minimum propagation distance away before the amplitude of the reverberation signals decays enough that the defect signal could be distinguished on top of it. The minimum distance required depends on the relative 'attenuations' of reverberations and the embedded guided wave. On the other hand, the maximum distance at which a defect could be detected depends primarily on the sensitivity of the test equipment and the attenuation of the guided wave in the embedded section of the bar, but not on the 'attenuation' of the reverberations in the free end of the bar.

As mentioned in the introduction to this section, the opposite problem, the reflection and transmission as a wave in an embedded section of steel bar enters a free section of steel bar, was also examined using a finite element model. For this case, the amplitude of the reflected wave is about 5 percent of the input wave and the transmitted wave is around 99 percent of the input. Because waves will not reverberate in the embedded section of the bar, the size of the reflection is not as important as for the transition from a free bar to an embedded bar. However, the transmission coefficient remains important, since as much energy as possible must be transferred from the embedded region into the free region (where the receiving transducer is located). The large transmission coefficient that is observed in the finite element studies is very promising.

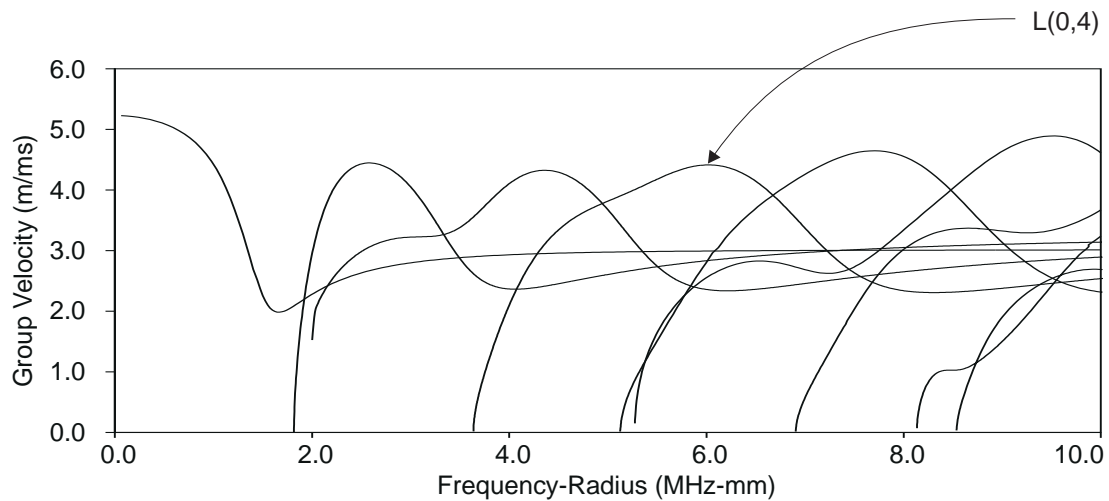


Figure 6.21: The dispersion curves for an embedded steel bar.

## 6.4 Higher Order Reflection Coefficients

The previous cases in this chapter have looked at the reflection of the fundamental longitudinal mode,  $L(0,1)$ , at a relatively low frequency-radius. However, as will be seen in chapter 7, particular points of higher order modes are able to inspect longer lengths of certain systems, such as post-tensioned tendons. These points of low attenuation correspond to the concentration of energy in the centre of the bar and occur near the maximum group velocity of the higher order longitudinal modes. One of the first modes to show this behavior is the  $L(0,4)$  mode at 6.0 MHz-mm, which is indicated in figure 6.21. To model this higher order mode using finite element techniques, a much denser mesh must be used than was used for the previous cases. Satisfying the requirements of the number of nodes per wavelength requires that the number of nodes through the radius of the bar be increased from 7 to 25. This fine mesh prohibits modelling the surrounding grout, since it would cause the finite element model to be too large. Therefore, the reflection coefficients for the embedded case need to be estimated from the reflection coefficients for the free case, which can be calculated.

The substitution of the reflection coefficients for the free case can be justified by studying the modal characteristics of the equivalent points on the dispersion curves for the free and embedded cases, which are shown in figure 6.22. Except for the attenuation that is present in the embedded case, the dispersion curves are very similar for the two cases, especially for the  $L(0,4)$  mode around its maximum energy velocity. The mode shapes for the two modes are also very similar, as can be seen in the strain energy density and displacement profiles in figure 6.22. This similarity is expected, since this location on the dispersion curves was chosen for non-destructive testing since it has a relatively low attenuation (which can be attributed to the fact that there is minimum amount of interaction between the steel bar and the surrounding grout). The  $L(0,1)$  cases described above, which also occur at a minimum of attenuation, have shown that there can be good agreement between the reflection coefficients for free and embedded

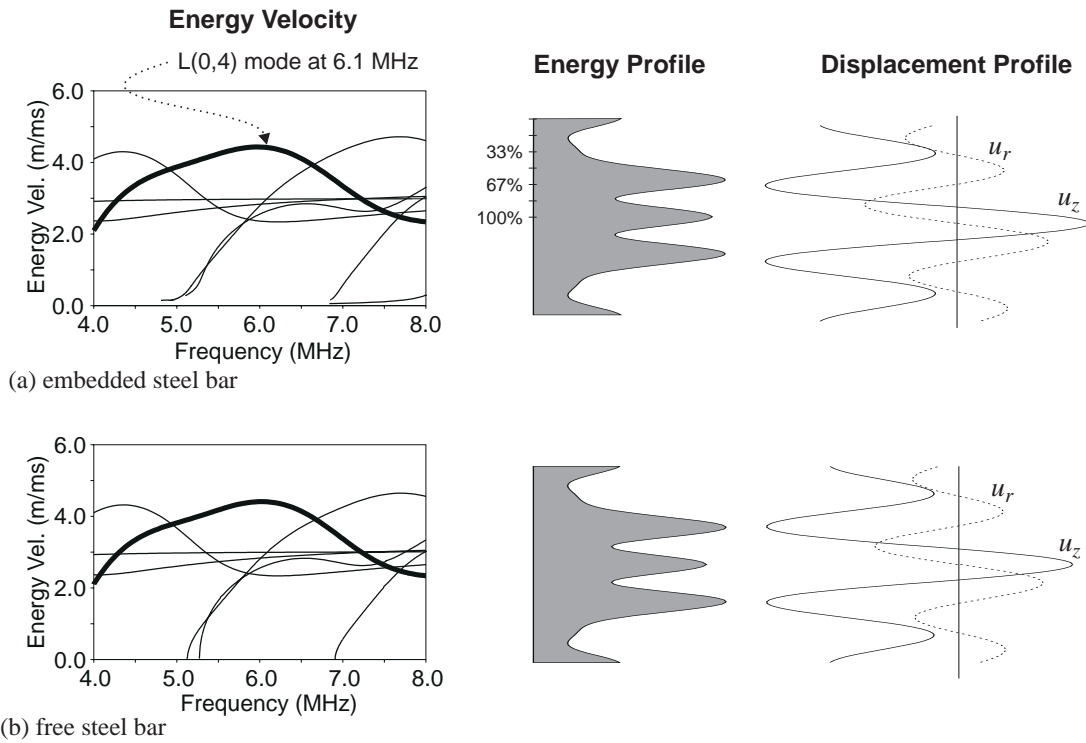


Figure 6.22: A comparison of the energy velocity dispersion curves, strain energy density profile, and displacement profiles for the L(0,4) mode in a free and embedded steel bar.

steel bars for square notches. Substituting the reflection coefficients for the free case of the L(0,4) mode should yield results that are accurate enough that they can be used to evaluate the sensitivity of the mode to notches of varying depth. If more accurate results are required for future work, there are a few extensions that could be added to the finite element program to possibly allow higher order leaky systems to be modelled. These extensions are described in section 5.3.

Substituting the reflection coefficients of the free bar for the embedded bar yields the reflection coefficients for the L(0,4) mode at 6.0 MHz-mm frequency-radius that are shown in figure 6.23. Each of the curves represents how much of each of the propagating modes will be created and reflected back down the bar when the L(0,4) mode is incident on a square notch of the depth shown. For this case, only the curve that represents the amount of L(0,4) reflected has relevance to determining the sensitivity of the non-destructive testing technique. The other modes, which are generated by mode conversion at the notch, all suffer from very high attenuation and will therefore not be detected. Thus for the technique to detect a notch as far into the embedded section as possible, the majority of reflected energy must be concentrated in the L(0,4) mode. As can be seen in figure 6.23, when the defect extends through the entire radius of the bar, there is a large proportion of L(0,4) reflected (around 90 percent), which is very promising. For defects that are not as deep, a large proportion of the L(0,4) mode continues to be reflected from the notch as L(0,4), indicating that there is a strong possibility that these less serious defects can be detected in a real situation. The irregular shape of the reflection coefficient as the depth changes reflects the non-constant energy profile seen in figure 6.22.



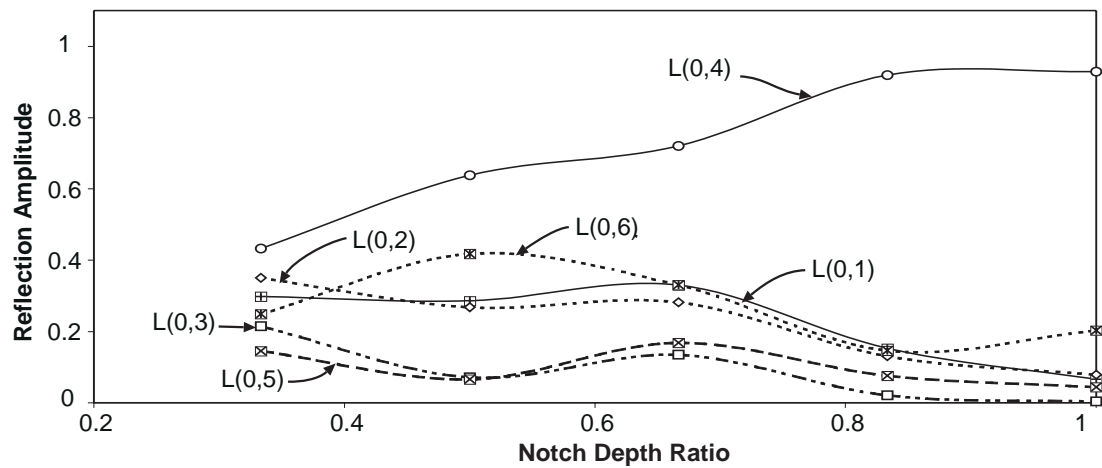


Figure 6.23: The reflection coefficients for a free steel bar when the L(0,4) mode is incident on a square notch.

## 6.5 Summary of Embedded Reflection Coefficients

This chapter has presented the reflection coefficients for several different cylindrical systems that provide insight into the size and type of defects that can be detected in embedded bars. These results have shown that the reflection coefficients for the L(0,1) mode in a free and embedded steel bar are similar when the notch walls are perpendicular to the direction of the mode's propagation, allowing the free case to be substituted for the much more difficult to calculate embedded case. It has also been found that the reflections at the boundary between free and embedded systems do not present significant problems for testing with the fundamental longitudinal mode at low frequency-radii. Modelling of a higher order mode, L(0,4) indicates that a majority of the energy that is reflected from a defect is reflected as the L(0,4) mode, which indicates that it should be possible to detect relatively small defects if this mode is used to test embedded bars. The results presented in this chapter will be used later in chapter 7 to help evaluate the applicability of different modes for testing embedded structures.

## **Chapter 7**

# **Application to Post Tensioned Bridges**

The previous chapters of this thesis have developed the tools necessary to study guided wave propagation in cylindrical systems. This chapter assembles those pieces and uses them to evaluate how guided ultrasonic waves could be used to inspect post-tensioned bridges, the application that motivated this work.

The recent collapse of several post-tensioned construction bridges before the end of their expected lifetime[1,95,96] has raised many concerns about the safety of this type of construction. At the moment, there is no cheap and effective way of inspecting the numerous bridges of this type[3]. This chapter explores the possibility of sending guided waves along embedded tendons to test the integrity of the bridge. This method has the possibility of providing an inexpensive, reliable way to quickly test large sections of the bridge.

The first section of this chapter provides some background information on why an adequate inspection technique is needed for post-tension construction bridges, as well as how this type of bridge is constructed and what type of access is possible. The following section outlines what criteria will be used to identify promising guided wave modes and choose one for testing. This information will be used to propose a method of inspection and predict its capabilities of detection. Results obtained from experimental tests on samples produced in the Imperial College NDT Laboratory and at the Transport Research Lab (TRL) in England are also presented.

### **7.1 Background of Post Tensioned Bridge Inspection**

The 1985 collapse of the Ynys-y-Gwas bridge in South Wales[1] especially highlighted the need for a reliable method to test post-tensioned bridges. The need was further highlighted by the 1993 collapse

of a post-tensioned bridge in Palau[96,97]. The work contained in this thesis was started to address this concern. The inspection problem is described below.

### 7.1.1 Construction

Post-tensioning continues to be used for bridge construction, especially for long spans. In this method of construction, the bridge gains its strength from the tensioning of internal tendons that occurs once the concrete framework of the bridge has already hardened. The tendons can be single wires (usually found in older bridges) or strands of seven wires (usually found in newer bridges). The wires are frequently 5 or 7 mm in diameter (although they can be much larger) and the strands are typically 12-15 mm total diameter. The tendons are located in metal or plastic tubes called ducts that are usually around 100 mm in diameter and contain 4 to 20 tendons. The ducts are placed at predetermined locations (usually around points of maximum tension) when the concrete form of the bridge is first poured. The tensioning of the tendons compresses the surrounding concrete so that it can support the required loads. To provide corrosion protection for the tendons, the ducts are filled with grout (cement, water, and possible additives) once the tendons have been tensioned. However, large air voids can be trapped in the grout. Over time these voids can fill with salt water as de-icing salts leach through small cracks in the concrete or joints between segments of the bridge. Contact with salt water causes the tendons to corrode quickly and can lead to the failure of the bridge. An effective non-destructive test method needs to be able to detect the onset of corrosion in the tendons (or the complete break of one individual tendon of the several that are present in each duct).

The collapse of the Ynys-y-Gwas bridge was attributed to corrosion of the embedded steel tendons where they intersected expansion joints in the bridge[1]. Poor construction techniques allowed water to reach the steel, causing severe localized corrosion. When one segment of the bridge failed early in the morning, it started a chain reaction that led to the complete collapse of the bridge. Fortunately, no one was injured.

### 7.1.2 Current Inspection Techniques

Following the collapse of the Ynys-y-Gwas bridge, a great number of different inspection techniques have been tried on post-tensioned bridges. A few of these are summarised below, however, none of them has yet provided a solution that is entirely satisfactory.

Currently, the most common form of testing is visual inspection[98]. In its simplest form, inspectors search for evidence of corrosion products on the underside of the bridge. However, since the critical tendons form a small portion of the bridge, the inspection must be very detailed. Even small cracks can indicate that problems may exist since small cracks can provide a route for the ingress of moisture[99].

Invasive inspection methods are also used in conjunction with visual inspection. Typically, several vulnerable locations, such as the high and low points of ducts, are identified on a bridge. The condition of the ducts and the tendons at these locations are monitored by drilling small holes in from the side of the bridge and using bore-scopes or endo-scopes to look at the tendon. By sampling several small locations, the general condition of the bridge is extrapolated[98]. The large amount of reinforcing that occurs near the tendon anchorages prohibits this drilling method from inspecting the region near the end of the tendons. Therefore, if it is believed that the anchorages are very vulnerable to corrosion in a particular bridge, the concrete that covers the anchorages is removed by using high pressure water and the anchorages are inspected directly. To examine a portion of the tendons, the grouting hole in the anchorage can be drilled out for endo-scope access[98]. However, concerns have been raised about whether this type of invasive inspection (both for the tendons in mid-span and for the anchorages) causes too much damage. Inadequate repairing of the access points can leave the bridge very vulnerable to future corrosion[99]. Although visual inspection provides some information on the overall condition of a bridge, a method that can quickly and non-destructively scan the entire bridge for problems is desired.

Radiographic testing has also been used to test several post-tensioned bridges[100,101]. The main purpose of these systems is to detect problems with the grouting (for example voiding) although very large defects in the tendons may be detectable[101]. Most of these systems use ionising radiation, which means that a large exclusion zone must be established around the test site. For example, a French system called SCORPION, which provides real time images, requires an exclusion zone of a few hundred metres. Other systems [101] use an x-ray source and require much smaller exclusion zones, but must have a long exposure time (15 minutes for a 600mm thick concrete section). Another difficulty with this type of inspection is that access to both sides of the structure is required, which limits the number of bridges that can be examined. Ground penetrating radar and impulse radar have also been used to try to evaluate the tendons. However, their poor resolution and inability to penetrate the steel ducts that are present in older bridges have effectively limited their application to duct location[98,102].

Several other inspection techniques have been developed in various laboratories. Time domain reflectometry, which examines the reflections of electromagnetic signals as they travel down a wire (such as a tendon), has been investigated[103]. However, the method has difficulties since the tendons touch each other and the metal walls of the ducts, and the ducts are in contact with the reinforcement cage of the bridge. Any electrical signal would be carried by the entire bridge structure and would not be able to be used to test the integrity of a specific tendon. Therefore, the method has had difficulty getting out of the laboratory and into field practice.

Ultrasonic methods have also been extensively investigated. The majority of these methods attempt to locate voided areas in the ducts[104–107]. Researchers at UMIST have developed a system that scans low frequency ultrasonic probes along a bridge looking for reflections from voided ducts[104]. This method relies on frequency filtering of the received data to help reduce noise from scattering. Researchers at Darmstadt have developed an array of low frequency transducers to overcome the scattering problem[105]. Other researchers have examined the possibility of using impact echo testing to look for

voids[106,107]. Unfortunately, the grout used in older bridges did not contain many additives to stop it from shrinking as it cured. Therefore, the grout has usually pulled away from the duct walls. When this happens, ultrasonic methods will detect a voided duct, even though the tendon is well grouted. John Weight, of City University, investigated the possibility of sending high frequency ultrasonic waves down the length of the tendons[108]. His early research revealed that the ultrasound could travel down the tendons and be detectable for up to 20 metres. This method directly interrogates the condition of the critical tendons and relies on sending long bursts of high frequency guided waves down the tendons.

The inspection technique investigated in this chapter uses the same principle as Weight and examines the possibility of sending ultrasound down the actual tendons, so that their condition can be directly determined. The investigation carried out in this chapter differs from the work done by Weight because it uses wave propagation modelling to predict the behaviour of the guided waves before experiments are performed. Weight's work concentrated on experimental results and was limited to high frequency modes. However, the conclusions of this chapter and Weight's report agree, except that Weight predicted longer propagation distances. The basic idea behind this type of testing is that ultrasonic waves that are propagated along the steel tendons will reflect from fractures or loss of section due to corrosion. These reflections will return down the tendons and can be detected by the same transducer that is used to generate the waves. Ideally, a guided wave could be found that is trapped in the steel and does not leak energy into the surrounding grout. Such a wave will allow large sections of each tendon to be inspected rapidly from one position. If a non-leaky mode is not found, high frequency, low attenuation modes, whose energy is concentrated in the centre of the bar, may also be investigated.

### 7.1.3 Guided Wave Access

An ideal method for generating a guided mode in the steel tendon would be non-invasive. However, since the tendons are embedded in layers of concrete, ducts, and grout, it is unlikely that a test will be able to isolate the condition of an individual tendon from outside the structure. The next best methods of generating a guided wave would access the tendons through the small holes that are currently drilled for visual inspection with endo-scopes. Special probes could be developed that attach to individual tendons in this restricted space. Alternatively, tests could be conducted from the end of the tendon. This type of test would look for fractures or corrosion patches near the anchor points. These are usually high or low points on the tendons and are particularly vulnerable to voids. They are also usually over the bridge piers and so are most difficult to access by drilling and endo-scoping. However, gaining access to the ends of the tendons requires extensive work that would temporarily close the bridge since both the road surface and a substantial amount of protective concrete must be removed. Bridge owner groups have suggested that they are willing to go to this effort, if it yields conclusive results[109].

The unexpected collapse of the Ynys-y-Gwas bridge led to a temporary ban in the United Kingdom on grouted tendon construction in 1992 pending the development of new construction standards and

inspection techniques. The ban has recently been lifted on the strength of the new standards aimed at preventing future failures [2]. However, there is still no reliable method of testing the thousands of existing bridges that are at risk.

## 7.2 Model Parameters

Wave propagation modelling is used in this chapter to identify promising guided wave modes for non-destructive testing. The modelling concentrates on the wave propagation in the grouted tendons, since they comprise the critical portion of the post-tensioned bridges that need to be inspected. This section explains how the system is modelled and what criteria are used to identify promising modes.

### 7.2.1 How the System is Modelled

Guided waves that are concentrated directly in the steel tendons will be able to travel the farthest and will be the most sensitive to corrosion. For these waves, only the steel tendons and their interface with the surrounding grout have a significant effect. The duct wall and surrounding concrete are effectively decoupled because the partial waves are quickly attenuated in the grout, due to its very lossy nature. Therefore, for the analysis contained in this chapter, the embedded system is simply modelled as a visco-elastic isotropic steel bar embedded in an infinite space of visco-elastic grout. The material properties for the system are listed in table 7.1. The steel needs to be considered to be visco-elastic when high frequencies and long propagation distances (for which the effect of visco-elasticity would be significant) are being evaluated. Typical properties for steel are assumed for the density, velocities, and visco-elastic constants of the steel [110]. The material properties for the grout were measured from a small set of grout samples (0.6 water/cement ratio) created at Imperial College. However, because the shear attenuation was quite high, it could not be measured and had to be assumed. The steel - grout bond is assumed to be perfect in order to model the case with the highest attenuation, although this may not always be the true. Weak coupling between the tendon and the grout will dramatically reduce the observed attenuation. Both single wires and multi-wire strands (composed of 7 circular wires) were modelled as bars since guided waves are assumed to propagate down each of the wires of the strand individually and the modes in the different wires will be uncoupled, especially at high frequencies. The spiral winding of the strands around a central core should have no effect since the resulting curvature of the outer wires is very gradual in comparison to the wavelength of the guided wave modes (although the outer wires of the strand may prevent the grout from continually contacting the innermost wire of the strand). Five mm diameter steel bars, a typical size for tendon wires, are used for the preliminary modelling. However, since the dispersion curves can be normalized by the radius of the bar, the behaviour of other diameters can be easily predicted from the same dispersion curves.

Table 7.1: Material constants used in the wave propagation modelling of grouted tendons.

Material	Density ( $g/cm^3$ )	$v_l$ (m/s)	$v_s$ (m/s)	$\alpha_l$ (np/ $\lambda$ )	$\alpha_s$ (np/ $\lambda$ )
Steel	7.932	5960	3260	0.003	0.008
Grout	1.6	2810	1700	0.043	0.1

Guided waves could also be generated in the walls of the duct or the grout filling. However, ducts are usually made from flexible pipework that consists of many individual sections linked together. Therefore, they do not support long-range guided waves. Similarly, the grout will not support guided waves. The cracks and voids that inevitably form in the grout cause guided waves to quickly die away if their energy is concentrated in the grout. In addition, because the tendons are not always at the same location in the duct, the thickness of the surrounding grout varies greatly, which would affect any guided wave that propagates primarily in the grout.

### 7.2.2 Mode Selection Criteria

In order to choose a mode for ultrasonic testing, some criteria should be identified. For an embedded system such as a bar in grout, the attenuation is the dominant factor in mode selection. If the attenuation is too high, the mode will not propagate far enough to test a reasonable length of the tendon. However, other factors such as group velocity, ease of generation, and reflection characteristics must also be taken into account.

The primary mode selection criterion is low attenuation. Realistic ultrasonic testing systems can compensate for about 80-100 decibels of attenuation before the received signals become lost in the noise. The attenuation will be caused by poor coupling of the wave into the tendon, small reflections from defects, visco-elastic damping, and leakage of energy into the surrounding medium. Leakage forms the largest component of the attenuation in this type of system and is therefore the component of the most concern. To reliably send guided waves from one point on a tendon to another point 20 metres away at the other end of a span to check if the tendon is still intact, the attenuation cannot realistically be greater 4 dB per metre. If, on the other hand, the testing technique is searching for defects close to the testing point by looking for reflected signals, an attenuation of 40 dB per metre should allow a defect one metre away to be detected (since the wave must travel to the defect and then back to the transducer). In order to detect a reflection from a defect two metres into the grout, the attenuation should be less than 20 dB per metre. These values assume that the reflection from the defect is substantial, for example the reflection from a complete break. The ranges will be reduced for smaller reflections caused by only partial loss of section due to corrosion.

A concern that relates to the generation of guided waves is the ability to couple energy into the tendon. The interface between the transducer and the tendon becomes more critical as the frequency increases. Low frequencies do not 'see' many surface roughnesses that higher frequencies see since they have

much longer wavelengths. At high frequencies, a rough surface causes a large portion of the energy to be randomly scattered instead of being transmitted into the test specimen as a coherent wave.

The wavelength of the mode affects the reflection from defects in the tendon and must be taken into account. If the wavelength is long enough (i.e. the frequency is low enough), the wave will reflect strongly from an arbitrarily oriented defect. However, as the wavelength becomes smaller (and the frequency higher), the energy of the mode will start to be deflected into the surrounding medium if the normal to the fracture surface is at a sharp angle to the axis of the tendon or the sides of the area of corrosion are very rounded (see section 6.3.3). Therefore, waves with small wavelengths will be less effective because their energy may be reflected sideways into the surrounding grout instead of back down the tendon where they can be detected. However, guided waves with long wavelengths are more affected by the surrounding material and are therefore more sensitive to defects in that material. In addition, the axial resolution of the inspection technique decreases as the wavelength increases. These effects must be balanced.

The ease of generating waves also contributes strongly to the choice of modes. The best method of generating a specific mode varies greatly between modes. In general, the displacement profile produced by the transducer should match the profile of the desired mode in the tendon as much as possible. Therefore a mode which is primarily comprised of axial displacements on the surface of the tendon should be generated by a transducer that couples to the outside of the tendon and can efficiently produce motion in the axial direction. Likewise, a mode whose energy is concentrated in the centre of the bar should be generated from the end of the bar with a transducer that matches the displacement profile of the desired mode. Since we would ideally inspect the tendon through the small holes that are currently drilled for endo-scope inspection, we would prefer a mode that can be generated and received efficiently from the outer surface of the tendon. However, as shown later, most of these modes suffer from high attenuation. Therefore, the mode may need to be generated from the end of the tendon, which requires the removal of the bridge surface to gain access. If generation is from the end of the tendon, longitudinal modes are preferred because they are easier to generate than flexural modes since their displacement profile is constant with angle. Modes that are not axi-symmetric require that the transducer be divided into segments that are driven differentially.

Another consideration that must be taken into account is the reflection of waves from the interface where the tendon enters the surrounding grout and where the collet clamps the tendon. Because there is a large impedance change between a steel bar that is free (surrounded by air or vacuum) and a bar that is embedded, a portion of the guided wave will be reflected as it adapts to the new impedance. This reflection needs to be minimised for two reasons. First, as much energy as possible needs to be transmitted into the embedded tendon so that as long a length as possible can be investigated. Second, a portion of the wave that is reflected will come back to the transducer, be reflected off the end of the tendon, head back to the interface and be reflected. If this reverberation of the reflected signal is too large, the reflected signal from any defects in the embedded portion of the tendon can be masked. For common lengths of the protruding sections of the tendons and realistic attenuation values, the amplitude



of the reflected wave usually needs to be less than 5 percent of the input signal (see section 6.3.5). The reflection and transmission coefficients of the modes cannot be determined from the dispersion curves, however they can be calculated using finite element techniques. In addition to the reflection from the interface where the tendon enters the grout, there will also be a reflection from the location where the collet clamps the tendon. If this reflection is too large, similar problems will be experienced.

The group velocity of the modes provides another criterion for selecting the best guided mode and frequency of operation (operating point). If the test is designed to locate or size the defect, it is helpful if the operating point coincides with a peak in the group velocity. If it does coincide with a peak in the group velocity the shape of the wave packet will not change significantly as the mode propagates down the tendon and therefore a reflection will be more easy to detect. In traditional guided wave ultrasonic testing, it is also advantageous to use a mode that travels faster than any other modes (at the test frequency) so that if the same mode is reflected from a defect, its signal will be the first to arrive at the receiving transducer[111]. For the grouted tendon system being investigated, this benefit is reduced because most of the modes are so attenuative that they will become too small to detect once they have travelled to the receiving transducer. Only the low attenuation mode that was transmitted will be detected.

### 7.3 Search for a Non-Leaky Mode

An ideal testing technique would be able to inspect the entire length of the steel tendons from one position. In order to propagate guided waves far enough for this type of testing, a mode that has very low attenuation must be found.

Since the majority of the attenuation for a tendon embedded in grout occurs because of leakage of energy into the grout, a non-leaky mode such as the one described in section 3.3.1 would be very desirable. Before the cylindrical wave propagation model was properly implemented, the grouted tendon system was modelled as a flat plate surrounded by grout using the material properties in table 7.1 to determine if a non-leaky mode would exist. The results, shown in figure 7.1(a), were very promising. At a low enough frequency, the A0 mode, which is similar to the F(1,1) mode in a bar, has a non-leaky section where its phase velocity dips below the shear bulk velocity of the surrounding medium. However, as figure 7.1(b) shows, this non-leaky section does not exist for the equivalent cylindrical system. The F(1,1) mode cannot be traced below the bulk shear velocity in the surrounding medium.

The three-dimensional, phase velocity–frequency–attenuation plots in figure 7.2 examine this difference in further detail. For the plate case, as the phase velocity of the A0 mode nears the shear bulk velocity, the attenuation drops rapidly. Below the shear bulk velocity, all of the attenuation is due to visco-elastic losses. However, for the cylindrical case, the attenuation increases as the phase velocity of the F(1,1) mode approaches the shear bulk velocity of the grout. Unfortunately, no non-leaky section has been found for this case.

The existence or non-existence of non-leaky mode sections is an area that warrants more research. The parameters that control the existence of a non-attenuating guided wave that exists at the interface of two semi-infinite solids, which is called a Stoneley wave, has previously been studied and expressed in an explicit form[66,67]. However, this knowledge has not been expanded to include finite thickness plates and cylinders. The derivation and experimental confirmation of the comparable conditions for an embedded bar and plate would be very valuable for helping design ultrasonic testing systems. However, it has not yet been performed.

Although the reason why a non-leaky mode section appears in the Cartesian system and not in the cylindrical system is not completely understood, examining some similar cases reveals some clues. When the density of the surrounding grout is dramatically reduced from its actual value of  $1600 \text{ kg/m}^3$ , a non-leaky mode section appears. This effect can be seen in figure 7.3, which shows the phase velocity dispersion curves of the F(1,1) mode of a 5 mm diameter steel bar which has been embedded in grout. The density of the grout has been varied from 500 to  $800 \text{ kg/m}^3$  while the other material properties were kept constant (Long. Vel. = 2810 m/s, Shear Vel. = 1700 m/s, no visco-elastic damping). As the density of the grout increases, the phase velocity of the non-leaky section of the mode increases towards the bulk shear velocity of the grout. For comparison, figure 7.4 shows the non-leaky sections of the A0 mode for an equivalent Cartesian system, a 5 mm thick steel plate embedded in the same grout. The phase velocity of each of the curves in the Cartesian system are much farther away from the bulk shear velocity in the grout than they are for the corresponding cylindrical system. Since the global matrix method introduces mathematical singularities at the bulk velocities of the constitutive materials (see section 2.8.1), the solution routines cannot locate dispersion curves that are too close to the bulk velocities. Therefore, even if a non-leaky section exists in the actual system (when the density is  $1600 \text{ kg/m}^3$ ), the solution routines would probably not be able to converge on the roots.

Although no non-leaky section of the F(1,1) mode in an embedded steel bar could be traced using the solution routines developed in this thesis, a non-leaky mode section may still exist in the actual system. Therefore, the properties of a hypothetical non-leaky mode section should still be examined to see if a non-leaky mode could satisfy the inspection requirements. To perform this analysis, the dispersion curves for the equivalent Cartesian system and for a steel bar in low density grout will be used to help evaluate the possibility of using this mode to inspect grouted tendons. The behaviour of the actual mode (if it exists) needs to be inferred.

The primary criterion for mode selection remains the attenuation. Even non-leaky sections of modes will experience attenuation because of the material damping present in all materials. In the frequency range where non-leaky modes exist, the visco-elastic nature of the steel adds a small amount of attenuation to the propagation of the guided wave. However, the strong material damping of the grout causes significantly more attenuation. Although no bulk wave is created in the surrounding grout for a non-leaky mode section, there is still significant displacement in the grout. As shown in figure 7.5, the displacement is large at the boundary between the steel and the grout (since there is perfect bonding) and dies away exponentially from the interface. Like a Rayleigh or Stoneley wave, a non-leaky mode section

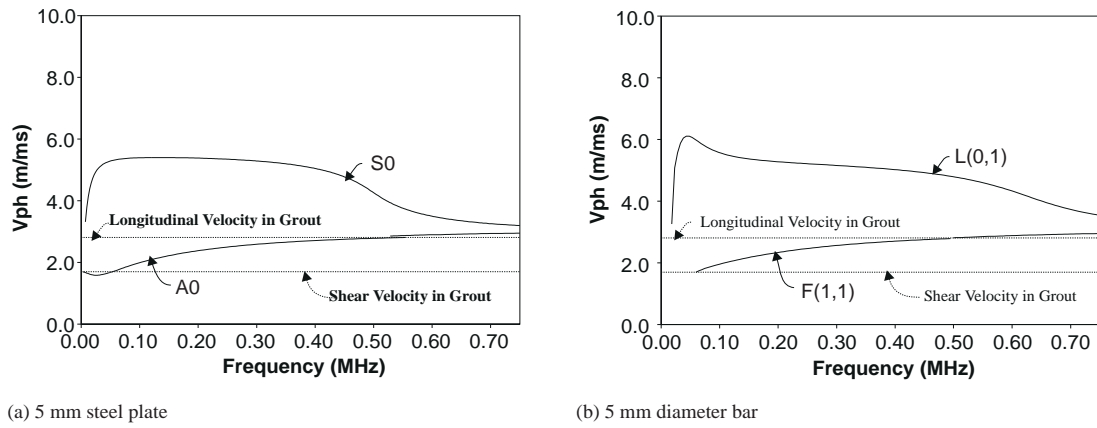


Figure 7.1: Comparison of the phase velocity dispersion curves for (a) a 5 mm steel plate and (b) a 5 mm diameter bar embedded in grout.

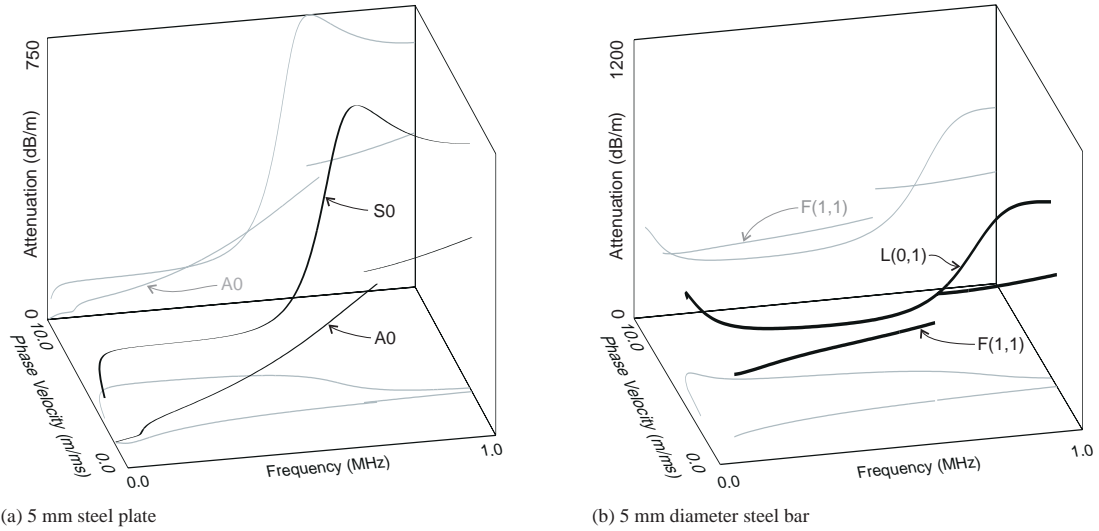


Figure 7.2: A three dimensional comparison of the dispersion curves for (a) a 5 mm steel plate and (b) a 5 mm diameter steel bar embedded in grout. The bottom plane shows the projection of the frequency and phase velocity and the back plane shows the projection of the frequency and attenuation.

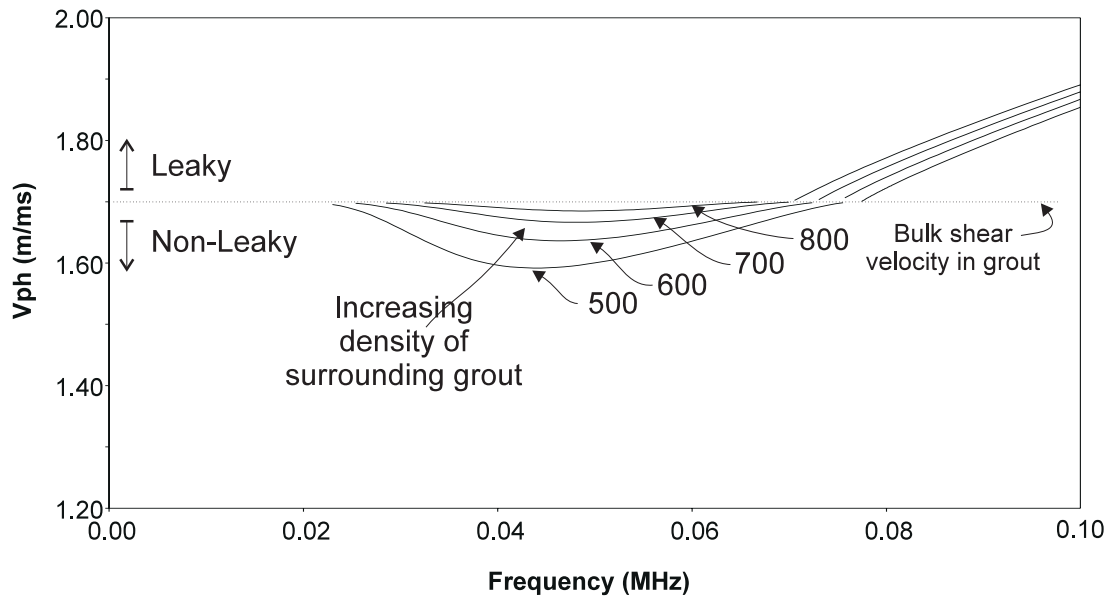


Figure 7.3: The phase velocity dispersion curves for the F(1,1) mode of a 5 mm diameter steel bar embedded in different densities of grout.

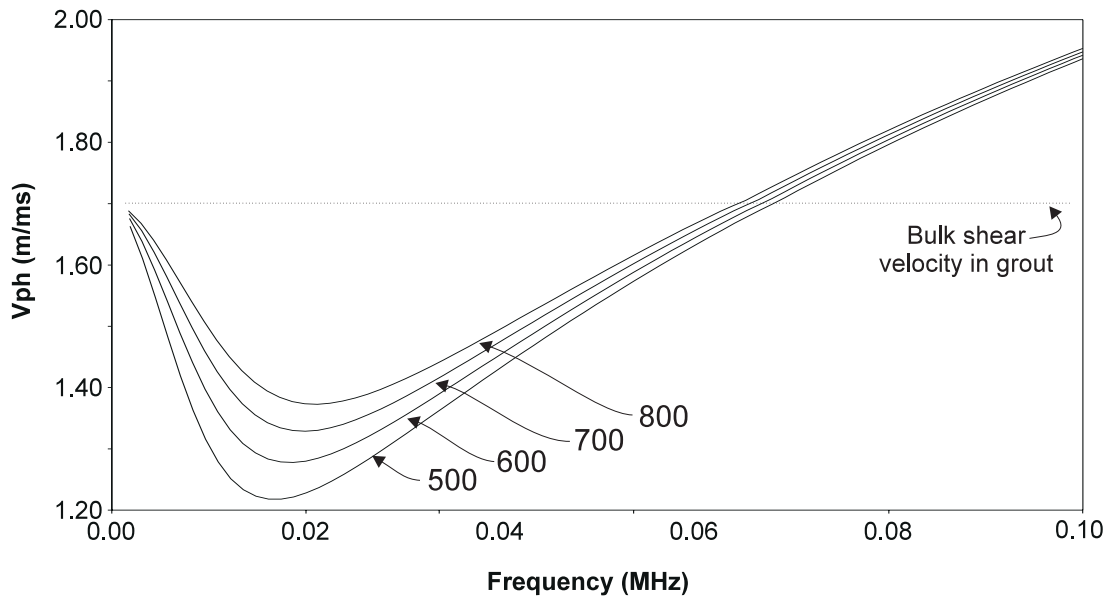


Figure 7.4: The phase velocity dispersion curves for the A0 mode of a 5 mm thick steel plate embedded in different densities of grout.

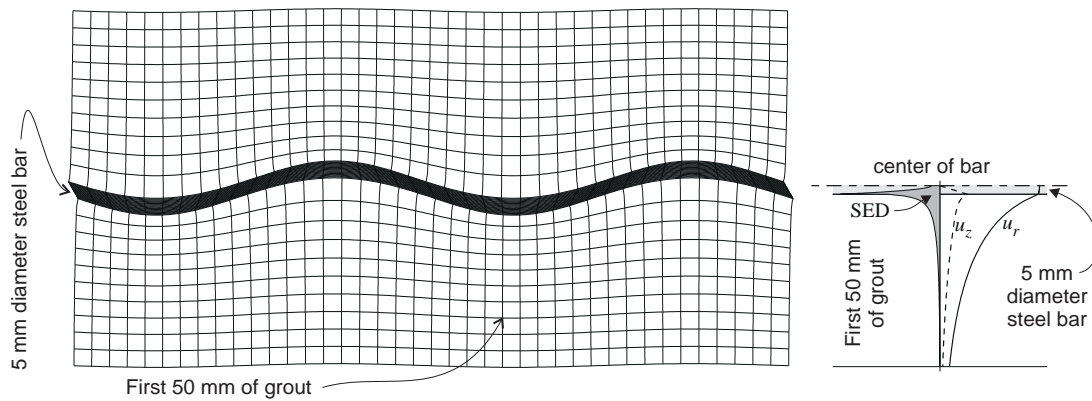


Figure 7.5: The displacement and strain energy density (SED) profile at a non-leaky section of the F(1,1) mode in a steel bar embedded in very low density grout. (A non-leaky mode section has not been found for a steel bar embedded in normal density grout)

has most of its motion contained within one wavelength of the surrounding material. At the frequencies considered for this system, a wavelength in the grout is over 40 mm. Therefore a large amount of grout is affected and a significant amount of attenuation can be introduced. Figure 7.6 shows the attenuation values of the non-leaky section of the F(1,1) mode in a 5 mm diameter steel bar and a 5 mm thick steel plate embedded in a grout that has a density of  $500 \text{ kg/m}^3$  and a small amount of visco-elastic damping ( $\alpha_l = 0.004np/\lambda$  and  $\alpha_s = 0.010np/\lambda$ ). The attenuation for the bar is three times greater than the attenuation for the Cartesian case. This difference is caused by the relatively high surface area for the bar. In the wave propagation model, a plate is considered to be infinitely wide. Therefore, the steel plate only contacts the grout at the top and the bottom of the plate. However, the bar contacts the grout around the entire circumference of the steel bar. Because of this larger contact area (versus cross-sectional area), the attenuation is higher. When the density and visco-elastic properties of the grout are increased to more realistic values ( $\rho = 1600 \text{ kg/m}^3$ ,  $\alpha_l = 0.043np/\lambda$ , and  $\alpha_s = 0.100np/\lambda$ ), the attenuation of the A0 mode at 50 kHz in the Cartesian system increases from 0.54 dB/m to over 14 dB/m. A similar increase would be expected for a non-leaky section of a mode in a cylindrical system. Therefore, if a non-leaky mode section did exist in a steel bar embedded in normal grout, its attenuation would probably be between 15 and 40 dB/m.

These estimated attenuation values for a hypothetical non-leaky mode section remain too large for testing an entire bridge segment in one test. Even if an optimistic 20 dB/m attenuation value is assumed for the hypothetical non-leaky mode section, the longest length that could be tested in a pitch catch setup would be around 5 metres and the longest range for a pulse echo system would be around 2 metres. Therefore only a local section, such as the tendon anchorages could be inspected.

Even if the attenuation of a hypothetical non-leaky mode section was much lower, there are severe problems that further hamper the application of these modes for inspecting grouted tendons. The biggest complications are caused by the large displacements that would be present in the grout. As discussed in section 6.3.4, modes that are propagating in an embedded structure will be reflected from defects

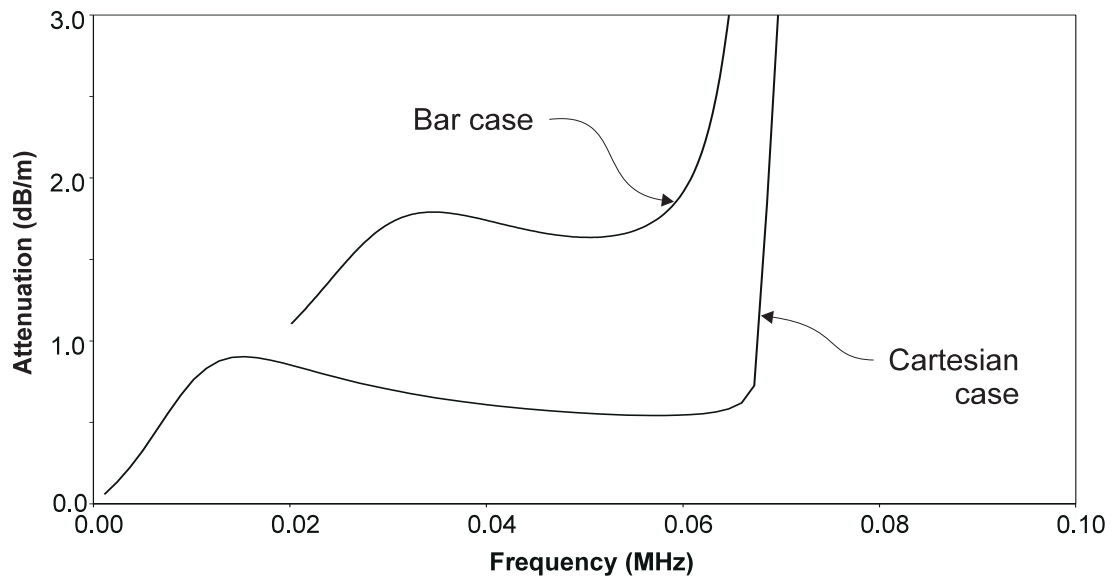


Figure 7.6: A comparison of the attenuation values for the non-leaky mode section of a 5 mm diameter steel bar and a 5 mm thick steel plate embedded in grout that has a density of  $500 \text{ kg/m}^3$ .

in the surrounding grout in addition to defects in the structure itself. For example, at .70 MHz-mm frequency-radius (equivalent to 280 kHz in a 5 mm diameter bar), about 7 percent of the fundamental longitudinal mode (L(0,1)) in an embedded steel bar is reflected from a 1 mm deep circumferential notch in the grout. A similar size reflection would be expected from a hypothetical non-leaky mode. Although this reflection is relatively small and will probably not be confused with a large defect in the embedded bar, the reflection would reduce the amplitude of the transmitted wave. Since there are inevitably a large number of such cracks, the observed attenuation could be dramatically greater than that predicted. In addition, at this frequency, the thickness of the grout changes dramatically and rapidly within one wavelength since the tendons are not always at the same location in the duct. These changes would also cause small reflections, adding to the observed attenuation. Another problem only appears in experimental results. Fifty kHz is near the resonance frequencies of many of the collets and end-plates that are used in grouted tendon construction. Therefore, they resonate when a mode is excited in a tendon to which they are attached. The subsequent reverberations are larger than the reverberations in the protruding end of the tendon and make pulse-echo testing very difficult. The centre frequency that would have to be used to excite these modes is very low. Although this would allow for good reflections from arbitrarily oriented defects, the axial resolution would be very poor. A final complication that would appear when using these hypothetical non-leaky mode sections is that they travel very slowly and are relatively dispersive. Therefore, the received signals will be the last to arrive and will have a different shape than when they were excited.

## 7.4 Search for a High Frequency Alternative

In the previous section, a search was made for a low frequency, non-leaky mode that could inspect long lengths of grouted tendons. None was found. This section evaluates what other modes could be used for the ultrasonic inspection of grouted tendons. Since all of the modes under consideration will experience leakage, very long propagation distances cannot be expected. Therefore, instead of searching for a mode that can inspect the entire length of a grouted tendon from a single location, a mode will be sought which can detect defects over a few metres distance.

Figure 7.7 expands the dispersion curves of figure 7.1(b) to include all of the zero circumferential order modes that will propagate below 20 MHz. A definite pattern emerges in the attenuation dispersion curves seen in part (b). There are several series of modes that have dips in attenuation at higher frequencies. The prediction of low attenuation at high frequency contradicts the intuitive expectation that the attenuation increases with frequency, especially for materials that include visco-elastic material damping. By examining the mode shapes of two of these dips in attenuation, which are shown in figure 7.8, their behaviour can be better understood. These dips in attenuation correspond to locations where the energy is concentrated in the centre of the steel bar. Since the energy is concentrated in the centre of the bar, it does not leak into the surrounding grout as readily as at other locations where energy is distributed more towards the outside of the steel bar. This concentration only exists for high order modes propagating at high frequencies. It occurs when the phase velocity of the high order modes nears the bulk longitudinal wave in the steel and the energy velocity reaches a local maximum.

Each of the attenuation dips occur over a narrow frequency band, whose width and location can be predicted. The minimum attenuation of each of the dips can also be predicted. For the lower frequency dips, leakage of energy into the surrounding medium is the dominant mechanism of loss. For higher frequency dips, the attenuation increases because of material damping in the steel bar. Therefore, for each set of material properties, there is a specific optimum mode that a testing procedure should target in order to minimize the losses and therefore maximize the test range. For the material properties used in the modelling, the optimum test frequency (in MHz) is around 45 divided by the diameter of the steel bar (in mm). The narrow frequency ranges of the attenuation minima causes the system to act as a mechanical filter and not pass frequency components that are not very near an attenuation minimum. The higher frequency flexural modes also have dips in attenuation like the axi-symmetric modes. However, the minimum attenuation of the dips for the flexural modes is much greater than for the axi-symmetric modes. Therefore, they were eliminated from consideration.

The dips in attenuation appear to be very promising regions of the dispersion curves for inspecting grouted tendons. Their attenuation is moderate and they will be relatively insensitive to defects in the grout. In addition, they can be generated efficiently and can be separated from the other propagating modes.

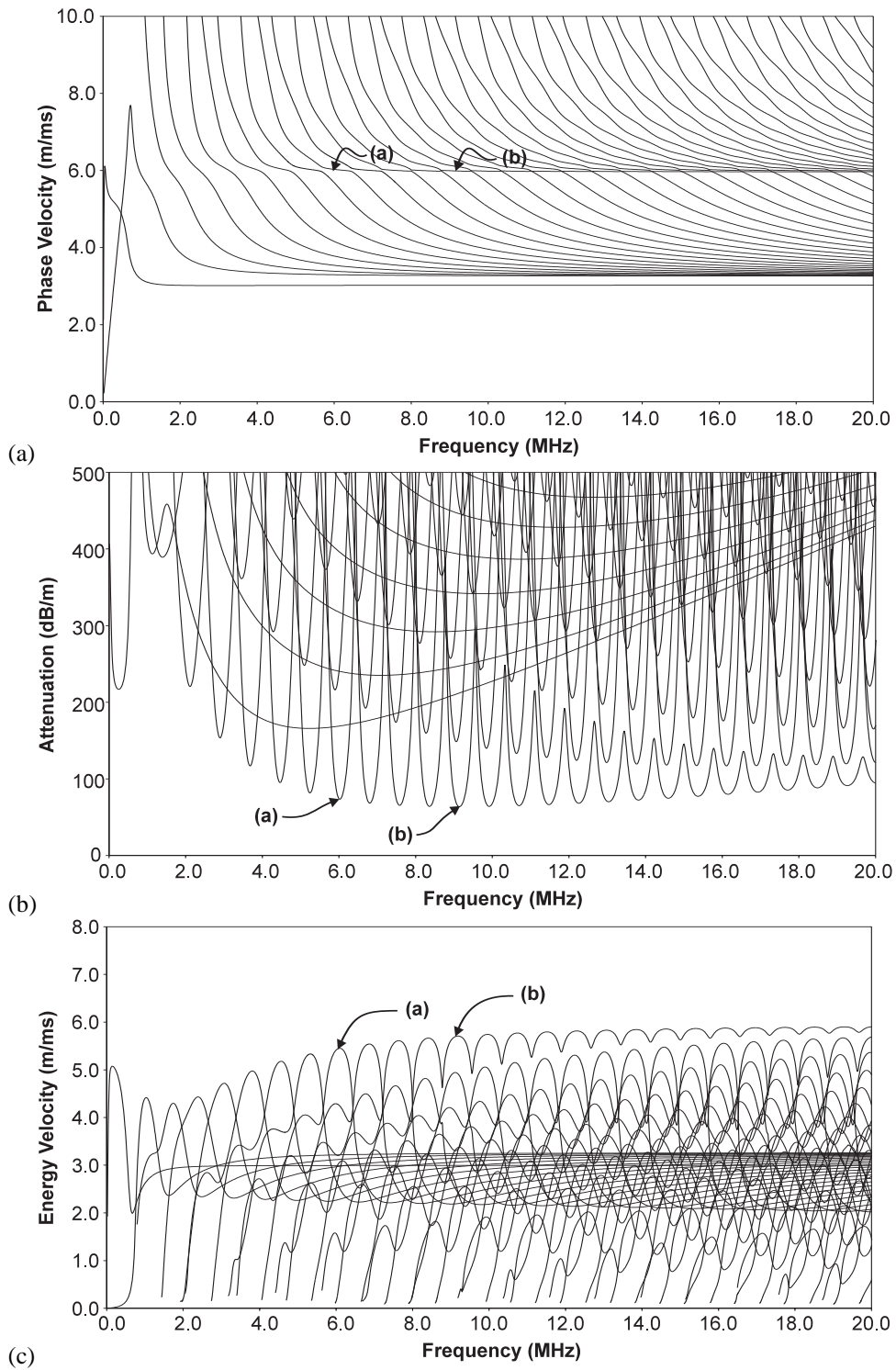


Figure 7.7: (a) Phase velocity, (b) attenuation, and (c) energy velocity dispersion curves for the longitudinal modes of a 5 mm diameter steel bar embedded in grout.



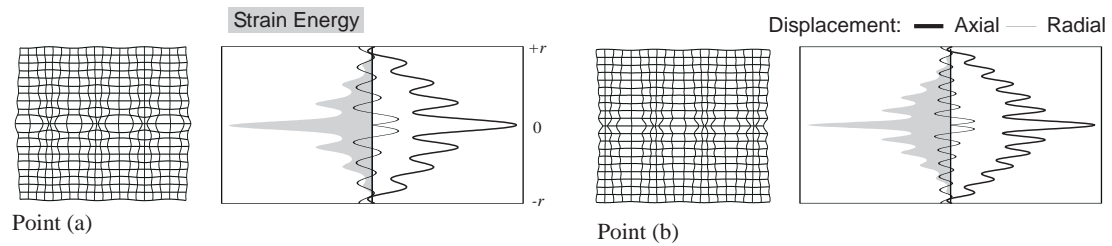


Figure 7.8: The mode shapes corresponding to the points marked (a) and (b) in the previous figure. Only the displacements in the steel bar are shown.

The lowest attenuation of any of the dips is about 60 dB/m for a 5 mm diameter steel bar with the material properties given in table 7.1. This attenuation is higher than desired, however, it remains low enough that a reasonable amount of tendon can be inspected. A rough estimate of the maximum test distance can be predicted. The estimate can be represented by the equation,

$$d = \frac{(Sensitivity - 10)}{2} \frac{2r}{0.32} \quad (7.1)$$

where the pulse echo detection distance,  $d$ , (in metres) is determined by several factors relating to the sensitivity of the testing equipment and the losses due to transmission along the embedded bar and reflection from a defect. The sensitivity of the test equipment,  $Sensitivity$ , is given in dB. The expected reflection from a defect is assumed to be 10 dB lower than the incident signal. This value was taken from the finite element predictions of the reflection of the L(0,4) mode in a bar, which is one of the first modes to show a dip in attenuation (see section 6.4). This loss equates to a square notch that extends one third of the way through the radius of the bar. The factor of 2 in equation 7.1 accounts for transmission to and from the defect. The minimum loss due to transmission along the bar has been taken from the attenuation dispersion curves shown in figure 7.7 and is represented by the expression,  $2r/0.32$ , which is proportional to the radius,  $r$ , (in metres). Estimating that our broad-band digital pulse-echo system can compensate for about 100 dB of loss, a significant defect could be located 0.7 m from the end of the tendon if the bar is 5 mm in diameter, 1.1 m if the bar is 8 mm in diameter, 2.1 m if the bar is 15 mm in diameter, and 2.8 m if the bar is 20 mm in diameter. These ranges may be increased in actual testing situations. Imperfect bonding between the steel and grout can significantly reduce the attenuation. This situation is likely to occur for the centre wire of a seven wire strand, since the outside wires can block the grout from reaching all points on the central core. In addition, optimizing the transducer and the amplifiers could improve the 100 dB sensitivity factor, which would extend the range.

The relatively high test frequency has several advantages and disadvantages. Because of the high frequency of the attenuation dips, the inspection technique would have good axial resolution. The wavelength of the lowest attenuation dip in a 5 mm bar is around 0.26 mm. Therefore, the entire length of a 50 cycle tone burst would be less than 15 mm. On the other hand, the wavelength of a possible non-leaky mode would be around 60 mm, spreading a 50 cycle toneburst over 3 metres. The fine resolution of the high frequency modes considerably enhances pulse-echo testing since areas close to the trans-

ducer could be inspected and multiple defects that are close together could be separated. Because of the high frequencies involved and also because of the nature of the modes at the dips in attenuation, a test procedure using these modes would be relatively insensitive to changes in the grout. At the frequencies corresponding to the attenuation minima, the displacements and energy at the steel – grout interface are also at minima, indicating that there is little influence of the grout. In addition, the wavelength in the grout is very short. The combination of the short wavelength with the large viscous damping of the material at this frequency means that the leaky bulk waves die away quickly and that only a very small amount of grout affects the wave propagation. Therefore, the modes will be insensitive to changes in the thickness of the grout. The high frequencies involved also cause some difficulties. Firstly, the surface where the guided wave is generated will have to be carefully prepared because its surface roughness will have a strong effect. Secondly, if the defects are not perpendicular to the direction of propagation, the resulting reflections will be significantly reduced.

In guided wave testing, using higher order modes frequently causes problems because too many other modes can be generated which hampers the interpretation of the received signal, since they travel at different velocities. However, this should not be a problem for this system. Since the attenuation at the attenuation dips is so much lower than the attenuation of all of the other modes that can exist at the same frequency, only one mode should have a significant amplitude after propagation through the embedded part of the system. The generation and detection of unwanted modes is therefore only critical in the protruding end of the tendons, where reverberations can occur.

Because the points on the modes that correspond to the dips in attenuation have mainly axial displacement that is concentrated in the centre of the bar (as shown by the displacement profiles in figure 7.8), the modes cannot be effectively generated from the outside of the bar. Instead, the modes will best be generated from the ends of the tendons, as demonstrated in figure 7.9. Ideally the surface profile of the transducer should be adapted so that it matches the displacement profile of the desired mode. In order to get access to the end of a tendon, the road surface and some other protective coverings will need to be removed. Although gaining this type of access will be disruptive, it will allow the tendons to be inspected near their anchorages. This region is most difficult to examine using traditional inspection techniques because pier supports block access. The anchorage area is very susceptible to corrosion because it is usually a high or low point in the duct, which greatly increases the chances of voids and corrosion forming. Therefore, being able to inspect this region would significantly enhance current inspection methods.

## 7.5 Experimental Results

In order to validate the results that the model produced and to try the test procedure on some realistic test specimens, several experiments were performed. The results presented in this section were obtained from two types of systems, 8.1 mm diameter steel bars embedded in grout and 15.2 mm Dyform strands

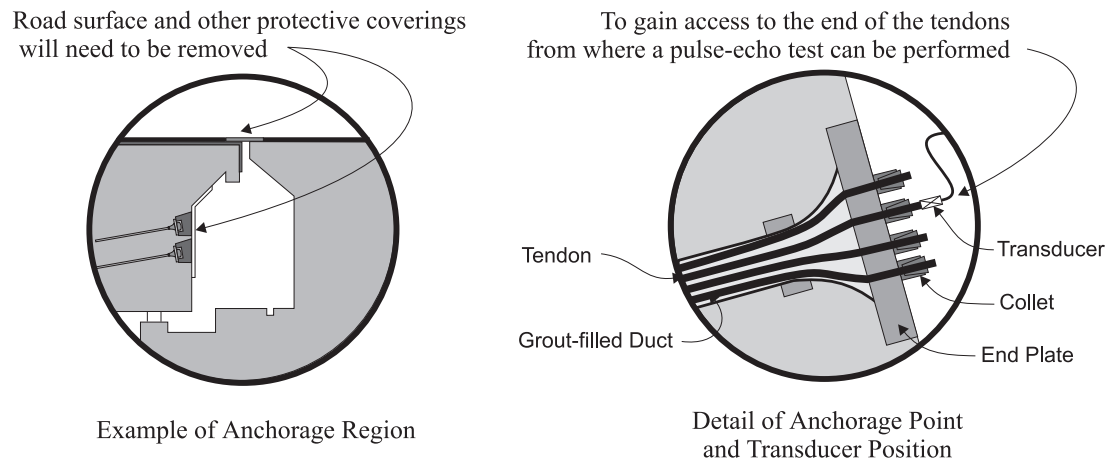


Figure 7.9: A schematic view of the proposed test procedure. Once access to the ends of the tendons has been gained by removing protective coverings, a guided ultrasonic wave can be launched down each grouted tendon. Reflections from any defects in the tendon will then return to the transducer.

embedded in grout. The bar samples, which were produced at Imperial College, are used to validate the numerical modelling and test the feasibility of inspecting embedded bars. The strand samples, which were provided by the Transport Research Laboratory (TRL) in England, are used to verify assumptions about the modelling of wave propagation in strands and evaluate the ability of the technique to test new bridge designs. At this stage, no experiments have been performed on actual post-tensioned bridges. The experiments are designed for verification of concept as opposed to detailed development of the technique. Some of the test results are presented below.

### 7.5.1 Experiments on Grouted Bars

Both the through transmission and pulse-echo responses of 8.1 mm diameter steel bars embedded in grout were examined. Two test specimens were constructed. Both specimens consisted of a 8.1 mm mild steel bar surrounded by an annular ring of grout approximately 50 mm thick within a stiff plastic pipe, which provided support and simulated a duct. The grout had a 0.6 water to cement ratio (no additives) and was pumped into the plastic pipe using a small version of the pumps typically used in grouted tendon construction. Slightly corroded steel bars were used to improve the bonding between the steel and the grout. The grouted sections covered about two metres of the steel bars, leaving around 50 mm sections of the bars protruding from the grout. For one of the specimens, the bar was undamaged. For the second specimen, a notch was cut 450 mm in from each end (measured from where the grouted section begins). The notches were created with a saw; one is 2 mm deep and the other is 4 mm deep, which cuts halfway through the bar. The notches were not covered when the grout was poured, therefore they are probably filled with grout. The tests were performed using a LeCroy 9101 arbitrary waveform generator that sent a desired toneburst to a custom built power and receiver amplifier that has pulse-echo capabilities (built by Tim Orr of Macro Design Ltd.). Standard 5.0 MHz centre frequency plane

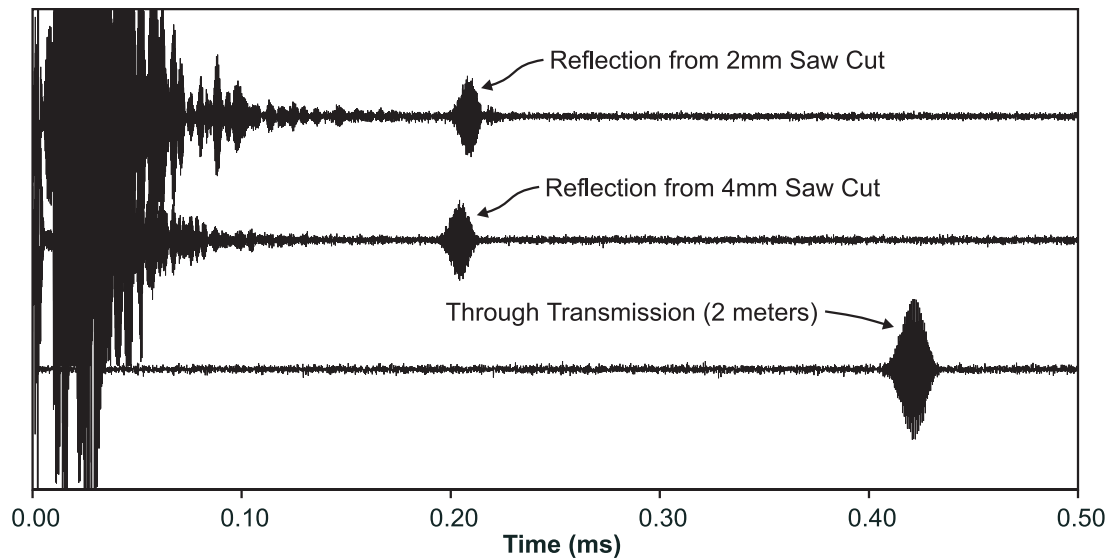


Figure 7.10: Sample time traces from 8.1 mm steel bars embedded in grout after reflection from a 2 mm saw cut 450 mm into the grout, after reflection from a 4 mm saw cut 450 mm into the grout, and after transmission along two metres of undamaged embedded steel bar.

wave immersion transducers were used. The received signals were averaged 250 times on a digital oscilloscope, after passing through a band-pass filter.

The results from three experiments on the 8.1 mm diameter bars are shown in figure 7.10. The bottom trace shows a 3.75 MHz, 50 cycle Hanning windowed tone burst after propagation along two metres of embedded steel bar. On the same amplitude scale, the top two traces show the signal that returned after reflecting from 2 mm and 4 mm deep saw cuts approximately 450 mm from where the bars enter the grout. The multiple echoes at the beginning of the response correspond to reverberations in the short length of bar that protrudes from the grout.

For an 8 mm diameter bar, the predicted test range is around one metre. Even though 3.75 MHz is not the optimum frequency for this system, the through transmission results clearly show that the signal can propagate along two metres of undamaged embedded bar. The returned signal from the reflection from a defect a metre into the specimen would be reduced in amplitude, but should remain detectable. The reflection from relatively small notches half a metre into the embedded section can also be easily detected, as shown in the top two traces. Using the optimum frequency for this testing system (5.2 MHz), a very narrow band pass filter to reduce noise, and 1000 averages, even longer distances can be inspected. Figure 7.11 shows the reflection from the end of the intact two metre bar. This signal has travelled through four metres of embedded section (suffering over 160 dB of attenuation) and is 20 dB below the noise floor of the unaveraged signal.

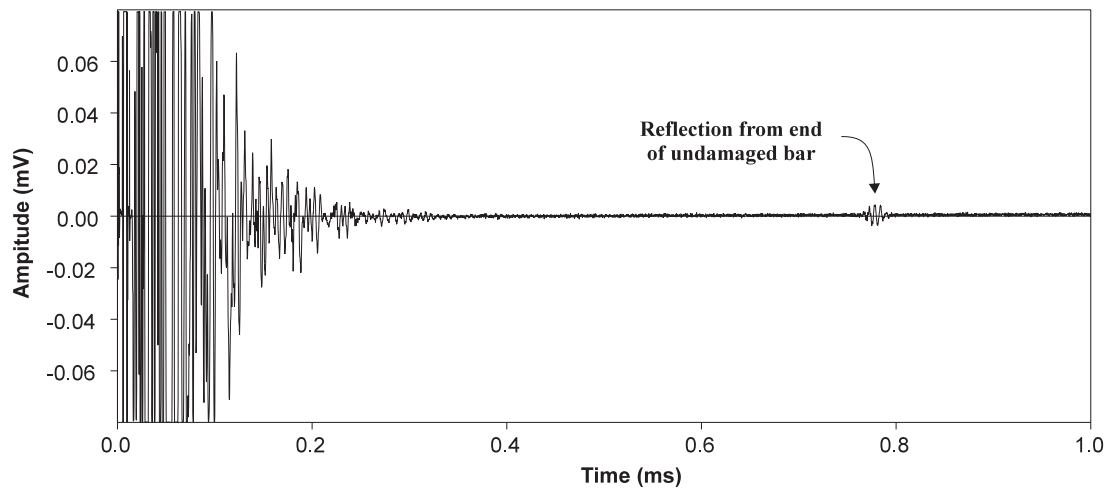


Figure 7.11: Sample time trace showing the reflection from the end of a 2 metre long 8.1 mm diameter steel bar embedded in grout.

Careful examination of reflected or transmitted signals reveals interesting behaviour of these guided wave modes. Figure 7.12(a) shows a detailed view of the signal reflected from a 4 mm deep square notch in an embedded 8.1 mm steel bar when a 5 cycle Gaussian windowed tone burst is used to excite the modes. The wavelet transform of this portion of the signal, which is shown as the contour plot in figure 7.12(b), shows how the frequency content of this signal changes with time. Each of the guided wave modes that can exist within the frequency bandwidth of the signal is excited and travels at a slightly different speed. The interference of the various modes causes the complicated time signal shown in figure 7.12(a). For comparison, the solid lines in figure 7.12(b) represent the energy velocity dispersion curves for an 8.1 mm embedded bar after they have been converted into a time delay for a signal to travel 1.13 metres (the total pulse echo distance for this system). The agreement between the energy velocity dispersion curves and the experimentally calculated arrival time for each of the modes is good.

In order to further verify the modelling work and help analyze the results, additional measurements were taken for which the centre frequency of the input signal was varied in steps from 3.0 to 8.0 MHz. Each of the signals that had been transmitted through two metres of embedded steel bar was Fourier transformed and the results are plotted in figure 7.13. A series of peaks are clearly visible in this plot, which shows the response frequency versus the centre frequency of the excitation signal. Each peak corresponds to one of the minima in attenuation that was predicted by the modal wave propagation solution. The shape of each peak along the 'excitation frequency' axis corresponds to the frequency profile of the input signal that was used, in this case a 10 cycle Gaussian windowed tone-burst. The overall shape along the 'response frequency' axis, which is shown as the solid line in figure 7.14, is controlled by the frequency response of the transducer, filters, and amplifiers used, in addition to the attenuation of each of the modes. The dotted line shown in figure 7.14 describes the frequency response of the testing equipment that was used. It was sampled by using the same configuration that was used for the previous tests, but instead of transmitting the signal through the embedded bar, it was transmitted through a 50 mm thick block of steel.

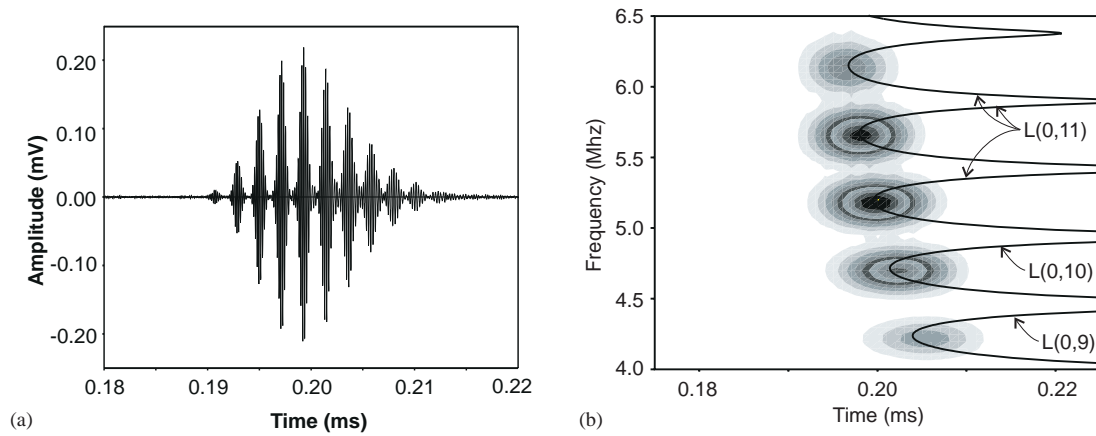


Figure 7.12: The reflection of a five cycle Gaussian windowed tone burst from a 4 mm deep square notch in an embedded 8.1 mm steel bar, showing (a) the time trace and (b) the wavelet transform. The lines which overlay the wavelet transform correspond to the arrival times predicted by the wave propagation model.

The frequency response that is shown in figure 7.14 can be converted into a relative attenuation for each of the modes. The first step of this procedure involves normalising the frequency response obtained from the embedded bar (the solid line in figure 7.14) by the response of the transduction system (the dashed line in figure 7.14). After this step has been performed, the results can be converted into an equivalent attenuation by using the expression,  $\text{attenuation in dB} = -20 \log_{10} (a/a_{ref})$ , where  $a$  is the amplitude of the normalised frequency response of the embedded system and  $a_{ref}$  is a reference amplitude. The results of this calculation are shown as the solid line in figure 7.15. (Please note that the attenuation values have been converted into units of dB/m by dividing by the two metre propagation distance.) The jagged portions of the line that occur at high attenuations correspond to the noise in the experimental data. For the results shown in figure 7.15,  $a_{ref}$  was set to be the amplitude of the largest component of the normalised frequency response of the embedded system. Therefore, all of the experimental attenuation values are relative to the mode in the frequency range of interest that has the lowest attenuation. The actual attenuation values could be obtained by adding the base attenuation of this reference mode to all of the values. Alternatively,  $a_{ref}$  could be set to be the amplitude of the guided waves that are excited in the embedded bar. However, this amplitude is difficult to measure because it is difficult to obtain calibration data that can exactly duplicate the coupling between the transducer and the test specimen. The dotted lines in figure 7.15 show the attenuation dispersion curves over the same frequency range for an embedded 8.1 mm diameter steel bar. The attenuation values have been normalised so that they are relative to the point on a mode in this system which has the least amount of attenuation. The agreement between the two sets of curves is very good. In both the experimental and the modelling results, there are a series of sharp attenuation minima that occur at a regular frequency spacing. The width of the minima and their location closely match for the two calculation methods. The depth of the attenuation minima follow the same trend for both cases. In general, the higher frequency modes have lower attenuation than the lower frequency modes. This good agreement between experimental and modelling results increases confidence in the accuracy of the modelling.

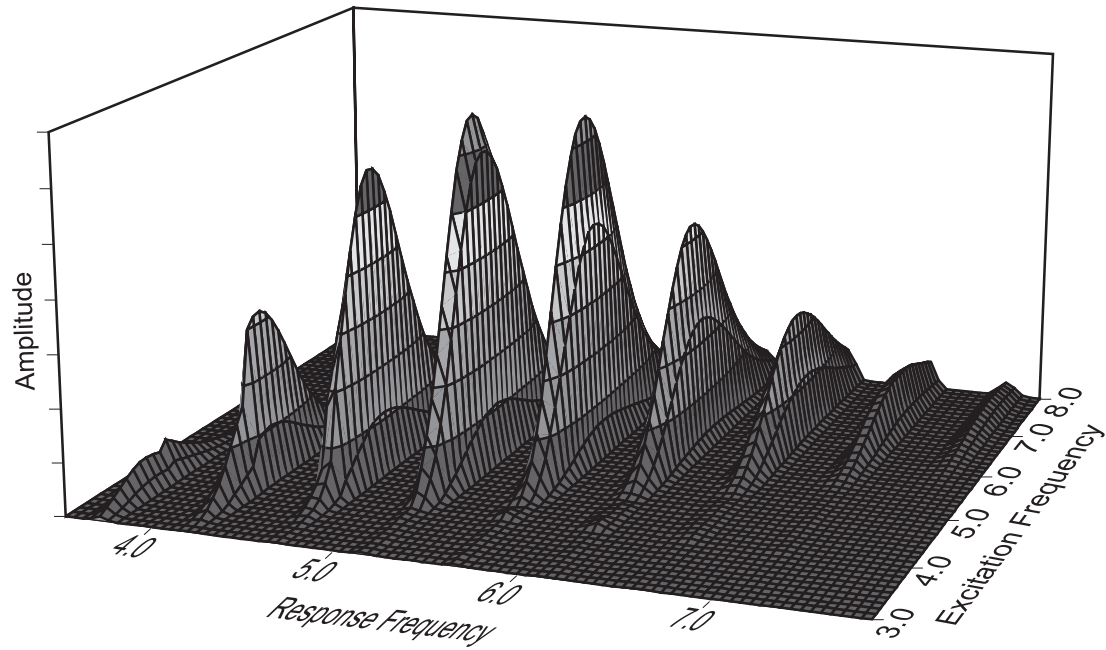


Figure 7.13: The frequency spectrum of a signal transmitted through two metres of embedded steel bar as the centre frequency of the input signal was changed from 3.0 to 8.0 MHz.

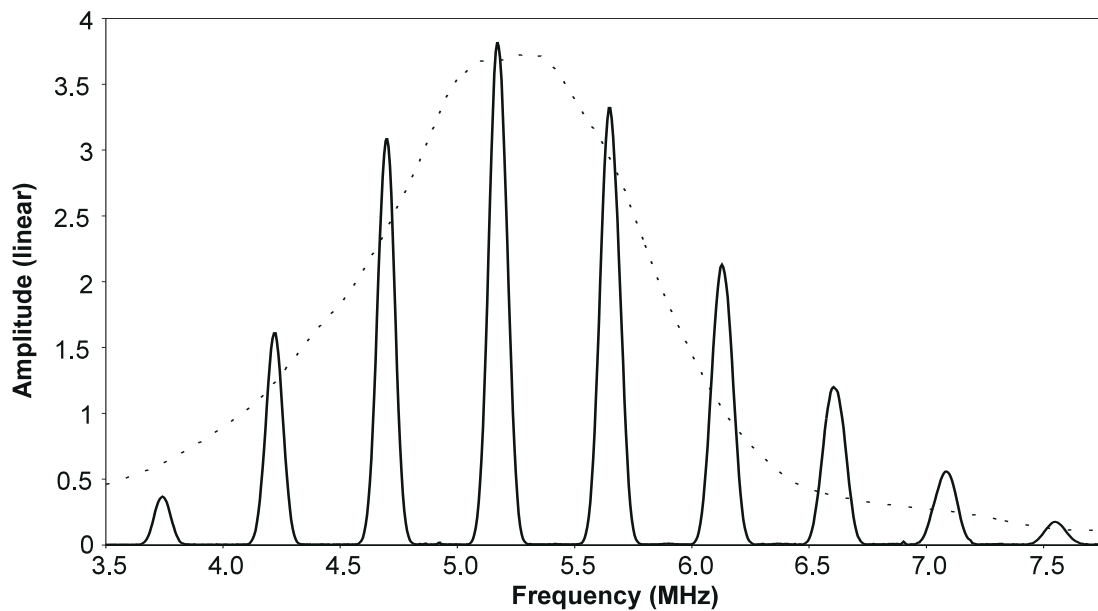


Figure 7.14: The profile of the experimental frequency response shown in the previous figure. The dashed line represents the frequency response of the test equipment used for these experiments.

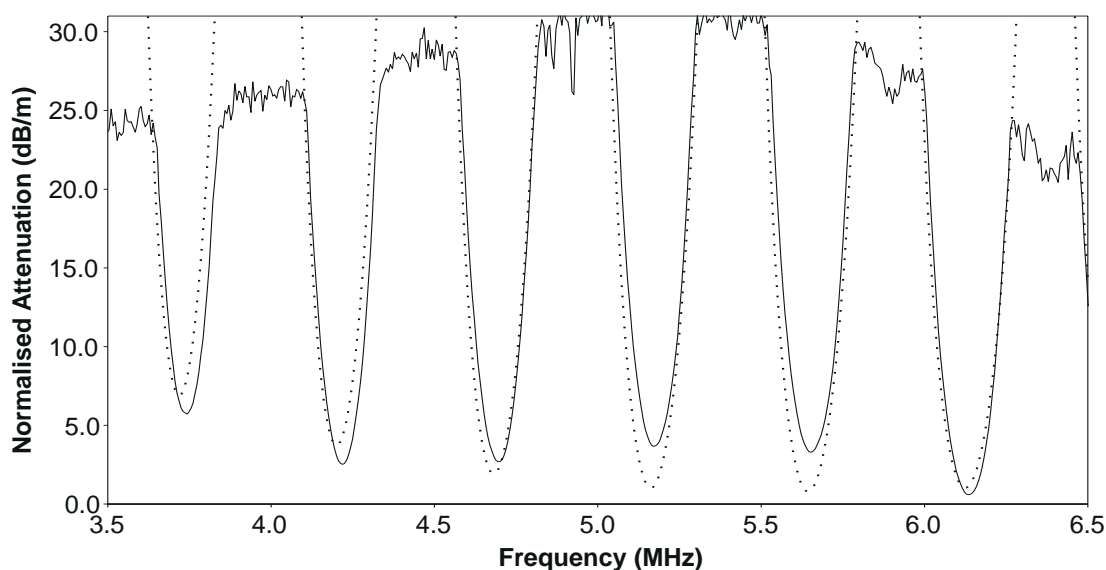


Figure 7.15: The response of an 8.1 mm diameter steel bar embedded in grout converted to a relative attenuation. The dotted lines indicate the attenuation predicted by the wave propagation model.

### 7.5.2 Experiments on Grouted Seven Wire Strands

In addition to the experimental tests that were performed on embedded 8.1 mm steel bars, tests were performed on a series of embedded seven wire steel strands in order to try the technique on the alternative type of tendons that are used in modern bridges and compare these results with those obtained for the bars. These results can be used to verify the assumption that strands can be modelled as bars of the same diameter as the centre wire in the strand.

The strand samples were provided by the Transport Research Laboratory (Crowthorne, England) under the supervision of Richard Woodward and Sarwan Sumon. They contain 15.2 mm Dyform strands consisting of a centre wire that is approximately 5.5 mm in diameter and is surrounded by six spiralling wires of slightly smaller diameter. Various simulated defects from a single wire breaks to complete fractures are present in the 5 metre long samples. The test results for complete fractures (at a 45 degree angle to the axis of the strand) that varied in distance from 500 to 2000 mm from the free end are shown in figure 7.16. The time traces have been enveloped by applying a Hilbert transform, so that the defect echoes could be more clearly seen. Each of the enveloped reflections was generated by a 25 cycle Hanning windowed tone burst centred on 4.75 MHz. The same test equipment was used as for the previous tests on embedded steel bars. The reflections from the breaks at 500 mm and 1000 mm into the grout can be clearly seen in the signals. In addition, the break at 1500 mm can also be detected. However, the defect at 2000 mm cannot be seen. The signal present at the beginning of the time traces corresponds to mode converted reverberations in the length of the strand under the collet and reflections from changes in contact of the seven component wires.

A large amount of ringing is present at the beginning of each of the signals in figure 7.16. These reverberations could cause a defect to be obscured, especially when the defect is close to the point



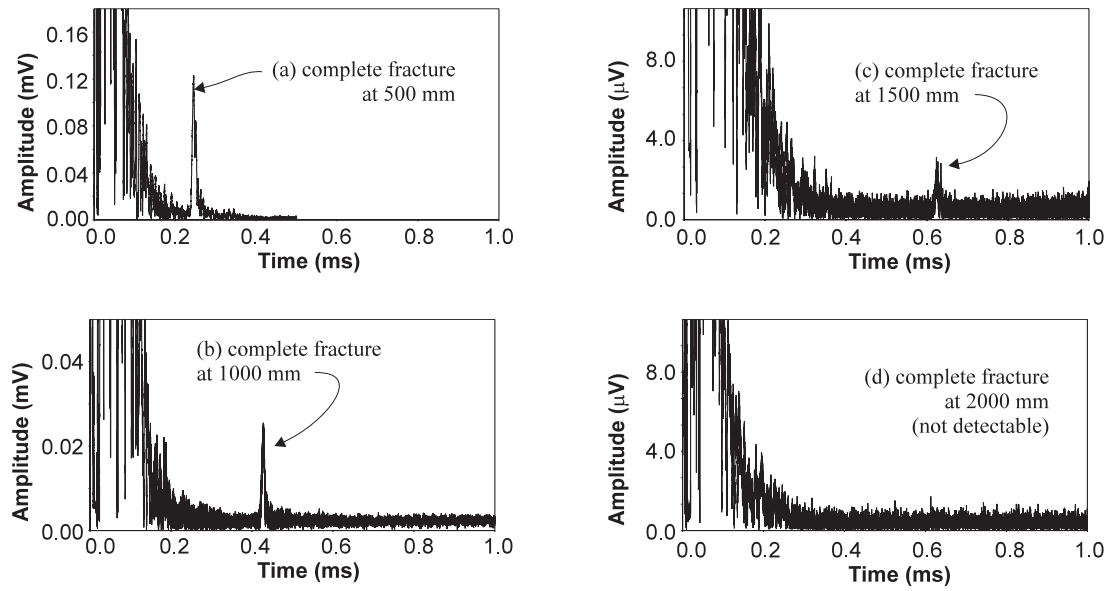


Figure 7.16: The enveloped reflections from complete breaks in grouted strands at (a) 500 mm, (b) 1000 mm, (c) 1500 mm, and (d) 2000 mm from the beginning of the grout.

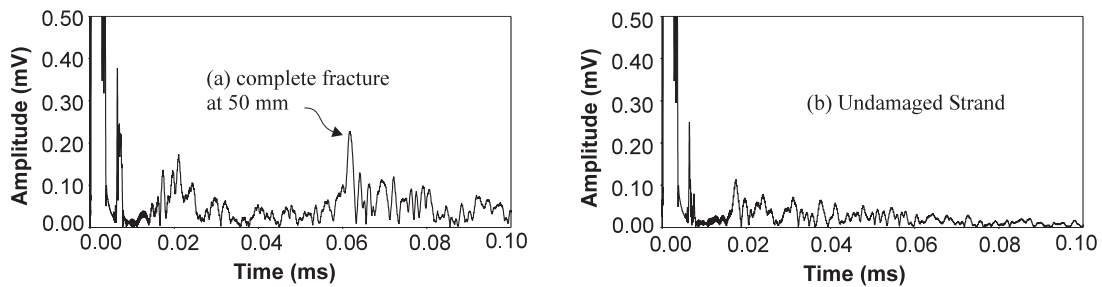


Figure 7.17: A comparison of the enveloped reflections of the guided waves (a) when there is a defect very close to the end of the embedded strand and (b) when the strand is undamaged.

where the tendon enters the grout. Fortunately, however, the results shown in figure 7.17 demonstrate that defects close to the beginning of the tendon can be distinguished from the reverberations. The enveloped trace in figure 7.17(a) was obtained from a strand that is completely broken 50 mm from the point where the tendon enters the grout. A relatively small, but distinct, echo can be seen, especially when this trace is compared to the results on an undamaged strand shown in figure 7.17(b).

The results from the strand samples seem to indicate that the guided wave travels primarily down the centre wire. Reflections from simulated defects that did not damage the centre wire are very much smaller than reflections from defects that did damage the centre wire. For example, figure 7.18 compares the enveloped reflections when there are three wires (of the seven in the grouted strand) cut and when there are five wires cut (including the centre wire). While there is a very clear echo from the sample with five wires cut, no reflection can be seen from the sample with three wires cut. Examining the frequencies at which minima in attenuation occur in the experimental results also indicates that the energy travels

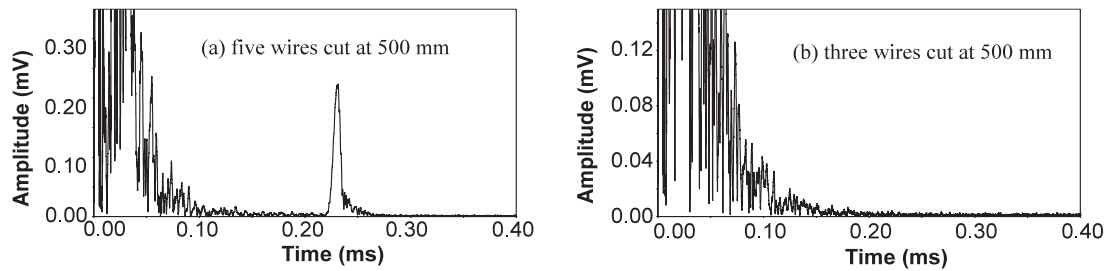


Figure 7.18: A comparison of the enveloped reflections of the guided waves (a) when 5 of the 7 wires (including the centre wire) in the embedded strand are cut and (b) when 3 of the wires are cut.

primarily down the centre wire. The experimental minima better correspond to the frequencies of the dips in attenuation for the theoretical results of a bar of the same diameter as the centre wire than for the diameter of the composite strand. This agreement is shown in figure 7.19. Part (a) compares the frequency response of a 15.2 mm strand, which has been converted to a relative attenuation, to the predicted attenuation for a 5.5 mm diameter bar (the diameter of the centre strand). The experimental results were obtained by analysing the reflection from five wires cut 500 mm into the embedded section of the strand using the same technique as was used for figure 7.15. The agreement between these two sets of curves is much better than the agreement between the experimental results and the predicted attenuation curves for a 15.2 mm diameter bar, which are shown in part (b). However, some differences are observed between the propagation in a strand and the propagation in a bar with the same diameter as the centre wire of the strand. The most significant of these differences is that the guided waves are able to propagate farther down the strand than the equivalent bar. For example, in figure 7.16, defects are detected 1500 mm into the grout although the predicted test range on a 5.5 mm diameter bar is only half that range. The additional propagation distance is most likely gained by imperfect coupling between the centre core, the surrounding wires, and the grout.

## 7.6 Summary of Grouted Tendon Inspection

An effective means of inspecting the grouted tendons in post tensioned bridges is needed. This chapter has evaluated the possibility of inspecting these tendons using guided ultrasonic waves. It has examined the possible guided wave modes that can exist in a steel bar embedded in grout and established that those with the least loss could propagate over a few metres length of tendon. Although much shorter than the bridge spans, this range of testing would nevertheless be useful for the regions adjacent to the anchors at the ends of the tendons. These are high points on the tendons and are particularly vulnerable to voids. They are also usually over the bridge piers and so are most difficult to access by drilling, the most common form of current tendon inspection. This inspection method would be quite sensitive to corrosion since each of the tendons in a duct could be tested individually. The number and location of tendons showing corrosion could be used to map out the affected area.

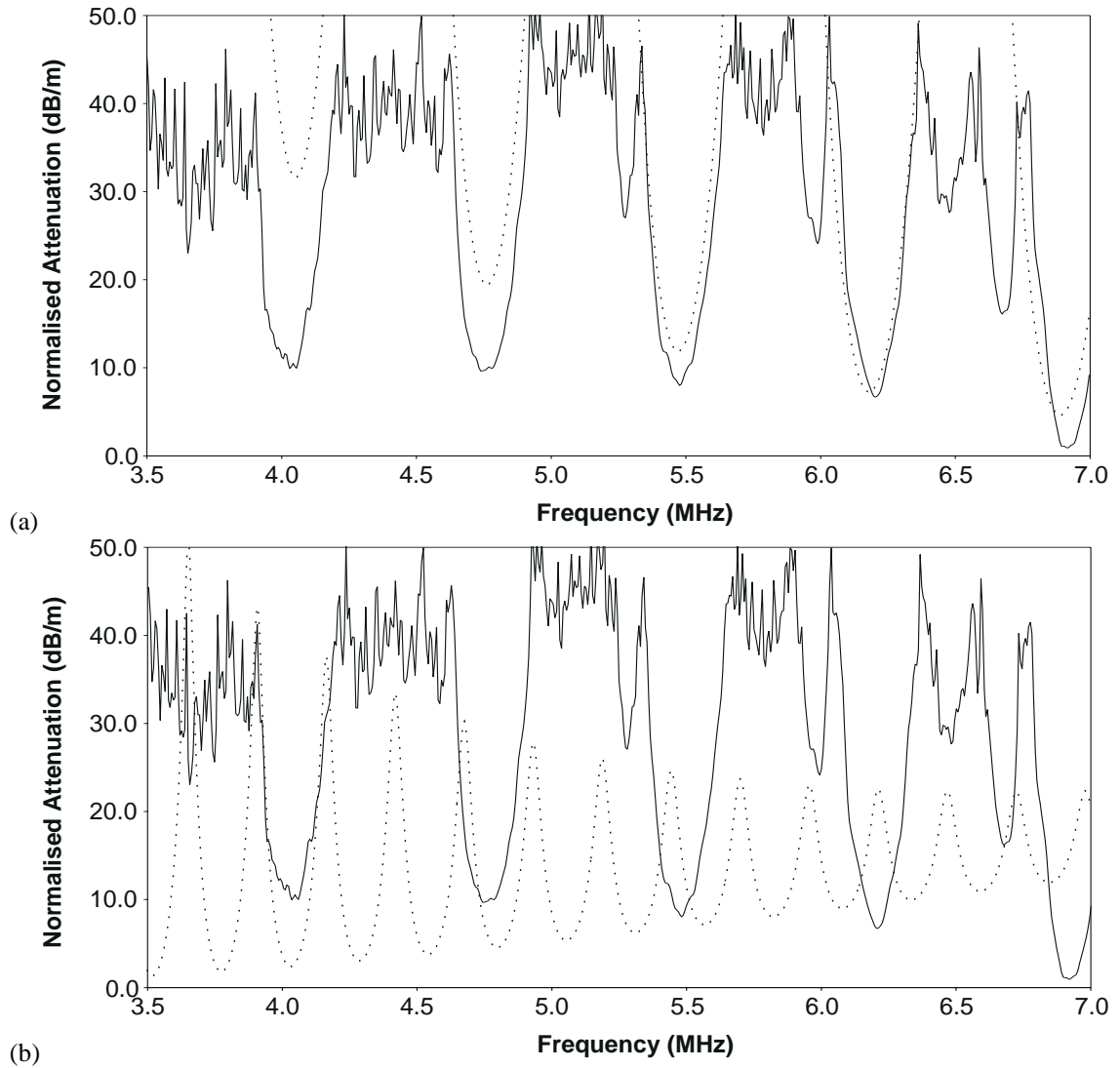


Figure 7.19: The frequency response of the reflection from 5 wires cut in a 15.2 mm embedded Dyform strand, converted to a relative attenuation. The dotted lines indicate the predicted attenuation in (a) a 5.5 mm diameter bar and (b) a 15.2 mm diameter bar.

The actual test procedure is relatively straight forward. First access to the end of the tendons must be gained. This usually involves removing part of the bridge surface and some protective layers. Then the ends of the tendons must be ground square and smooth, since high frequencies will be used. Once the tendons are prepared, a simple pulse echo test can be performed. However, to obtain good results, very low noise digital testing equipment will need to be used and the operating frequency should be carefully chosen. The frequency can be chosen by scaling the dispersion curves for an embedded steel bar (so that they model the correct diameter) and choosing the frequency with the least amount of attenuation. A resonant transducer centred on this frequency should be chosen. To reduce noise, a very narrow band pass filter should be designed that is centred on this frequency. In addition, at least 100 averages will be needed to further reduce noise. Sixty decibels of amplification is standard. The reliable test range for bars can be predicted by equation 7.1. When testing strands, the diameter of the centre wire should be used for the frequency and test range calculations, although the test range will probably be increased in practice.

This inspection method does not provide a complete solution to the problem of post-tensioned bridge inspection. However, it can provide valuable information that can be combined with existing techniques to characterise the condition of existing post-tensioned bridges.

# Chapter 8

## Conclusions

This thesis concentrated on the development of modelling tools that can be used to study wave propagation in embedded cylindrical structures. It then applied these tools to examine the possibility of using guided ultrasonic waves to inspect the grouted tendons in post-tensioned bridges.

Chapter 2 developed the modal wave propagation model for a very wide number of cylindrical systems. The model is based on the global matrix method, which efficiently provides for the modelling of structures that are composed of multiple layers and also supports the modelling of structures that are immersed in a fluid or embedded in a solid. The solutions were developed for both isotropic materials (which can incorporate material damping) and transversely isotropic materials. These solutions have been integrated with the previously developed Cartesian solutions[10] into an easy-to-use software package, Disperse, that allows the nature of the guided waves to be quickly evaluated.

The general behaviour of a number of different cylindrical systems was discussed in chapter 3. The nature of the modes that can exist was discussed, as well as the effect of changing the radius of the pipe. Further examples explained the effects of filling the pipe with fluid, as well as immersing it in a liquid and embedding it in a solid. These examples illustrated how energy can leak into a surrounding material, causing the guided wave to be attenuated. To inspect long distances using guided ultrasonic waves, this attenuation must be minimised.

Chapter 4 used some of the examples of cylindrical wave propagation to validate the wave propagation model. Asymptotic limits, published literature, internal consistency checks, finite element results, and experimental results were also used to validate the results. There is very good agreement between the wave propagation model and the validation results for all of the cases examined. This agreement provides strong confidence in the accuracy of the model and the ability to use wave propagation modelling to simulate non-destructive testing scenarios that use guided waves.

Chapter 5 described how the modal wave propagation solutions can be combined with finite element modelling techniques so that the interaction with defects can be better quantified. To perform this integration, techniques for generating a pure mode in the finite element model and extracting individual modes from a multi-mode signal were expanded to handle leaky cylindrical systems. In addition, a method of extracting the amplitudes of propagating modes via a through – thickness mode extraction routine was developed.

The application of these techniques for integrating modal wave propagation solutions and finite element results was demonstrated in chapter 6. The reflection of the L(0,1) mode from several types of defects in an embedded steel bar was studied. When the notch is perpendicular to the direction of propagation, the reflection coefficients for the embedded case are very similar to the free case. The reflection of the L(0,4) mode in a free bar was also considered. It has been found that when the L(0,4) impinges on a defect, most of the reflected energy is contained in the L(0,4) mode, although the other possible modes are also generated by mode conversion at the defect.

Now that the modelling tools have been developed, a wide range of potential applications for guided ultrasonics can be rapidly evaluated. Chapter 7 examined the possibility of using guided ultrasonic waves to inspect the grouted tendons in post-tensioned bridges. The wave propagation modelling revealed that the ends of the tendons near their anchorages could be inspected using guided waves. Preliminary experiments on test specimens appear to confirm this hypothesis. Although low frequencies are usually used to inspect systems that suffer from high attenuation (such as grouted tendons), high frequency ultrasound provides the best means of inspecting grouted tendons using guided waves. Using these waves, up to several meters of tendon could be reliably inspected from a single location.

There are several other similar systems that can be evaluated using the same methodology. For example, anchor bolts that are used to secure guy wires or prevent the collapse of rock walls behave in the same manner as embedded tendons and can be inspected using the same basic techniques. The modelling tools also allow the evaluation of the applicability of guided ultrasonic waves to other embedded systems such as pipes that pass through cement. The understanding of the basic wave propagation behaviour in these types of systems dramatically reduces NDT development time and therefore saves money and resources.

The work presented in this thesis forms a significant amount of original research that contributes to the understanding of leaky guided ultrasonic wave propagation in cylindrical systems. It includes both modal wave propagation solutions and links with finite element modelling, as well as the application of these techniques to new systems. The originality of the work can be summarized as,

- the implementation of a general purpose modal wave propagation model for cylindrical systems,
- the close integration of time marching finite element modelling results and the modal wave propagation solutions via a through – thickness mode extraction routine,
- the calculation of the reflection coefficients for the L(0,1) mode in an embedded steel bar,

- the application of the analytical wave propagation solutions to evaluate the possibility of inspecting grouted tendons using guided ultrasonic waves and the identification of the most promising modes for non destructive evaluation of the tendons.

# Bibliography

- [1] R. Woodward and F. Williams, "Collapse of the Ynys-Y-Gwas bridge, West-Glamorgan," *Proceedings of the Institution of Civil Engineers*, vol. 84, pp. 635–669, August 1988.
- [2] C. S. W. P. D. Group), "Durable bonded post-tensioned concrete bridges," Technical report 47, The Concrete Society, 1996.
- [3] J. Darby, "Testing methods for grouting systems," in *One day Seminar on Durable Post-tensioned Concrete Bridges*, pp. 36–64, The Concrete Society/CBDG, 1994.
- [4] D. Gazis, "Three dimensional investigation of the propagation of waves in hollow circular cylinders," *Journal of the Acoustical Society of America*, vol. 31, no. 5, pp. 568–578, 1959.
- [5] I. Mirsky, "Wave propagation in transversely isotropic circular cylinders part i: Theory," *Journal of the Acoustical Society of America*, vol. 37, no. 6, pp. 1016–1021, 1965.
- [6] M. Lowe, "Matrix techniques for modelling ultrasonic waves in multilayered media," *IEEE Transactions on Ultrasonics, Ferroelectrics and Frequency control*, vol. 42, no. 4, pp. 525–542, 1995.
- [7] L. Knopoff, "A matrix method for elastic wave problems," *Bulletin of the Seismological Society of America*, vol. 54, no. 1, pp. 431–438, 1964.
- [8] M. Randall, "Fast programs for half-space problems," *Bulletin of the Seismological Society of America*, vol. 57, no. 6, pp. 1299–1315, 1967.
- [9] H. Schmidt and G. Tango, "Efficient global matrix approach to the computation of synthetic seismograms," *Geophysics Journal of the Royal Astronomical Society*, vol. 84, pp. 331–359, 1986.
- [10] M. Lowe, *Plate Waves for the NDT of Diffusion Bonded Titanium*. Phd, Imperial College of Science Technology and Medicine, 1993.
- [11] B. Pavlakovic, M. Lowe, D. Alleyne, and P. Cawley, "Disperse : a general purpose program for creating dispersion curves," in *QNDE* (D. Thompson and D. Chimenti, eds.), vol. 16A, pp. 155–192, Plenum Press, New York, 1997.
- [12] D. N. Alleyne, *The Nondestructive Testing of Plates using Ultrasonic Lamb Waves*. Phd, Imperial College of Science Technology and Medicine, 1991.
- [13] W. Thomson, "Transmission of elastic waves through a stratified solid medium," *Journal of Applied Physics*, vol. 21, pp. 89–93, 1950.
- [14] N. Haskell, "The dispersion of surface waves on multi-layered media," *Bulletin of the American Seismological Society*, vol. 43, pp. 17–34, 1953.



- [15] J. Pochhammer, "Über die fortpflanzungsgeschwindigkeiten kleiner schwingungen in einem berggrenzten isotropen kreiscylinder," *J fur reine und angewandte Math.*, vol. 81, pp. 324–336, 1876.
- [16] C. Chree, "The equations on an isotropic elastic solid in polar and cylindrical coordinates, their solutions, an applications," *Trans. Cambridge Philos. Soc.*, vol. 14, pp. 250–369, 1889.
- [17] R. M. Davies, "A critical study of the hopkinson pressure bar," *Phil. Trans. Roy. Soc. London A*, vol. 240, pp. 375–457, 1948.
- [18] G. E. Hudson, "Dispersion of elastic waves in solid circular cylinders," *Phys. Rev.*, vol. 63, pp. 46–51, 1943.
- [19] T. R. Meeker and A. H. Meitzler, "Guided wave propagation in elongated cylinders and plates," in *Physical Acoustics, Principles and Methods* (W. P. Mason and R. N. Thurston, eds.), vol. 1A, (New York), pp. 111–167, Academic Press, 1972.
- [20] M. Onoe, H. McNiven, and R. Mindlin, "Dispersion of axially symmetric waves in elastic solids," *Journal of Applied Mechanics*, vol. 29, pp. 729–734, 1962.
- [21] Y.-H. Pao and R. Mindlin, "Dispersion of flexural waves in an elastic, circular cylinder," *Journal of Applied Mechanics*, vol. 27, pp. 513–520, 1960.
- [22] Y. H. Pao, "The dispersion of flexural waves in an elastic, circular cylinder – part 2," *J. Appl. Mech.*, vol. 29, pp. 61–64, 1962.
- [23] R. Thurston, "Elastic waves in rods and clad rods," *Journal of the Acoustical Society of America*, vol. 64, no. 1, pp. 1–37, 1978.
- [24] D. C. Gazis, "Three-dimensional investigation of the propagation of waves in hollow circular cylinders. ii. numerical results," *Journal of the Acoustical Society of America*, vol. 31, no. 5, pp. 573–578, 1959.
- [25] A. Fitch, "Observation of elastic-pulse propagation in axially symmetric and nonaxially symmetric longitudinal modes of hollow cylinders," *Journal of the Acoustical Society of America*, vol. 35, no. 5, pp. 706–708, 1963.
- [26] R. Kumar, "Flexural vibrations of fluid-filled circular cylindrical shells," *Acoustica*, vol. 24, pp. 137–146, 1971.
- [27] R. Kumar, "Dispersion of axially symmetric waves in empty and fluid-filled cylindrical shells," *Acoustica*, vol. 27, no. 6, pp. 317–329, 1972.
- [28] R. Morse, "Compressional waves along an anisotropic circular cylinder having hexagonal symmetry," *Journal of the Acoustical Society of America*, vol. 26, no. 6, pp. 1018–1021, 1954.
- [29] P.-C. Xu and S. Datta, "Characterisation of fibre-matrix interface by guided waves : axisymmetric case," *Journal of the Acoustical Society of America*, vol. 89, no. 6, pp. 2573–2583, 1991.
- [30] V. Dayal, "Longitudinal waves in homogeneous anisotropic cylindrical bars immersed in fluid," *Journal of the Acoustical Society of America*, vol. 93, no. 3, pp. 1249–1255, 1993.
- [31] P. Nagy, "Longitudinal guided wave propagation in a transversely isotropic rod immersed in fluid," *Journal of the Acoustical Society of America*, vol. 98, no. 1, pp. 454–457, 1995.
- [32] M. Berliner and R. Solecki, "Wave propagation in fluid-loaded, transversely isotropic cylinders. part i. analytical formulation," *Journal of the Acoustical Society of America*, vol. 99, no. 4, pp. 1841–1847, 1996.

- [33] A. Safaai-Jazi, C.-K. Jen, and G. Farnell, "Cutoff conditions in an acoustic fiber with infinitely thick cladding," *IEEE Transactions on Ultrasonics, Ferroelectrics and Frequency control*, vol. UFFC-33, no. 1, pp. 69–73, 1986.
- [34] J. Simmons, E. Drescher-Krasicka, and H. Wadley, "Leaky axisymmetric modes in infinite clad rods. i," *Journal of the Acoustical Society of America*, vol. 92, no. 2, pp. 1061–1090, 1992.
- [35] M. Viens, Y. Tshukahara, C. Jen, and J. Cheeke, "Leaky torsional modes in infinite clad rods," *Journal of the Acoustical Society of America*, vol. 95, no. 2, pp. 701–707, 1994.
- [36] M. Berliner and R. Solecki, "Wave propagation in fluid loaded, transversely isotropic cylinders. part ii. numerical results," *Journal of the Acoustical Society of America*, vol. 99, no. 4, pp. 1848–1853, 1996.
- [37] A. H. Nayfeh and P. Nagy, "General study of axisymmetric waves in layered anisotropic fibers and their composites," *Journal of the Acoustical Society of America*, vol. 99, no. 2, pp. 931–941, 1996.
- [38] P. M. Morse and H. Feshbach, *Methods of Theoretical Physics*. McGraw-Hill Book Company, 1953.
- [39] B. A. Auld, *Acoustic Fields And Waves In Solids*, vol. II. Stanford: Krieger Publishing Company, 2nd ed., 1990.
- [40] E. Kreyszig, *Advanced Engineering Mathematics*. Ohio: John Wiley and Sons, Inc., 7th ed., 1993.
- [41] F. Schwab and L. Knopoff, "Fast surface wave and free mode computations," in *Methods in Computational Physics*, vol. 11, New York: Academic Press, bolt, b.a. ed., 1972.
- [42] F. Schwab and L. Knopff, "Surface waves on multilayered anelastic media," *Bulletin of the Seismological Society of America*, vol. 61, no. 4, pp. 893–912, 1971.
- [43] M. Castaings and B. Hosten, "Delta operator technique to improve the thomson-haskell method stability for propagation in multilayered anisotropic absorbing plates," *Journal of the Acoustical Society of America*, vol. 95, no. 4, pp. 1931–1941, 1994.
- [44] B. Hosten and M. Castaings, "Transfer matrix of multilayered absorbing and anisotropic media. measurements and simulations of ultrasonic wave propagation through composite materials," *Journal of the Acoustical Society of America*, vol. 94, no. 3, pp. 1488–1495, 1993.
- [45] H. Schmidt and F. Jensen, "Efficient numerical solution technique for wave propagation in horizontally stratified environments," *Computers and Maths with Applications*, vol. 11, no. 7/8, pp. 699–715, 1985.
- [46] T. Pialucha, *The reflection coefficient from interface layers in NDT of adhesive joints*. Phd, University of London, 1992.
- [47] P.-C. Xu and A. Mal, "Calculation of the inplane green's functions for a layered viscoelastic solid," *Bulletin of the Seismological Society of America*, vol. 77, pp. 1823–1837, 1987.
- [48] P. Cervenka and P. Challande, "A new efficient algorithm to compute the exact reflection and transmission factors for plane waves in layered absorbing media (liquids and solids)," *Journal of the Acoustical Society of America*, vol. 89, no. 4, pp. 1579–1589, 1991.
- [49] M. Deschamps, "L'onde plane htrogne et ses applications en acoustique lineaire," *Journal d'Acoustique*, vol. 4, pp. 269–305, 1991.
- [50] B. Hosten, "Bulk heterogeneous plane wave propagation through viscoelastic plates and stratified media with large values of frequency domain," *Ultrasonics*, vol. 29, pp. 445–450, 1991.

- [51] D. McCammon and S. McDaniel, "The influence of the physical properties of ice on reflectivity," *Journal of the Acoustical Society of America*, vol. 77, no. 2, pp. 499–507, 1985.
- [52] H. Kolsky, *Stress waves in solids*. Dover Publications, New York, 1963.
- [53] D. J. Ewins, *Modal Testing : Theory and Practice*. Research Studies Press Ltd John Wiley and Sons inc., 1986.
- [54] M. North, *Forced oscillations of a single degree of freedom dynamic system with Reid model hysteretic damping*. Msc, University of London, 1974.
- [55] D. Chimenti, A. Nayfeh, and D. Butler, "Leaky rayleigh waves on a layered halfspace," *Journal of Applied Physics*, vol. 53, no. 1, pp. 170–176, 1982.
- [56] A. Nayfeh and D. Chimenti, "Ultrasonic leaky waves in the presence of a thin layer," *Journal of Applied Physics*, vol. 52, no. 8, pp. 4985–4994, 1981.
- [57] P. Nagy and L. Adler, "Non-destructive evaluation of adhesive joints by guided waves," *Journal of Applied Physics*, vol. 66, no. 10, pp. 4658–4663, 1989.
- [58] D. Chimenti and A. Nayfeh, "Ultrasonic reflection and guided wave propagation in biaxially laminated composite plates," *Journal of the Acoustical Society of America*, vol. 87, no. 4, pp. 1409–1415, 1990.
- [59] M. Abramowitz and I. A. Stegun, *Handbook of Mathematical Functions - with formulas, graphs and mathematical tables*. Dover Publications inc., New York, 1970.
- [60] B. A. Auld, *Acoustic Fields And Waves In Solids*, vol. I. Stanford: Krieger Publishing Company, 2nd ed., 1990.
- [61] H. Schmidt and F. Jensen, "A full wave solution for propagation in multilayered viscoelastic media with application to gaussian beam reflection at liquid-solid interfaces," *Journal of the Acoustical Society of America*, vol. 77, no. 3, pp. 813–825, 1985.
- [62] M. Silk and K. Bainton, "The propagation in metal tubing of ultrasonic wave modes equivalent to lamb waves," *Ultrasonics*, pp. 11–19, 1979.
- [63] I. Viktorov, *Rayleigh and Lamb waves: Physical theory and applications*. New York: Plenum Press, 1 ed., 1967.
- [64] Sinclair and Addison, "Acoustic diffraction spectrum of a SiC fiber in a solid elastic medium," *Journal of the Acoustical Society of America*, vol. 94, pp. 1126–1135, 1993.
- [65] K. F. Graff, *Wave Motion In Elastic Solids*. Ohio: Clarendon Press, Oxford, 1975.
- [66] R. Stoneley, "Elastic waves at the surface of separation of two solids," in *Conference of the Royal Society*, (London), pp. 416–428, 1924.
- [67] J. Scholte, "The range of existence of rayleigh and stoneley waves," *Geophysics*, vol. 5, pp. 120–126, 1947.
- [68] P. Nagy, "Leaky guided wave propagation along imperfectly bonded fibers in composite materials," *Journal of Non-destructive Evaluation*, vol. 13, no. 3, pp. 137–145, 1994.
- [69] J. Jones and J. Whittier, "Waves at flexibly bonded interface," *Journal of Applied Mechanics*, pp. 905–909, 1967.
- [70] M. Schoenberg, "Elastic wave behaviour across linear slip interfaces," *Journal of the Acoustical Society of America*, vol. 68, no. 5, pp. 1516–1521, 1980.

- [71] A. Bernard, M. Lowe, and M. Deschamps, "Energy velocity and group velocity for guided transient attenuated waves propagating within a plate," *In Preparation*, 1998.
- [72] D. Hitchings, "Fe77 user manual," tech. rep., Imperial College of Science Technology and Medicine, 1987.
- [73] W. Sachse and Y.-H. Pao, "On the determination of phase and group velocities of dispersive waves in solids," *Journal of Applied Physics*, vol. 49, no. 8, pp. 4320–4327, 1978.
- [74] T. Pialucha, C. Guyott, and P. Cawley, "Amplitude spectrum method for the measurement of phase velocity," *Ultrasonics*, vol. 27, no. 5, pp. 270–279, 1989.
- [75] K.-J. Bathe, *Finite Element Procedures In Engineering Analysis*. New Jersey: Prentice-Hall, 1982.
- [76] D. Alleyne and P. Cawley, "A two-dimensional fourier transform method for the measurement of propagating multimode signals," *Journal of the Acoustical Society of America*, vol. 89, no. 3, pp. 1159–1168, 1991.
- [77] A. Harker, "Numerical modelling of the scattering of elastic waves in plates," *Journal of Non-destructive Evaluation*, vol. 4, no. 2, pp. 89–106, 1984.
- [78] R. Blake, *Numerical models of Rayleigh wave scattering from surface features*. Phd, University of London, 1988. Reflection Coefficients.
- [79] C. W. Chan, *The ultrasonic nondestructive evaluation of welds in plastic pipes*. Phd, London, 1996.
- [80] M. Evans, *The use of diffuse field measurements for acoustic emission*. Phd, University of London, 1997. Reflection Coefficients.
- [81] J. Cao and S. He, "An exact absorbing boundary condition and its application to three-dimensional scattering from thin dispersive structures," *Journal of the Acoustical Society of America*, vol. 99, no. 4, pp. 1854–1861, 1996.
- [82] L. Kallivokas and J. Bielak, "Time-domain analysis of transient structural acoustics problems based on the finite element method and a novel absorbing boundary element," *Journal of the Acoustical Society of America*, vol. 94, no. 6, pp. 3480–3492, 1993.
- [83] C. Randall, "Absorbing boundary condition for the elastic wave equation," *Geophysics*, vol. 53, no. 5, pp. 611–624, 1988.
- [84] N. Saffari and J. Zhou, "New absorbing boundary conditions for finite-difference modeling of elastic waves," in *Review of Progress in Quantitative NDE* (D. Thompson and D. Chimenti, eds.), (Snowmass, CO), 1994.
- [85] H. Simons and M. Randolph, "Comparison of transmitting boundaries in dynamic finite element analyses using explicit time integration," Technical Report 149, Cambridge University, Engineering Department, 1984.
- [86] P. Young, "Recursive approaches to time series analysis," *Journal of the Institute of Mathematics and its Applications*, pp. 209–224, 1974.
- [87] A. Poggio, M. Van Blaricum, E. Miller, and R. Mittra, "Evaluation of a processing technique for transient data," *IEEE Transactions on Antennas and Propagation*, vol. AP-26, no. 1, pp. 165–173, 1978.
- [88] P. Davies, "A recursive approach to prony parameter estimation," *Journal of Sound and Vibration*, vol. 89, no. 4, pp. 571–583, 1983.

- [89] J. Torvik, "Reflection of wave trains in semi-infinite plates," *Journal of the Acoustical Society of America*, vol. 41, pp. 346–353, 1967.
- [90] J. Ditri, "Utilization of guided elastic waves for the characterization of circumferential cracks in hollow cylinders," *Journal of the Acoustical Society of America*, vol. 96, no. 6, pp. 3769–3775, 1994.
- [91] R. Blake and L. Bond, "A general model for rayleigh wave-surface feature scattering problems," in *QNDE* (D. Thompson and D. Chimenti, eds.), vol. 9A, pp. 77–84, Plenum Press, New York, 1989.
- [92] Z. You and W. Lord, "Finite element study of elastic waves interaction with cracks," in *QNDE* (D. Thompson and D. Chimenti, eds.), vol. 8A, pp. 109–116, Plenum Press, New York, 1988.
- [93] S. Datta and A. Shah, "Ultrasonic scattering by planar and non-planar cracks," in *QNDE* (D. Thompson and D. Chimenti, eds.), vol. 7A, pp. 69–78, Plenum Press, New York, 1987.
- [94] M. Rezaul Karim and A. Mal, "Hybrid finite element analysis of wave scattering by cracks and inclusions in plates : in-plane case," *International Journal for Numerical Methods in Engineering*, 1990.
- [95] R. Woodward and F. Williams, "Collapse of the Ynys-Y-Gwas bridge, West-Glamorgan - discussion," *Proceedings of the Institution of Civil Engineers*, vol. 86, pp. 1177–1191, December 1988.
- [96] D. Parker, "Tropical overload," *New Civil Engineer*, pp. 18–21, 12/26 December 1996.
- [97] D. Parker, "Pacific bridge collapse throws doubts on repair method," *New Civil Engineer*, pp. 3–4, 17 October 1996.
- [98] H. T. Williams and M. E. Hulse, "From theory to field experience with inspection of post-tensioned bridges," in *Proceeding of the sixth international conference on structure faults and repair* (M. C. Forde, ed.), vol. 1, pp. 199–202, Engineering Technics Press, 1995.
- [99] M. B. Leeming, J. S. Lane, and P. J. Wade, "Post tensioned bridge investigation - the way forward," in *Proceeding of the sixth international conference on structure faults and repair* (M. C. Forde, ed.), vol. 1, pp. 193–197, Engineering Technics Press, 1995.
- [100] D. Parker, "X-rated video," *New Civil Engineer*, April 1994.
- [101] P. Kear and M. Leeming, "Radiographic inspection of post-tensioned concrete bridges," *Insight*, vol. 36, no. 7, pp. 507–510, 1994.
- [102] T. Saarenketo and M. Soderqvist, "Ground penetration radar applications for bridge deck evaluations in finland," *Insight*, vol. 36, no. 7, pp. 496–501, 1994.
- [103] E. I. Okanla, P. A. Gaydecki, S. Manaf, and F. M. Burdekin, "Detecting faults in posttensioned cuts by electrical time-domain reflectometry," *Journal of Structural Engineering - ASCE*, vol. 123, no. 5, pp. 567–574, 1997.
- [104] P. J. Duncan, P. A. Gaydecki, and F. M. Burdekin, "Ultrasonic ndt prototype for the inspection of ducted post stressing tendons in concrete beams," in *Review of QNDE* (D. Thompson and D. Chimenti, eds.), vol. 15, Plenum Press, New York, 1995.
- [105] O. Kroggel, R. Jansohn, and M. Ratmann, "Novel ultrasound system to detect voided ducts in post-tensioned bridges," in *Proceeding of the sixth international conference on structure faults and repair* (M. C. Forde, ed.), vol. 1, pp. 203–208, Engineering Technics Press, 1995.

- [106] J. Martin, M. S. A. Hardy, A. S. Usnami, and M. C. Forde, "Quantifying the defects in post-tensioned bridges using impulse ultrasonics," in *Proceeding of the sixth international conference on structure faults and repair* (M. C. Forde, ed.), vol. 1, pp. 199–202, Engineering Technics Press, 1995.
- [107] B. J. Jaeger, M. J. Sansalone, and R. W. Poston, "Detecting voids in grouted tendon ducts of post-tensioned concrete structures using the impact-echo method," *ACI Structural Journal*, vol. 93, no. 4, pp. 462–473, 1995.
- [108] J. Weight, "Unpublished report on high frequency ultrasonics tests on grouted tendons supplied to the Transport Research Laboratory," 1994.
- [109] M. Lowe, "Personal communication between M. Lowe and R. Woodward," 1996.
- [110] G. Kaye and T. Laby, *Tables of physical and chemical constants*. Harlow: Longman, 16 ed., 1995.
- [111] D. Alleyne and P. Cawley, "Optimization of lamb wave inspection techniques," *NDT and E International*, vol. 25, pp. 11–22, 1992.

# Index

- Absorbing boundaries, 137
- Absorbing core, 39, 76
- Alleyne, 135, 138, 150
- Angle of incidence
  - projection, 65
- Assumptions, 27
- Attenuation, 25
  - calculation method
    - frequency response, 206
    - frequency spectrum, 123
    - measure signal decay, 122
  - Cartesian vs. cylindrical, 197
  - finite element
    - calibration, 167
    - modelling techniques, 136
  - liquid filled pipes, 79
  - minima
    - embedded bar, 199–202
  - mode selection criterion, 191
  - nepers definition, 65
  - non-leaky modes, 194
  - projection, 65
  - types
    - hysteretic, 32
    - leakage, 34, 38
  - validation
    - experiments, 125–129
    - finite element, 121–123
- Axi-symmetric
  - constraint, 27, 144
  - wave propagation, *see* Longitudinal modes
- Bar
  - experiments
    - validation, 123
  - velocity, 95
  - wave model
    - history, 26
- Berliner, 27, 46, 48
  - validation, 104
- Bernard, 105
- Bessel functions, 27
  - choice of, 37–38, 45, 52, 55
  - Hankel functions, 37
  - modified, 37
  - operator, 35
  - phase, 39
  - recurrence relationships, 37
- Blake, 136
- Boundary conditions, 28
  - absorbing, 137
  - solid-liquid, 29, 46
  - solid-solid, 28
  - solid-vacuum, 29
- Bridge collapse, 19, 187
- Centre mode shapes, *see* Pure mode excitation
- Chree, 26
- Christoffel, 51
- Conservation of energy
  - in reflection coefficients, 162
- Cylindrical
  - coordinates
    - expansion, 33
  - examples, 62–92
    - embedded, 81–84
    - immersed, 76–81
    - multi-layered, 84
  - large radius, 37, 74
  - modelling of core, 76
  - naming convention, 66
  - nature of modes
    - bars, 67
    - pipes, 69
  - pure mode excitation, 155
  - substitution of Cartesian, 74
  - types of leakage, 83
  - validation, 94–131
- Damping
  - material, 31
- Dayal, 27
- Defects
  - effect of orientation, 173
  - filled, 171
  - in surrounding material, 176
  - modelling, 134
- Derivation
  - mode extraction, *see* Mode extraction
  - pure mode excitation, *see* Pure mode

- wave model, *see* Wave model
- Dilatation field, 31
- Disperse, 22, 24, 43, 56, 58, 67, 95, 96, 100, 101, 150, 165, 213
  - demonstration copy, 56
- Displacement field
  - cylindrical, 40
  - equation of motion, 32
  - isotropic
    - layer matrix, 44
    - liquid, 45
    - potentials, 41
  - transversely isotropic
    - matrix, 53
    - potentials, 49
- Dyform strands, 208
- Energy conservation
  - in reflection coefficients, 162
- Energy density
  - KED vs. SED, 110
- Energy velocity
  - calculation, 113
  - experiments
    - embedded bar, 205
  - validation, 112
- Euler equation, 30, 47
  - vector format, 31
- Exact mode shapes, *see* Pure mode excitation
- Examples
  - cylindrical, 62–92
    - embedded, 81–84
    - immersed, 76–81
    - in vacuum, 63
- Experiments
  - application of 2-D FFT, 128
  - immersed bar
    - F(1,1), 125
    - F(1,2), 128
    - L(0,1), 125
    - L(0,3), 128
  - model validation, 123–129
  - post-tensioned, 202–210
    - arrival time, 205
    - centre wire, 209
    - on bars, 203
    - on strands, 208
    - test equipment, 203
- Explicit time marching, 135
- Finel, 115, 135
- Finite Element
  - Mesh Size, 135
  - Time Step, 136
- Finite element
  - absorbing boundaries, 137
  - calibration, 134
  - error level, 167
  - leakage
    - extensions, 136–138
    - extraction, 121
  - mesh size, 183
  - mode extraction, 139–149
  - model validation, 115–119
  - modelling defects, 134
  - phase velocity extraction, 117
  - program, 135
  - pure mode excitation, 149–160
  - reflection coefficients, 145, 161
  - resource costs, 135
  - stability, 135
  - stiffness, 118, 134, 167
  - techniques, 135–136
  - why use it, 133–134
- Fitch, 26
- Flexural modes
  - attenuation minima, 199
  - experimental validation, 125, 128
  - finite element modelling
    - limitations, 156
  - fundamental mode behaviour, 67
  - naming convention, 66
  - SCS fiber, 69
  - validation against, 99
- Fluid, *see* Liquid
- Fourier
  - transform
    - frequency sweep, 205
    - mode extraction, 140
    - phase velocity extraction, 117
    - predicted signals, 118
    - pure mode excitation, 153
    - reflection coefficients, 162
  - Two-D transform, 138–139
- Frequency spectrum method, 123
- Fundamental modes
  - bar
    - experiments, 123
    - F(1,1), 67
    - L(0,1), 67
    - SCS fiber, 104
    - velocity, 95
  - pipe
    - F(1,1), 71
    - L(0,1), 71
    - multi-layered, 84
    - T(0,1), 71



- Gauge invariance, 32, 36
- Gazis, 26, 30, 62
  - corrections, 42, 45, 101
  - validation, 99
- Generation
  - mode selection criterion, 192
  - pure mode excitation, 149–160
- Global matrix, 56–57
  - half spaces, 57
  - introduction, 25
  - singularities, 57, 194
- Gravity, 30
- Group velocity
  - energy velocity comparison, 113
  - mode selection criterion, 193
  - projection, 63
- Grouted tendons, *see* Post-tensioned
- Guided waves
  - introduction, 20
  - model, *see* Wave Model
- Hankel functions, 37, 38
  - sink at origin, 39
- Harker, 135
- Haskell, 56
- Helmholtz
  - decomposition, 32
  - equation, 33
  - potentials, 35
- Hilbert transform, 208
- Historical background, 26–27
- Hitchings, 115, 135
- Hooke, 30, 31, 47
- Hudson, 26
- Immersion
  - cylindrical examples, 76–81
  - experiments, 125–129
  - global matrix formulation, 57
  - wave modelling, 38
- Imperfect boundary
  - SCS fiber, 92, 104
- Interface layer, *see* Imperfect boundary
- Iteration
  - logic, 57–59
- Knopoff, 56
- Kumar, 26
- Lamé, 31, 32
- Laplacian, 36
- Large radius, *see* Radius, large
- Layer matrix
  - isotropic, 44
  - liquid, 46
  - order of columns, 43
  - scaling, 45
  - transversely isotropic, 53
- Leakage
  - angle, 81
  - examples
    - embedded, 81–84
    - immersed, 76–81
  - finite element
    - calibration, 167
    - modelling, 136–138
    - validation, 121
  - liquid filled pipes, 76
  - non-leaky modes, 81
    - post-tensioned, 193
  - normalizing reflection coeff., 165
  - pure mode excitation, 158
  - types, 83
- Liquids
  - Cartesian, 45
  - cylindrical core, 39
  - cylindrical derivation, 45
  - cylindrical layer matrix, 46
  - filled pipes, 39, 76
    - sink at centre, 78
  - immersion example, 76–81
- Longitudinal modes
  - bar velocity, 95
  - fundamental mode behaviour, 67
  - naming convention, 66
  - pure mode excitation, 156
  - reflection of L(0,1), 168–182
  - reflection of L(0,4), 183–184
  - validation experiments, 125, 128
  - wave modelling history, 26
- Lowe, 24, 56, 58, 60
- Macro Design, 203
- Material damping, 31
  - cylindrical example, 84
  - finite element, 137
  - Voigt, 31
- Material properties
  - isotropic, 93
  - transversely isotropic, 93
- McNiven, 26
- Meeker, 26
- Meitzler, 26
- Mindlin, 26
- Mirsky, 26, 46, 48
- Mode extraction
  - algorithm, 141
  - benefits, 140, 148

- derivation, 139–149
  - disadvantages, 140, 149
  - example, 167
  - power flow, 141
  - pure mode excitation, 149–160
  - reflection coefficients, 145, 162
  - Two-D FFT method, 138
- Mode names
- cylindrical, 66
- Mode selection
- criteria, 191–193
- Mode shapes
- calculation method, 61
  - comparison
    - fundamental modes, 67
    - L(0,4), 183
  - display formats, 61
  - embedded bar, 84
  - immersed bar, 80
  - strain energy density, 61
  - use in mode extraction, 140
  - use in pure mode excitation, 153
- Model, *see* Wave model
- Morse, 26
- Multi-layered
- cylindrical, 84
  - global matrix method, 56–57
  - validation, 106
- Nagy, 27, 51, 69, 86
- validation, 101
- Naming
- cylindrical modes, 66
- Navier, 31, 33
- Nayfeh, 27, 69, 86
- Nepers
- definition, 65
- Newton, 30
- Non-leaky modes, 81
- existence criteria, 194
  - post-tensioned, 193
- Onoe, 26
- Originality, 22–23, 27
- Orr, 203
- Orthogonality
- combining FE and modal solutions, 134
  - cylindrical modes, 144
  - guided waves, 139
  - pure mode excitation, 150
  - relationship, 141
- Palau
- bridge collapse, 186
- Pao, 26
- Phase velocity
- extraction, 117
  - projection, 63
- Pipes
- embedded, 82
  - examples, 69–84
    - large radius, 74
    - transversely isotropic, 104
  - large radius, 37
  - validation against Gazis, 99
- Pochhammer, 26
- Post-tensioned
- attenuation
    - minima, 199
    - mode selection criterion, 191
    - non-leaky modes, 194
  - axial resolution, 201
  - construction, 19, 187
  - dispersion curves
    - high frequency, 199
    - low frequency, 193
  - experiments, 202–210
    - bars, 203
    - strands, 208
  - generation
    - method, 202
    - mode selection criterion, 192
  - inspection, 19
    - access, 189
    - current, 187
    - under development, 188
  - mode selection criteria, 191–193
  - model, 190
  - optimum test frequency, 199
  - predicted test range, 201
  - protruding bar, 192
  - summary, 210
  - wave types
    - grout bourne, 190
    - high frequency, 199
    - non-leaky mode, 193
    - steel bourne, 190
- Potential functions, 32
- isotropic, 35, 36
  - transversely isotropic, 48
- Power flow
- in energy velocity, 113
  - in mode extraction, 141
- Projections, 63–66
- angle of incidence, 65
  - attenuation, 65
  - group velocity, 63
  - phase velocity, 63

- wavenumber, 63
- Pure mode excitation, 149–160
  - centre mode shapes, 151
  - cylindrical extensions, 155
  - exact mode shapes, 153
  - example
    - Cartesian, 151–152, 154–155
    - cylindrical, 156
    - leaky, 158–160
  - flexural modes, 156
  - for reflection coefficients, 162
  - in leaky systems, 158
- Radiation
  - leaky waves, 38
- Radius
  - effect of changing, 74–76
  - large
    - Bessel function choice, 37
    - stability limit, 97
    - substitution of plate, 74
    - validation against plate, 96
- Randall, 56
- Rayleigh
  - velocity, 95, 135
  - wave, 81, 194
- Reflection coefficients
  - calculation, 162
  - embedded bar, 168–182
    - configuration, 168
    - error level, 167
  - energy conservation
    - definition, 162
    - example, 147, 165
  - example
    - mode extraction, 145
    - S0, 162
    - visual, 162
  - filled defects, 171
  - finite element, 161
  - free bar, 183–184
  - free vs. embedded bar, 169
  - from surrounding material, 176, 198
  - L(0,4), 184, 201
  - leaky systems, 165–182
  - orientation effects, 173
  - protruding bar
    - post-tensioned, 192
  - reverberations, 179
  - substitution
    - free case for embedded, 183
  - techniques, 161
  - transition
    - free / embedded systems, 178
  - wavelength effect
    - mode selection, 192
- Resolution (axial)
  - post-tensioned, 201
- Reverberations
  - post-tensioned, 192
  - of collets, 198
  - of high frequency modes, 208
  - protruding bar, 179
- Rotational field, 31
- Safaai-Jazi, 27
- Schmidt, 56
- SCS fiber
  - embedded example
    - first order, 88
    - zero order, 86
  - imperfect boundaries, 92
  - validation, 102
  - wave propagation example, 69
- Simmons, 27
- Singularities, *see* Stability
- Sink at origin, 39, 78
- Solecki, 27, 46
- Solenoidal, 32
- Stability
  - Bessel functions, 37
  - finite element, 135
  - global matrix, 57, 194
- Stiffness
  - abbreviated subscripts, 47
  - of finite element model, 118
  - reduction to isotropic, 31
  - tensor, 30
  - transversely isotropic, 48
- Stoneley waves, 96, 194
- Strain
  - tensor, 30
- Strain energy density, 61
- Stress field
  - cylindrical, 41
  - diadic, 31
  - finite element discontinuities, 143
  - isotropic
    - layer matrix, 44
    - potentials, 42
  - liquid, 45
    - layer matrix, 46
  - tensor, 30
  - transversely isotropic, 53
    - layer matrix, 53
- Substitution
  - Cartesian for cylindrical, 74
  - reflection coefficients

- free case for embedded, 183
- Sumon, 208
- Sweeping
  - dispersion curves, 58
  - fine sweep, 59
- Thomson, 56
- Thurston, 27
- Torsional modes
  - attenuation, 82
  - behaviour, 71
  - mode shapes, 67
  - naming convention, 66
- Torvik, 142
- Tracing
  - dispersion curve, 60
  - extrapolation, 60
- Transfer matrix, 56
- Transversely isotropic
  - cylindrical wave model, 46–55
  - examples, 69
  - layer matrix, 53
  - multi-layered example, 86
- TRL, 203, 208
- Two-D FFT
  - benefits, 141
  - derivation, 138–139
  - disadvantages, 140, 148
  - example
    - for reflection coefficients, 145
  - experiments, 129
- Validation
  - against Berliner and Solecki, 104
  - against Gazis, 99
  - against Nagy and Nayfeh, 101
  - asymptotic limits, 95–98
  - attenuation extraction, 121
  - bar velocity, 95
  - energy density, 110
  - energy velocity, 112
  - experiments, 123–131
  - finite element, 115–123
  - internal consistency, 105–115
  - large radius, 96
  - mode shape consistency, 107
  - multiple layers, 106
  - phase velocity extraction, 117
  - predicted time signals, 118
  - published literature, 99–105
  - rayleigh velocity, 95
  - stonely waves, 96
- Viens, 27
- Voigt
  - viscous damping, 31
- Wave model
  - assumptions, 27–28
  - boundary conditions, 28–29
  - circumferential dependence, 52
  - cylindrical, 24–61
    - isotropic, 30–46
      - transversely isotropic, 46–55
  - historical background, 26–27
    - leaky, 27
    - transversely isotropic, 27
  - infinite media, 29–30
  - software, 56–61
  - validation, 94–131
- Wavelength
  - mode selection criterion, 192
- Wavelet transform, 140, 205
- Wavenumber
  - complex, 34
  - matching at layer interfaces, 81
  - projection, 63
- Woodward, 208
- Ynys-y-Gwas, 19, 186, 187